Hydrodynamics and Thermodynamics of Ice Accretion through Impact of Supercooled Large Droplets: Experiments, Simulations and Theory

Vom Fachbereich Maschinenbau
an der Technischen Universität Darmstadt
zur
Erlangung des Grades eines Doktor-Ingenieurs (Dr.-Ing.)
genehmigte

D i s s e r t a t i o n

vorgelegt von

Markus Schremb, M.Sc.

aus Mainz

Berichterstatter:	Prof. Dr.-Ing. C. Tropea
Mitberichterstatter:	Prof. Dr.-Ing. B. Weigand
	Apl. Prof. Dr.-Ing. S. Jakirlić
Tag der Einreichung:	25.01.2018
Tag der mündlichen Prüfung:	16.04.2018

Darmstadt 2018
D17 (Diss. Darmstadt)

Schremb, Markus:
Hydrodynamics and Thermodynamics of Ice Accretion through Impact of Supercooled Large Droplets: Experiments, Simulations and Theory
Darmstadt, Technische Universität Darmstadt

Jahr der Veröffentlichung der Dissertation auf TUprints: 2018
URN: urn:nbn:de:tuda-tuprints-73984
Tag der mündlichen Prüfung: 16.04.2018

Veröffentlicht unter CC BY-NC-ND 4.0 International:
Namensnennung - Keine kommerzielle Nutzung - Keine Bearbeitung

Dedicated to my father...

Abstract

Icing of solid surfaces is an ever-present problem for many engineering applications. In particular ice accretion due to the impact and freezing of supercooled water drops is rich in various physical processes and of relevance for aviation, road traffic, shipping, wind turbines, and high-voltage power lines and insulators. It is initiated by the impact of water drops being in a thermodynamic meta-stable state, followed by nucleation of the impacting drops and ending up with solidification of the liquid, potentially influenced by the impact surface. All of these processes have been separately the focus of extensive experimental, theoretical and numerical studies for many decades. However, for the first time the present work attempts to consolidate the understanding of all involved mechanisms, and to examine them in the context of icing of surfaces.

Following the aforementioned subdivision, the subprocesses of ice accretion are separately examined using experimental, theoretical and numerical approaches. Non-isothermal impact of both supercooled water drops and water drops initially at room temperature onto surfaces below the freezing point of water is studied experimentally and numerically, and the heat transfer during drop impact is theoretically modeled. Nucleation during drop impact is experimentally studied and theoretically modeled. The freezing process of supercooled water drops with wall contact is investigated, employing a novel experimental approach, and the influence of the wall is theoretically modeled. Finally, the mutual influence between fluid flow during drop impact and freezing of the impinging liquid is experimentally examined and theoretically modeled.

Due to its comprehensive nature and the application of new experimental approaches, the present work constitutes a fundamental contribution to a better understanding of the processes taking place during ice accretion by supercooled water drops. It provides theoretical models which allow the prediction of heat transfer during non-isothermal drop impact, the quantitative analysis of experiments aimed at nucleation during drop impact, the prediction of the characteristic solidification velocity for the case of water freezing with wall contact, and the prediction of the residual ice layer thickness after impact of an individual supercooled water drop.

Kurzfassung

Vereisung von Oberflächen ist ein allgegenwärtiges Problem in vielen technischen Bereichen. Vor allem die Vereisung aufgrund unterkühlter Wassertropfen beinhaltet verschiedenste physikalische Vorgänge und ist relevant für die Luftfahrt, den Straßenverkehr, die Schifffahrt, Windkraftanlagen sowie Hochspannungsleitungen und -isolatoren. Der Vorgang wird durch den Aufprall von Wassertropfen im thermodynamisch metastabilen Zustand initiiert und Nukleation der aufprallenden Tropfen führt schließlich zur Erstarrung der Flüssigkeit. Obwohl diese Teilprozesse im einzelnen jeweils seit einigen Jahrzehnten Gegenstand experimenteller, theoretischer und numerischer Untersuchungen sind, stellt die hier vorliegende Arbeit den ersten Versuch einer umfangreichen Untersuchung aller Teilprozesse vor dem Hintergrund der Vereisung dar.
Entsprechend der vorangegangenen Beschreibung werden die Teilprozesse mittels experimenteller, theoretischer und numerischer Methoden separat erforscht. Der nicht-isotherme Aufprall von Wassertropfen auf Oberflächen unterhalb des Schmelzpunktes von Wasser wird experimentell und numerisch untersucht, und die Wärmeübertragung während des Aufpralls theoretisch modelliert. Nukleation während des Aufpralls sowie die Erstarrung unterkühlter Tropfen mit Wandkontakt werden experimentell beobachtet und mathematisch modelliert. Die Interaktion von Fluidströmung und Erstarrung während des Tropfenaufpralls wird experimentell untersucht und mathematisch beschrieben.
Aufgrund ihres Umfangs und der Anwendung neuer experimenteller Ansätze, stellt die vorliegende Arbeit einen fundamentalen Beitrag zu einem besseren Verständniss der Vorgänge während der Vereisung aufgrund unterkühlter Wassertropfen dar. Die daraus resultierenden Modelle ermöglichen die Vorhersage der Wärmeübertragung während des nicht-isothermen Tropfenaufpralls, die quantitative Beschreibung der Nukleation während des Aufpralls, die Vorhersage der charakteristischen Erstarrungsgeschwindigkeit im Falle von Wasser mit Wandkontakt sowie die Vorhersage der resultierenden Eisschichtdicke nach dem Aufprall eines einzelnen unterkühlten Wassertropfens.

Acknowledgements

At the beginning of the present work, which represents the end of my doctoral candidature, I would like to express my gratitude to those people who contributed to the existence and success of this work in very different ways. I want to thank:

Professor Dr.-Ing. **Cameron Tropea** for letting me work at the *Institute for Fluid Mechanics and Aerodynamics* of the *Technische Universität Darmstadt*, and advising me during my doctoral candidature. Working at his institute enabled me gaining scientific and professional experience in facing and solving complex problems, and presenting and defending their solution on international conferences all around the world.

Professor Dr.-Ing. **Suad Jakirlić** for giving me the opportunity to be a part of the collaborative research center SFB-TRR 75, which enriched my professional expertise by enabling me to be part of a large interdisciplinary research project.

Professor Dr. **Ilia V. Roisman** for his encouragement and scientific support towards approaching and solving new complex problems, in particular by providing new perspectives.

Dr. rer. nat. **Hubert Marschall** for his motivation and encouragement, and his expertise in mathematics and fluid mechanics, which he handed on in the scope of the preparation of the Technische Strömungslehre exercise, and moreover always provided willingly when requested.

Dr.-Ing. **Edin Berberović** (University of Zenica) for our fruitful collaboration, involving his always available help and steady support in all questions regarding the numerical work.

Dr. **James M. Campbell** & Dr. **Hugo K. Christenson** (University of Leeds) for our fruitful collaboration, which enabled me to gain experience in approaching problems based on a non-engineering perspective, and to have a look outside of the box in Darmstadt.

Birgit Neuthe & **Stephanie Lath** for their always sympathetic ear and helpfulness in all non-scientific and administrative tasks.

Ilona Kaufhold and her team from the mechanical workshop for their support in designing and preparing the experimental facilities.

Furthermore, I want to thank some friends and colleagues at the TU Darmstadt who eased the all-day work and (mostly) made it worth commuting from Mainz to Darmstadt more than 800 times; which is equivalent to more than 1.7 circumnavigations of the world. In particular I want to thank **Benjamin Krumbein**, Dr.-Ing. **Daniel Kintea**, Dr.-Ing. **Rüdiger Röhrig**, **Jens M. Löwe** and **Vignesh Thamanna Gurumurthy** for some fruitful discussions and their willingness to provide help whenever requested. I in particular thank Daniel and Rüdiger for our collaboration in the probably most exciting project besides our regular research topics.
I also want to thank **Silvia Iannella** (M.Sc.), **Konstantin Kröll** (M.Sc.), **Sven Borchert** (B.Sc.) and **Thoren Webert** (B.Sc.) for their support in terms of research hours carried out during their Master's and Bachelor's Theses. Parts of their work have already been published and/or constitute significant part of the present study.

Last but definitely not least, I thank my mother **Birgit Schremb**, my grandmother **Frieda Schremb**†, and my girl friend **Johanna Gilavci** for their continuous support, facilitation, encouragement and bearing with me during the last years; probably this was the most important of all contributions, and enabled the existence of the present work in the first place.

The present work was financially supported by the *Deutsche Forschungsgemeinschaft* in the framework of the collaborative research center SFB-TRR 75.

Nomenclature

Latin letters, lower-case

Symbol	SI unit	Meaning
a	m^2/s	Thermal diffusivity
a^*	-	Square root of the ratio of the thermal diffusivities of water and ice
b_i	-	Polynomial coefficients in numerical value equation (Eq. A.22), $\mathrm{i} \in \mathbb{N}$
c	m/s	Speed of sound
c_i	-	Coefficients arising in several relations (Eqs. 3.14 and 4.10), $\mathrm{i} \in \{1, 2\}$
$c_{\mathrm{p,i}}$	J/(kg K)	Heat capacity at constant pressure of phase i, $\mathrm{i} \in \{\mathrm{s}, \mathrm{l}, \mathrm{sub}, \mathrm{g}\}$
c_s	kg/m^3	Solubility
$c_{\mathrm{v,i}}$	J/(kg K)	Heat capacity at constant volume of phase i, $\mathrm{i} \in \{\mathrm{s}, \mathrm{l}, \mathrm{sub}, \mathrm{g}\}$
c_dr	-	Drag coefficient
d	m	Diameter
e	$\mathrm{Ws}^{0.5}/(\mathrm{m}^2\ \mathrm{K})$	Thermal effusivity
f_i	1/s	Frequency of molecule attachment (Eqs. 2.23 and 2.35), $\mathrm{i} \in \{0, 1\}$
f_Hoff	°	Hoffman function
g	m/s^2	Magnitude of the gravitational acceleration
$\mathbf{g}$	m/s^2	Gravitational acceleration

Continued on next page

Latin letters (lower-case) continued from previous page

Symbol	SI unit	Meaning
Δg	J	Activation energy for molecule transfer across the solid-liquid interface
h	Js	Planck constant
h	m	Height or thickness
j	$1/(\mathrm{m}^2\mathrm{s})$	Nucleation rate per unit area
k	J/K	Boltzman constant
k	W/(m K)	Thermal conductivity
l	m	Length
m	kg	Mass
$\dot{m}$	kg/s	Mass flow
$\mathbf{n}$	m	Normal vector
n_{i}	$1/\mathrm{m}^2$	Nucleation site density (Eq. 2.51), $\mathrm{i} \in \{\mathrm{si}, 0\}$
p	N/m^2	Pressure
q	J/m^2	Area specific heat
$\dot{\mathbf{q}}$	$\mathrm{J}/(\mathrm{m}^2\mathrm{s})$	Heat flux
r	m	Radial coordinate
$s(t)$	m	Function associated with temporal viscous boundary layer expansion (Eq. 6.5)
t	s	Time
Δt	s	Computational time step
u_{i}	m/s	Component i of a velocity field
v	m/s	Velocity
x	m	x-coordinate

Continued on next page

Latin letters (lower-case) continued from previous page

Symbol	SI unit	Meaning
x	-	Dummy variable for Hoffman function
$\mathbf{x}$	m	Horizontal coordinate in a moving cartesian coordinate system
$\mathbf{x}'$	m	Horizontal coordinate in a fixed cartesian laboratory coordinate system
Δx	m	Computational cell size
y	m	y-coordinate
z	m	z-coordinate

Concluded

Latin letters, upper-case

Symbol	SI unit	Meaning
A	m^2	Area
B	m/s	Mass transfer coefficient
C_{H2O}	$\mathrm{mol/m}^3$	Molar concentration of water vapor
C_{i}	$1/\mathrm{m}^3$	Number of molecules per unit volume (Eqs. 2.22 and 2.35), $\mathrm{i} \in \{0, 1, \mathrm{R}^*\}$
D	m^2/s	Mass diffusivity
$\mathrm{E}_1(\mathrm{Pe}_0)$	-	Exponential integral of Pe_0
F	N	Force
G	J	Gibb's free energy

Continued on next page

Latin letters (upper-case) continued from previous page

Symbol	SI unit	Meaning
ΔG_v	$\mathrm{J/m^3}$	Energy of fusion per unit volume
J	$\mathrm{1/(m^3 s)}$	Nucleation rate per unit volume
$\dot{J}$	mol/s	Molar flow
L	J/kg	Latent heat of fusion per unit mass
L_eva	J/kg	Latent heat of evaporation per unit mass
L_v	$\mathrm{J/m^3}$	Latent heat of fusion per unit volume
M	kg/mol	Molar mass
N	-	Number
P	-	Dimensionless scale for solidification during drop impact (Eqs. 6.14)
P	-	Probability
Q	J	Heat
$\dot{Q}$	J/s	Heat flow
$\bar{\mathrm{R}}$	J/(mol K)	Universal gas constant
R	m	Radius
R^2	-	Coefficient of determination of a fitted relation
R_a	µm	arithmetic average of surface roughness values
$\mathrm{RH_i}$	%	Relative humidity at position i, $\mathrm{i} \in \{\infty, \mathrm{sur}\}$
$\mathrm{S}(\Theta)$	-	Shape factor characterizing heterogeneous nucleation depending on the contact angle Θ
T	K	Absolute temperature in K

Continued on next page

Latin letters (upper-case) continued from previous page

Symbol	SI unit	Meaning
$\mathbf{T}$	Pa	Viscous stress tensor
$\dot{T}$	K/s	Cooling rate
T_{m}	K	Melting temperature
$\mathbf{U}$	m/s	Velocity field
U_{cl}	m/s	Contact line velocity
V	m^3	Volume
$\dot{V}$	m^3/s	Volume flow
Y	N/m^2	Yield stress
Z	Pas/m	Specific acoustic impedance

Concluded

Greek letters

Symbol	SI unit	Meaning
α	$\mathrm{W}/(\mathrm{m}^2\ \mathrm{K})$	Heat transfer coefficient
α_{imp}	deg	Drop impact angle
β	1/K	Coefficient of thermal expansion
β_{wet}	-	Dimensionless spreading factor during drop impact
γ	-	Liquid phase fraction
γ_{el}	S/m	Electrical conductivity
γ_{f}	-	Frozen phase fraction

Continued on next page

Greek letters continued from previous page

Symbol	SI unit	Meaning
δ	-	Dimensionsless boundary layer thickness
ζ	s	Dummy variable for integration (Eq. 6.12)
η	kg/(m s)	Dynamic viscosity
θ	deg	Contact angle of a sessile drop
Θ	deg	Contact angle of an ice nucleus during heterogeneous nucleation
ϑ	°C	Relative temperature in °C
κ	1/m	Curvature
λ	$1/m^2$	Cumulative number of active nucleation sites per unit surface area
λ_{cr}	m	Critical wavelength for a morphological instability (Eq. 2.72)
λ_i	-	Constants in the relation for the computational time step (Eq. 3.14), $i \in \{1, 2\}$
λ_s	-	Prefactor in Stefan solution (Eq. 2.58)
Λ	-	Cumulative number of active nucleation sites
μ	m/(s K)	Kinetic coefficient for solidification
ν	m^2/s	Kinematic viscosity
ξ	-	Dimensionless time
Ξ	-	Denotes the water-ice interface
ρ	kg/m^3	Density
σ	N/m or J/m^2	Interfacial energy
τ_0	K	Coefficient in relation for nucleation site density (Eq. 2.51)

Continued on next page

Greek letters continued from previous page

Symbol	SI unit	Meaning
τ_i	-	Coefficients in the (in)viscid solution for the flow in a spreading drop (Eqs. 2.5, Eq. 2.7 and Eq. 6.14), $i \in \{1, 2, 3\}$
ϕ	-	Dummy variable for an arbitrary property (Eq. 3.5)
φ	-	Coefficient in theoretical relation for the heat transferred during drop spreading (Eq. 3.24)
Φ	K^2	Coefficient arising during modeling of nucleation (Eq. 2.25)
χ	m	Dummy boundary for integration (Eq. 6.4)
ψ	-	Dimensionless function in relation for contact temperature during drop impact (Eq. 2.11)
ω	1/s	Drop freezing rate

Concluded

Dimensionless groups

The listed dimensionless groups are defined in the following using characteristic scales for length, velocity and temperature difference, l, v and ΔT, respectively. In the case of drop impact these are commonly the drop diameter d_d and drop impact velocity v_d, and for non-isothermal drop impact the temperature difference between the drop and the substrate. Unless mentioned differently, in the context of nucleation and solidification, ΔT denotes a temperature difference with respect to the melting temperature T_m. The characteristic velocities used for the Capillary number and Courant number are the contact line velocity U_cl and the magnitude of the field velocity $|\mathbf{U}|$.

Symbol	Name	Definition and Meaning
Bi	Biot number	$\mathrm{Bi} = \frac{\alpha l}{k} \mathrel{\widehat{=}} \frac{\text{conductive resistance}}{\text{convective resistance}}$
Ca	Capillary number	$\mathrm{Ca} = \frac{\eta v}{\sigma} \mathrel{\widehat{=}} \frac{\text{viscous forces}}{\text{surface tension forces}}$
Cou	Courant number	$\mathrm{Cou} = \frac{v\Delta t}{\Delta x} \mathrel{\widehat{=}} \frac{\text{advection per time step}}{\text{spatial discretization}}$
Ec	Eckert number	$\mathrm{Ec} = \frac{v^2}{c_\mathrm{p}\Delta T} \mathrel{\widehat{=}} \frac{\text{kinetic energy}}{\text{enthalpy difference}}$
Gr	Grashof number	$\mathrm{Gr} = \frac{g\beta\Delta T l^3}{\nu^2} \mathrel{\widehat{=}} \frac{\text{buoyancy forces}}{\text{viscous forces}}$
Le	Lewis number	$\mathrm{Le} = \frac{a}{D} \mathrel{\widehat{=}} \frac{\text{thermal diffusion rate}}{\text{mass diffusion rate}}$
Nu	Nusselt number	$\mathrm{Nu} = \frac{\alpha l}{k} \mathrel{\widehat{=}} \frac{\text{convective heat flux}}{\text{conductive heat flux}}$
Pe	Peclet number	$\mathrm{Pe} = \frac{lv}{a} \mathrel{\widehat{=}} \frac{\text{advective transport}}{\text{diffusive transport}}$
Pr	Prandtl number	$\mathrm{Pr} = \frac{\nu}{a} \mathrel{\widehat{=}} \frac{\text{viscous diffusion rate}}{\text{thermal diffusion rate}}$

Continued on next page

Dimensionsless groups continued from previous page

Symbol	Name	Definition and Meaning
Ra	Rayleigh number	$\mathrm{Ra} = \mathrm{GrPr} \mathrel{\widehat{=}} \dfrac{\text{convective heat flux}}{\text{conductive heat flux}}$
Re	Reynolds number	$\mathrm{Re} = \dfrac{vl}{\nu} \mathrel{\widehat{=}} \dfrac{\text{inertial forces}}{\text{viscous forces}}$
Sc	Schmidt number	$\mathrm{Sc} = \dfrac{\nu}{D} \mathrel{\widehat{=}} \dfrac{\text{viscous diffusion rate}}{\text{mass diffusion rate}}$
Sh	Sherwood number	$\mathrm{Sh} = \dfrac{Bl}{D} \mathrel{\widehat{=}} \dfrac{\text{mass convection rate}}{\text{mass diffusion rate}}$
St	Stefan number	$\mathrm{St} = \dfrac{c_\mathrm{p}\Delta T}{L} \mathrel{\widehat{=}} \dfrac{\text{sensible heat}}{\text{latent heat}}$
We	Weber number	$\mathrm{We} = \dfrac{\rho v^2 l}{\sigma} \mathrel{\widehat{=}} \dfrac{\text{inertial forces}}{\text{surface tension forces}}$
		Concluded

Subscripts

Subscripts	Meaning
∞	far field
0	initial
adv	advancing
air	air
amb	ambient
av	average
bl	boundary layer
c	contact
cap	capillary
cl	contact line
clu	cluster
co	cooling
com	compression
con	convective
cr	critical
d	drop
del	delay
dr	drag
dyn	dynamic
eff	effective
el	electrical
eva	evaporative

Continued on next page

Subscripts continued from previous page

Subscripts	Meaning
exp	experimental
f	frozen
fl	fluid
for	forced
fro	front
g	gaseous
het	heterogeneous
hom	homogeneous
H2O	water
i	dummy for arbitrary subscript
int	interface
ice	ice
imp	impact
inv	inviscid
kin	kinetic
l	liquid
la	lamella
lam	laminar
lat	latent
lay	layer
life	life time
loc	local
med	median

Continued on next page

Subscripts continued from previous page

Subscripts	Meaning
m	melting
max	maximum
min	minimum
mod	model
n	normal
nat	natural
new	new
nu	nucleus
nuc	nucleation
num	numerical
old	old
p	pressure
P	point P
pr	present
pro	projected
r	in r-direction
R	radius
rec	receding
rel	relative
res	residual
s	solid
sat	saturation
sen	sensible

Continued on next page

Subscripts continued from previous page

Subscripts	Meaning
si	site
spr	spreading
st	static
sub	substrate
sur	surface
t	time
tan	tangential
tbl	thermal boundary layer
tr	transient
th	theoretical
tip	tip
tot	total
tur	turbulent
u	velocity
vis	viscous
v	volume
w	wall
wb	wet bulb
wet	wetted
x	in x-direction
y	in y-direction
z	in z-direction
σ	surface energy

Concluded

Abbreviations

Abbreviation	Meaning
approx.	approximately
A/D	analog/digital
CA	contact angle
const	constant
CCMU	computer control and monitoring unit
CSF	continuum surface force
HTC	heat transfer coefficient
i.e.	that is to say (from latin: id est)
LED	light-emitting diode
MST	marginal stability theory
PID	proportional-integral-derivative
PMMA	Poly(methyl methacrylate)
PTFE	Polytetrafluoroethylene
SLD	supercooled large droplets
VOF	volume-of-fluid

Concluded

Contents

Part I

Preface

1 Introduction

Icing of surfaces is ubiquitous in nature and engineering systems. If it occurs in nature, it mostly results in aesthetic structures, as shown for example in Fig. 1.1. However, despite the beauty of such ice formations, icing is an ever-present safety issue for many transportation systems, such as aviation [37, 65, 124, 142, 223, 275], shipping [217, 260, 305, 339] and road traffic [348]. Moreover, icing also affects the operational reliability and efficiency of wind turbines [78, 163, 262], photovoltaic devices [113, 164] and power supply systems [103, 189, 218, 350].

a) Clear ice rim

b) Rime ice feathers

Figure 1.1: Typical forms of ice accretion on tree branches caused by supercooled fog: a) glaze ice, and b) rime ice. Depending on the ambient conditions, these forms of ice accretion are also observed during aircraft icing, as shown in Fig. 1.3. (Photos are taken on 11/30/2014 in Niederroßbach, Germany. The ambient temperature was $\vartheta_{\mathrm{amb}} \approx -1 \ldots 0\,^{\circ}\mathrm{C}$ [284].)

The underlying processes which may result in ice accretion on surfaces are very different, comprising:

1. re-sublimation from the vapor phase (frost formation),
2. impingement and accretion of ice particles on warm surfaces,
3. freezing of water drops at rest on a solid surface, and
4. impingement and simultaneous freezing of liquid water drops.

While the physical mechanisms eventually resulting in ice accretion are manifold, in most cases icing represents a severe problem for the respective system. Ice accretion alters the outer shape, weight and surface morphology of the covered part, often resulting in a malfunction and reduced efficiency of the affected system. Icing due to re-sublimation from the vapor phase [173, 344, 389] in particular is a problem reducing the efficiency of cooling systems and heat exchangers [4, 180, 327, 328]. Accretion of impinging ice particles occurs on warm parts of aircraft's jet engines and heated measuring probes, negatively influencing the jet engine's operation and distorting the estimation of the flight conditions [177, 222, 223]. Freezing of sessile water drops on a solid surface [99, 172, 221, 249, 250, 323, 337, 353] may happen after drop impact onto a surface or drop condensation from the vapor phase, and is relevant for various fields. Icing due to the impingement and simultaneous freezing of water drops is of relevance for many different technical applications. It not only affects the operational reliability and efficiency of the respective system, but also poses a severe safety issue.

The latter form of ice accretion is rich in different physical processes whose experimental, numerical and theoretical examination is the focus of the present work.

1.1 Motivation

In particular the impingement and freezing of supercooled water drops is a well-known problem for various engineering applications. It may lead to ice accretion on cold parts of an aircraft such as an airplane's frame or wing [61, 65, 124, 142], helicopter rotor blades [60, 71, 114] or aircraft measuring probes, as shown in Fig. 1.2. Depending on the impact conditions and ambient temperature, different types of ice accretion such as glaze ice, rime ice or mixed ice, all exhibiting different characteristics, may result from the impingement of supercooled water drops [111, 210, 248, 304], as already shown for ice accretion in nature in Fig. 1.1. Similarly, these types of icing are also found in the case of aircraft icing as pictured in Fig. 1.3. A special case of aircraft icing is ice accretion due to supercooled large droplets (SLD) with diameters larger than approx. $50\,\mu m$ [160]. Only a small amount of these droplets freezes immediately after impact, while the remaining liquid can move on the surface due to the surrounding shear flow. It may result in ice accretion far aft of the leading edge of an airplane

a) Aircraft's airframe

b) Aircraft's wing

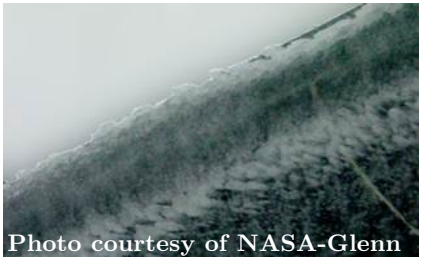

c) Helicopter rotor blade

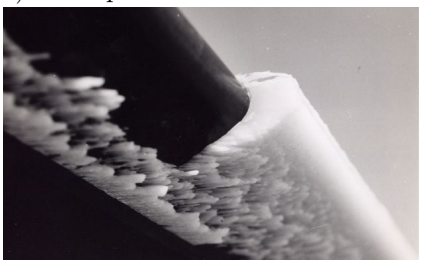

d) Aircraft pitot tube

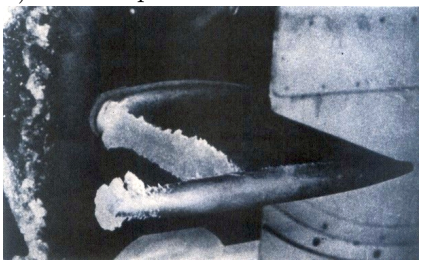

Figure 1.2: Typical positions of aircraft icing due to supercooled water droplets. (Figure c) is reprinted by permission of the UK Ministry of Defence, UK Crown Copyright. Figure d) is reprinted from [108], by permission of the Federal Aviation Administration, USA.)

wing, as shown in Fig. 1.3 d), which is commonly referred to as runback ice accretion.

Similar to the different types of icing which are accompanied by different ice accretion shapes, also the respective position of ice accretion has various effects on an aicraft's performance. In the case of iced airplane wings and helicopter rotor blades, ice accretion affects the aerodynamics of the aircraft [61], resulting in a decreased lift [53] accompanied by an increased drag [73], which finally causes a decrease of the aerodynamic efficiency of the aircraft. Ice accretion in general leads to increased weight of an aircraft, causing higher fuel consumption. Icing of aircraft's measuring probes can result in a wrong estimation of the flight conditions, which in the worst case may cause an aircraft crash [56]. To prevent ice accre-

a) Light rime ice

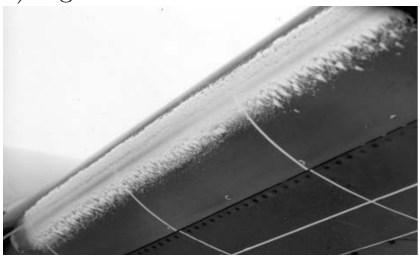

b) Severe glaze ice

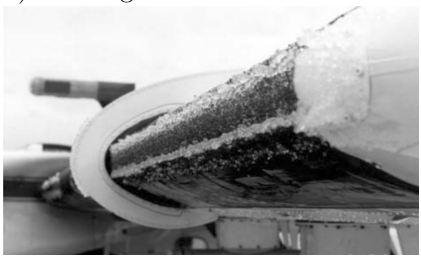

c) Moderate mixed ice

d) Supercooled large droplet ice

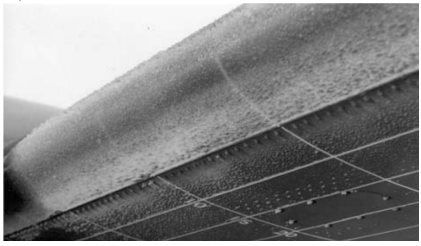

Figure 1.3: Forms of icing at the wings of a research aircraft of the NASA Glenn Research center after flight in different icing conditions. (Reprinted from [274], with permission from Elsevier.)

tion, the leading edge of some aircraft wings and measuring probes are heated [142]. This may help to avoid ice accretion due to supercooled water drops; however, it can promote the other mechanism of aircraft icing, namely accretion of impinging ice particles [177, 223]. Several techniques exist for the removal of existing ice accretion at the leading edge of an airplane wing such as pneumatic boots. These partially cover the leading edge of a wing and are inflated during flight which causes cracking and dispersion of an accumulated ice layer [142].

Ice accretion due to impinging water drops is not only related to aviation. It may also occur due to freezing sea water spray [212, 217] resulting in ice layers on the super structure of ships [260, 305, 339] and off-shore platforms [82, 209, 302–304, 345], as shown for example in Fig.1.4. Icing of ships causes an increasing weight of a ship and in turn increases the gauge of the vessel, which results in a higher drag and fuel consumption. Moreover, it poses a safety issue since it may cause capsizing of a ship

Figure 1.4: Iced ship superstructure after operation in marine icing conditions. (Reprinted by permission of DNV GL/Graeme Davies.)

if ice layers grow unbalanced [391]. Finally, marine icing by freezing sea spray negatively influences the operation of offshore production facilities comprising an increased repair time and failure rate [23].

Besides aeronautic and maritime systems, icing also affects technical onshore applications such as power supply systems [102, 189, 218], as shown in Fig.1.5. In this case, ice accretion has very different effects. On the one hand, icing of high-voltage insulators may alter the shape and the insulating properties of an insulator. It can deteriorate the properties of an insulator with respect to the surface conductivity or insulating clearance, potentially causing a partial or complete failure of the insulation [102]. In addition to electrical effects, ice accretion also affects the mechanical stability of the pylons, conductors and insulators. An increasing loading and non-uniform load distribution may result in a mechanical breakdown of the pylons or power line galloping [102, 104].

Another hazard of ice accretion related to power supply is icing of wind turbine blades [78, 153, 154, 163, 262], as shown for example in Fig. 1.6. It results in a reduced efficiency of a wind turbine and moreover may lead to an increased load and wear of the mechanical parts due to an imbalance of the rotor. Severe icing conditions may shut down entire wind farms, resulting in a drastic decrease of the production of electric energy. Moreover, iced rotor blades cause increased acoustic noise emissions [326], and ice layers shedding from the rotor blades pose a severe danger for pedestrians or technical systems nearby the wind turbine.

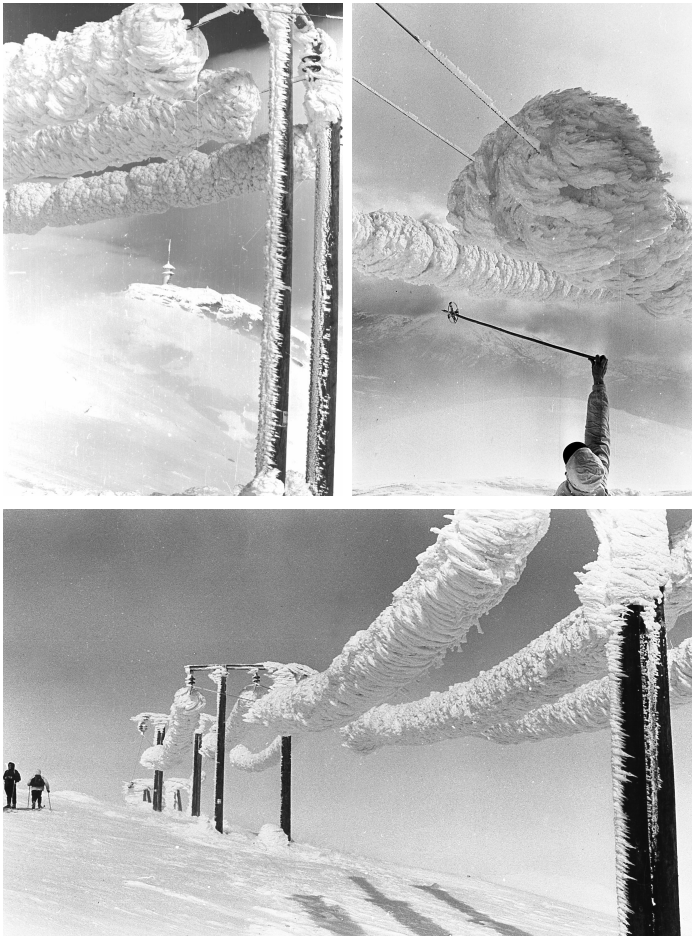

Figure 1.5: Iced power lines to the telecom tower on top of the Lønahorgi mountain (1410 m asl.) in Norway April 1961, leading to an ice load of 305 kg/m [112]. (Photos: O. Wist, reproduced by permission of S. M. Fikke.)

In summary, iced surfaces do not only affect the proper and reliable function of the respective system; they can also represent a serious safety issue, since aircraft may crash, ships can capsize, and power lines and pylons of high-voltage transmission systems can collapse as a consequence

Figure 1.6: Rime ice accretion on the leading edges of a 600 kW wind turbine's blades on the Olos mountain (Lapland, Finland), as a consequence of a deactivated electro-thermal anti-icing system. (Photo: A. Vignaroli, reproduced by permission of VTT Technical Research Centre of Finland.)

of the additional loading by ice accretion. Therefore, tools for the prediction and methods for the prevention of icing have attained increased attention during the last years. However, despite the necessity for, and the existence of such tools and methods, the physical mechanisms during ice accretion are still not completely understood. Accordingly, the aim of the present work is to improve the understanding of the physics during ice accretion due to impinging water drops. In particular, the focus of this study is on the physics of icing due to supercooled water drops. The distinct processes involved during icing of an individual water drop are separately examined by means of experimental investigations, theoretical modeling and numerical simulations.

1.2 Thesis outline

The outline of the present work follows mainly the subdivision of ice accretion due to impinging supercooled water drops into the involved sub-processes namely **drop impact**, **nucleation** and **solidification**.

Chapter 2 provides the theoretical background necessary for understanding the present work, comprising a thorough description of the different sub-processes, and an overview of relevant literature for each process.

Chapter 3 is devoted to the hydrodynamics and thermodynamics during non-isothermal drop impact at subfreezing conditions. The hydrodynamics during inclined and normal impact are examined experimentally and numerically in *Chapter 3.1*, while *Chapter 3.2* focuses on the thermodynamics during non-isothermal drop impact, which is investigated numerically and theoretically.

The subject of *Chapter 4* is nucleation of supercooled water during drop impact. It is experimentally investigated, and theoretically described and analyzed utilizing a statistical nucleation model.

Chapter 5 deals with the solidification of supercooled water drops resting on substrates of varying materials, which is experimentally examined and theoretically modeled.

After separate examination of the involved processes, *Chapter 6* is devoted to the mutual interaction of fluid flow and phase change during the impact of supercooled water drops on an ice surface. It is experimentally examined and theoretically modeled.

Each of the chapters involves a short introduction associating the respective study with the global context of the present work, which is followed by the description of the applied experimental or numerical method. After presentation of the experimental, numerical or theoretical results, each section is closed with a separate conclusion.

Chapter 7 and *8* complete the present work with a conclusion and outlook for future research, summarizing the results of the entire work and giving an outlook on open questions necessary to approach in future studies.

Part II

Theoretical Background

2 Phenomena involved in icing due to supercooled water drops

The term *supercooled* refers to the state of a material which is liquid, although its temperature is below the material's melting temperature T_m[1]. Since it emphasizes the fact that the temperature is below the melting point, also the term *undercooled* is often found in the literature [79]. However, in the scope of the present work, "supercooled" is consistently used to refer to this state of a liquid. Starting anno 1721 with observations by Daniel Gabriel Fahrenheit [101], the supercooling of water has been repeatedly examined since almost three centuries [8, 90, 351]. Water temperatures down to approx. $-40\,^\circ\mathrm{C}$ are possible without solidification [119, 192, 213, 390]. For lower temperatures, homogeneous nucleation necessarily results in solidification of the liquid. A comprehensive review about the properties, specialities and physics of supercooled water is found in [118].

The thermodynamically stable and thus preferable state of a material below its melting point is the solid phase [276]. A supercooled liquid below its melting temperature is in a meta-stable state. A certain energy is required to overcome the energy barrier of the Gibbs free energy for the formation of a stable nucleus during nucleation, which is the onset of the phase change process. The impact of a supercooled water drop onto a solid surface may provide this energy, thus triggering nucleation. Nucleation results in the formation of a stable nucleus and the subsequent solidification of the liquid. In comparison to the solidification at the melting temperature, a supercooled liquid changes its phase in a much more rapid, kinetic way. Therefore, the time scale of solidification of a supercooled liquid is much more comparable to the time scale of other processes such as drop impact, than it is in the case of planar solidification at the melting temperature. Solidification fixes the current shape of the potentially deformed impinging drop and leads to ice accretion on the impact surface.

[1] Since T_m per definition refers to the temperature at which the interface separating the solid and the liquid phase of a material is stationary, according to [360] "equilibrium crystallization temperature" would be a more appropriate term for T_m. However, for convenience "melting temperature" is used in the present work to refer to this temperature.

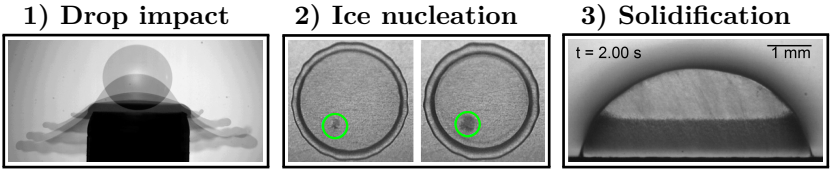

Figure 2.1: Processes involved in ice accretion due to impinging water drops: 1) The drop spreads during drop impact resulting in a dynamic change of the drop shape and the solid-liquid contact area. 2) Heterogeneous nucleation at the impact surface initiates drop freezing (highlighted by circles). 3) Solidification of the liquid ultimately fixes the shape of the deformed liquid. Note that, although the processes are shown in succesion, they may partially overlap.

Accordingly, several physical processes, taking place in parallel or succession, are involved in icing due to impinging supercooled water drops, as illustrated in Fig. 2.1. Ice accretion starts with

1. fluid flow and possible heat transfer during **drop impact**, followed by
2. **nucleation** of the liquid which is still mobile on the surface, ending up with
3. **solidification** of the liquid in successive stages, which may be thermally affected by the impact surface.

Following this subdivision of the process, the investigations concerning ice accretion in the present work focus on the three phenomena drop impact, nucleation and solidification of supercooled water. The theoretical background concerning these processes, which is necessary for the understanding of the present study, is separately introduced in the following sections. It involves known theoretical and mathematical descriptions of each sub-process as well as a review of related literature.

2.1 Drop impact

Due to its importance for various processes in nature and engineering, the phenomenon of drop impact onto a solid substrate has been extensively studied experimentally, theoretically and numerically for more than

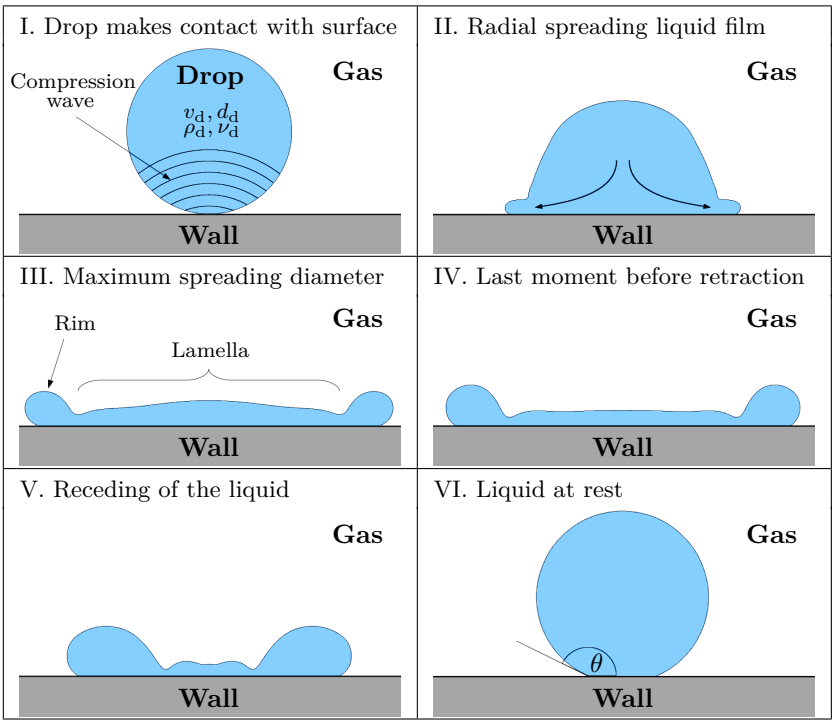

Figure 2.2: Schematic of the phases of normal impact of a drop (blue) onto a non-wettable solid wall. v_d is the impact velocity, d_d denotes the drop diameter, and ρ_d and ν_d are the liquid's density and kinematic viscosity, respectively. θ is the contact angle.

a century [379–381].

The different stages of a normal drop impact onto a solid substrate are illustrated in Fig. 2.2, corresponding to the labels in Fig. 2.3 which shows the temporal evolution of the diameter of the surface area wetted during impact, d_{wet}. When the drop makes contact with the solid substrate at time $t = 0$ (I.), the contact point of the drop is abruptly decelerated to zero velocity. This results in a large increase of the pressure at the contact point, and a compression wave propagating through the liquid drop with the speed of sound, c. The compression wave conveys the information of the change of velocity from the contact point into the drop [288]. Assum-

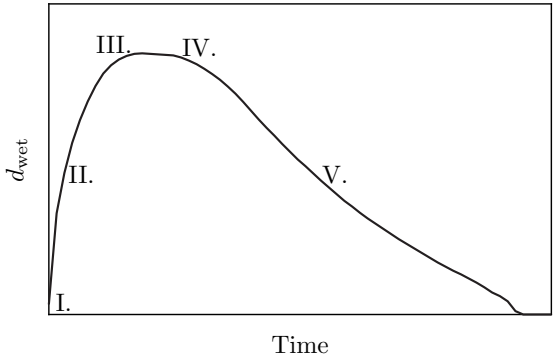

Figure 2.3: Temporal evolution of the diameter of the wetted surface area, d_{wet}, during normal drop impact onto a superhydrophobic surface. The labels in the diagram correspond to the stages of drop impact shown in Fig. 2.2.

ing a drop diameter of $d_{\mathrm{d}} \approx 3\,\mathrm{mm}$ and considering the speed of sound in water $c \approx 1482\,\mathrm{m/s}$ at $\vartheta_{\mathrm{d}} = 20\,^{\circ}\mathrm{C}$ [40, 83], the compression wave reaches the trailing edge (apex) of the drop after $t \approx 2\,\mu\mathrm{s}$. During this period, the apex of the drop advances completely undisturbed with its initial velocity. After that, liquid viscosity results in a deceleration of the entire bulk liquid. The pressure rise upon impact at the contact point of the drop, Δp, can be estimated as [288]

$$\Delta p = Z v_{\mathrm{d}}, \tag{2.1}$$

where $Z = \rho_{\mathrm{d}} c$ is the liquid's specific acoustic impedance and v_{d} is the drop's impact velocity; ρ_{d} denotes the liquid density. The impact velocity of a water drop with $\rho_{\mathrm{d}} \approx 10^3\,\mathrm{kg/m^3}$ and a falling height of $h = 0.3\,\mathrm{m}$ may be estimated as $v_{\mathrm{d}} = \sqrt{2gh}$, where g is the magnitude of the gravitational acceleration. Such a drop impact results in an enormous pressure rise of $\Delta p \approx 36\,\mathrm{bar}$, potentially causing erosion of the impact surface [54, 139, 356], which is a severe problem, e.g. for turbine blades [138, 197, 347, 401].

After the first contact between the drop and the surface, the liquid's inertia results in a fast radial spreading of a thin liquid film (the so-called *lamella*), wetting the substrate's surface by a rolling motion of the liquid (II.) [290]. As a result of capillary forces acting at the edge of the spreading liquid, a pronounced rim forms around the spreading lamella

(see III.) [298, 354]. The wetted surface area is surrounded by the so-called contact line where the three phases liquid, gaseous and solid meet.

The drop deformation and the wetting of the surface result in an increase of the total surface energy of the drop. Moreover, a viscous boundary layer at the impact surface develops in the spreading film. Its thickness $h_{\mathrm{vis}} \sim \sqrt{\nu_{\mathrm{d}} t}$ grows with time t and depends on the drop's kinematic viscosity, ν_{d} [294]. When the sum of the increase of the surface energy of the deformed drop and the energy dissipated by viscous friction during spreading equals the initial kinetic energy of the drop, the liquid flow comes to rest preventing further drop spreading (III.) [267, 386].

The processes taking place after maximum spreading significantly depend on the wettability of the impact surface. The wettability depends on the surface morphology and surface chemistry [80], and can be characterized by means of the contact angle (CA) θ, which is defined at the three phase contact line as shown in the last image in Fig. 2.2. The CA is not fixed but takes different values depending on the velocity of the contact line. During the spreading phase of a liquid film, the CA increases with the contact line velocity; it decreases with an increasing velocity in the case of a receding liquid film. In the case of a stagnant contact line (*sticking*), the CA may take different values in a certain range which is referred to as *contact angle hysteresis*. Incipient motion of the contact line starts at the bounds of this range. The CA present at the instant of incipient motion of a spreading film is called the advancing CA, θ_{adv}. In analogy, the CA at incipient motion of a receding liquid film is called the receding CA, θ_{rec}. Despite the possibility of very small contact angle hysteresis in the case of superhydrophobic surfaces ($\theta > 150°$), the advancing CA is generally larger than the receding CA.

After maximum spreading of the drop, when the contact line has stopped, capillary forces tend towards a minimization of the drop's liquid-gaseous interface. They cause the decrease of the CA from θ_{adv} to θ_{rec} without a significant change of the wetted surface area (compare III. & IV. in Figs. 2.2 and 2.3). The wetted surface area decreases after the CA takes the value of θ_{rec} (IV. & V.). After retraction of the liquid, the drop is at rest on the surface (VI.). The CA at rest is called the static CA, θ_{st}, with $\theta_{\mathrm{rec}} \leq \theta_{\mathrm{st}} \leq \theta_{\mathrm{adv}}$. For drop diameters smaller than the capillary length $l_{\mathrm{cap}} = \sqrt{\sigma_{\mathrm{lg}}/(\rho_{\mathrm{d}} g)}$, the shape of a sessile drop can be approximated as a truncated sphere ($\theta_{\mathrm{st}} > 90\,°$) or a spherical cap ($\theta_{\mathrm{st}} < 90\,°$) [229]; σ_{lg} is the surface energy of the liquid-gas interface, which is also referred to

as the surface tension.

The duration of the different phases and the exact outcome of a drop impact significantly depends on the wettability of the substrate and the impact conditions [293]. The receding phase of drop impact on a hydrophilic, wettable surface ($\theta < 90°$) is rather short, resulting in a large residual wetted surface area. In the case of a hydrophobic non-wettable surface ($\theta > 90°$), the receding phase is enhanced and leads to a smaller residual wetted surface area. In particular in the case of an energetic drop impact onto a superhydrophobic surface, the fluid's retraction may be even large enough to cause a partial or complete rebound of the liquid from the surface, as indicated by $d_{\mathrm{wet}} = 0$ in Fig. 2.3 [169, 293], or the formation of a singular liquid jet [26]. After rebound, the drop re-impacts on the surface. Depending on a balance of viscous, capillary and inertial forces, the drop finally comes to rest on the surface.

Depending on the impact conditions and the morphology of the impact surface, various phenomena may take place during drop impact, comprising prompt or corona splash during liquid spreading, receding breakup during the liquid's retraction [293, 386], or the entrapment of small gas bubbles below the liquid in particular during drop spreading over a rough surface [22, 273]. However, also drop impact onto a perfectly smooth surface is always associated with the entrapment of a larger gas bubble in the center of drop impact [169]. Due to the increase of the lubrication pressure of the surrounding gas between the drop and the surface before the moment of impact, the bottom of the impinging drop deforms, resulting in the entrapment of a disc-shaped portion of the surrounding gas, which then forms a bubble in the center of drop impact below the liquid [169].

Also hydrodynamic processes after drop impact such as liquid motion on the surface or drop shedding from the surface may be influential for icing. However, they are not the focus of the present study and have been examined in several previous studies [205, 206, 219, 297].

According to the initial temperatures of the drop and the surface, drop impact may be subdivided into isothermal drop impact (the drop and surface temperature are the same) and non-isothermal drop impact (the drop and surface temperature are different). While only the hydrodynamics determine the outcome after isothermal drop impact, also heat transfer is present during non-isothermal drop impact, which may additionally affect the hydrodyamics during, and the outcome of, drop impact.

2.1.1 Isothermal drop impact

The dynamics during isothermal drop impact particularly depend on the impact parameters, such as the impact velocity and drop diameter. Together with the liquid properties, which may strongly depend on temperature, the impact parameters determine the maximum drop spreading, which represents the potential maximum of the iced area after a single drop impact. The outcome of a drop impact can be quantified in terms of the temporal evolution of the wetted surface area and the thickness of the impinging drop. These quantities may be described by means of semi-empirical equations, involving dimensionless groups. The most important groups for the quantification of a drop impact are the Reynolds number

$$\mathrm{Re} \equiv \frac{d_\mathrm{d} v_\mathrm{d}}{\nu_\mathrm{d}} \tag{2.2}$$

and the Weber number

$$\mathrm{We} \equiv \frac{\rho_\mathrm{d} d_\mathrm{d} v_\mathrm{d}^2}{\sigma_\mathrm{lg}}. \tag{2.3}$$

While the Reynolds number is a means for the estimation of the predominance of inertial forces compared to viscous forces during drop impact, the Weber number compares inertial forces with capillary forces attributed to the free interface of the drop.

For impact Reynolds and Weber numbers of $\mathrm{Re} \gg 25$ and $\mathrm{We} \gg 2.5$, the flow in the spreading lamella of an impacting drop is dominated by inertia; viscous and surface tension effects do not play a role [296]. For a certain time during the initial impact period, the rear part of the impacting drop moves similar to a rigid body with the initial impact velocity. Accordingly, the lamella thickness at the center of impact, i.e. at the radial position $r = 0$, in the period $t < 0.4\, d_\mathrm{d}/v_\mathrm{d}$ can be described as [296]

$$h_\mathrm{la}(t, r{=}0) = d_\mathrm{d} - v_\mathrm{d} t. \tag{2.4}$$

For later times $t > 0.7\, d_\mathrm{d}/v_\mathrm{d}$, as long as the viscous boundary layer at the wall is small compared to the lamella thickness, $t < t_\mathrm{vis}$, expressions for the radial velocity of the lamella flow and the lamella thickness are obtained from the inviscid solution for the flow in a spreading liquid [296, 388] as

$$u_\mathrm{r}(t, r) = r\left(\frac{d_\mathrm{d}}{v_\mathrm{d}}\tau_1 + t\right)^{-1}, \quad h_\mathrm{la}(t, r{=}0) = \tau_2 d_\mathrm{d}\left(\tau_1 + \frac{v_\mathrm{d}}{d_\mathrm{d}} t\right)^{-2}, \tag{2.5}$$

with the dimensionless constants obtained in [296] as $\tau_2 \approx 0.39$ and $\tau_1 \approx 0.25$. Equations (2.4) and (2.5) are part of a universal solution for the flow in the lamella of a spreading drop, which is valid for all impact conditions in the aforementioned ranges of Re and We. Both conditions are satisfied in all studies of drop impact in the present work.

The aforementioned expressions were modified for times $t > t_{\mathrm{vis}}$, when viscosity starts to play an important role for the lamella flow. It accounts for the influence of the expanding viscous boundary layer on the flow in the thinning liquid, and results in an expression for the lamella thickness as

$$h_{\mathrm{la}}(t, r=0) = d_{\mathrm{d}}(h_{\mathrm{inv}} + h_{\mathrm{vis}}), \tag{2.6}$$

with

$$h_{\mathrm{inv}} = \tau_2 \left(\frac{v_{\mathrm{d}}}{d_{\mathrm{d}}} t \right)^{-2}, \quad h_{\mathrm{vis}} = \frac{4\tau_3}{5} \frac{\sqrt{\frac{v_{\mathrm{d}}}{d_{\mathrm{d}}} t}}{\sqrt{\mathrm{Re}}}, \tag{2.7}$$

and the constant $\tau_3 \approx 0.626$ [294]. For long times after impact, when the thickness of the viscous boundary layer is of the order of the lamella thickness, viscosity damps the flow in the lamella. The residual lamella thickness after drop impact with large Reynolds numbers can be estimated by equating the thickness of the expanding viscous boundary layer and the thickness of the thinning lamella, resulting in [294]

$$h_{\mathrm{la}}(t \to \infty, r=0) = 0.79 d_{\mathrm{d}} \mathrm{Re}^{-2/5}. \tag{2.8}$$

With consideration of different phenomena during drop spreading, varying approaches for the estimation of the maximum spreading of an impacting drop, $d_{\mathrm{wet,max}}$, have been proposed [70, 95, 267, 294, 308, 362]. These approaches are based on a dynamic energy balance, the dynamics of the contact angle, a simple mass balance or the expansion of a viscous boundary layer. All models reveal different scaling laws involving the Reynolds number and Weber number, and are reviewed in [169]. Since it will be used later in the present study, only one of these expressions, namely the one proposed in [294] is given here as

$$d_{\mathrm{wet,max}} = d_{\mathrm{d}} \left(0.87\,\mathrm{Re}^{1/5} - 0.4\,\mathrm{Re}^{2/5}\,\mathrm{We}^{-1/2} \right). \tag{2.9}$$

2.1.2 Non-isothermal drop impact

Under isothermal conditions, when the temperature of the drop and the impact surface are equal, the temperature of the impinging drop does not significantly change upon impact. The outcome of drop impact only depends on the material properties of the impinging liquid, the impact conditions and the surface properties. However, in the case of non-isothermal drop impact, the temperature at the interface between the impacting liquid and the substrate changes to the contact temperature T_c as soon as the drop is in contact with the surface. The emergence of the contact temperature upon first contact between the drop and the surface is accompanied by the expansion of thermal boundary layers in both the spreading liquid and the impact surface. With neglect of convective heat transfer in the spreading liquid, the temporal evolution of the boundary layer thickness, h_tbl, can be estimated as [52]

$$h_\mathrm{tbl} \sim \sqrt{at}, \tag{2.10}$$

where $a = k/(\rho c_\mathrm{p})$ is the thermal diffusivity of the respective phase; k denotes the thermal conductivity and c_p is the heat capacity at constant pressure. The contact temperature is constant as long as the thermal boundary layers in the solid substrate and the spreading liquid expand undisturbed; i.e. as long as their thickness is smaller than the solid's and the liquid's thickness itself, respectively. With consideration of the fluid flow during spreading, the temporal evolution of the temperature profile in the spreading liquid and the solid substrate have been described in [295], where the contact temperature during drop impact at the substrate surface, $z = 0$, is obtained as

$$T_\mathrm{c} = \frac{e_\mathrm{d} T_\mathrm{d} + e_\mathrm{sub}\psi(\mathrm{Pr}) T_\mathrm{sub}}{e_\mathrm{d} + e_\mathrm{sub}\psi(\mathrm{Pr})}. \tag{2.11}$$

In this equation, $e_\mathrm{i} = \sqrt{\rho_\mathrm{i} c_\mathrm{p,i} k_\mathrm{i}}$ is the thermal effusivity of phase i and T_i is its initial temperature; the subsripts d and sub refer to the drop and the impact substrate, respectively. The term $\psi(\mathrm{Pr})$ is a dimensionless function depending on the Prandtl number

$$\mathrm{Pr} \equiv \frac{\nu_\mathrm{d}}{a_\mathrm{d}}. \tag{2.12}$$

The Prandtl number relates viscous diffusion to thermal diffusion in a fluid and is of relevance for the estimation of convective heat transfer during non-isothermal drop impact. Note that in the case of high Prandtl

numbers, $\psi(\mathrm{Pr} \to \infty) = 1$, and Eq. 2.11 reduces to the solution for the contact temperature between two semi-infinite solid slabs of different initial temperature, suddenly brought into contact [20]. The contact temperature T_c is an important parameter in the scope of non-isothermal drop impact with phase change. Depending on the contact temperature, different phase transitions may be initiated upon contact of the liquid drop with the surface. While the surface remelts [14, 295, 311, 393] in the case of a contact temperature above the substrate's melting temperature, $T_\mathrm{c} > T_\mathrm{m,sub}$, solidification of the impinging drop [264, 265] may be observed for $T_\mathrm{c} < T_\mathrm{m,d}$.

The temporal evolution of the heat flux into the substrate normal to its surface is obtained as [295]

$$\dot{q}(r,t) = \frac{e_\mathrm{d} e_\mathrm{sub} (T_\mathrm{sub,0} - T_\mathrm{d,0})}{[e_\mathrm{d} + e_\mathrm{sub}\psi(\mathrm{Pr})]\sqrt{\pi(t - t_\mathrm{wet}(r))}}, \tag{2.13}$$

where $t_\mathrm{wet}(r)$ is the instant of the beginning of the thermal boundary layer growth depending on wetting of the surface; i.e. it is the inverse function of the spreading radius $r_\mathrm{wet}(t)$. The heat transfer into the substrate and the resulting contact temperature do not only determine the type of the phase transition, but also significantly affect the speed of it, as will be shown in the present work.

2.1.3 Related literature

Experimental results, modeling approaches, and numerical investigations concerning drop impact are comprehensively reviewed in [169, 220, 287, 288, 294, 296, 386, 387]. While the hydrodynamics of drop impact are well understood, there is still a lack of understanding of processes involved in non-isothermal drop impact [200]; despite its importance for many technical applications comprising thermal spray coating [91, 107, 214], spray cooling [176, 201, 202], fuel drop impingement in internal-combustion engines [259] and icing of surfaces. During icing, the unsteady heat transfer between the liquid and the wall is an important effect concerning nucleation and subsequent freezing of an impinging drop. While a changing liquid temperature may affect nucleation [152, 280], the absolute liquid temperature is the dominating quantity for the solidification velocity of the liquid [79, 280]. Heat transfer during non-isothermal drop impact has been examined numerically [28, 33, 263, 264], experimentally [51, 52, 234, 264, 400] as well as theoretically [28, 51, 52, 224, 295, 399].

However, examination of non-isothermal drop impact remains a challenge due to its inherent unsteadiness and the large ranges of length and time scales involved. Direct experimental insight into the phenomena during non-isothermal drop impact is difficult, thus motivating the examination of the phenomena using theoretical modeling and numerical simulations.

If drop impact is accompanied by phase change, as in many cases of non-isothermal drop impact, the process becomes even more complicated. While the liquid-gas phase change is related to the impact of a colder drop onto a hot wall [176, 200–202], the solid-liquid phase transition is mainly involved during the impingement of a warm drop onto a colder surface [165–167, 277]. However, if the impinging liquid is supercooled, also an impact onto a warmer surface may be accompanied by a solid-liquid phase transition. Drop impact with solid-liquid phase change [14, 15, 265, 266] is present in various technical applications such as microcasting [311, 393], net-form manufacturing [257], and thermal or plasma spray coating [105, 106]. While solidification during drop impact serves a certain purpose in the aforementioned applications, it is a severe hazard in the scope of icing. Therefore, a deep knowledge of the processes during drop impact with phase change is of fundamental importance not only for the improvement of various technical applications, but also for the understanding of icing.

Drop impact with solid-liquid phase change has been studied theoretically [31, 32, 214], numerically [14, 239, 264, 265], and experimentally [15, 38, 85, 225, 264, 266] for many decades in the scope of thermal and plasma spray coating; reviews are found in [91, 105, 106]. Icing due to the impingement of (supercooled) water drops [53, 210, 211, 248, 261, 349, 350] and its consequences for system performance [47–49, 73, 153, 163] as well as methods for icing prevention [189, 262] have been studied on a rather macroscopic scale for several decades. Examination was mostly based on field experiments under icing conditions, icing wind tunnel experiments, and theoretical modeling and numerical simulations. Reviews of the work in this field are found in [60, 65, 71, 73, 103, 124, 260].

In recent years the impact and freezing of individual water drops has attained more attention in an effort to improve the understanding of the physical mechanisms during icing. It has been studied theoretically [21, 97, 384], numerically [41, 385] and experimentally [166, 232, 394]. Despite the increasing number of studies in this field, the physics during icing are not completely understood. In the abscence of phase change, the

impact of supercooled water drops does not substantially differ from the impact of non-supercooled water drops. However, only few studies explicitly took into account the special case of phase change during the impact of supercooled drops [9, 21, 97, 195, 196, 282, 385]. More often, the hydrodynamics during impact onto superhydrophobic surfaces were the focus of the experimental investigations [11, 171, 215, 216, 231, 232, 385]. These studies often aim to examine the applicability of superhydrophobicity for the design of anti-icing surfaces [9, 10, 21, 43, 66, 120, 171, 230, 324]. Two means often used for the estimation of a surface's so-called *icephobicity* are the freezing delay time and nucleation temperature of water drops in contact with the respective surface [94, 227, 228, 357]. The freezing delay is the time by which nucleation and freezing of a drop is delayed with respect to a characteristic instant, e.g. the moment of first contact between the drop and the surface. The nucleation temperature denotes the temperature at which nucleation is observed in a drop. However, until now a very important aspect has mostly been ignored during these evaluations of a surface's icephobicity: Nucleation is a stochastic process. An appropriate means for the estimation of a surface's icephobicity is to completely take into account the stochastic nature of nucleation, involving comparison of nucleation rates as already done in some studies concerning freezing of sessile drops [42, 98]. However, despite its relevance also for the case of drop impact, so far the statistics of nucleation has been almost completely ignored during evaluation of icephobicity by means of the freezing delay, and examination of phase change during drop impact in general [6, 148, 171, 366, 384]. Although the statistics of nucleation is mostly recognized and thus also reported in the respective studies, mean values of the freezing delay time or the nucleation temperature obtained from only a few experiments are often used for the evaluation of a surface's icephobicity [94, 148, 171]. The problem is that due to the statistics of nucleation, these quantities obtained from a few repeated experiments are not necessarily representative for the underlying nucleation process. Therefore, there is still a lack of understanding of the physics during the impact of supercooled water drops, in particular with respect to the statistics of nucleation during impact, which will be thoroughly examined in the present work for the first time.

2.2 Nucleation

The onset of a first-order phase transition is called nucleation; it is the first irreversible formation of a nucleus (latin: "kernel", "inner part") of the stable phase [5, 175]. In the case of a phase transition from gaseous to liquid, or from liquid to solid, this nucleus has to be large enough to overcome the energy barrier of the Gibbs free energy ΔG which is associated with the formation of an interface between the solid and the liquid phase, and the release of latent heat. A prerequisite for nucleation is a temporary thermodynamic unstable state of the system [280], such as a supersaturation or supercooling for the formation of a liquid nucleus from the vapor phase or a solid nucleus from the liquid phase, respectively [175]. While melting commonly takes place at the melting temperature, solidification always occurs after a supercooling of the liquid more or less below the melting temperature [276]. The solid nucleus formation is based on molecular motion which results in temporal and spatial fluctuations of temperature and density of the liquid phase [280]. Since the molecular motion is of stochastic nature, also nucleation is a stochastic process. It can be statistically modeled which is commonly referred to as the *classical nucleation theory*.

Depending on the circumstances under which nucleation takes place, it can be divided into homogeneous and heterogeneous nucleation. Homogeneous nucleation occurs in a pure liquid and is based only on the aforementioned fluctuations of temperature and density. These fluctuations eventually cause the formation of a cluster of molecules sufficiently large to overcome the barrier of the Gibbs free energy. Heterogeneous nucleation takes place at the solid-liquid interface between the supercooled liquid and the solid phase of a foreign material, which in the following is referred to as the nucleant. For a certain temperature, the rate of heterogeneous nucleation is commonly higher than the rate of homogeneous nucleation. It depends on the surface morphology and the chemical properties of the nucleant [152, 155, 280].

As long as an impinging drop of supercooled water is liquid, it may continue deformation or move on the substrate until solidification fixes its current shape. Therefore, the stochastic nature of nucleation, being the onset of solidification, may strongly influence the shape and size of the area iced after a drop impact onto a dry surface; even if the impact conditions are constant. Hence, the statistics of nucleation is an important aspect in the scope of icing. Besides its significance for ice accretion,

both homogeneous and heterogeneous nucleation are of great relevance for meteorology and weather forecast. They control condensation and glaciation of clouds in the atmosphere, and thus are important for the formation of precipitation [280].

2.2.1 Homogeneous nucleation

The Gibbs free energy ΔG for nucleation in a volume of supercooled liquid is the difference of the total energy of the volume of supercooled liquid and the total energy of the same supercooled liquid comprising a solid nucleus which has formed from the liquid. It corresponds to the surface energy required for the formation of the solid-liquid interface of the solid nucleus, and the energy of fusion which is released during formation of the nucleus. Therefore, the Gibbs free energy for the formation of a spherical nucleus with radius R, is [276]

$$\Delta G = -\frac{4}{3}\pi R^3 \Delta G_\mathrm{v} + 4\pi R^2 \sigma_\mathrm{sl}, \tag{2.14}$$

where ΔG_v is the energy of fusion per unit volume and σ_sl is the interfacial energy per area between the solid and the liquid phase. With the assumption of a constant heat capacity of the solid and the liquid phase, the volumetric energy of fusion can be approximated as [276]

$$\Delta G_\mathrm{v} = \frac{L_\mathrm{v} \Delta T}{T_\mathrm{m}}, \tag{2.15}$$

where $L_\mathrm{v} = \rho_\mathrm{s} L$ is the latent heat of fusion per unit volume and ΔT is the liquid supercooling; ρ_s and L are the density of the solid phase and the latent heat of fusion per unit mass, respectively. The resulting dependence of the Gibbs free energy, ΔG, on the nucleus radius is shown in Fig. 2.4. Due to the fact that the energy of fusion is proportional to R^3 while the surface energy is proportional to R^2, the difference of the two energies results in a maximum of the free energy at $\Delta G^* = \Delta G(R^*)$, as schematically shown in the figure. It represents the aforementioned energy barrier for nucleation and is also referred to as the critical energy for nucleation; R^* denotes the critical nucleation radius. According to the principle of minimum total potential energy, the considered system of supercooled liquid, eventually comprising a solid nucleus, tends to a minimization of the Gibbs free energy. Therefore, for a solid nucleus smaller than the critical radius, $R < R^*$, dissolving of the nucleus is

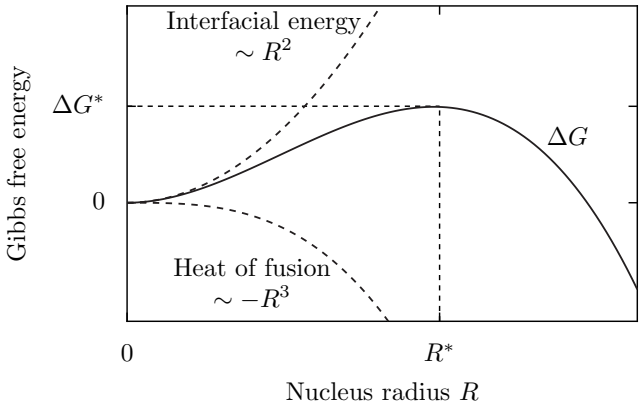

Figure 2.4: Change of the Gibbs free energy ΔG associated with the formation of a spherical nucleus with radius R.

favorable to lower the Gibbs free energy, as seen in Fig. 2.4. A nucleus whose size is $R > R^*$ will further grow, since this is also accompanied by a decrease of the Gibbs free energy; the liquid starts freezing.

The critical nucleus radius R^* and the critical Gibbs free energy ΔG^* are obtained by derivation from

$$\frac{\mathrm{d}\,(\Delta G)}{\mathrm{d}R} = 0 \tag{2.16}$$

as

$$R^* = \frac{2\sigma_{\mathrm{sl}}}{\Delta G_{\mathrm{v}}}, \tag{2.17}$$

and

$$\Delta G^* = \frac{16\pi\sigma_{\mathrm{sl}}^3}{3\Delta G_{\mathrm{v}}^2}. \tag{2.18}$$

Using Eq. 2.15 for the energy of fusion per unit volume, these quantities can be expressed as functions of the liquid supercooling

$$R^* = \left(\frac{2\sigma_{\mathrm{sl}} T_{\mathrm{m}}}{L_{\mathrm{v}}}\right) \frac{1}{\Delta T} \tag{2.19}$$

$$\Delta G^* = \left(\frac{16\pi\sigma_{\mathrm{sl}}^3 T_{\mathrm{m}}^2}{3L_{\mathrm{v}}^2}\right) \frac{1}{(\Delta T)^2}. \tag{2.20}$$

As seen from Eq. 2.20, the critical Gibbs free energy decreases with increasing supercooling. Thus, nucleation is more likely to happen at lower liquid temperatures since the energy barrier for nucleation decreases. Similarly, the critical nucleus radius also decreases with increasing supercooling, also making nucleation more favorable for a given liquid volume.

The formation of a nucleus of a certain size only depends on molecular motion, and thus is a stochastic process. Therefore, also the event when a nucleus reaches the critical nucleation radius is stochastic in time. The rate of homogeneous nucleation, i.e. the rate of appearance of nuclei with $R > R^*$ per liquid volume may be described considering the population density of nuclei of critical size and the rate at which molecules attach to these nuclei. The average number of spherical molecule clusters with radius R in a system consisting of $N_{\mathrm{clu,tot}}$ water molecules can be approximated by the Boltzman expression as [276]

$$N_{\mathrm{clu,R}} = N_{\mathrm{clu,tot}} \exp\left(-\frac{\Delta G(R)}{\mathrm{k}\,T}\right), \tag{2.21}$$

where $\Delta G(R)$ is the Gibbs free energy associated with a cluster of radius R according to Eq. 2.14, $\mathrm{k} = 1.381 \times 10^{-23}$ J/K is the Boltzmann constant and T denotes the liquid temperature. Equation 2.21 is generally valid for $T > T_{\mathrm{m}}$. However, for $T < T_{\mathrm{m}}$, the relation is only valid for $R \leq R^*$, since molecule clusters of size $R > R^*$ are stable nuclei and already part of the solid phase [276]. ΔG increases rapidly with the cluster size R and N_{R} decreases exponentially with ΔG. Therefore, the probability for the occurrence of a cluster with a certain size decreases very rapidly with increasing cluster size.

According to Eq. 2.21, the number of clusters per unit volume that have reached the critical nucleus size R^* is [152]

$$C_{\mathrm{R}^*} = C_0 \exp\left(-\frac{\Delta G^*}{\mathrm{k}\,T}\right), \tag{2.22}$$

where C_0 is the number of molecules per unit volume of the liquid. Since C_{R^*} refers to the number of clusters of critical size R^*, addition of only one further molecule to a cluster causes $R > R^*$, resulting in stable growth of the cluster associated with a decrease of the Gibbs free energy of the system. If molecules attach to a cluster of critical size with a frequency f_0, the homogeneous nucleation rate with dimensions of nuclei per unit

time and unit volume can be calculated as

$$J_{\mathrm{hom}} = f_0 C_0 \exp\left(-\frac{\Delta G^*}{\mathrm{k}\,T}\right). \tag{2.23}$$

The frequency f_0 is a complex function of the vibration frequency of the molecules, the activation energy for diffusion in the liquid, and the surface area of the critical nuclei [276]. An exact value for f_0 is hard to derive, however it is sufficient to assume $f_0 \approx 10^{11}\,\mathrm{s}^{-1}$, as proposed for the nucleation of pure metals [276]. Nevertheless, based on the theory of absolute reaction rates [125], a relation for f_0 has been proposed as [361]

$$f_0 \approx \frac{\mathrm{k}T}{\mathrm{h}} \exp\left(-\frac{\Delta g}{\mathrm{k}T}\right), \tag{2.24}$$

where h is Planck's constant and Δg is the activation energy for molecule transfer across the solid-liquid interface. With the expression for the critical Gibbs free energy from Eq. 2.20, the relation for the homogeneous nucleation rate, Eq. 2.23, may be rewritten as

$$J_{\mathrm{hom}} = f_0 C_0 \exp\left[-\frac{\Phi}{(\Delta T)^2}\right], \tag{2.25}$$

where the parameter

$$\Phi = \frac{16\pi\sigma_{\mathrm{sl}}^3 T_{\mathrm{m}}^2}{3L_{\mathrm{v}}^2 \mathrm{k}T} \tag{2.26}$$

is relatively insensitive to temperature T for the relevant range of liquid temperatures. Therefore, the homogeneous nucleation rate is approx. $J_{\mathrm{hom}} \sim \exp[-(\Delta T)^{-2}]$. This strong dependence on the supercooling results in a large variation of the homogeneous nucleation rate in a narrow range of supercoolings, which has also been found experimentally [118]. Using Eq. 2.25 and the properties of water $\sigma_{\mathrm{sl}} \approx 0.033\,\mathrm{J/m^2}$ [149], $C_0 \approx 3.34 \times 10^{28}\,\mathrm{m}^{-3}$, $T_{\mathrm{m}} = 273.15\,\mathrm{K}$, $L_{\mathrm{v}} \approx 333.3 \times 10^6\,\mathrm{J/m^3}$ [203], $\mathrm{k} \approx 1.38 \times 10^{-23}\,\mathrm{J/K}$ and $T = (T_{\mathrm{m}} - \Delta T)$, the homogeneous nucleation rate of supercooled water depends on supercooling as shown in Fig. 2.5. The two dashed vertical lines in the figure correspond to $\Delta T = 40\,\mathrm{K}$ and $\Delta T = 42\,\mathrm{K}$, in between which the nucleation rate increases by approx. three orders of magnitude. According to this steep increase of the nucleation rate, a critical supercooling for homogeneous nucleation may be introduced. For $\Delta T < \Delta T_{\mathrm{nuc}}$, virtually no nuclei are formed, and for $\Delta T > \Delta T_{\mathrm{nuc}}$, the rate of nuclei formation drastically increases. This

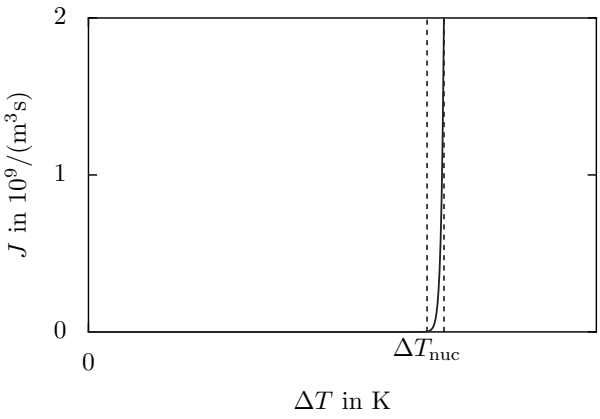

Figure 2.5: Dependence of the homogeneous nucleation rate on the liquid undercooling ΔT, shown as a solid line. The two dashed vertical lines correspond to the range $\Delta T = [40, 42]\,\mathrm{K}$ in which the nucleation rate drastically increases several orders of magnitude.

dependence represents a rather discontinuous behavior with respect to temperature, meaning that the statistics of nucleation become increasingly unimportant for $\Delta T > \Delta T_{\mathrm{nuc}}$, since nucleation takes place on a small time scale which is irrelevant for many applications. Moreover, due to impurities suspended in the water, or the liquid being in contact with a solid such as in the case of casting processes, homogeneous nucleation is unimportant for many technical applications.

2.2.2 Heterogeneous nucleation

Homogeneous nucleation is rather irrelevant for icing of surfaces. In particular due to the liquid's contact with a foreign material during drop impact, heterogeneous nucleation is the preferred mechanism for the initiation of solidification. Heterogeneous nucleation takes place due to the contact of the liquid with a solid phase, impurities suspended in the liquid, or more generally if a nucleant is involved in the process. In these cases, an ice nucleus forms favorably at so called nucleation sites on the nucleant. Nevertheless, the approach for the mathematical description of heterogeneous nucleation is similar to the mathematical approach to

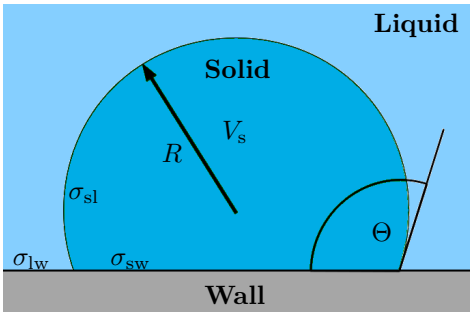

Figure 2.6: Heterogeneous nucleation of a spherical ice nucleus of volume V_s and radius R at a flat solid wall. Θ denotes the contact angle associated with the attraction of ice to the solid wall, related to the interfacial energies σ_{ij} via Eq. 2.28.

homogeneous nucleation.

If an ice nucleus forms at a flat surface of a nucleant as shown in Fig. 2.6, the interfacial term in Eq. 2.14 reduces with respect to a constant nucleus volume according to the reduction of the interfacial area between the liquid and the solid phase. During the formation of a solid nucleus of spherical shape with radius R and volume V_s at a wall, as shown in the figure, an interface between the solid and the liquid phase of area A_{sl} and interfacial energy σ_{sl} is formed. Moreover, the interface between the solid and the wall of area A_{sw} and interfacial energy σ_{sw} is formed; it replaces the initial interface between the liquid and the wall of the same area, but with the interfacial energy σ_{lw}. According to these formations and deformation of the interfaces, and the release of latent heat, the Gibbs free energy for the heterogeneous formation of a nucleus, as shown in Fig. 2.6, is [276]

$$\Delta G_{het} = -V_s \Delta G_v + A_{sl}\sigma_{sl} + A_{sw}\sigma_{sw} - A_{sw}\sigma_{lw}. \tag{2.27}$$

The shape of the solid nucleus may be described by means of the contact angle Θ at the contact line where the solid, the liquid and the nucleant meet. Based on a balance of the interfacial energies, the contact angle Θ can be expressed as [152]

$$\Theta = \operatorname{acos}\left(\frac{\sigma_{lw} - \sigma_{sw}}{\sigma_{sl}}\right). \tag{2.28}$$

In analogy to the contact angle θ used to quantify the attraction between a surface and a liquid, the contact angle Θ is a measure for the attraction of ice to a surface. Accordingly, $\Theta = 0\,^\circ$ corresponds to a surface maximally attractive to ice, while $\Theta = 180\,^\circ$ characterizes a surface which is abhorrent to ice, and thus not influential for ice nucleation. Using Eq. 2.28, the relation for the Gibbs free energy in the case of heterogeneous nucleation, Eq. 2.27, may be rewritten as a function of the contact angle Θ as

$$\Delta G_{\mathrm{het}} = \left(-\frac{4}{3}\pi R^3 \Delta G_{\mathrm{v}} + 4\pi R^2 \sigma_{\mathrm{sl}} \right) \mathrm{S}(\Theta), \tag{2.29}$$

where

$$\mathrm{S}(\Theta) = \frac{(2+\cos\Theta)(1-\cos\Theta)^2}{4} \tag{2.30}$$

is a shape factor only depending on the spherical nucleus geometry, described by the contact angle Θ. The shape factor takes values in the interval $[0, 1]$. A surface characterized by $\Theta = 90\,^\circ$ is indifferent to ice, i.e. the interfacial energy between the wall and the ice is the same as between the wall and the liquid. However, according to Eq. 2.29, heterogeneous nucleation at such a surface is associated with a reduced Gibbs free energy of nucleation.

In analogy to the case of homogeneous nucleation, the critical nucleus radius and critical Gibbs free energy are found from

$$\frac{\mathrm{d}\left(\Delta G_{\mathrm{het}}\right)}{\mathrm{d}R} = 0 \tag{2.31}$$

as

$$R^* = \left(\frac{2\sigma_{\mathrm{sl}} T_{\mathrm{m}}}{L_{\mathrm{v}}} \right) \frac{1}{\Delta T} \tag{2.32}$$

and

$$\Delta G^* = \left(\frac{16\pi \sigma_{\mathrm{sl}}^3 T_{\mathrm{m}}^2}{3 L_{\mathrm{v}}^2} \right) \frac{1}{(\Delta T)^2} \mathrm{S}(\Theta). \tag{2.33}$$

As seen from a comparison with Eqs. 2.17 and 2.18, the critical nucleation radius is unaffected by the wall. However, the critical Gibbs free energy for heterogeneous nucleation is lowered by the shape factor $\mathrm{S}(\Theta)$ with respect to the case of homogeneous nucleation at the same liquid temperature, thus

$$\Delta G^*_{\mathrm{het}} = \mathrm{S}(\Theta) \Delta G^*_{\mathrm{hom}}. \tag{2.34}$$

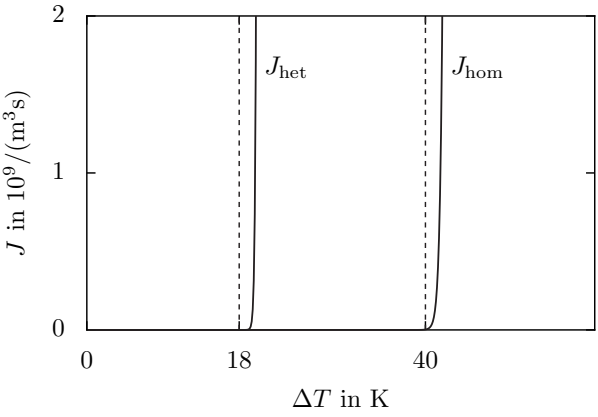

Figure 2.7: Dependence of the nucleation rate on the liquid supercooling ΔT for the case of homogeneous nucleation and heterogeneous nucleation with $\mathrm{S}(\Theta) = 0.25$, shown as solid lines. The dashed lines correspond to the critical supercooling above which the nucleation rate drastically increases with supercooling.

For $\Theta \to 0\,^\circ$, representing a flat disc shaped nucleus as in the case of ice being the nucleant, $\mathrm{S} \to 0$, resulting in a vanishing energy barrier for nucleation, i.e. $\Delta G_{\mathrm{het}} \to 0$. However, in the case of $\Theta = 0\,^\circ$, the nucleus shape has to be modeled in a different way, as described e.g. in [276]. In the limit $\Theta = 180\,^\circ$, the shape factor $\mathrm{S} = 1$ results in $\Delta G_{\mathrm{het}} = \Delta G_{\mathrm{hom}}$; the nucleant does not promote the nucleation process.

In analogy to homogeneous nucleation, the heterogeneous nucleation rate with dimensions of nuclei per unit time and unit volume is [276]

$$J_{\mathrm{het}} = f_1 C_1 \exp\left(-\frac{\Delta G^*_{\mathrm{het}}}{\mathrm{k}\,T}\right) = f_1 C_1 \exp\left[-\frac{\Phi}{(\Delta T)^2}\mathrm{S}(\Theta)\right], \qquad (2.35)$$

where f_1 is the frequency of attachment of molecules to a nucleus with critical size and C_1 denotes the number of molecules per unit volume of the liquid which are in contact with the nucleant.

As in the case of homogeneous nucleation, the nucleation rate is approx. $J_{\mathrm{het}} \sim \exp[-(\Delta T)^{-2}]$. Therefore, similar to the existence of a critical supercooling for homogeneous nucleation, also the heterogeneous nucleation rate is rather discontinuous with respect to temperature, resulting in a

small time scale of nucleation, if $\Delta T > \Delta T_{\mathrm{nuc}}$. However, due to the shape factor $\mathrm{S}(\Theta) \leq 1$ in the exponential in Eq. 2.35, the critical heterogeneous nucleation temperature is reduced in comparison to the critical homogeneous nucleation temperature as shown for example in Fig. 2.7. The calculations concerning the relation between ΔT and J_{het} are based on the assumptions $f_1 = f_0$, $C_1 = C_0$, $\mathrm{S}(\Theta) = 0.25$, and the material properties used for the calculation of J_{hom} in Sec. 2.2.1. The exact reduction of the critical supercooling for nucleation depends on the contact angle Θ characterizing the nucleant. As indicated in Fig. 2.7, the rate of increase of the nucleation rate increases with decreasing $\mathrm{S}(\Theta)$, corresponding to a decreasing critical supercooling. By this, the discontinuous character of nucleus formation is even more pronounced for heterogeneous nucleation in comparison to homogeneous nucleation.

So far, a flat surface of the nucleant has been assumed during the derivation. For the case of a curved surface such as in the case of impurity particles causing heterogeneous nucleation, the description follows a similar statistical approach. In that case the geometric effect of the nucleant curvature on the interfacial terms in Eq. 2.27 is accounted for by means of a geometric factor similar to the shape factor in Eq. 2.30 [116]. The critical nucleation temperature T_{nuc} and the heterogeneous nucleation rate J_{het} increase for increasing size of the impurity particles which is associated with a decreasing nucleant curvature.

Also imperfections of a nucleant surface such as steps and corners on a crystalline nucleant surface, pits in the surface of an ice nucleating particle, or grooves in a nucleant surface may affect a nucleant's influence on nucleation. While these effects theoretically may promote heterogeneous nucleation [115, 117, 258, 359], experimental evidence exists for an only small influence of surface scratches on the ice nucleating ability of a nucleant [58]. The modeling of the effect of surface imperfections on nucleation is not described here and can be found in [152].

2.2.3 Experimental approach to nucleation

As shown in the previous sections, both homogeneous and heterogeneous nucleation are stochastic processes based on molecular motion. Therefore, experiments and their analysis regarding both types of nucleation may follow the same statistical approach, which is reviewed in [182].

Due to its irreversibility, nucleation in an amount of supercooled liquid

causes freezing of the entire liquid. According to the relations presented in the previous sections, the probability of freezing of an amount of water is not only determined by the temperature dependent nucleation rate, but also by the liquid volume and time. The nucleation rate for certain conditions may be derived from observations of the repeated freezing of a liquid with a known volume. Experimental investigations are mostly based on the observation of freezing events in a large ensemble of equal-sized drops, which are simultaneously exposed to equal conditions [182]. However, experiments may also be performed using one liquid specimen, e.g. in a small capillary, which is successively exposed to the same conditions multiple times [24, 144, 376, 377]. Although these experimental procedures differ, the theoretical background for the analysis of the respective experimental results is based on the same theory.

Two important theories namely the *statistical nucleation model* [192, 193] and the *singular nucleation model* [152] may be used for the description and analysis of experimental data concerning nucleation. The statistical nucleation model is based on the stochastic nature of nucleation and involves time as an important parameter. It often serves for the calculation of nucleation rates at a constant temperature for both homogeneous and heterogeneous nucleation. The singular nucleation model is only applied for experiments regarding heterogeneous nucleation and is based on the fact that nucleation is rather a discontinuous process with respect to temperature, as shown in Figs. 2.5 and 2.7. It is often used for the estimation of ice nucleating abilities of different materials and their influence on the nucleation temperature T_{nuc}, obtained from experiments involving a constant cooling of the liquid specimen. The statistical nucleation model predicts a dependence of the freezing of drops in an ensemble on the cooling rate of the ensemble. However, this dependence is not predicted by the singular nucleation model, in which time in general does not play any role. According to this varying account for time as an influential or irrelevant parameter, the appropriate application of one of the theories depends on the relevance of time for the process in the scope of which nucleation is examined. The singular nucleation model is the appropriate means for the description of nucleation in the scope of slow processes such as cloud glaciation where time is rather irrelevant, and the process is primarily determined by the ice nucleating ability of dust particles or other atmospheric contaminants potentially affecting nucleation. For a dynamic process such as a drop impact, the time dependence of nucleation may play an important role, as will be shown in the present work.

Therefore, in this case the account for nucleation using the stochastic nucleation model is in general more appropriate.

Both the statistical and the singular nucleation model as well as related experimental studies are thoroughly reviewed in [363]. Note that the vocabulary, used in the present work in the context of nucleation, is based on the ice nucleation terminology proposed in [364].

2.2.3.1 The statistical nucleation model

Experimental data concerning homogeneous nucleation are well described by means of the statistical nucleation model. However, in the case of a homogeneous distribution and homogeneous ice nucleating ability of the involved ice nucleating particles and sites, the theory may also be applied for experiments concerning heterogeneous nucleation. Based on the descriptions in [64, 152, 276, 280] , the statistical nucleation model is derived as follows.

Consider a large ensemble of N_0 isolated and equal sized drops of a pure liquid at a temperature $T < T_\mathrm{m}$. Each drop has the volume V_d and is exposed to the same conditions. Then the probability for homogeneous nucleation in an individual drop during the time interval $[t, t+\mathrm{d}t]$ is equal for each drop of the ensemble, and is calculated as the number of active nuclei per drop as $V_\mathrm{d} J_\mathrm{hom}(T)\mathrm{d}t$. Assuming that freezing of a drop is caused by only one nucleation event per drop, the average probability for nucleation in a drop until time t is

$$P_\mathrm{nuc}(V_\mathrm{d}, t) = \frac{N_\mathrm{f}(t)}{N_0}. \tag{2.36}$$

where $N_\mathrm{f}(t)$ denotes the number of frozen drops of the ensemble at time t. The assumption of only one nucleation event per drop is reasonable at least for homogeneous nucleation in small drops, since the large growth velocity of ice at low temperatures is very likely to cause solidification of the entire liquid before the formation of a second nucleus [280][2]. The average probability for nucleation in a drop increases with time. Since $N_\mathrm{f}(t)/N_0 = 1$ corresponds to the instant when all drops of the ensemble

[2]For the case of large nucleation rates, small growth velocities and large liquid volumes, i.e. if more than one nucleus forms in a drop, the decrease of the liquid volume available for further nucleation events may be accounted for with the extended volume method according to the Kolmogorov-Johnson-Mehl-Avrami equation [16–18, 168, 179] (see [175]).

are frozen, Eq. 2.36 is only valid for times associated with $P_{\mathrm{nuc}}(V_{\mathrm{d}}, t) \leq 1$. The number of frozen drops at time $t + \mathrm{d}t$ is

$$N_{\mathrm{f}}(t + \mathrm{d}t) = N_{\mathrm{f}}(t) + [N_0 - N_{\mathrm{f}}(t)] V_{\mathrm{d}} J_{\mathrm{hom}}(T) \mathrm{d}t, \tag{2.37}$$

and normation of this relation with N_0 yields

$$P_{\mathrm{nuc}}(V_{\mathrm{d}}, t + \mathrm{d}t) = P_{\mathrm{nuc}}(V_{\mathrm{d}}, t) + [1 - P_{\mathrm{nuc}}(V_{\mathrm{d}}, t)] V_{\mathrm{d}} J_{\mathrm{hom}}(T) \mathrm{d}t. \tag{2.38}$$

Moreover

$$P_{\mathrm{nuc}}(V_{\mathrm{d}}, t + \mathrm{d}t) = P_{\mathrm{nuc}}(V_{\mathrm{d}}, t) + \frac{\partial}{\partial t} P_{\mathrm{nuc}}(V_{\mathrm{d}}, t) \mathrm{d}t, \tag{2.39}$$

and with Eq. 2.38, it follows

$$\frac{\partial}{\partial t} P_{\mathrm{nuc}}(V_{\mathrm{d}}, t) = [1 - P_{\mathrm{nuc}}(V_{\mathrm{d}}, t)] V_{\mathrm{d}} J_{\mathrm{hom}}(T). \tag{2.40}$$

With

$$N_{\mathrm{l}}(t)/N_0 = P_{\mathrm{l}}(V_{\mathrm{d}}, t) = 1 - P_{\mathrm{nuc}}(V_{\mathrm{d}}, t), \tag{2.41}$$

where $N_{\mathrm{l}}(t)$ and $P_{\mathrm{l}}(V_{\mathrm{d}}, t)$ are the number of liquid drops at time t and the average probability of an individual drop to be still liquid at time t, respectively, integration of Eq. 2.40 finally results in the relation for the decay of the relative number of liquid drops

$$\frac{N_{\mathrm{l}}(t)}{N_0} = \exp\left[- \int_0^t V_{\mathrm{d}} J_{\mathrm{hom}}(T) \mathrm{d}t \right]. \tag{2.42}$$

If the ensemble temperature is kept constant which is associated with a constant nucleation rate, the relative number of liquid drops exponentially decays with time as

$$\frac{N_{\mathrm{l}}(t)}{N_0} = \exp\left[- V_{\mathrm{d}} J_{\mathrm{hom}}(T)\, t \right], \tag{2.43}$$

while it is

$$\frac{N_{\mathrm{l}}(t)}{N_0} = \exp\left[- \frac{V_{\mathrm{d}}}{\dot{T}} \int_{T_0}^{T^*} J_{\mathrm{hom}}(T) \mathrm{d}T \right], \tag{2.44}$$

when the drops are cooled down from T_0 to T^* with a constant cooling rate $\dot{T} = \partial T / \partial t$, where $t \mathrel{\widehat{=}} (T_0 - T)/\dot{T}$. While the nucleation rate is the

physical quantity, characterizing the nucleation process, the experimentally observed decay of the drop ensemble is characterized by the freezing rate [364]

$$\omega = -\frac{1}{N_\mathrm{l}} \frac{\mathrm{d}N_\mathrm{l}}{\mathrm{d}t}, \tag{2.45}$$

which is directly proportional to the underlying nucleation rate and the sample volume, $\omega = J_\mathrm{hom} V_\mathrm{d}$, as evident from Eq. 2.43. The term freezing rate often also denotes the growth velocity of ice. Therefore, to avoid any mix-up and confusion, in the present work the term drop freezing rate is used in the context of the decay of a drop ensemble by nucleation, while freezing rate is only used in the context of ice growth.

Since the probability for nucleation in a drop is independent of nucleation in the other drops, and just depends on the average number of nucleation sites per drop until time t, the freezing of an ensemble of drops can also be modeled as a Poisson process. With the average number of active nucleation sites per drop until time t being $\Lambda = V_\mathrm{d} J_\mathrm{hom}(T)\, t$, the probability for the occurrence of exactly N_nu nucleation events per drop until time t is [109]

$$P(N_\mathrm{nu}, t) = \frac{\Lambda^{N_\mathrm{nu}} \exp(-\Lambda)}{N_\mathrm{nu}!}, \quad N_\mathrm{nu} \in \mathbb{N}_0. \tag{2.46}$$

With $N_\mathrm{nu} = 0$, corresponding to a drop free of nuclei, Eq. 2.46 reduces to the probability for a drop to be liquid until time t as

$$P(0, t) = P_\mathrm{l}(V_\mathrm{d}, t) = \exp[-V_\mathrm{d} J_\mathrm{hom}(T)\, t] \mathrel{\widehat{=}} \frac{N_\mathrm{l}(t)}{N_0}, \tag{2.47}$$

which is equivalent to Eq. 2.43.

The previous derivations refer to homogeneous nucleation in a pure liquid. However, the same approach may be applied for heterogeneous nucleation in the case of a homogeneous distribution of ice nucleating particles in the liquid which is the source of the drop ensemble. In this case, also the heterogeneous nucleation rate is proportional to the liquid volume, and the decay of the relative number of liquid drops is calculated in analogy to the case of homogeneous nucleation [152]. It is

$$\frac{N_\mathrm{l}(t)}{N_0} = \exp\left[-V_\mathrm{d} J_\mathrm{het}(T) t\right] \tag{2.48}$$

and

$$\frac{N_\mathrm{l}(t)}{N_0} = \exp\left[-\frac{V_\mathrm{d}}{\dot{T}}\int_{T_0}^{T^*} J_\mathrm{het}(T)\mathrm{d}T\right], \tag{2.49}$$

for the case of a drop ensemble exposed to a constant temperature or constant cooling rate, respectively. Note that both Eqs. 2.44 and 2.49 predict a decreasing rate of decay of a drop ensemble for an increasing cooling rate $\dot{T}$.

While heterogeneous nucleation only implicitly depends on the liquid volume, it directly depends on the surface area of the nucleant which is in contact with the liquid. Assuming the nucleation sites to be equally effective in nucleating ice and to be homogeneously distributed all over the surface of the nucleant, A_wet, the absolute rate of the formation of nuclei, $V_\mathrm{d}J_\mathrm{het}$, may be substituted by $A_\mathrm{wet}j_\mathrm{het}$, where j_het denotes the heterogeneous nucleation rate coefficient with dimensions of nuclei per unit time and unit area [363, 364]. In analogy to the case of homogeneous nucleation, with the assumption of exactly one nucleation event causing freezing of a drop, the heterogeneous nucleation rate coefficient is related to the experimentally observed drop freezing rate ω of a drop ensemble as

$$j_\mathrm{het} = \frac{\omega}{A_\mathrm{wet}}. \tag{2.50}$$

Equations 2.43 - 2.49 enable the calculation of the rate of homogeneous or heterogeneous nucleation based on experimental observations of the macroscopic freezing of an ensemble of liquid drops exposed to equal conditions, which allow the measurement of $N_\mathrm{l}(t)/N_0$. Typical results of nucleation experiments at a constant supercooling are illustrated in Fig. 2.8, showing the decay of a drop ensemble depending on the liquid supercooling. According to Eqs. 2.23 and 2.35 the slope of the decay curve in the semi-logarithmic plot represents the average rate of nuclei formation per drop; i.e. the drop freezing rate ω.

The statistical significance of the nucleation rate obtained with Eqs. 2.43 - 2.49 increases with an increasing number of drops contained in the ensemble, which is often of the order of $10 \ldots 10^2$ drops [55, 58, 375]. However, according to [183], a statistical analysis is already possible for an ensemble size of $N_0 = 5$.

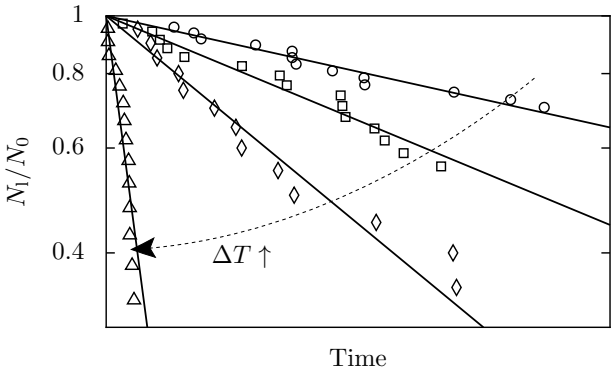

Figure 2.8: Temporal decay of the relative number of liquid drops, $N_l(t)/N_0$, as the typical result of nucleation experiments at constant temperature. While the varying symbol types correspond to the temperature of the drop ensemble, each symbol of an ensemble represents the observation of the freezing of one drop of the ensemble. The solid lines are fits of Eq. 2.43 to the experimental data. Due to the logarithmic scale of the y-axis, the negative slope of these lines is representative for the average rate of nuclei formation per drop, $\omega = V_d J_{hom/het}$, which increases for increasing supercooling, as predicted by the classical nucleation theory.

2.2.3.2 The singular nucleation model

As shown in the previous section, the stochastic nucleation model may be used for the description of both homogeneous and heterogeneous nucleation, and the time dependence of the nucleation process is explicitly taken into account. In contrast, the singular nucleation model is only used for the analysis of experimental data concerning heterogeneous nucleation, in particular when the liquid used for the preparation of the ensemble of drops contains ice nucleating particles or sites with a spectrum of varying ice nucleating abilities [363, 364]; e.g. due to a varying size of the particles suspended in the liquid. As shown in Fig. 2.7, the nucleation rate drastically increases at a certain critical temperature T_{nuc}, which depends on the ice nucleating ability of the foreign phase. Based on this almost discontinuous relation between the temperature and the nucleation rate, in the scope of the singular nucleation model each of the potential nucleation

sites in the liquid is associated with a critical nucleation temperature, regardless of the stochastic behavior of nucleation. Nucleation at a certain nucleation site is assumed to occur exactly at this temperature. Accordingly, a drop containing nucleation sites of varying effectiveness will freeze when the temperature reaches the critical nucleation temperature corresponding to the most effective nucleation site. Although the distribution of ice nucleating particles in an ensemble of drops is also based on certain statistics, in the present work stochastics and statistics of nucleation always refer to a nucleation behavior which is stochastic in time; i.e. to the time dependent behavior of nucleation described using the stochastic nucleation model.

The singular nucleation model is commonly used for the examination of experimental data obtained from drop ensembles cooled down with a defined cooling rate. The time dependence of nucleation is usually not taken into account and the singular nucleation model is based on expressions for the nucleation site density or nucleus spectra [152, 364]. The nucleation site density $n_{\mathrm{si}}(\Delta T)$ is the cumulative number of nucleation sites per unit surface area of the nucleant that become active during cool down to $T = T_{\mathrm{m}} - \Delta T$ [364]. Based on results of atmospheric measurements of the concentration of ice nucleating particles, the dependence of the averaged nucleation site density on temperature can be estimated as [152, 192, 280]

$$n_{\mathrm{si}}(\Delta T) = n_0 \exp\left(\frac{\Delta T}{\tau_0}\right), \tag{2.51}$$

where n_0 and τ_0 are constants. Based on Poisson statistics, the nucleation site density is related to the relative number of liquid drops at the supercooling ΔT as [72, 152, 375]

$$\frac{N_{\mathrm{l}}(\Delta T)}{N_0} = \exp[-n_{\mathrm{si}}(\Delta T) A_{\mathrm{wet}}], \tag{2.52}$$

where $N_{\mathrm{l}}(\Delta T)$ is the number of liquid drops left at ΔT, and A_{wet} is the surface area of the nucleant in contact with the liquid in each drop of the ensemble. This relation allows the estimation of the nucleation site density from an experimentally observed drop ensemble decaying with decreasing temperature, if the wetted surface area of the nucleant is known.

Using Eqs. 2.51 and 2.52, the dependence of the relative number of liquid drops on the liquid supercooling is described by the Gompertz function

$$\frac{N_{\mathrm{l}}(\Delta T)}{N_0} = \exp\left[-n_0 \exp\left(\frac{\Delta T}{\tau_0}\right) A_{\mathrm{wet}}\right]. \tag{2.53}$$

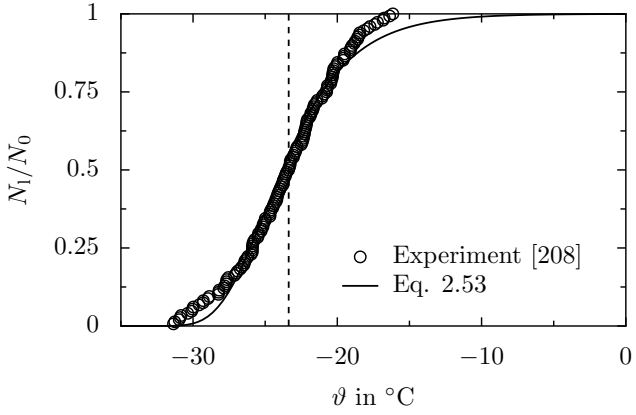

Figure 2.9: Survival curve of an ensemble of 148 sessile water drops exposed to a constant cooling rate of $\dot{T} = 5\,\mathrm{K/s}$ [208]. Each symbol represents freezing of one drop and the solid line is a fit of the data using Eq. 2.53. The dashed vertical line corresponds to the median freezing temperature $\vartheta_{\mathrm{nuc,med}} \approx -23.4\,^{\circ}\mathrm{C}$, where $N_1(\vartheta_{\mathrm{nuc,med}})/N_0 = 0.5$.

In contrast to the stochastic nucleation model, the singular nucleation model does not predict a dependence of the decay of the relative number of liquid drops on the cooling rate of the drop ensemble.

A typical result of a nucleation experiment at a constant cooling rate is illustrated in Fig. 2.9 as the survival curve depending on temperature for a drop ensemble containing 148 drops [208]. Experimental data are shown as circles and the solid line represents a fit of Eq. 2.53 to the experimental data. In the scope of nucleation experiments at constant cool down, the median freezing temperature $\vartheta_{\mathrm{nuc,med}}$ may be used as a characteristic measure for nucleation. It corresponds to the freezing of half of the drops of the ensemble, $N_1(\vartheta_{\mathrm{nuc,med}})/N_0 = 0.5$, and is shown as a dashed line in the figure.

Figure 2.10 shows the nucleation site density as a function of supercooling, obtained from the same experiment as the data shown in Fig. 2.9. The experimental data are shown as circles and the solid line represents a fit of Eq. 2.52 to the data. Using the area of the nucleant wetted by an indivudal drop, $A_{\mathrm{wet}} \approx 0.503 \times 10^{-6}\,\mathrm{m}^2$, fitting of Eq. 2.52 to the

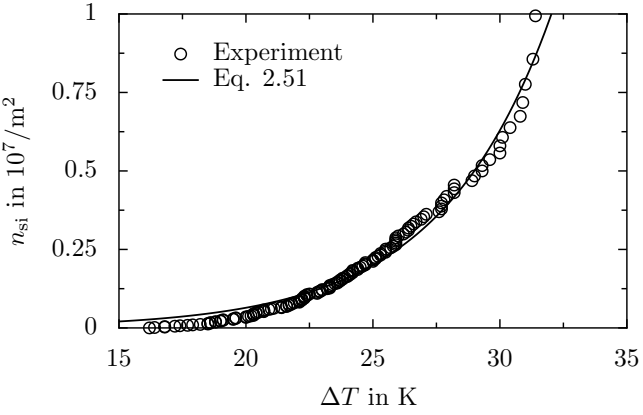

Figure 2.10: Nucleation site density n_{si} as a function of supercooling, obtained from an experiment with $N_0 = 148$ drops, exposed to a constant cooling rate, corresponding to the results shown in Fig. 2.9 [208]. Each symbol represents freezing of one drop and the solid line is a fit of the data using Eq. 2.51.

experimental data yields the constants $n_0 = 6692\,\mathrm{m}^{-2}$ and $\tau_0 = 4.382\,\mathrm{K}$.

As shown above, the time dependence of nucleation is generally not taken into account in the singular nucleation model. However, also in the case of a singular behavior, heterogeneous nucleation may be modeled statistically. In this case, the stochastic nature of nucleation is accounted for at each of the different nucleation sites of the nucleant associated with a different nucleation temperature. The first approach for this kind of modeling of heterogeneous nucleation is the VS66 model [365]. Several related models have been developed in recent years [155, 252, 325, 363].

2.2.4 Related literature

Statistical modeling of nucleation presented in the previous sections enables investigation of parameters influencing nucleation, based on a macroscopic approach. Experimental investigation of homogeneous nucleation of water involves some difficulties, since it requires the use of perfectly pure water without any impurities or contamination [182]. However, homogeneous nucleation has been extensively studied, in particular for the case of nucleation of ice [13, 30, 93, 156, 174, 185, 187, 192, 246, 342, 343,

371, 378, 398]. The research in this field, and the involved experimental and theoretical concepts are thoroughly reviewed in [182].

Starting in 1724 with Daniel Gabriel Fahrenheit's observation that fluid motion may facilitate nucleation [101], various influences on the nucleation process which are related to the liquid itself, such as the liquid cooling rate [365], a pressure wave propagating through the liquid [135, 270], liquid shear stress [271, 286], temperature gradients in the liquid [240, 285], or the drop diameter [39, 88, 147] have been studied. However, even more studies focused on external influences on nucleation comprising the effect of the ice nucleating ability of suspended particles [155] or gas bubbles suspended in the liquid [68, 143, 253], the wettability [42, 98, 357] and surface roughness or structure of a nucleant [58, 94], the effect of a free liquid-gas interface [199], or the influence of external electric fields [87, 251, 278, 340, 382, 383]. While most of the studies concerning nucleation are based on experimental investigation [58, 87, 98, 155, 278], in recent years molecular dynamics simulations revealed deeper insight into the nucleation process [29, 36, 198, 226, 236].

When an electric field is involved in nucleation and freezing of water, the phenomenon is referred to as electro-freezing. The influence of an electric field on nucleation is based on the fact that the structure of water clusters may change in an external electric field [170, 368, 369, 392] due to the alignment of water molecules from random directions to the direction of the electric field vector [256]. Electro-freezing has been extensively studied experimentally [50, 87, 278, 340] and theoretically during the last decades. Nowadays it is also the focus of molecular dynamics simulations [251, 382, 383]. One of the first systematic investigations concerning ice nucleation in an electric field is found in [278], where the effect of a constant tangentially aligned electric field on the nucleation of supercooled water droplets has been investigated. Similar to the results of many subsequent studies, an enhanced nucleation rate due to the electric field has been observed [278]. However, several other studies did not reveal an effect of an electric field on nucleation [87, 208, 340], leaving the concrete influence of an electric field on nucleation unknown.

As shown, the statistics of nucleation has been studied in-depth for the case of a liquid at rest, considering a large variety of influences. A freezing delay of impacting supercooled water drops as the consequence of the statistics of nucleation has been reported in several studies [6, 148, 171]. However, as already mentioned in Sec. 2.1, the statistics of nucleation

has never been taken into account in detail for the complex process of a drop impact; despite of its importance for icing of surfaces. Therefore, this special case of nucleation deserves further examination to improve the understanding of the processes during ice accretion. It will be focused on in the present work.

2.3 Solidification

The morphology and characteristics of a freezing process generally depend on the temperature of the solidifying liquid [3, 276]. In the case of solidification of a liquid being at its melting temperature, the solidification front is stable, resulting in locally planar freezing of the entire liquid [3, 79, 152, 276]. In the case of a supercooled liquid, the freezing front may become unstable causing dendritic freezing of the liquid [79, 276]. Only a portion of the entire liquid changes its phase [152], resulting in a porous solid structure surrounded by liquid, both being in a local thermodynamic equilibrium at the melting temperature. The planar solidification at the melting temperature as well as the instability of a freezing front evolving in a supercooled liquid can be mathematically modeled. This microscopic mathematical approach for a freezing process as well as a rather macroscopic description of the growth of a single ice dendrite, and the freezing of a supercooled liquid are presented in the following.

2.3.1 Mathematical modeling of solidification

A freezing process, i.e. a solid-liquid phase interface propagating due to the solidification of the liquid phase, can be mathematically described as a Stefan problem [3, 79]. It is a particular kind of a boundary value problem and involves a moving-boundary Ξ separating two distinct regions which are separately described by partial differential equations (PDEs). Boundary conditions for the PDEs are imposed at the moving boundary whose position is part of the solution of the PDEs itself.

2.3.1.1 The Stefan problem

Mathematical modeling of a freezing process is generally based on the release of latent heat of fusion at the solid-liquid interface Ξ during phase change. The latent heat per unit area of the solid-liquid interface, q_{lat},

which is released per time, is proportional to the mass of the liquid solidifying per unit time and unit area of the interface, which is in turn proportional to the normal velocity of the interface, v_n, thus

$$\frac{\partial q_\mathrm{lat}}{\partial t} = \rho_\mathrm{s} L v_\mathrm{n}, \tag{2.54}$$

where ρ_s is the density of the solid phase and L is the latent heat of fusion per unit mass. In the absence of a bulk flow of the liquid phase, heat may be dissipated away from the interface into the solid and liquid phase only by diffusion. Energy is conserved in both the solid and the liquid phase of the material, and thus heat conduction in the phases is described by the heat-conduction equation

$$\frac{\partial}{\partial t}(\rho_\mathrm{i} c_{\mathrm{v,i}} T_\mathrm{i}) = \nabla \cdot (k_\mathrm{i} \nabla T_\mathrm{i}), \tag{2.55}$$

where T_i is the temperature in phase i (solid: $i = s$, liquid: $i = l$). The temperature fields in the solid and the liquid phase are independently described by Eq. 2.55. However, the temperature fields are coupled with a boundary condition, based on an energy balance in a control volume of infinitesimal thickness around the solid-liquid interface as shown in Fig. 2.11. This so-called Stefan condition results from a balance of the latent heat of fusion released during phase change (Eq. 2.54), and the diffusional heat flux from the interface into the phases, $\dot{\mathbf{q}}_\mathrm{i}|_\Xi$, which is according to the Fourier law of heat conduction

$$\dot{\mathbf{q}}_\mathrm{i}|_\Xi = -k_\mathrm{i} \nabla T_\mathrm{i}|_\Xi \,. \tag{2.56}$$

Using Eqs. 2.54 and 2.56, the Stefan condition relates the heat dissipated into the solid and the liquid phase to the speed of the interface as

$$\rho_\mathrm{s} L v_\mathrm{n} = \left[(k_\mathrm{s} \nabla T_\mathrm{s} - k_\mathrm{l} \nabla T_\mathrm{l}) \cdot \dot{\mathbf{n}} \right]_\Xi , \tag{2.57}$$

where $\dot{\mathbf{n}}$ denotes the interface normal vector directed into the liquid phase.

In addition to the Stefan condition, the temperature fields in the solid and the liquid phase are coupled by a further boundary condition at the solid-liquid interface: the temperature is continuous across the interface, $T_\mathrm{l}|_\Xi = T_\mathrm{s}|_\Xi$. For the case of a planar solidification front, the interface temperature is usually modeled to be at the melting temperature, $T|_\Xi = T_\mathrm{m}$ [3, 79]; although this in fact refers to an interface being stationary as will be described later.

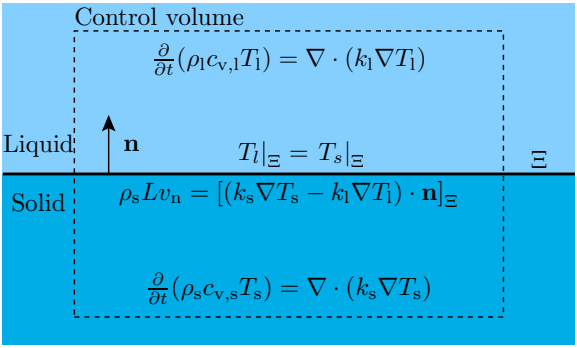

Figure 2.11: Control volume around a solid-liquid interface, Ξ, used for the formulation of an energy balance at a solidification front. The temperature fields in the solid and the liquid phase result from the heat-conduction equation (Eq. 2.55) separately applied in each phase, and are coupled at the phase interface by means of the Stefan condition (Eq. 2.57) and the continuity of temperature across the interface, $T_\mathrm{l}|_\Xi = T_\mathrm{s}|_\Xi$.

According to the number of phases "active" for dissipation of heat away from the interface, the problem is referred to as the *one-Phase* Stefan-problem or *two-phase* Stefan-problem. In the case of the one-phase Stefan problem, heat may be dissipated either into the solid or into the liquid phase. Considering a supercooled liquid, heat is only dissipated into the liquid phase, initially at $T_{\mathrm{l},0} < T_\mathrm{m}$, while the temperature of the solid phase equals the interface temperature, $T_\mathrm{s} = T_\Xi$. In the case of the two-phase Stefan problem, heat is also dissipated into the solid phase, $T_\mathrm{s} < T_\mathrm{m}$. The resulting temperature distributions normal to the phase interface are shown in Fig. 2.12 for both types of the Stefan problem.

Due to the density difference of liquid water and ice, $\rho_\mathrm{s} < \rho_\mathrm{l}$, water expands during solidification resulting in an increase of the front velocity compared to the theoretical case of $\rho_\mathrm{s} = \rho_\mathrm{l}$. The absolute contribution of the volume expansion to the resulting front velocity depends on the freezing rate. However, its relative influence on the total front velocity only depends on the density ratio $\rho_\mathrm{l}/\rho_\mathrm{s}$. Since the densities of the liquid and the solid phase depend on temperature, also the density ratio is temperature dependent; it decreases for decreasing temperature. Using $\rho_\mathrm{s} \approx 917\,\mathrm{kg/m^3}$ and $\rho_\mathrm{l} \approx 1000\,\mathrm{kg/m^3}$ for ice and water at the melting

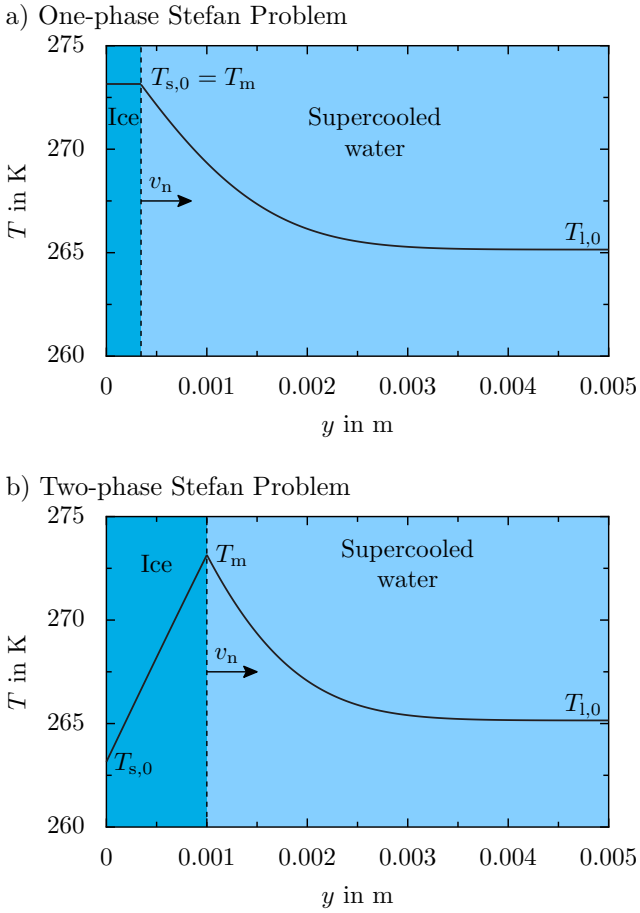

Figure 2.12: Temperature distribution in the solid and liquid phase normal to the phase interface at time $t = 5.2\,\mathrm{s}$ during one-dimensional solidification of water supercooled to $T_{l,0} = 265.15\,\mathrm{K}$. a) One-phase Stefan problem corresponding to $T_{s,0} = T_s(y = 0, t \geq 0) = T_m$ (Eqs. 2.63 and 2.64). b) Two-phase Stefan problem with $T_{s,0} = T_s(y = 0, t \geq 0) = 263.15\mathrm{K}$ (Eqs. 2.68 and 2.69).

temperature [203], the density ratio is $(\rho_l/\rho_s)|_{T_m} \approx 1.09$. This means

that approx. 9% of a present freezing front velocity are attributed to the volume expansion upon phase change. The increased front velocity slightly affects the temperature distribution around the moving interface, which controls the front velocity attributed to the release of latent heat according to Eq. 2.57. However, in the following the solutions of the Stefan problem are presented for the assumption of constant densities of the liquid and the solid phase, $\rho_\mathrm{s} = \rho_\mathrm{l}$. The analytical solutions with consideration of a density change upon freezing are not presented here, but are found in [3, 63].

Analytical solution of the two-phase Stefan problem

The general mathematical approach for a freezing problem is the two-phase Stephan problem, when heat is dissipated into both the solid and the liquid phase. A similarity solution for the propagation of the solid-liquid interface described by the relations in the previous section is found for the following initial conditions [3]. Consider a semi-infinite slab, $0 \leq y < \infty$, of supercooled water initially at $T_{\mathrm{l},0} < T_\mathrm{m}$. At time $t = 0$, a temperature $T_{\mathrm{s},0} < T_\mathrm{m}$ is imposed at the boundary $y = 0$. Solidification starts at $t = 0$ and results in the propagation of a planar freezing front being parallel to the plane $y = 0$ and moving into the supercooled liquid $y > 0$. For the case of constant densities $\rho_\mathrm{l} = \rho_\mathrm{s}$, the temporal evolution of the ice thickness is

$$h(t) = 2\lambda_\mathrm{s}\sqrt{a_\mathrm{s} t}, \quad t > 0, \tag{2.58}$$

where the parameter λ_s is found as the root of the transcendental equation

$$\frac{\mathrm{St_s}}{\lambda_\mathrm{s}\sqrt{\pi}\,\exp(\lambda_\mathrm{s}^2)\,\mathrm{erf}(\lambda_\mathrm{s})} + \frac{\mathrm{St_l}}{a^*\lambda_\mathrm{s}\sqrt{\pi}\,\exp[(a^*\lambda_\mathrm{s})^2]\,\mathrm{erfc}(a^*\lambda_\mathrm{s})} = 1. \tag{2.59}$$

$\mathrm{St_i}$ are the Stefan numbers defined with respect to the solid and the liquid phase as

$$\mathrm{St_s} = \frac{c_\mathrm{s}(T_\mathrm{m} - T_{\mathrm{s},0})}{L} \qquad \text{and} \qquad \mathrm{St_l} = \frac{c_\mathrm{l}(T_\mathrm{m} - T_{\mathrm{l},0})}{L}, \tag{2.60}$$

respectively. The parameter a^* in Eq. 2.59 is defined as the square root of the ratio of the thermal diffusivities of the solid and the liquid phase

$$a^* = \sqrt{\frac{a_\mathrm{s}}{a_\mathrm{l}}}. \tag{2.61}$$

Differentiation of Eq. 2.58 yields the transient normal interface velocity

$$v_{\mathrm{n}}(t) = \lambda_{\mathrm{s}} \sqrt{\frac{a_{\mathrm{l}}}{t}}, \tag{2.62}$$

and the temperature distribution in the solid and the liquid phase is obtained as

$$T_{\mathrm{s}}(x,t) = T_{\mathrm{s},0} + (T_{\mathrm{m}} - T_{\mathrm{s},0}) \frac{\operatorname{erf}\left(\frac{y}{2\sqrt{a_{\mathrm{s}} t}}\right)}{\operatorname{erf}(\lambda_{\mathrm{s}})}, \quad 0 \le y \le h(t), \quad t > 0, \tag{2.63}$$

$$T_{\mathrm{l}}(x,t) = T_{\mathrm{l},0} + (T_{\mathrm{m}} - T_{\mathrm{l},0}) \frac{\operatorname{erfc}\left(\frac{y}{2\sqrt{a_{\mathrm{l}} t}}\right)}{\operatorname{erfc}(a^* \lambda_{\mathrm{s}})}, \quad y \ge h(t), \quad t > 0, \tag{2.64}$$

respectively.

Analytical solution of the one-phase Stefan problem

The one-phase Stefan problem is a special case of the two-phase Stefan problem, when heat is only dissipated into one phase; in the case of a supercooled liquid, the liquid phase is the sole active phase. In analogy to the two-phase Stefan problem, a similarity solution for that case is found for the following initial conditions [3]. Consider a semi-infinite slab, $0 \le y < \infty$, of supercooled water initially at $T_{\mathrm{l},0} < T_{\mathrm{m}}$. At time $t = 0$, a temperature $T_{\mathrm{s},0} = T_{\mathrm{m}}$ is imposed at the boundary $y = 0$. After the beginning of solidification at $t = 0$ a planar freezing front being parallel to the plane $y = 0$ propagates into the liquid $y > 0$. Analogous to Eq. 2.58, the temporal evolution of the ice thickness for the case of constant densities $\rho_{\mathrm{l}} = \rho_{\mathrm{s}}$ is

$$h(t) = 2\lambda_{\mathrm{s}} \sqrt{a_{\mathrm{l}} t}, \quad t > 0. \tag{2.65}$$

In the case of the one-phase Stefan problem, λ_{s} is obtained from

$$\lambda_{\mathrm{s}} \sqrt{\pi}\, \exp[(\lambda_{\mathrm{s}})^2] \operatorname{erfc}(\lambda_{\mathrm{s}}) = \mathrm{St}_{\mathrm{l}}. \tag{2.66}$$

The transient normal interface velocity is found as

$$v_{\mathrm{n}}(t) = \lambda_{\mathrm{s}} \sqrt{\frac{a_{\mathrm{s}}}{t}} \tag{2.67}$$

and the temperature fields in the solid and liquid phase are

$$T_{\mathrm{s}}(x,t) = T_{\mathrm{m}}, \quad 0 \le y \le h(t), \quad t > 0, \tag{2.68}$$

$$T_\mathrm{l}(x,t) = T_{\mathrm{l},0} + (T_\mathrm{m} - T_{\mathrm{l},0}) \frac{\mathrm{erfc}\left(\frac{x}{2\sqrt{a_\mathrm{l} t}}\right)}{\mathrm{erfc}(\lambda_\mathrm{s})}, \quad y \geq h(t), \quad t > 0, \tag{2.69}$$

respectively.

According to Eqs. 2.62 and 2.67, for both the one-phase Stefan problem and the two-phase Stefan problem, the freezing front velocity is infinite at $t = 0$ and decreases with time.

2.3.1.2 Capillary undercooling - the Gibbs-Thomson effect

All aforementioned considerations refer to a planar freezing front with the melting temperature present at the solid-liquid interface, $T_\Xi = T_\mathrm{m}$. In the case of a curved phase interface, the interface temperature reduces due to the Gibbs-Thomson relation. The effect is called capillary undercooling and it is based on the Laplace-Young relation for a curvature dependent pressure jump across a curved phase interface [3]

$$p_\mathrm{s} - p_\mathrm{l} = 2\sigma_\mathrm{sl}\kappa, \tag{2.70}$$

where p_i is the pressure of phase i, and κ denotes the mean curvature of the interface being positive for a convex shape of the solid phase. For constant material properties of the liquid and the solid phase, $c_{\mathrm{p,s}} = c_{\mathrm{p,l}} = c_\mathrm{p}$ and $\rho_\mathrm{s} = \rho_\mathrm{l} = \rho$, the interface temperature is obtained as [3]

$$T_\Xi = T_\mathrm{m} - \Delta T_\mathrm{cap}, \quad \Delta T_\mathrm{cap} = 2\frac{\sigma_\mathrm{sl} T_\mathrm{m} \kappa}{\rho L}. \tag{2.71}$$

In the case of a perturbation of an initially planar interface, according to Eq. 2.71, the interface temperature, and therefore also the temperature gradients at the interface decrease. Therefore, less latent heat of fusion is dissipated away from the disturbed interface and according to Eq. 2.57, the interface velocity decreases at the curved locations, resulting in a decay of the perturbation. Thus, the Gibbs-Thomson effect acts stabilizing against perturbations of the solid-liquid interface. As a consequence, freezing of non-supercooled liquid generally takes place with a smooth solid-liquid interface minimizing the surface energy between the two phases.

2.3.1.3 Morphological instability of a solid-liquid interface

In the case of a supercooled liquid, a perturbation of the interface, i.e. a protrusion of the interface into the liquid phase, results in a compression

of the temperature field in the liquid phase, and by this causes an increase of the temperature gradient in the liquid at the location of the perturbation. As a result of the increased temperature gradient, more heat is dissipated into the liquid phase which according to Eq. 2.57 results in an increase of the interface velocity finally enhancing the interface perturbation. Therefore, the heat flux into the liquid phase, i.e. the supercooling of the liquid, acts destabilizing towards interface perturbations.

Both the destabilizing effect of supercooling and the stabilizing effect of surface energy depend on the interface curvature, and thus the wave length of the interface perturbation. By means of a linear stability analysis of the phase interface during directional solidification, and with the assumption of constant material properties of the solid and the liquid phase, the critical wavelength of interface perturbations has been found as [243, 244]

$$\lambda_{\mathrm{cr}} = \sqrt{2a \frac{T_{\mathrm{m}} \sigma_{\mathrm{sl}} c_{\mathrm{v}}}{v_{\mathrm{n}}^0 L \rho}}, \tag{2.72}$$

where c_{v} is the heat capacity at constant volume and v_{n}^0 denotes the normal velocity of the unperturbed interface, which serves as the characteristic velocity of the problem. Interface perturbations with wave length larger than λ_{cr} are enhanced and grow further. They result in dendritic freezing of the liquid which is the most common form of phase change in all macroscopic castings [79], and in particular in the case of a supercooled liquid. A porous dendritic structure of the solid phase infuses the entire liquid and initially causes freezing of only a portion of the liquid. According to Eqs. 2.62 and 2.67, the velocity during planar freezing tends to infinity for $t = 0$. However, apart from small times, $t \ll 1$, the typical dendrite velocity, which is constant in time and just depends on the liquid supercooling, is much higher than the transient front velocity of a planar freezing front.

Note that the descriptions of the morphological instability were based on a planar solid-liquid interface. However, also a homogeneously curved interface may become unstable. In particular the surface of a spherical ice nucleus becomes unstable when the radius of the nucleus equals a critical radius R_{cr}. It results in the formation of bumps on the surface which finally form dendrites [79], eventually leading to the well-known hexagonal snow-flake shaped ice crystals.

2.3.1.4 Kinetic undercooling

A further effect which has to be accounted for in the mathematical description of a solidification process plays an increasingly important role for large freezing rates associated with higher liquid supercooling. So far, in the absence of interface curvature, the interface temperature has been assumed as $T_\Xi = T_\mathrm{m}$. However, a solid-liquid interface at T_m would be, or indeed it is, in thermodynamic equilibrium: the rate of molecules attaching to the interface equals the rate of molecules which detach from the interface [79]. Thus, in the case of an interface at T_m, the solid phase effectively does not increase and the interface does not move. Hence, a certain undercooling of the interface below T_m is always required for the propagation of a solid-liquid interface. In the case of an interface temperature below the melting point, $T_\Xi < T_\mathrm{m}$, the bounding of molecules to the interface increases [79]. As a consequence, the rate of molecules detaching from the interface decreases, while the rate of molecule attachment is unaffected. It results in an effective increase of the solid phase and thus an advancing interface. The interface velocity increases with increasing undercooling of the interface, $T_\mathrm{m} - T_\Xi$. Albeit a certain interface undercooling is always required for a freezing process, it is negligible small for many purposes [276]. Nevertheless, for larger supercooling, the mobility of the molecules decreases. Therefore, also the rate of increase of the interface velocity for increasing interface undercooling decreases, since the molecules become more sluggish. Consequently, the so-called kinetic undercooling results in a decreasing increase of the solidification rate for increasing liquid supercooling (see Fig. 2.14), which is referred to as *kinetic effects* in the present work.

For materials with a small latent heat of fusion (e.g. metals), the interface velocity can be approx. related to the interface undercooling, ΔT_kin, using the kinetic coefficient μ, as [79]

$$v_\mathrm{n} \approx \mu \Delta T_\mathrm{kin}, \quad \Delta T_\mathrm{kin} = (T_\mathrm{m} - T_\Xi). \tag{2.73}$$

Considering the kinetic undercooling according to Eq. 2.73 and the capillary undercooling according to Eq. 2.71, the temperature of an advancing curved solid-liquid interface is described as

$$T_\Xi = T_\mathrm{m} - \left(\frac{\sigma_\mathrm{sl} T_\mathrm{m} \kappa}{\rho} + \mu^{-1} v_\mathrm{n} \right). \tag{2.74}$$

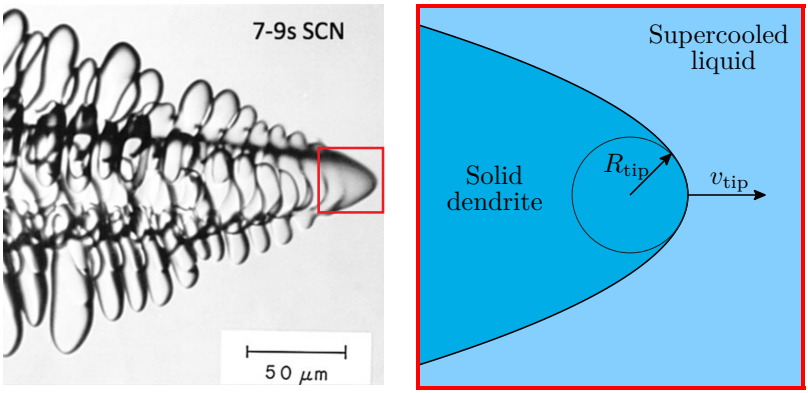

Figure 2.13: Single dendrite with the tip radius R_{tip} propagating into a supercooled liquid with the speed v_{tip}. Left: Experimentally observed dendrite growing in supercooled succinonitrile [126]. Right: Paraboloidal model geometry as the basis for the Ivantsov solution. It corresponds to the dendrite tip region highlighted with a red square in the left image. (Reprinted by permission from Springer Nature. *Metallurgical and Materials Transactions A*, 43B:207-220. Mechanism of Dendritic Branching, Glicksman M. E., copyright 2012.)

2.3.2 Growth of a single dendrite

A typical dendrite resulting from an instability of the solid-liquid interface during the solidification of supercooled succinonitrile[3] is shown in Fig. 2.13 a). As indicated by the red square in the figure, the interface at the tip of the dendrite is smooth. It gets unstable at some distance behind the tip resulting in the formation of sidebranches, as in the case of the growth of a snowflake.

Due to the special shape of the dendrite and the resulting heat diffusion around the solid-liquid interface, the dendrite tip propagates with a constant tip velocity v_{tip}. Assuming a paraboloidal shape of the dendrite tip region, as shown in Fig. 2.13 b), and by neglecting kinetic effects

[3]Due to its transparency and its melting temperature above room temperature, succinonitrile is an often-used test material for dendritic growth experiments [127, 128, 130, 157, 184].

at the solid-liquid interface, the velocity of a single dendrite growing in a supercooled liquid has been theoretically modeled by considering only heat conduction in the liquid and the solid phase [161]. The resulting

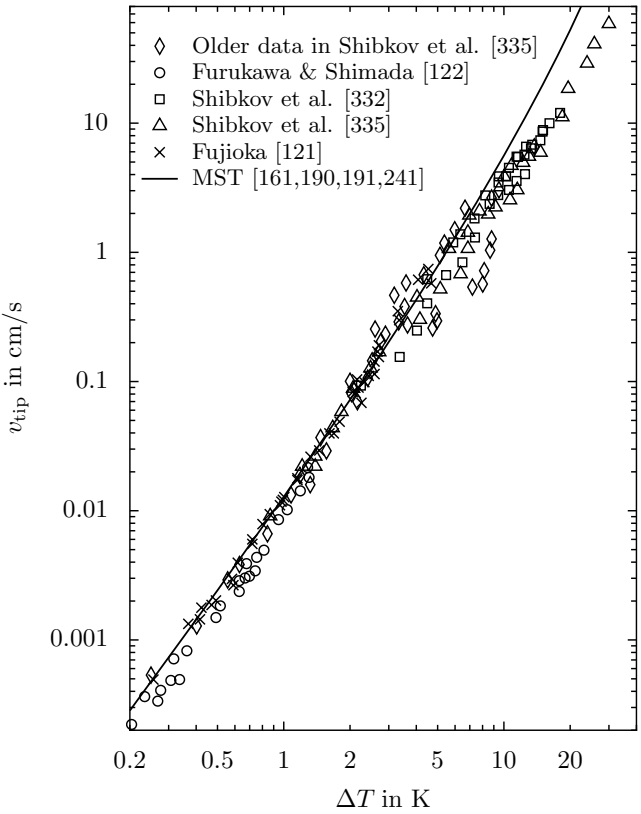

Figure 2.14: Tip velocity of an ice dendrite depending on liquid supercooling. Comparison of experimental results (symbols) from [121, 122, 332, 335] and theoretical predictions (solid line) according to the Ivantsov solution [161] combined with the marginal stability theory [190, 191, 241]. Overestimation of the tip velocity especially for larger supercooling corresponds to kinetic effects becoming increasingly important for larger supercooling (see Sec. 2.3.1.4), which are not accounted for in the diffusion based theoretical model.

so-called *Ivantsov solution* for a single dendrite and all related studies are thoroughly reviewed in [79]. The Ivantsov solution provides a relation between the dimensionless liquid supercooling $\mathrm{St} = (c_{\mathrm{p,s}}\Delta T)/L$, and the product of the dendrite tip velocity and tip radius R_{tip} in the following form

$$\mathrm{St} = \mathrm{Pe}_0 \exp(\mathrm{Pe}_0)\mathrm{E}_1(\mathrm{Pe}_0). \tag{2.75}$$

In this relation $\mathrm{Pe}_0 = R_{\mathrm{tip}}/(2l_{\mathrm{T}})$ is the Peclet number, defined using the thermal length scale of the problem, $l_{\mathrm{T}} = a_{\mathrm{l}}/v_{\mathrm{tip}}$, and $\mathrm{E}_1(\mathrm{Pe}_0) = \int_{\mathrm{Pe}_0}^{\infty} z^{-1}\exp(-z)\,\mathrm{d}z$ is the exponential integral. Being obvious from Eq. 2.75, the Ivantsov solution yields no separate solution for the tip velocity or tip radius. However, a further relation between these quantities is obtained by the assumption that the tip radius of a dendrite equals the critical wave length of a stable solidification front according to Eq. 2.72. This approach is called the *marginal stability theory* (MST) [190, 191, 241], which together with the Ivantsov solution results in separate expressions for the tip radius and tip velocity depending on the liquid supercooling. The theoretical predictions for the tip velocity of a single dendrite according to the MST are shown in Fig. 2.14 in comparison to experimental data [121, 122, 332, 335]. As shown in the figure, the theoretical model is in very good agreement with the experimental data up to a supercooling of approx. $4 \ldots 5\,\mathrm{K}$. For this range of supercooling, the freezing process is mainly dominated by heat diffusion, and is well described by the diffusion based theoretical model. However, for larger supercooling, kinetic effects as described in the previous section, play a more important role [332, 335]. They result in a decreasing increase of the tip velocity for increasing supercooling, as shown in the figure. Furthermore, in particular in the transition region, $\Delta T \approx 3 \ldots 10\,\mathrm{K}$, the spread of the velocity data is significantly larger compared to the remaining ranges of supercooling.

2.3.3 Macroscopic freezing of a supercooled liquid

Due to its transient character, the planar freezing of a supercooled liquid is not characterized by an intrinsic length scale [79]. However, the thermal diffusion length $\delta_{\mathrm{T}} = a_{\mathrm{l}}/v_{\mathrm{tip}}$ may be used as a thermal length scale for the dendritic freezing process [79]. With the thermal diffusivity of water, $a_{\mathrm{l}} \sim 10^{-7}\,\mathrm{m}^2/\mathrm{s}$, and the tip velocity of a single dendrite from Fig. 2.14, $v_{\mathrm{tip}} \sim 10^{-6} \ldots 1\,\mathrm{m/s}$, the diffusion length varies over many orders of magnitude between several tenth of micrometers to several tenth

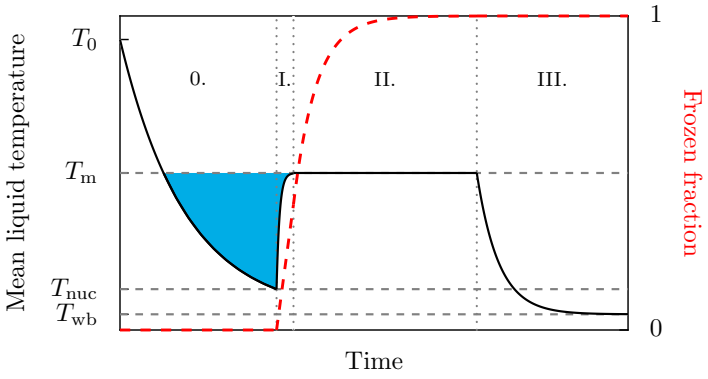

Figure 2.15: Schematic evolution of the mean temperature (black solid line) and frozen fraction (dashed red line) of a macroscopic amount of liquid initially at T_0 during 0.) cool down below the melting temperature T_m, I.) nucleation at T_nuc and dendritic freezing of a portion of the liquid, II.) freezing of the remaining liquid at T_m, and III.) cool down of the entirely frozen volume to the wet-bulb temperature T_wb. The blue region represents the supercooled state of the liquid.

of meters, $\delta_\mathrm{T} \sim 10^{-7} \ldots 10^{-1}\,\mathrm{m}$. However, for a significant supercooling, $\Delta T > 1\,\mathrm{K}$, the diffusion length is $\delta_\mathrm{T} < 10^{-3}\,\mathrm{m}$, and rapidly decreases with increasing temperature. Thus, it is small compared to the typical length scale of many technical applications. In particular, δ_T in this temperature range is small compared to the typical length scale of the investigations in the present work which is approx. $10^{-3}\,\mathrm{m}$. Therefore, the microscopic processes in the vicinity of the solidification front often are irrelevant, justifying a closer look also onto the macroscopic freezing process of a supercooled liquid.

Although the mathematical derivations in the previous section refer to a rather microscopic description of the solidification process, the mentioned partial dendritic freezing of a supercooled liquid already indicates that the solidification of a macroscopic amount of a supercooled liquid proceeds in several successive stages [77, 150, 172]. The temporal evolution of the mean temperature and frozen fraction of an amount of liquid during these stages is illustrated in Fig. 2.15. The liquid initially being at $T_{\mathrm{l},0}$ is cooled down below the melting temperature T_m (0.). Nucleation

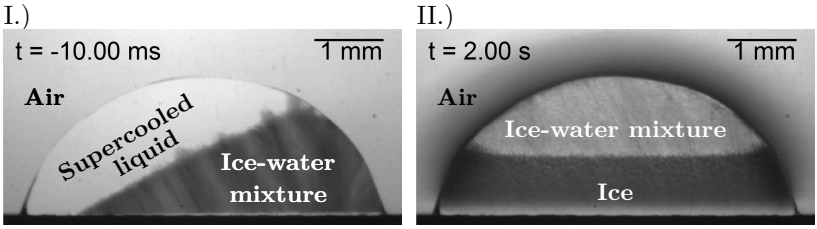

Figure 2.16: The two phases of solidification of a supercooled sessile water drop in a Hele-Shaw cell corresponding to the evolution of temperature and frozen fraction shown in Fig. 2.15. I.): A porous dendritic ice structure infuses the supercooled liquid, leading to a local thermodynamic equilibrium of the resulting ice-water mixture being at T_m. II.): Further cool down of the mixture results in planar freezing of the remaining water at T_m. (Reprinted figure (adapted) with permission from [321]. Copyright 2016 by the American Physical Society.)

at T_nuc initiates the freezing process. During the first phase of nucleus growth, the nucleus surface is stable and may be described by the equations presented in the previous section [243]. The critical nucleus radius associated with an instability of the surface, and the time of stable nucleus growth are very small, $R_\mathrm{cr} \sim 10^{-8} \ldots 10^{-7}$ m and $t_\mathrm{cr} \sim 10^{-9} \ldots 10^{-7}$ s, respectively [89]. Therefore, the phase of stable nucleus growth can be neglected for the freezing of a macroscopic amount of liquid, and nucleation may be assumed to directly initiate dendritic freezing during the so called first phase of solidification, which is often referred to as the recalescence phase (I.). During this phase, not the entire liquid but only a portion of the liquid freezes: a porous dendritic structure of the solid phase infuses the entire volume, as shown in Fig. 2.16 I.) for a sessile drop entrapped in a Hele-Shaw cell. The latent heat of fusion released during dendritic freezing warms up the solid-liquid mixture to the melting temperature, i.e. the system is brought to a local thermodynamic equilibrium during this first phase of solidification. Accordingly, the exact amount of liquid freezing in this phase is proportional to the initial liquid supercooling. Assuming adiabatic boundaries of the liquid volume, the portion of freezing water, γ_f, corresponds to the amount of latent heat of fusion which is required to warm up the resulting solid-liquid mixture to the freezing temperature T_m. With neglect of the temperature dependence of the material properties, from balancing the latent heat released during dendritic freezing of

a liquid volume V,

$$Q_{\mathrm{lat}} = \gamma_{\mathrm{f}} \rho_{\mathrm{s}} L V \tag{2.76}$$

and the sensible heat required to warm up the resulting solid-liquid mixture from $T_{\mathrm{l},0} = T_{\mathrm{m}} - \Delta T$ to T_{m},

$$Q_{\mathrm{sen}} = \gamma_{\mathrm{f}} V \rho_{\mathrm{s}} c_{\mathrm{v,s}} \Delta T + (1 - \gamma_{\mathrm{f}}) V \rho_{\mathrm{l}} c_{\mathrm{v,l}} \Delta T, \tag{2.77}$$

the portion of frozen liquid after dendritic growth is obtained as

$$\gamma_{\mathrm{f}} = \frac{\rho_{\mathrm{l}} c_{\mathrm{v,l}} \Delta T}{\rho_{\mathrm{s}} L + \Delta T (\rho_{\mathrm{l}} c_{\mathrm{v,l}} - \rho_{\mathrm{s}} c_{\mathrm{p,s}})}. \tag{2.78}$$

Note that in the case of constant thermophysical properties of the solid and the liquid phase, $\rho_{\mathrm{s}} = \rho_{\mathrm{l}}$, $c_{\mathrm{v,s}} = c_{\mathrm{v,l}}$, Eq. 2.78 reduces to the Stefan number of the liquid, $\gamma_{\mathrm{f}} \mathrel{\widehat{=}} \mathrm{St} = c_{\mathrm{v,l}} \Delta T / L$.

After dendritic freezing, the solid-liquid mixture is at T_{m}, and a further removal of heat results in stable freezing of the liquid entrapped in the dendritic ice structure at T_{m}, as shown in Fig. 2.16 II.). It is often referred to as the second phase of solidification. Except the solid-liquid mixture in the vicinity of the planar solidification front, the remaining mixture resulting from dendritic freezing is in thermodynamic equilibrium. When the entire liquid is frozen, a further removal of heat is accompanied by a cool down of the solid (III.).

In the case of freezing of a supercooled liquid taking place at a solid wall, a further phase is observed before dendritic freezing of the bulk liquid [181]. Freezing is initiated by heterogeneous nucleation at the wall, which is followed by the spreading of a thin ice layer along the wall. The tangential growth rate of this layer is constant and even larger than the dendrite tip velocity, if the growth is thermally influenced by the neighboring wall [181]. The initial ice layer thickness is of the order $h_{\mathrm{lay}} \sim 10^{-5}\,\mathrm{m}$. Depending on the liquid supercooling, it may become unstable, resulting in dendritic freezing of the bulk liquid. After the initial ice layer became unstable, the further processes follow the stages previously described. Stable freezing of the water left after dendritic freezing proceeds in the opposite direction of the applied heat flux, which is directed into the substrate in the case of a water drop at rest on a cooled surface, as shown in Fig. 2.16 II.). Since the dendritic ice-water mixture is in a local thermodynamic equilibrium at T_{m}, and latent heat of fusion from the moving interface is only dissipated through the solid phase, the second phase of freezing may be described as a one-phase Stefan problem, as described before. While

the freezing velocity in the dendritic freezing phase is constant, according to Eq. 2.67 the interface velocity in the second phase of solidification decreases with time as $\sim t^{-0.5}$.

2.3.4 Related literature

Initiated by the findings of Fahrenheit [101], the solidification of a supercooled liquid and the involved dendritic growth have been examined in depth by means of experimental investigations since almost three centuries [59, 86, 90, 133, 146, 150, 162, 238, 268, 279, 330–335, 351, 353], often utilizing succinonitrile as a test material [127–130, 184]. During the last decades, the topic has also been investigated by means of numerical simulations [75, 76, 338, 341], and in recent years also with molecular dynamics simulations [62, 236, 240, 336, 346], both revealing deeper insight into the solidification of a supercooled liquid.

Most of the aforementioned studies focused on free dendrite growth, i.e. dendritic solidification of a supercooled liquid which is unaffected by any foreign phases or phase interfaces. Although freezing processes influenced by such features have also been examined during the last decades, the number of studies in this field is rather limited. If the solidification of a liquid takes place with wall contact [2, 57, 172, 181, 204, 281, 353, 372, 396, 397], several other phenomena become important such as the contact line arrest during solidification of a spreading liquid [81, 309, 310, 352]. In the case of a sessile drop at rest, the surface wettability may influence the freezing process [140, 395]. As already mentioned, the substrate may thermally affect the phase change process [57, 181, 204, 281]. Solidification processes involving a free liquid-gas interface are influenced by the dynamics of the contact angle at the moving contact line where the solid, the liquid and the surrounding gaseous phase meet [1, 7, 323, 372], which results in a certain pointy drop shape evolving during phase change [99, 221, 249, 250].

Accordingly, possible influences on the freezing process of a supercooled liquid are various; and all of these influences may also be influential for ice accretion due to supercooled water drops. Despite of its importance for icing of surfaces, the solidification of supercooled water is not fully understood. In particular, the macroscopic solidification process of supercooled water and its thermal interaction with the impact surface is not completely clear and deserves further examination. It will be the subject of the present work.

Part III

Results

Parts of the work presented in the following chapter are based on the Master-Thesis of Konstantin Kröll [186] and the Bachelor-Thesis of Sven Borchert [44], and have already been published and presented in the following publications and conference contributions:

[313] M. Schremb, S. Borchert, E. Berberović, S. Jakirlić, I. V. Roisman and C. Tropea. Computational modelling of flow and conjugate heat transfer of a drop impacting onto a cold wall. *International Journal of Heat and Mass Transfer*, 109:971-980, 2017.

[315] M. Schremb, I. V. Roisman, S. Jakirlić and C. Tropea. Spreading and freezing of a droplet impacting onto an inclined colled surface: Different outcomes for same conditions. In *In Book of Abstracts of the SAE 2015 International Conference on Icing of Aircraft, Engines, and Structures*, Prague, Czech Republic, 2015.

[318] M. Schremb, I. V. Roisman and C. Tropea. Different outcomes after inclined impacts of water drops on a cooled surface. In *Proceedings of the 13^{th} Triennial International Conference on Liquid Atomization and Spray Systems*, Tainan, Taiwan, 2015.

[320] M. Schremb, I. V. Roisman and C. Tropea. Transient effects in ice nucleation of a water drop impacting onto a cold substrate. *Physical Review E*, 95:022805, 2017.

3 Drop impact at subfreezing conditions

The present chapter is devoted to the hydrodynamics and thermodynamics during non-isothermal drop impact at subfreezing conditions, which are examined experimentally, numerically and theoretically. The hydrodynamics generally determine the surface area wetted after a single drop impact. Therefore, they determine the maximum surface area potentially iced after drop impact. Solidification fixes the shape of the impinging liquid, and therefore determines the surface area finally iced after drop impact. Since the liquid temperature which is transient during non-isothermal drop impact is one of the most important parameters for nucleation and solidification, the heat transfer during non-isothermal drop impact implicitly affects the surface area actually iced after drop impact.

In the following, at first the hydrodynamics during non-isothermal drop impact is examined. The influence of a varying surface temperature on the hydrodynamics during inclined impact is experimentally investigated. Moreover, the hydrodynamics during normal drop impact is numerically studied. Afterwards, the thermodynamics during non-isothermal normal drop impact is investigated. The evolution of the minimum liquid temperature and the heat transfer during non-isothermal normal drop impact are numerically examined, and the amount of heat transferred during normal drop impact is theoretically modeled.

3.1 Hydrodynamics

The hydrodynamics during drop impact are crucial in the scope of ice accretion. They are influenced by the impact conditions such as the drop size and drop impact velocity. In the case of non-isothermal drop impact, the hydrodynamics may be further influenced by the transient heat transfer between the impact surface and the impinging liquid. The liquid temperature changes during impact and in turn causes a change of the temperature dependent material properties of the liquid which eventually affects the hydrodynamics of impact. Thus, also the heat transfer during drop impact may influence the surface area potentially iced after drop impact.

3.1.1 Experimental investigation of inclined drop impact

The inclined impact of water drops at room temperature is experimentally studied. The influence of a varying surface temperature on the evolution of the wetted surface area during drop impact is examined and its consequences for ice nucleation are outlined.

3.1.1.1 Experimental setup

The experimental setup for the impact experiments is basically the same for all drop impact experiments in the present work. The experiments of the present study concerning inclined drop impact are performed with drops at room temperature; i.e. without using the supercooling method which is utilized for the remaining drop impact experiments with supercooled water drops. Nevertheless, the entire experimental setup,

comprising the drop supercooling procedure is described in the present section.

The setup consists of five major parts comprising a cooling system, a drop generation system, an observation system, a measuring system and a computer control and monitoring unit (CCMU), which are separately described in the following.

Cooling system

In order to investigate the impact of supercooled water drops with temperatures well below the melting temperature of water, and to prevent the formation of frost or condensate on any parts of the experimental setup, the experiments are performed in a controlled atmosphere with ambient temperatures below 0 °C and relative humidities associated with a dew point well below the ambient temperature. An appropriate atmosphere for the experiments is maintained in an enclosure comprising a lower hor-

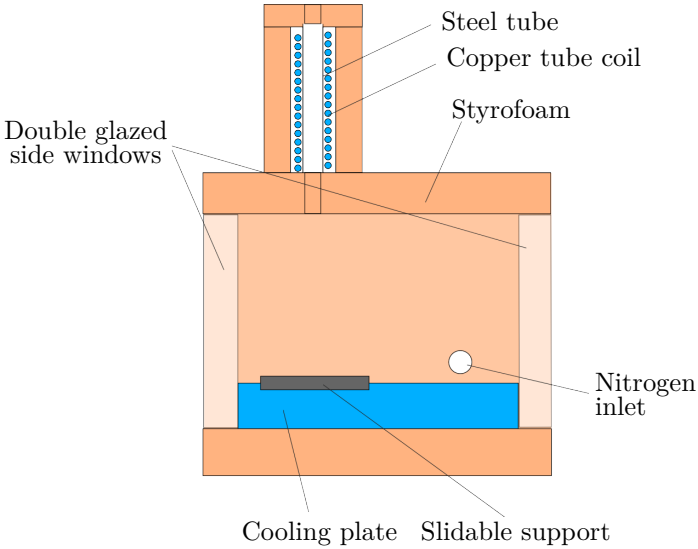

Figure 3.1: Cross sectional side view of the cooling system providing controlled environmental conditions for the drop impact experiments.

izontal[1] and an upper vertical styrofoam chamber, as shown in Fig. 3.1. The styrofoam chambers are core components of the experimental setup and house the parts used for cooling of the impact surface in the lower horizontal chamber, and of the water drops in the upper vertical chamber. A thickness and thermal conductivity of the styrofoam walls of approx. 4 cm and 0.03 W/mK, respectively, provides sufficient insulation from influences of the surrounding on the cold atmosphere in the chambers. To avoid frost and condensate on any cold parts of the setup, gaseous nitrogen is continuously injected into the lower styrofoam chamber. The relative humidity in the chambers is manually adjusted by a change of the nitrogen flow rate, using a pressure regulating valve (*Landefeld, R M5-2-NB*), which then provides a nearly constant volume flow rate.

An aluminum cooling plate (*Lytron, CP10G18*) is placed on the ground of the lower chamber serving as a heat sink for the impact surface. Different kinds of impact targets may be placed onto an aluminum support which is inserted into the styrofoam chamber and placed on top of the cooling plate through a lateral inlet in the chamber. A vertically oriented stainless steel tube is wrapped by a copper tube coil and placed in the upper styrofoam chamber where it serves as the heat sink for the ambient of the generated drops.

An external chilling machine (*Huber, UC020Tw*) is used to supply both the copper coil in the upper styrofoam chamber and the cooling plate in the lower chamber with a cold cooling fluid. Heating of a bypass flow of the cooling fluid allows an independent control of the drop and surface temperature; a schematic of the corresponding closed cooling circuit is shown in Fig. 3.2. All ducts are outside of the styrofoam chambers and are insulated separately to minimize heat exchange with the ambient. As shown in the figure, the chilling machine supplies three different ducts with the cooling fluid. Duct ① and ③ provide a direct connection between the chilling machine, and the copper coil and cooling plate, respectively. The flow of the cooling liquid in these ducts can be controlled by the ball valves Ⓐ. Duct ② is the already mentioned heated by-pass; a heating wire Ⓒ is wound around a copper tube which is part of this duct. The heating wire is connected to an external power supply (*Voltcraft, VSP 2405*), which in turn is connected to the CCMU. By applying a certain voltage to the heating wire, the cooling fluid in duct ② is warmed up.

[1] The lower styrofoam chamber has already been used in [195] and has been modified to serve for the specific purpose of the present work.

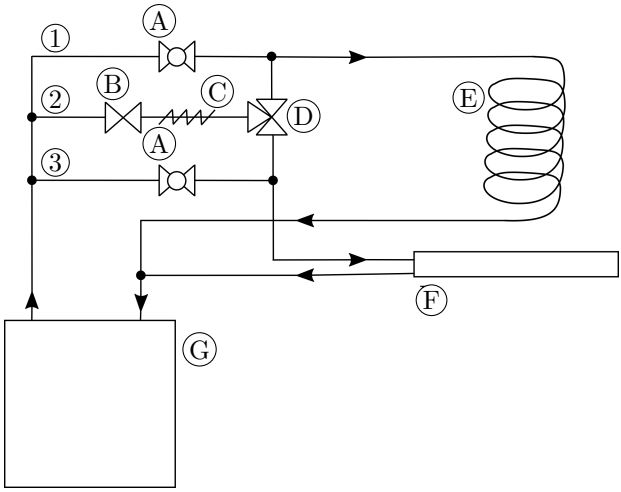

Figure 3.2: Schematic of the cooling system comprising **A**: ball valve, **B**: needle valve, **C**: heating wire, **D**: cross valve, **E**: copper coil, **F**: cooling plate, **G**: chilling machine. [374]

Since the heat input by means of the heating wire Ⓒ is not sufficient to warm up the unlimited flow through duct ②, the volume flow rate through this duct is throttled with the needle valve Ⓑ. Depending on the setting of the cross valve Ⓓ, the warmed up cooling liquid flows either through the copper coil Ⓔ, or through the cooling plate Ⓕ. The throttled volume flow rate of the warmed up cooling liquid in duct ② is small compared to the unlimited volume flow through ducts ① and ③. Therefore, depending on the setting of the cross valve Ⓓ, either the ball valve in duct ① or that in duct ③ has to be closed to enable an effective temperature control by means of the heating wire Ⓒ. To maintain the copper coil warmer than the cooling plate, the ball valve in duct ① is closed and the cross valve connects duct ② with the copper coil, while the ball valve in duct ③ is open. Accordingly, for the cooling plate to be warmer than the copper coil, the ball valve in duct ③ is closed and the cross valve connects duct ② with the cooling plate, while the copper coil is directly supplied by the chilling machine through duct ①.

Drop generation system

Drops are generated at a PTFE tube (*Bohlender GmbH, S 1810-06*) with an inner diameter of 0.4 mm and an outer diameter of 0.9 mm, which is slowly supplied by a micropump (*Bartels Mikroelektronik, mp6*). After reaching a certain size, a drop detaches from the tube due to gravity. A very small volume flow rate ($\dot{V} \approx 4\,\mu\mathrm{l/min}$) of the micropump guarantees a reproducible drop size which is unaffected by the fluid's inertia, and only depends on the diameter of the PTFE tube. Purified de-ionized water (*Millipore, Milli-Q® Type 1*, electrical conductivity $\gamma_{\mathrm{el}} = 5.5 \times 10^{-6}\,\mathrm{S/m}$ at 25 °C) is used for the experiments to avoid influences of impurities in the water on both nucleation of the supercooled drops, and the drop impact hydrodynamics.

The drop generation system is mounted on a vertically slidable support, as shown in Fig. 3.3. Together with exchangeable upper vertical styrofoam chambers of different heights, it allows a variation of the impact velocity by a variation of the falling height of the drop. To increase the mechanical stability of the PTFE tube, it is immersed in a hypodermic needle which is mounted at the end of a vertical extension of the support. As shown in the figure, this extension comprising the PTFE tube at its end is loosely inserted into the vertical styrofoam chamber through an inlet in the upper enclosure of the chamber. Soft insulating foam around the extension seals the inlet of the chamber. When inserted into the styrofoam chamber, the PTFE tube and the drop growing at it are surrounded by the cooled stainless steel tube; i.e. they are placed in the controlled environment in the upper chamber. Therefore, the water drops supercool during their slow growth at the PTFE tube. The drop temperature is continuously measured during drop generation with a K-Type thermocouple (*ES Electronic Sensor, IKT025/10*, diameter: 0.25 mm) which is immersed into the PTFE tube and ends in the suspended drop, as shown in Fig. 3.3. The described method allows a variable drop supercooling of up to $\Delta T = 18\,\mathrm{K}$ by adjustment of the ambient conditions in the steel tube.

However, freezing of a drop during its growth at the tube cannot be completely ruled out. In the case of a drop freezing during its generation, the loose connection between the styrofoam chamber and the drop generation system allows a fast removal of the frozen drop out of the chamber. This eased removal enables melting of a frozen drop outside of the chamber, without heating up the entire experimental setup.

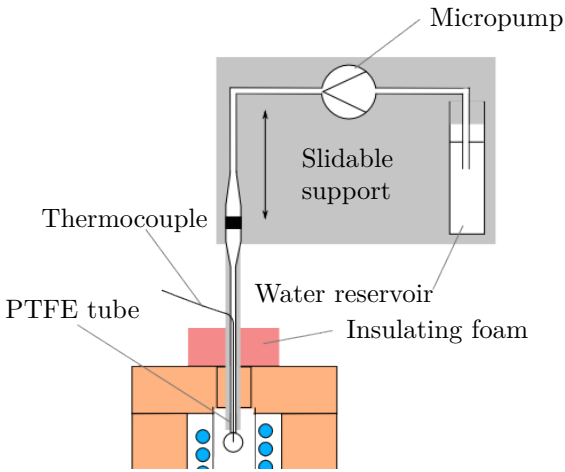

Figure 3.3: Schematic of the drop generation system partially inserted into the upper styrofoam chamber of the cooling system.

Observation system

The main results of the experimental investigations concerning drop impact are obtained from the analysis of captured high-speed videos of the process. Optical access to the impact surface is provided by means of a double-glazed side window fit and sealed into the lower styrofoam chamber, as shown in Fig. 3.1. The impact process is captured using a high-speed video camera (in most cases *Vision Research, Phantom V12.1*) working with 2500 frames/s and a spatial resolution of 45 µm/pixel. The camera is equipped with a zoom lens and several distance tubes to appropriately adjust the field of view to the impact process. As shown in Fig. 3.4, the high-speed camera is placed next to the lower chamber and the impact process is observed in a top view, using a mirror placed above the impact surface. Perspective distortions which would influence length measurements in the captured videos are corrected by a linear transformation of the video frames during post-processing using an analysis tool implemented in a commercial software (*MathWorks, MATLAB*).

The impact process is indirectly illuminated using a high-power LED (*Nichia, 130B*) placed outside of the chamber below the high-speed camera, and a diffusion screen placed above the impact surface. Positioning of the LED outside of the chamber does not thermally affect the conditions

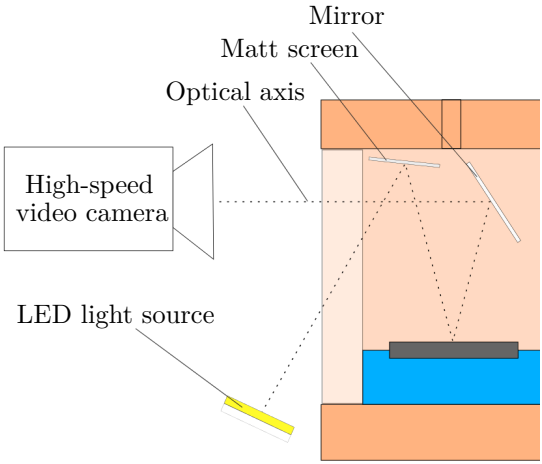

Figure 3.4: Schematic of the observation system used to capture the drop impact process in a top view.

within the styrofoam chambers and the diffusion screen in the chamber provides homogeneous illumination of the impact surface.

Measuring system

As already mentioned, the main results of the experimental investigations concerning drop impact are obtained from the captured high-speed videos. A high spatial and temporal resolution of the captured videos allows both the qualitative analysis of the impact hydrodynamics, and an accurate quantitative measurement of the temporal evolution of the wetted surface area using video processing tools implemented in a commercial software (*MathWorks, MATLAB*). The impact conditions such as the drop diameter and impact velocity are obtained from separate calibration videos captured in a side view using backlight illumination.

The thermal conditions are set prior to the experiments, and monitored during the experiments by continuous measurement of temperature and humidity at various positions of the experimental setup as shown in Fig. 3.5. The temperature is measured using K-Type thermocouples which are connected to a measurement computer via a thermocouple A/D con-

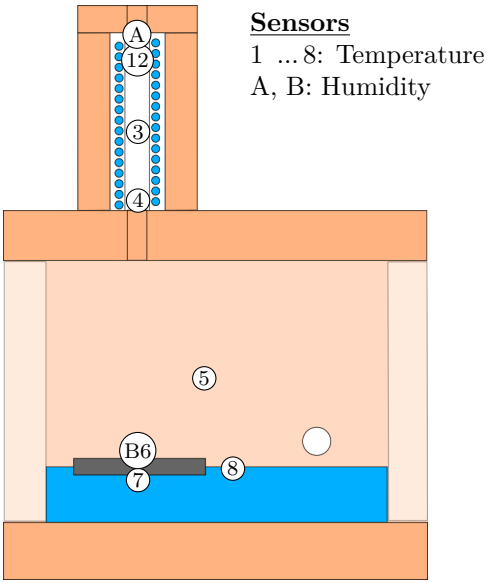

Figure 3.5: Sensor positions for the measurement of temperature and humidity in the styrofoam chambers.

verter (*National Instruments, USB-9213*). The humidity sensors (*B+B Thermo-Technik, Hytelog-USB*) are directly connected to the measurement computer. As mentioned earlier, the drop temperature is continuously measured during drop generation using a thermocouple immersed in the suspended drop (1). The measured data is used to control the drop temperature during the experiments. Furthermore, it is used for triggering of the high-speed camera after drop detachment from the PTFE tube.

As shown in Fig. 3.5, in addition to the thermocouple measuring the drop temperature, three more thermocouples are installed inside of the stainless steel tube in the upper chamber (2-4). Their measurements serve for the adjustment of the ambient conditions in the upper chamber. Moreover, they have been used for a numerical estimation of the temperature change of a drop, induced by forced convection and evaporation during the drop's fall. In the present study, the maximum change of the drop

temperature during a drop's fall is well below 0.1 K for all conditions. A detailed description of the numerical model and the results is found in Appendix A.

A thermocouple measures the ambient temperature in the lower styrofoam chamber (5), used to detect thermal equilibrium in the chambers. The temperature of the impact surface is measured using a thermocouple fixed to its surface (6). It is used for the initial adjustment of the thermal conditions. A further thermocouple is located in between the impact surface and the cooling plate (7). Together with a thermocouple fixed next to the impact plate onto the cooling plate (8), it is used to monitor the thermal conditions of the impact surface during the experiments.

Two further thermocouples measure the temperature of the heating wire and the copper tube after the heating wire. The measurements are used to control and monitor the temperature of the warmed up cooling fluid by controlling the temperature of the heating wire using a PID-controller implemented in the CCMU.

Digital hygrometers are used to measure the relative humidity in the upper and lower styrofoam chambers. The first hygrometer (A) is mounted close to the PTFE tube for drop generation, since the relative humidity of the ambient air close to the suspended drop is a crucial parameter for the ability to supercool a drop. In the case of high humidities, the maximum drop supercooling which is possible without freezing of the drop during its generation is drastically decreased. The second humidity sensor (B) is used to monitor the relative humidity directly above the cooling plate. The relative humidity at this position is crucial for the formation of condensate and frost on the cooling plate or the impact surface, which could influence the impact hydrodynamics and in particular nucleation of an impinging drop. At any time, the humidity in the vicinity of the PTFE tube and above the impact surface have been $\mathrm{RH} < 10\,\%$ and $\mathrm{RH} < 5\,\%$, respectively. The resulting dew point at both positions is well below the respective ambient temperature, and therefore the formation of condensate and frost can be ruled out as an influential parameter for the investigated processes.

Computer control and monitoring unit

All measured data are monitored, processed and saved using a computer control and monitoring unit (CCMU). It is a self-made controller program implemented in a commercial data acquisition software (*National*

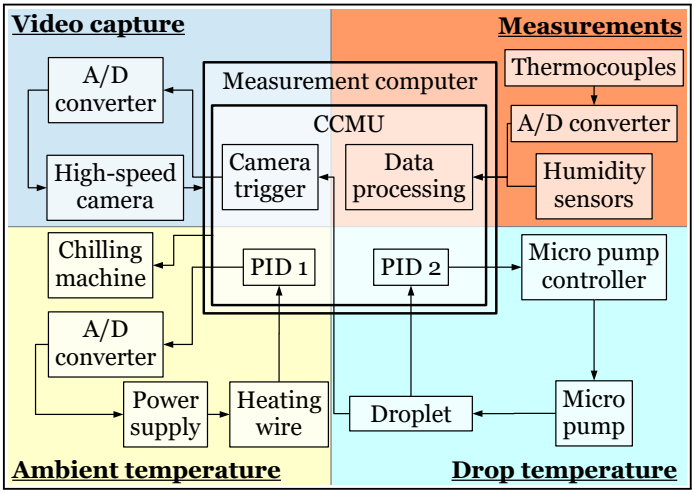

Figure 3.6: Schematic connection plan of the components used for measurements, controlling of the ambient and drop temperature, and video capturing.

Instruments, LabVIEW) which is continuously executed on the measuring computer during the experiments [186]. As indicated in Fig. 3.6, the CCMU in principle serves four purposes: Via a graphical user interface, the controller program monitors the measured data in real time, allows control of the ambient and drop temperature, and enables automated triggering of the high-speed camera.

The high-speed video camera (*Vision Research, Phantom V12.1*), the external chilling machine (*Huber, UC020Tw*), the external power supply for the heating wire (*Voltcraft, VSP 2405*), the control unit of the micropump (*Bartel Mikroelektronik, mp-x*), and several A/D converters (*National Instruments, USB-9213 & USB-6009*) for both input and output signals are connected to the computer, and are operated using the CCMU. Two digital PID controllers implemented in the CCMU are used to control the ambient temperature and the drop temperature via the aforementioned hardware.

As already mentioned, the previous description of the experimental setup corresponds to experiments with supercooled water drops. In the case of drop impacts of water at room temperature as in the present study, the upper styrofoam chamber is not used, and replaced by a vertical acrylic glass tube which shields the falling drop from the ambient. In this case, the upper orifice of the lower styrofoam chamber is kept close between two successive drop impacts to prevent a warm up inside the chamber.

For the present investigation of inclined drop impact both the observation system and the lower styrofoam chamber are mounted on a support which is tiltable around the optical axis of the camera. It allows examination of drop impact with inclination angles in the range $30\,° \ldots 90\,°$.

3.1.1.2 Experimental procedure

Although the drop temperature is continuously measured using a thermocouple immersed into the suspended drop, the measured temperature does not represent the mean temperature of a suspended drop. The water reservoir is located outside of the cold chambers, and thus the water supplied by the micropump is warm, until it reaches the tip of the PTFE tube in the upper chamber. At the same time, convection and evaporation in the cold and dry atmosphere in the upper chamber continuously cool down the growing drop at its surface. As a consequence, an uneven temperature profile develops in the drop. Its mean temperature depends on the ambient conditions in the steel tube, and on the temperature and volume flow rate of the supply water. By increasing the volume flow rate of water, relatively more warm water is supplied and the mean temperature of the drop rises. In the case of a decreasing volume flow rate of supply water, convection and evaporation predominate and the growing drop cools down. The tip of the thermocouple only slightly protrudes into the drop. Therefore, it is reasonable to assume that it measures the temperature of the incoming water, which is the highest possible temperature in the entire drop. The lowest possible temperature in the suspended drop is the wet-bulb temperature T_{wb}, determined by the ambient conditions which control evaporative cooling and convection at the drop surface. The actual mean drop temperature is somewhere in between these bounds. According to these considerations, the mean drop temperature can not be accurately determined, but it may be controlled based on a predefined tolerated uncertainty of the measurement as follows. For experiments with a mean drop temperature T and a desired accuracy of the temperature

measurement of $\pm\Delta T$, the ambient conditions in the steel tube are maintained in a way that the drop temperature measured during deactivation of the micropump is $T - \Delta T = T_{\mathrm{wb}}$. During drop generation, i.e. with an activated micropump, the measured drop temperature is controlled to $T + \Delta T$ by adjusting the volume flow rate of the micropump using one of the PID-controllers implemented in the CCMU. This method guarantees the actual mean drop temperature to be in the range $T \pm \Delta T$. Based on this approach, all experiments in the present study are performed with a mean drop temperature tolerated in a temperature range of $\pm 0.3\,\mathrm{K}$. A smaller temperature range is basically possible. However, a smaller uncertainty for the mean drop temperature is accompanied by a significantly increasing temporal effort for the experiments, since the volume flow rate of the micropump is representative for the width of this range. Using the mentioned temperature range results in a reasonable time of approx. $4 \ldots 6$ minutes for the generation of a single drop.

A complex and protracted iterative preparation of the environmental conditions precedes the experimental investigations, until thermal equilibrium of the experimental setup is reached. According to the previous description regarding the drop temperature measurement, the thermal conditions in the upper chamber are adjusted with respect to the temperature of a suspended drop, corresponding to the wet bulb temperature. Therefore, a drop has to be present at the PTFE tube during the adjustment of the correct ambient conditions in the upper chamber, while the micropump is deactivated during this procedure. The temperature of the cooling plate is adjusted with respect to the temperature measured on the impact surface. During the adjustment of the thermal conditions, the thermocouple placed on the impact surface is located at the theoretical position of drop impact. Since the micropump is deactivated, no drop impact takes place during the procedure. To create certain thermal conditions of the impact surface and in the upper styrofoam chamber, the valves of the cooling system are arranged according to the descriptions of Fig. 3.2. The lower of the temperatures of the cooling plate and the copper coil is controlled by adjusting the target temperature of the external chiller. Based on this initial temperature of the cooling fluid in the cooling circuit, the higher temperature of the remaining warmer heat sink is maintained by a manual one-off adjustment of the throttle valve in the heated bypass, and an iterative adjustment of the target temperature of the heating wire until the correct temperature of the ambient or the cooling plate is found. Afterwards, this temperature is controlled using a PID

controller in the CCMU, which appropriately adjusts the output voltage of the external power supply of the heating wire via an A/D converter. The relative humidity in the styrofoam chambers is controlled by a manual adjustment of the pressure regulating valve for the flow of gaseous nitrogen. Since the temperatures in the upper and the lower chamber, and the flow of gaseous nitrogen mutually influence each other, the described procedure (despite the adjustment of the throttle valve) has to be repeated until thermal equilibrium, and the desired temperatures and humidities are reached in both chambers.

When the correct target temperatures of the external chilling machine and the heating wire are found, the lower temperature in the cooling circuit is kept constant by the chilling machine, and the PID controller in the CCMU keeps the higher fluid temperature in the cooling circuit constant by controlling the temperature of the heating wire. Therefore, also the temperatures of the respective heat sinks in the upper and the lower chamber are kept constant, resulting in a constant wet-bulb temperature in the upper chamber, and a constant temperature of the impact surface in the lower chamber.

When both thermal equilibrium in the chambers, and the desired temperatures of the drop and the surface are reached, the impact plate is shifted sidewards to allow drop impact onto the clean impact surface. To account for a possible temperature gradient along the impact plate, a drop impact after shifting of the impact plate is only performed after some waiting time allowing thermal equilibrium to be reached again in the impact plate. Due to shifting of the impact plate with the attached thermocouple, the surface temperature at the point of drop impact cannot be directly measured during the experiments. However, this temperature is implicitly controlled by monitoring the temperatures measured on the cooling plate and below the impact plate (thermocouple (7) and (8) in Fig. 3.5), which are continuously compared to the respective temperatures measured after adjustment of the thermal conditions.

When thermal equilibrium in the impact plate is reached again, the suspended drop is supplied with water according to the described procedure. The volume flow rate is controlled to result in a measured drop temperature, which corresponds to the upper predefined bound of the allowed range for the mean drop temperature. Due to evaporative cooling at the surface of a suspended drop, and the very small volume flow rate of water provided by the micropump, the measured drop temperature is gen-

erally below the ambient temperature. Thus, the measured temperature abruptly increases when the thermocouple is dry after drop detachment from the PTFE tube. This rising edge of the temperature data is used to trigger the high-speed camera with the CCMU via one of the A/D converters.

After drop impact, the high-speed video is saved and the impact surface is shifted sidewards to allow the next drop impact onto a dry part of the substrate, when thermal equilibrium in the impact plate is reached again.

The length of the impact surface allows approx. 10 successive normal drop impacts side-by-side. However, only 1 inclined drop impact is possible on the impact surface. When the entire clean surface of the impact plate is exhausted, the impact plate is taken out of the lower chamber to melt potentially frozen drops. After the surface has been cleaned with Isopropanol, the impact plate is inserted again into the styrofoam chamber. When thermal equilibrium in the chambers and the impact plate is reached again, the next drop impacts are performed in the described way.

3.1.1.3 Results and discussion

The inclined impact of water drops at room temperature on a cold substrate has been investigated utilizing a mirror polished aluminum impact surface of 4 mm thickness. The drop diameter and impact velocity, the impact inclination angle α_{imp} and the initial drop temperature are constant for all experiments of the present study, while the initial temperature of the impact surface is varied between $\vartheta_{\mathrm{sub},0} = +17.0\,^{\circ}\mathrm{C}$ and $\vartheta_{\mathrm{sub},0} = -17.0\,^{\circ}\mathrm{C}$; the impact conditions are summarized in Tab. 3.1.

Figure 3.7 shows a qualitative comparison of an oblique drop impact onto a substrate at $+17.0\,^{\circ}\mathrm{C}$ (left column) with an impact onto a substrate at $-17.0\,^{\circ}\mathrm{C}$ (right column). The initial tangential velocity of the drops is directed from the right to the left in the shown photographs. This direction is referred to as the longitudinal direction, while the direction perpendicular to the initial drop motion is referred to as the lateral direction in the following descriptions. The drops are shown at different instants of time during the first 34 ms of the impact process. Note that the time interval between the first three frames is constant, while it increases between the last frames to account for the decreasing speed of the process. Vertical red lines in the images indicate maximum drop spreading to the right. Due to the absence of axisymmetry, the processes taking place during inclined impact generally depend on the position with

Table 3.1: Impact conditions and resulting dimensionless numbers, used for the investigation of inclined drop impact. Variation of the dimensionless numbers corresponds to a variation of the liquid temperature between its initial value $\vartheta_{\mathrm{d},0}$ and the contact temperature during impact, estimated using Eq. 2.11 as $\vartheta_{\mathrm{c}} \approx -14.7\,^{\circ}\mathrm{C}$.

Parameter	Value	Unit
d_{d}	3.09 ± 0.05	mm
v_{d}	4.08 ± 0.01	m/s
$\vartheta_{\mathrm{d},0}$	14.3 ± 1	°C
$\vartheta_{\mathrm{sub},0}$	$\pm 17.0 \pm 0.2$	°C
α	30.0 ± 0.2	deg
Re	1980 ... 5390	-
We	165 ... 175	-
Pr	8.3 ... 25.9	-

respect to the initial drop motion. However, for convenience, the following descriptions mostly refer to the positions in the photographs shown in Fig. 3.7, instead of referring to a position with respect to the initial drop motion. It is worth to mention here that nucleation is absent in all photographs shown in the figure, illustrating the delayed nucleation also in the case of drop impact; although the liquid at the contact area is abruptly at $\vartheta_{\mathrm{c}} = -14.7\,^{\circ}\mathrm{C}$ after contact with the substrate, as estimated using Eq. 2.11. In the case of nucleation, the subsequent solidification fixes the momentary shape of the liquid. Due to the variation of the wetted surface area over a wide range, also the surface area iced after drop impact may significantly vary depending on the moment of stochastic nucleation, as will be shown later.

As described in Sec. 2.1, liquid spreading leads to the formation of a thin liquid lamella bounded by a pronounced rim. In the case of oblique drop impact as shown in the figure, the lamella starts to form in the reverse direction of initial drop motion, while the remaining liquid continues its spreading in the direction of initial motion. As shown in the figure, the spreading behavior on the cold surface does not obviously differ from

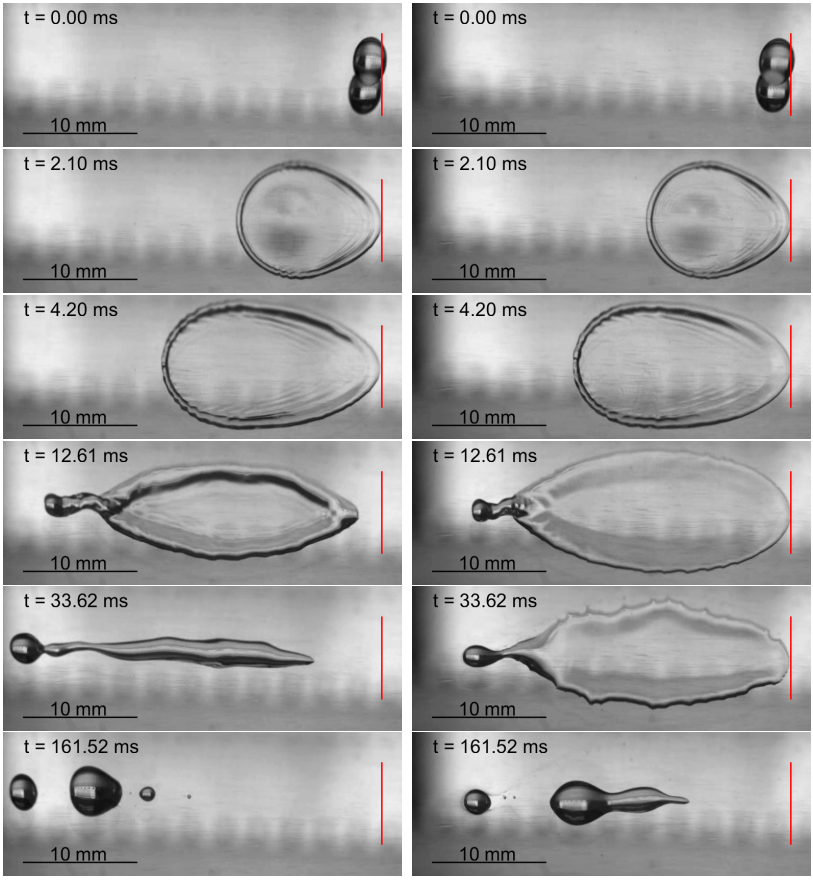

Figure 3.7: Oblique drop impact onto a polished aluminum surface at +17.0 °C (left) and at −17.0 °C (right). The drop diameter, impact velocity and impact angle are 3.09 mm, 4.09 m/s and 30 °, respectively. The drops are initially at 14.3 °C. Vertical lines in the photographs illustrate maximum drop spreading to the right. (Reprinted figure (adapted) with permission from [320]. Copyright 2016 by the American Physical Society.)

that on the warm surface for $t \leq 4.2\,\text{ms}$, which may be explained by a comparison of the typical time scales of drop impact and drop cooling.

The typical time of drop cooling by conduction without phase change can be estimated as $t_{\mathrm{co}} \sim h_{\mathrm{la}}^2/a_{\mathrm{d}}$, where h_{la} represents the liquid film thickness and a_{d} is the thermal diffusivity of the impinging liquid. According to Eq. 2.8, the residual lamella thickness after drop impact can be expressed in the form $h_{\mathrm{la,res}} = 0.79\, d_{\mathrm{d}}\, \mathrm{Re}^{-2/5}$, where the Reynolds number Re is defined using the normal drop impact velocity, $v_{\mathrm{d,n}}$, and the drop diameter as $\mathrm{Re} = v_{\mathrm{d,n}}\, d_{\mathrm{d}}/\nu$. Therefore, the ratio of the liquid cooling time to the hydrodynamic time of drop impact, $t_{\mathrm{imp}} = d_{\mathrm{d}}/v_{\mathrm{d,n}}$, can be estimated as

$$\frac{t_{\mathrm{co}}}{t_{\mathrm{imp}}} \sim \mathrm{Pr}\,\mathrm{Re}^{1/5}, \tag{3.1}$$

with $v_{\mathrm{d,n}} = v_{\mathrm{d}} \sin\alpha = 2.04\,\mathrm{m/s}$. The thickness of the thermal boundary layer developing in the impact plate during non-isothermal impact can be estimated as $h_{\mathrm{tbl,sub}} \sim \sqrt{a_{\mathrm{sub}} t}$. With the thermal diffusivity of aluminum, $a_{\mathrm{sub}} \approx 10^{-4}\,\mathrm{m^2/s}$, after the typical time of drop impact $t_{\mathrm{imp}} \approx 1.5 \times 10^{-3}\,\mathrm{s}$, the thermal boundary layer thickness in the substrate is $h_{\mathrm{tbl,sub}} \approx 4 \times 10^{-4}\,\mathrm{m}$, which is much smaller than the substrate thickness itself. Therefore, the finiteness of the substrate can be neglected for the heat transfer during drop impact, and the temperature at the contact surface between the impinging liquid and the substrate can be assumed as $\vartheta_{\mathrm{c}} = -14.7\,^{\circ}\mathrm{C}$ for the entire time of drop spreading. It is constant until the thermal boundary layers developing in the substrate and the impinging liquid pervade the entire respective phase. Therefore, the liquid temperature during impact may vary between the initial drop temperature $\vartheta_{\mathrm{d,0}} = 14.3\,^{\circ}\mathrm{C}$ and the contact temperature $\vartheta_{\mathrm{c}} = -14.7\,^{\circ}\mathrm{C}$. For this temperature range, the Prandtl number of water ranges from $\mathrm{Pr} = 8.3$ at $-14.0\,^{\circ}\mathrm{C}$ to approx. $\mathrm{Pr} = 25.9$ at $-14.0\,^{\circ}\mathrm{C}$. In the same temperature range, the Reynolds number for the experiments varies between $\mathrm{Re} = 5390$ to $\mathrm{Re} = 1980$, respectively. Accordingly, the ratio between the time for drop cooling and drop spreading, defined in Eq. 3.1, is between 46 at $\vartheta = 14.3\,^{\circ}\mathrm{C}$ and 118 at $\vartheta = -14.7\,^{\circ}\mathrm{C}$; thus $t_{\mathrm{imp}} \ll t_{\mathrm{co}}$ for all possible liquid temperatures. Since the time scale of drop spreading is much smaller than the time scale of drop cooling, the heat transfer between the drop and the surface is irrelevant during drop spreading. Therefore, the liquid properties only slightly change during drop spreading, and do not cause a significant change of the drop hydrodynamics, as shown in Fig. 3.7. Thus, only inertia and the initial properties of the impinging liquid, which both are constant for the shown experiments, control the first phase of drop impact.

A first change of the liquid behavior is found for $t \approx 4.2\,\mathrm{ms}$, when the spread liquid has reached its maximum lateral extent in the vertical direction in the photographs of Fig. 3.7. As shown in the figure, the thin liquid film in the right part of the spread drop starts to recede on the warm surface, while there has taken place no obvious motion in the case of the cold substrate. The influence of the substrate temperature becomes more obvious at $t = 12.61\,\mathrm{ms}$, when a pronounced rim has already formed during the ongoing recession on the warm surface. At the same time, the liquid splat on the cold surface remains almost in its initial spread shape. At $t \approx 33.62\,\mathrm{ms}$ the rim on the warm surface has merged, resulting in a rivulet which later breaks up into several smaller sessile drops, as shown in the last photograph in Fig. 3.7. During the same time, the drop receding on the cold surface is significantly decelerated by altered fluid properties, such as an increased viscosity and work of adhesion [148]. Therefore, the contact time and contact area between the liquid and the surface, both being important parameters in the scope of nucleation, are drastically affected by heat transfer between the substrate and the spread liquid. This in turn promotes a faster cooling down of the liquid, influencing the most crucial parameter for nucleation, namely the liquid temperature.

In contrast to a uniform receding on the warm surface, the contact line appears to be pined at several positions during receding on the cold surface, causing a partially concave shape of the contact line. This festoon-like shape of the contact line may be a result of capillary instabilities, in many cases driven by the Marangoni effect [74, 289]. However, local pinning of the contact line can also be caused by irregularities at the substrate surface, even if their size is only several nanometers [255].

A quantitative comparison of the hydrodynamics during oblique impact onto the warm and the cold substrate in terms of the temporal evolution of the wetted surface area A_{wet} is shown in Fig. 3.8. As already indicated by the previous qualitative comparison, the spreading phase is not influenced by the substrate temperature. Accordingly, the wetted surface area is unaffected by the substrate temperature until $t \approx 6\,\mathrm{ms}$. Due to liquid cooling during drop impingement accompanied by an increase of the liquid viscosity, a smaller maximum wetted surface could be expected for the impact onto the cold surface. However, as shown in the figure, a drop impact onto the cold surface results in a maximum wetted surface area which is even slightly larger than that on the warm surface. This is due to the concurrence of spreading and receding during inclined impact. As shown in Fig. 3.7, the drop impacting onto the warm surface starts to

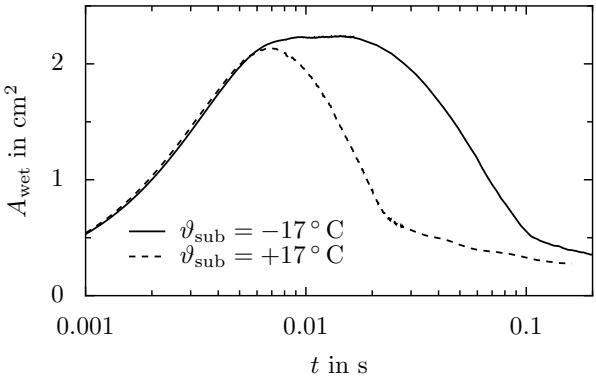

Figure 3.8: Temporal evolution of the wetted surface area, A_{wet}, during oblique drop impact onto a polished aluminum surface at 17.0 °C (dashed line) and at −17.0 °C (solid line). Drops are initially at 14.3 °C, their diameter is 3.09 mm and the impact velocity is 4.09 m/s. The impact angle is 30 °. (Reprinted figure (adapted) with permission from [320]. Copyright 2016 by the American Physical Society.)

recede on the right side while it is still spreading on the left side. This beginning receding on the right side causes a reduced further increase of the wetted surface area. On the cold surface, the receding on the right side is strongly damped by an increased viscosity, whereas the spreading on the left side is not yet affected by heat transfer and still dominated by inertia, which in sum results in a larger increase of the wetted surface area compared to an impact onto the warm surface.

3.1.1.4 Conclusion

The influence of a varying substrate temperature on the drop hydrodynamics during inclined impact of water drops has been experimentally investigated. The experimental setup and procedure have been thoroughly described, and enable examination of inclined drop impact, and moreover allow independent variation of both the substrate and drop temperature down to $\vartheta = -18.0\,^\circ$C. However, the present study has been devoted to the inclined impact of water drops initially at room temperature. In the specific cases shown in the present study (Figs. 3.7 and 3.8), no nucle-

ation occurred during the entire period of drop spreading and receding; although the liquid at the impact surface is abruptly cooled down to the contact temperature $\vartheta_c = -14.7\,^{\circ}\mathrm{C}$. The wetted surface area varies over a wide range during inclined impact. Since nucleation and subsequent freezing fix the momentary shape of the spread liquid, also the surface area effectively iced after drop impact may significantly vary depending on the moment of stochastic nucleation.

The impact onto a cold surface is associated with an increasing viscosity which is accompanied by an increase of viscous dissipation. Therefore, a decreased maximum wetted surface due to increased dissipation during spreading would be intuitive. However, for the examined experimental conditions, the time scale of drop cooling is much larger than the time scale of drop impact. Therefore, the heat transfer during drop spreading is marginal and has, if any, only a negligible influence on the spreading phase of an impinging drop. A first effect of the varying substrate temperature on the drop hydrodynamics is observed when the spreading liquid has reached its maximum lateral extent. Due to the increase of the liquid viscosity during impact onto the cold substrate, the receding of the liquid on the right is drastically damped, while spreading is ongoing on the left. However, on the warm surface the liquid receding on the right already starts, while liquid spreading is ongoing on the left. Therefore, an inclined drop impact onto a cold surface even results in a slightly larger wetted surface area, than drop impact onto a warm substrate. The increase of the maximum wetted surface area is only marginal. However, not only the maximum wetted surface area, but also the contact time between the liquid and the surface is increased during impact onto a cold surface. Both the larger maximum wetted surface area and the larger contact time result in an increased liquid cooling, which in turn causes a faster decrease of the liquid temperature. As shown in Sec. 2.2, all of these parameters namely the wetted surface area, the contact time and the liquid temperature are crucial for heterogeneous nucleation. Hence, although the spreading phase and the maximum extent of the wetted surface area are not significantly influenced by the substrate temperature, the thermally induced increase of the liquid viscosity at least implicitly influences subsequent nucleation by increasing the contact area and contact time between the impinging liquid and the substrate.

3.1.2 Numerical investigation of normal drop impact

Non-isothermal normal impact of supercooled water drops is computationally studied. To investigate the pure drop hydrodynamics, phase change of the impinging drops is not accounted for in the computational model. However, conjugate heat transfer with the impact surface is modeled. In the following, the numerical model is described, and validated by computing a series of configurations of two-phase fluid flow and conjugate heat transfer, for which experimental and analytical results are available in the literature. In a parametric study, the effect of the impact conditions on drop spreading and the maximum spreading diameter during drop impact onto a superhydrophobic surface of constant wettability is studied. Both the initial drop and substrate temperature, as well as the drop diameter and impact velocity are varied and their influence on the hydrodynamics during drop impact is examined.

3.1.2.1 Mathematical method and numerical approach

Drop impact is a highly complex phenomenon comprising a multitude of physics which deserve mathematical description and computational modeling. It is a multiphase flow comprising at least two different fluid phases: the impacting fluid and the ambient phase. The phases are separated by a moving boundary namely the phase interface requiring a special treatment. The hydrodynamic interaction of the impinging fluid with the impact surface has to be account for by means of a contact angle model describing the wettability of the surface. In the case of non-isothermal drop impact, the fluid temperature changes during impact and requires solution of the energy equation in parallel to the solution of the governing equations of fluid flow. Temporal and spatial variations of the liquid temperature are accompanied by a change of the temperature dependent fluid properties such as the density, viscosity, thermal conductivity, heat capacity and surface tension which in turn may affect fluid flow and heat transfer. Last but not least, during non-isothermal drop impact heat is transferred between the impinging fluid phase and the impact surface, resulting in a temperature field which continuously alters not only in the fluid but also in the substrate. Accordingly, the heat flux at the substrate surface is unsteady, prohibiting a fixed boundary condition for the energy at the surface. Therefore, the computational model for the hydrodynamics and accompanied heat transfer also has to incorporate simultaneous heat transfer in the underlying wall, i.e. conjugate heat transfer.

The numerical model is implemented in foam-extend 3.2 [355], an extension of the widely used open source software package OpenFOAM®, which utilizes the finite volume method to approximate the transport equations. The finite volume method and involved discretization schemes are not presented here; instead of that the reader is referred to comprehensive reviews for example found in [110, 307, 370]. The computational model employed in the present numerical study is based on the conjugate heat transfer solver *conjugateHeatFoam* which is combined with the multiphase solver *interFoam* to include both fluid phases, being water and air in the present study.

The numerical approach for the multiphase flow is an Eulerian interface capturing method based on the volume-of-fluid (VOF) method [151]. The liquid-gas interface is not explicitly reconstructed, but the information about the interface position is implicitly obtained by the field of the liquid volume fraction (commonly termed phase fraction). The mathematical formulation of the free surface flow involves an interface capturing methodology similar to the approach in [301], which is described in detail in [35]. To incorporate conjugate heat transfer, the model has been extended in [33]. The computational model is further extended for the present study to account for the temperature dependence of all relevant thermophysical properties of the fluids in the respective temperature range of the computational study.

Governing equations of fluid flow

The transport equations for the incompressible, laminar flow of Newtonian fluids, governing the presently considered flow during non-isothermal drop impact, are the conservation of mass and momentum

$$\nabla \cdot \mathbf{U} = 0, \tag{3.2}$$

$$\frac{\partial(\rho \mathbf{U})}{\partial t} + \nabla \cdot (\rho \mathbf{U}\mathbf{U}) = -\nabla p_{\mathrm{dyn}} - \mathbf{g} \cdot \mathbf{x} \nabla \rho + \nabla \cdot \mathbf{T} + \sigma \kappa \nabla \gamma, \tag{3.3}$$

where ∇ denotes the nabla operator, $\mathbf{U}$ is the velocity, ρ is the density, and p_{dyn} denotes the pressure modified by the hydrostatic contribution, $p_{\mathrm{dyn}} = p - \rho \mathbf{g} \cdot \mathbf{x}$. The variable $\mathbf{g}$ is the acceleration of gravity, $\mathbf{x}$ is the position vector in space, $\mathbf{T} = \eta \left[\nabla \mathbf{U} + (\nabla \mathbf{U})^T \right]$ is the viscous stress tensor for Newtonian fluids, σ is the surface tension coefficient, κ is the mean curvature of the liquid-gas interface, and γ is the volumetric phase fraction; $\eta = \rho \nu$ is the fluid's dynamic viscosity. The term containing

the density gradient on the right-hand side of Eq. 3.3 is derived from the pressure gradient by using the definition of the modified pressure p_{dyn}. This representation has the numerical advantage of a simpler specification of boundary conditions for the pressure, but also enables a more efficient computational treatment of the steep density change across the free liquid-gas interface [301].

Phase description and interface modeling

The fluid comprising liquid and gas is modeled as a mixture of two phases, both being Newtonian immiscible fluids, with the indicator function γ describing the distribution of each phase within the mixture. $\gamma = 0$ corresponds to the gaseous phase (air) and $\gamma = 1$ to the liquid phase (water); across the interface, γ varies smoothly between these bounds. Besides the general conservation of mass according to Eq. 3.2, the VOF approach also deserves for the conservation of the volumetric phase fraction described by the transport equation for the indicator function γ as

$$\frac{\partial \gamma}{\partial t} + \nabla \cdot (\mathbf{U}\gamma) = 0. \tag{3.4}$$

The thermophysical properties of the fluid mixture are determined as weighted averages corresponding to the distribution of the phase fraction as

$$\phi = \gamma\phi_{\mathrm{l}} + (1-\gamma)\phi_{\mathrm{g}}, \tag{3.5}$$

where ϕ is an arbitrary property, and the indices l and g denote the liquid and gaseous phase, respectively. The properties are equal to those of each separate phase in the region it occupies, and smoothly vary across the interface according to the variation of the indicator function.

The region of the free liquid-gas interface is determined from the solution of Eq. 3.4, which is limited to the range $\gamma = [0, 1]$, defining the regions in the fluid domain occupied by gas and liquid, as well as the interface region itself with $0 < \gamma < 1$. Surface tension, which plays a fundamental role in free surface flows such as drop impact, is incorporated into Eq. 3.3 by applying the Continuum Surface Force (CSF) model [46]. The resulting mass force term, $\sigma\kappa\nabla\gamma$, acts only in the transitional region separating the phases, i.e. in cells with $0 < \gamma < 1$, in the normal direction to the theoretical interface. The phase fraction γ theoretically has an infinite gradient at the interface, since it macroscopically represents a discontinuous function. This cannot be modeled within the current finite

volume VOF approach and instead, the phase fraction varies smoothly in the region of the phase-interface, being of very small thickness. As a consequence, the fluid properties and surface tension force change smoothly across the interface, enabling to calculate their changes and gradients in accordance with the CSF model.

As described in detail in [301], the compression of the interface incorporated in the *interFoam* solver is not achieved by using a specially designed compressive differencing scheme. Instead, to obtain an anti-diffusion contribution as in the case of compressive schemes, an additional compression term is introduced into the discretized equation for the phase fraction, Eq. 3.4, yielding

$$\frac{\partial \gamma}{\partial t} + \nabla \cdot (\mathbf{U}\gamma) + \nabla \cdot [\mathbf{U}_{\mathrm{com}}\gamma(1-\gamma)] = 0, \tag{3.6}$$

where $\mathbf{U}_{\mathrm{com}}$ is a kind of "compression velocity". The compression method incorporates a counter-gradient transport of the indicator function acting against numerical diffusion. It has been successfully used in other studies [33, 35, 301], where a detailed explanation of the discretization and calculation of the compressive flux is found. The compression flux acts only in the interface region, namely in cells with $0 < \gamma < 1$ normal to the interface. The additional term, $\nabla \cdot [\mathbf{U}_{\mathrm{com}}\gamma(1-\gamma)]$, is active only in the numerically-integrated form of the transport equation and exclusively within the thin interface region. It does not in any way affect the solution outside this region. The scheme is obviously consistent in the liquid and gaseous regions, and also in the transitional region, where the numerical error does not accumulate without a limit [194]. During the movement of the interface, the cells that were previously part of the liquid or gaseous region, become part of the interface region for a short period of time as the interface passes these cells. After that, the phase fraction in these cells returns to either 0 or 1, and the additional term becomes zero again, without a significant accumulation or transport of the numerical errors into the interface region. The consistency is also reflected in the fact that the thickness of the region where the compressive term is active tends to zero with increasing mesh resolution. As a matter of fact, in the theoretical case of a well defined sharp interface, the standard volume-of-fluid equation is recovered. The interface compression is very effective in the transitional region and is highly capable of improving the interface resolution by a reduction of numerical diffusion [84].

Governing equations of heat transfer

The governing equation describing heat transfer in the fluid phases is the conservation of energy. Heat sources due to viscous dissipation have negligible effects in inertia dominated flows involving small Eckert numbers, $\mathrm{Ec} \equiv v_\mathrm{d}^2/(c_\mathrm{p}\Delta T) \ll 1$, as in the case of the present study [33, 96, 141]. Therefore, they are disregarded and the transport equation for energy is used in the form of the equation for temperature

$$\rho c_\mathrm{p} \frac{\partial T}{\partial t} + \rho c_\mathrm{p} \mathbf{U} \cdot \nabla T = \nabla \cdot (k \nabla T), \tag{3.7}$$

where c_p is the heat capacity, k is the thermal conductivity, and T denotes the temperature. The system of equations for the hydrodynamics and thermodynamics of the fluid flow (3.2–3.7) is extended to include energy transport due to transient heat conduction in the substrate. The energy equation in the temperature form for the substrate reads

$$\rho_\mathrm{sub} c_\mathrm{v,sub} \frac{\partial T_\mathrm{sub}}{\partial t} = \nabla \cdot (k_\mathrm{sub} \nabla T_\mathrm{sub}), \tag{3.8}$$

where the subscript sub denotes the solid substrate. The discretization of the temperature equations follows the standard finite-volume procedure as applied in [33, 35].

Coupling of the energy equations for the fluid and the substrate domain, Eqs. 3.7 and 3.8, respectively, is based on the continuity of temperature and heat fluxes in the normal direction across the surface of the substrate. Due to different thermal conductivities of the substrate and the fluid, the temperature gradients normal to the substrate surface are discontinuous, i.e.

$$-k(\nabla T)|_\perp = -k_\mathrm{sub}(\nabla T_\mathrm{sub})|_\perp, \tag{3.9}$$

where the surface-normal temperature gradients $(\nabla T)|_\perp$ are evaluated at the shared boundary between the fluid and the substrate region.

The thermal conductivity of the fluid mixture is obtained as a linear weighted average of the conductivities of the respective phases according to Eq. 3.5. However, it should be noted that the mixture conductivity at cell-faces used in the diffusion term of the energy equation is obtained by harmonic interpolation of the values stored in the cell centers, in particular to account for the heat transfer across the interface between the fluid and the substrate region.

Temperature dependent material properties

The temperature dependence of the thermophysical properties such as the density, kinematic viscosity, thermal conductivity and heat cpacity of both fluids, as well as the surface tension between them, is accounted for. Based on tabulated literature data from [306, 367] for the temperature range between $\vartheta = -30.0 \ldots + 20.0\,^{\circ}\mathrm{C}$, their temperature dependence is described by polynomial numerical value equations, which are summarized in App. B for the properties of both water and air. Based on the transient temperature field, the thermophysical properties are calculated separately for both fluids using the found polynomials, and the properties of the fluid mixture are then obtained from Eq. 3.5.

Since the Peclet number $\mathrm{Pe} \equiv \mathrm{Re}\,\mathrm{Pr}$ is much larger than unity for the inertia-dominated flow of a spreading drop, the influence of energy transport on momentum transport is only weak. However, the present model allows computation of general cases by coupling the fluid flow equations with the energy equation via temperature-dependent properties of both considered fluids.

Contact angle modeling

The hydrodynamic interaction between the impact surface and the impinging liquid is described by the wettability of the surface. It is accounted for by applying the dynamic contact angle model according to Kistler [178], which was successfully used in [33, 35]. It gives a relation for the apparent contact angle depending on the contact line velocity as

$$\theta_{\mathrm{dyn}} = \mathrm{f}_{\mathrm{Hoff}}\left(\mathrm{Ca} + \mathrm{f}_{\mathrm{Hoff}}^{-1}(\theta_{\mathrm{adv/rec}})\right) \tag{3.10}$$

where $\mathrm{Ca} \equiv \eta U_{\mathrm{cl}}/\sigma$ is the capillary number, calculated using the contact line velocity U_{cl}, with $U_{\mathrm{cl}} > 0$ for an advancing and $U_{\mathrm{cl}} < 0$ for a receding contact line. The Hoffman function $\mathrm{f}_{\mathrm{Hoff}}$ is defined as

$$\mathrm{f}_{\mathrm{Hoff}}(\mathrm{Ca}) = \cos^{-1}\left\{1 - 2\tanh\left[5.16\left(\frac{\mathrm{Ca}}{1 + 1.31\mathrm{Ca}^{0.99}}\right)^{0.706}\right]\right\}. \tag{3.11}$$

Depending on the direction of the contact line movement, i.e. if the surface is wetted ($U_{\mathrm{cl}} > 0$) or dewetted ($U_{\mathrm{cl}} < 0$), $\theta_{\mathrm{adv/rec}}$ in Eq. 3.10 is substituted by the value of either the advancing contact angle θ_{adv} or the receding contact angle θ_{rec}, respectively, to calculate the resulting dynamic contact angle θ_{dyn} present in the case of a certain contact line velocity.

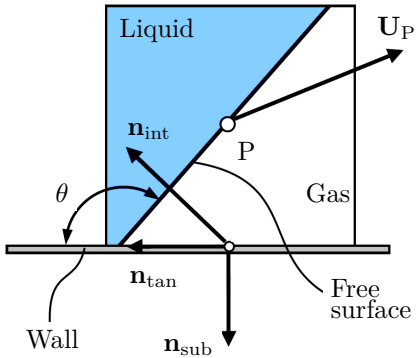

Figure 3.9: Geometry at the contact line used for the calculation of the contact line velocity U_cl with Eq. 3.12.

The contact line velocity is approximated as the component of the velocity at the phase-interface in the first computational cell closest to the substrate surface, which is normal to the contact line and tangential to the wall as

$$U_\mathrm{cl} = \left[\frac{\mathbf{n}_\mathrm{int} - (\mathbf{n}_\mathrm{sub}\cdot\mathbf{n}_\mathrm{int})\mathbf{n}_\mathrm{sub}}{|\mathbf{n}_\mathrm{int} - (\mathbf{n}_\mathrm{sub}\cdot\mathbf{n}_\mathrm{int})\mathbf{n}_\mathrm{sub}|}\right]\cdot\left[\mathbf{U}_\mathrm{P} - (\mathbf{n}_\mathrm{sub}\cdot\mathbf{U}_\mathrm{P})\mathbf{n}_\mathrm{sub}\right], \qquad (3.12)$$

where $\mathbf{U}_\mathrm{P}$ is the fluid velocity at the cell-center closest to the wall within the interface region, $\mathbf{n}_\mathrm{sub}$ is the normal vector of the substrate surface, $\mathbf{n}_\mathrm{int}$ is the normal vector of the liquid-gas interface, and $\mathbf{n}_\mathrm{tan} = \mathbf{n}_\mathrm{int} - (\mathbf{n}_\mathrm{sub}\cdot\mathbf{n}_\mathrm{int})\mathbf{n}_\mathrm{sub}$ is the projection of $\mathbf{n}_\mathrm{int}$ on the substrate surface; a schematic of the corresponding geometry is shown in Fig. 3.9.

The dependence of the dynamic contact angle θ_dyn on the contact line velocity, obtained with Eq. 3.10, for a superhydrophobic surface with $\theta_\mathrm{adv} = 160\,^\circ$ and $\theta_\mathrm{rec} = 150\,^\circ$ is illustrated in Fig. 3.10. As shown in the figure, the contact angle hysteresis explained in Sec. 2.1 is captured by the model: a stagnant or pinned contact line with $U_\mathrm{cl} = 0$ is associated with an apparent contact angle in the range $\theta_\mathrm{rec} < \theta_\mathrm{dyn} < \theta_\mathrm{adv}$. According to the implementation of the contact angle model in the multiphase solver *interFoam*, the contact angle is prescribed depending on the contact line velocity. In some cases involving contact line pinning such as during the incipient rolling motion of a sessile drop on an inclined surface, this causality may cause wrong computational results, which can be overcome by the prescription of the contact line velocity as a function of

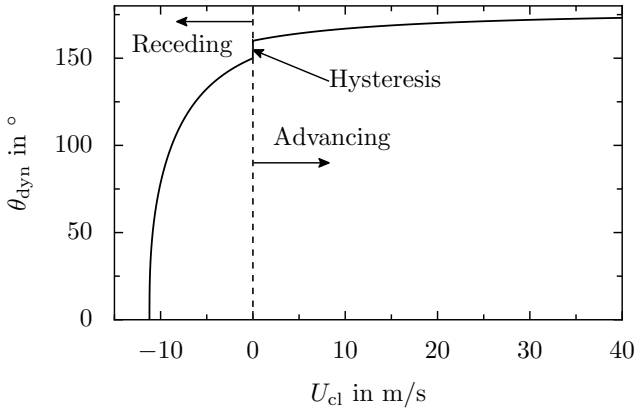

Figure 3.10: Dependence of the dynamic contact angle θ_{dyn} on the contact line velocity U_{cl} according to the Kistler model, Eq. 3.10.

the contact angle, as proposed in [206]. However, for the forced wetting during the dynamic process of a drop impact, the standard implementation of the contact angle model without an explicit pinning condition is sufficient to account for the surface wettability.

Time step control

The computational time step is appropriately adapted to the present flow conditions by comparing the maximum possible values for the time steps Δt_{i}, calculated based on different restrictions. The first condition is related to the convective transport in Eq. 3.3 and is based on the Courant number, $\mathrm{Cou} \equiv \Delta t|\mathbf{U}|/\Delta x$, where Δt and Δx are the time step size, and cell size of the computational mesh, respectively. The corresponding maximum time step size is

$$\Delta t_{\mathrm{u}} = \min\left[\frac{\mathrm{Cou}_{\mathrm{max}}}{\mathrm{Cou}_{\mathrm{max,loc}}}\Delta t_{\mathrm{old}}\ ,\ \left(1+\lambda_1\frac{\mathrm{Cou}_{\mathrm{max}}}{\mathrm{Cou}_{\mathrm{max,loc}}}\Delta t_{\mathrm{old}}\right), \lambda_2\Delta t_{\mathrm{old}}\right], \tag{3.13}$$

where $\mathrm{Cou}_{\mathrm{max,loc}}$ is the maximum Courant number of the actual time step in the computational domain, and $\mathrm{Cou}_{\mathrm{max}}$ is the maximum allowed Courant number which is predefined before simulation; $\mathrm{Cou}_{\mathrm{max}} = 0.2$ is used for the present simulations [35]. λ_{i} are damping factors, which take the values $\lambda_1 = 0.1$ and $\lambda_2 = 1.2$ [35], used to avoid time step oscillations

and yielding a smooth increase of the time step. The second condition corresponds to the capillary flow and was established in [123] as

$$\Delta t_\sigma = \frac{1}{2}\left[c_2\frac{\eta\Delta x}{\sigma} + \sqrt{\left(c_2\frac{\eta\Delta x}{\sigma}\right)^2 + 4c_1\frac{\rho\Delta x^3}{\sigma}}\right], \tag{3.14}$$

where $\eta\Delta x/\sigma$ and $\sqrt{\rho\Delta x^3/\sigma}$ may be interpreted as capillary time scales, based on a comparison of both viscous and inertial to capillary forces, respectively. c_i are constants with $c_1 = 0.01$ and $c_2 = 10$ [84]. The new time step Δt_{new} is finally obtained as

$$\Delta t_{\text{new}} = \min\left(\Delta t_{\text{u}}, \Delta t_\sigma, \Delta t_{\max}\right), \tag{3.15}$$

where $\Delta t_{\max}$ is the maximum time step manually predefined before simulation. According to Eq. 3.15, the time step size is adapted to the present flow conditions at the beginning of each computational time step.

Solution procedure

The solution procedure is performed within each step of a loop iterating through time. Each iteration step starts with an appropriate adaption of the new time step according to Eqs. 3.13 - 3.15, and is followed by the calculation of the fluid motion in the region above the substrate surface, and solving of the energy equations, Eqs. 3.7 and 3.8, in both regions simultaneously.

The solution of the flow equations is obtained by utilizing the solution procedure thoroughly described in [301], which is suitable for a collocated variable arrangement (velocities stored at cell centers and not staggered in cell-face centers). A bounded technique is used to compress the interface region, which is followed by the calculation of the surface tension term, and utilizing the solution procedure for the pressure-velocity coupling. The discretized momentum equation is constructed, followed by a correction loop to obtain the solution for the pressure, based on which the momentum is corrected.

During the solution of the energy equation in the fluid and substrate region, the meshes for the fluid domain and the substrate domain are combined into a single mesh and a single system of algebraic equations is solved for the temperature field. As already mentioned, the coupling of the temperature fields in the fluid and the substrate region is based

on the continuity of temperature and heat fluxes across the substrate surface. The conductivity at the cell-faces belonging to this fluid-substrate interface is evaluated using harmonic interpolation. Otherwise, the face value of the conductivity would be improper, and the heat flux balance at the substrate-fluid interface would not be preserved [269]. The heat fluxes across the substrate surface are internally conserved without the need for an explicit transfer across the shared fluid-substrate boundary during the computation.

All fluid properties are updated on completion of each time step, when new solutions for the phase fraction and temperature are known.

Numerical domain

Due to instabilities which may arise during spreading, even normal drop impact is in reality not perfectly axisymmetric. However, in the present study, it is treated axisymmetric with respect to the impact direction, and the influence of potential instabilities on the overall hydrodynamics and heat transfer is neglected. This allows two-dimensional simulations accompanied by a drastic decrease of the computational costs.

Figure 3.11 shows schematics of the two-dimensional wedge-type mesh and the computational domain. The meshes have dimensions of at least $2.6\,d_\mathrm{d} \times 2.6\,d_\mathrm{d}$ in the fluid region and $2.6\,d_\mathrm{d} \times 0.16\,d_\mathrm{d}$ in the substrate region. The mesh is stepwise refined in the region occupied by the drop during its deformation. By this, the drop is at any time resolved with a maximum cell size of $5\,\mu\mathrm{m}$, which is equivalent to a minimum of 200 cells per drop diameter for all impact conditions.

A no-slip boundary condition accompanied by the contact angle boundary condition according to the Kistler model are imposed at the fluid-substrate interface. Open boundaries, i.e. a zero gradient for the flow velocity and a fixed pressure are prescribed at the upper and the outer boundary of the wedge type domain. Symmetry boundary conditions are applied at the symmetry axis and symmetry planes of the wedge for both the flow and heat transfer equations. While the initial substrate temperature is fixed at the lower mesh boundary, adiabatic boundary conditions are imposed at all remaining boundaries.

The drop is initialized slightly above the impact surface, corresponding to $t = -0.001\,\mathrm{s}$, to allow the flow field below the drop to develop before impact. At this time the drop impact velocity is prescribed and further acceleration of the drop until impact is neglected.

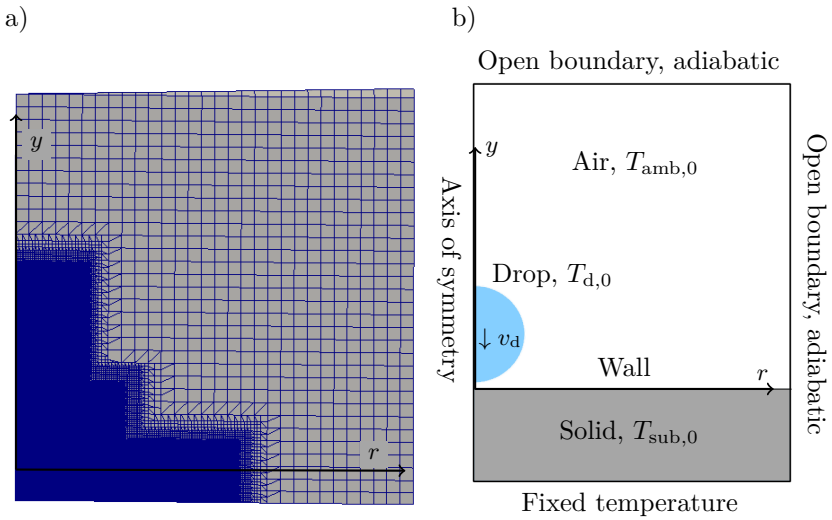

Figure 3.11: Schematic of the two-dimensional numerical mesh (a), and the computational domain and boundary conditions (b), with the substrate region (gray) and the fluid region comprising the drop (blue) and the ambient air (white). For the purpose of clarity, only every 3rd grid line of the numerical mesh is illustrated in a). (Reprinted with permission from [313]. Copyright 2017 Elsevier.)

3.1.2.2 Solver validation

In order to validate the functionality of the computational model and the implemented solver, the results of computations involving varying dominant physical mechanisms are compared to experimental results and analytical solutions available in the literature.

Correct coupling of the fluid and substrate region is verified with simulations of one-dimensional heat transfer without fluid flow. The substrate and fluid regions are initiated with different temperatures and the temperature between the regions developing in the simulations is compared to the analytical solution for the contact temperature between two semi-infinite slabs of different temperature, which are brought into contact. To verify energy conservation across the coupled boundary between the substrate and the fluid region, the temporal change of thermal energy

within the regions is compared to the heat flow across the coupling region during drop impact. Heat is transferred into the fluid region only across the wall and the remaining boundaries of the fluid region are adiabatic. Therefore, for energy conservation the change of heat in the fluid and substrate region, and the heat flow across the wall surface have to be equal at each time. The overall functionality of the model, with consideration of temperature dependent fluid properties, is validated by the simulation of non-isothermal normal impact of a water drop. The computed data is compared to experimental data in terms of the temporal evolution of the drop spreading ratio.

One-dimensional heat transfer without fluid flow

For the validation of the thermal coupling of the fluid and substrate region, the contact temperature arising between two materials of different initial temperatures is calculated and compared to the theoretical contact temperature. For that, a fluid layer is initiated above the solid substrate, both the fluid and the substrate having different initial temperatures, T_1 and T_2. While constant temperatures are prescribed at the bottom and the top of the computational domain, the remaining boundaries are adiabatic. Buoyancy driven fluid flow is not accounted for, and thus the fluid region is treated similar to a solid. The cell size in the fluid region, Δx_{fl}, is adapted to the cell size used for the computations of drop impact, $\Delta x_{\mathrm{fl}} = 5\,\mu\mathrm{m}$. Due to the heat flux continuity at the fluid-substrate interface, the temperature gradients at the interface in the fluid and the substrate region are related by their thermal conductivities according to Eq. 3.9. In order to resolve the temperature gradient arising in the substrate region, Δx_{sub}, with the same precision as in the fluid region, the cell size in the substrate region is adapted for each computation as $\Delta x_{\mathrm{sub}} \approx \Delta x_{\mathrm{fl}} k_{\mathrm{sub}}/k_{\mathrm{fl}}$.

The analytical solution of the contact temperature theoretically arising instantaneously at the interface between the regions is calculated as [20]

$$\vartheta_{\mathrm{c,th}} = \frac{e_1 \vartheta_1 + e_2\, \vartheta_2}{e_1 + e_2}, \tag{3.16}$$

where e_1 and e_2 are the thermal effusivities of the two phases. To validate the thermal coupling for a wide range of parameters, various initial temperatures and material properties of the fluid and the substrate region are used for the computations, as summarized in Tab. 3.2.

Figure 3.12 shows a comparison of the computationally obtained contact temperature, $\vartheta_{\mathrm{c,num}}$, and the analytical solution, $\vartheta_{\mathrm{c,th}}$, for the initial

Table 3.2: Material properties and temperatures of the fluid and substrate region, used for the validation cases involving one-dimensional heat transfer, shown in Fig. 3.12.

Parameter	Fluid region	Substrate region	Unit
ρ	983.8 ... 998.2	1150 ... 2700	$\mathrm{kg/m^3}$
k	0.4806 ... 0.5995	0.18 ... 236	W/(m K)
c_p	4185 ... 4801	712 ... 1500	J/(kg K)
ϑ	-30 ... $+20$	-30 ... $+20$	$^\circ$ C

conditions according to Tab. 3.2. It is shown for the computational times $t = 0.5\,\mathrm{ms}$, $t = 1.0\,\mathrm{ms}$ and $t = 2.0\,\mathrm{ms}$. As shown in the figure, the agreement of the simulation results with the analytical solution is very good at each time for the entire temperature range and for all combinations of the material properties. The maximum relative errors with respect to the computationally obtained temperatures in Kelvin for the times $t = 0.5\,\mathrm{ms}$, $t = 1.0\,\mathrm{ms}$ and $t = 2.0\,\mathrm{ms}$ are 0.724 %, 0.659 % and 0.198 %, respectively.

The present validation case involves a discontinuity of the temperature field across the fluid-substrate interface during initialization. This discontinuity may cause an initial overshoot of the calculated interface temperature, which is straightened out for increasing simulation time, resulting in a relative error decreasing for increasing simulation time. It indicates a numerical solution converging in time, and therefore a correct thermal coupling between the fluid and substrate regions. However, already at $t = 0.5\,\mathrm{ms}$ a very good agreement between the computational and theoretical results is achieved. In the case of the simulations of drop impact, a thermal boundary layer develops in the gas phase around the drop prior to impact. Therefore, the substrate is already thermally influenced by the drop when the thermal boundary layer around the drop makes contact with the substrate. By this, the discontinuity between the temperature fields in the fluid and solid region, evolving during impact is reduced, if not even suppressed. Due to an expected absence of an overshoot of temperature, the agreement of the theoretical and the computationally obtained contact temperature can be expected to be even better during drop impact than during the present validation case.

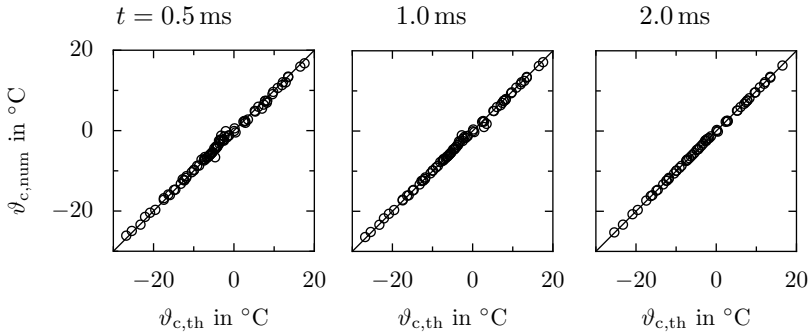

Figure 3.12: Contact temperature between two semi-infinite slabs for varying initial conditions, as summarized in Tab. 3.2. Comparison of computational results, $\vartheta_{\mathrm{c,num}}$, with the analytical solution, $\vartheta_{\mathrm{c,th}}$, for different computational times. The solid lines represent perfect agreement. (Reprinted with permission from [313]. Copyright 2017 Elsevier.)

Energy conservation during non-isothermal drop impact

Energy conservation across the fluid-substrate interface is verified by comparing the energy transferred across the interface during non-isothermal drop impact with the change of the thermal energy in both the fluid and the substrate region during this process. The change of the thermal energy in the substrate region is calculated as the change of the sensible heat with respect to the initial sensible heat, which is numerically integrated over the entire substrate domain V_{sub} as

$$Q_{\mathrm{sub}}(t) = \left| \int_{V_{\mathrm{sub}}} \int_{T_{\mathrm{sub},0}}^{T(t)} \rho_{\mathrm{sub}} c_{\mathrm{p,sub}} \,\mathrm{d}T \,\mathrm{d}V \right|. \tag{3.17}$$

In analogy, the energy in the fluid region is obtained as the sum of the sensible heats of both the liquid and the gaseous phase, numerically integrated over the entire fluid domain V_{fl} as

$$Q_{\mathrm{fl}}(t) = \left| \int_{V_{\mathrm{fl}}} \gamma \int_{T_{\mathrm{fl},0}}^{T(t)} \rho_{\mathrm{l}} c_{\mathrm{p,l}} \,\mathrm{d}T \,\mathrm{d}V + \int_{V_{\mathrm{fl}}} (1-\gamma) \int_{T_{\mathrm{fl},0}}^{T(t)} \rho_{\mathrm{g}} c_{\mathrm{p,g}} \,\mathrm{d}T \,\mathrm{d}V \right|, \tag{3.18}$$

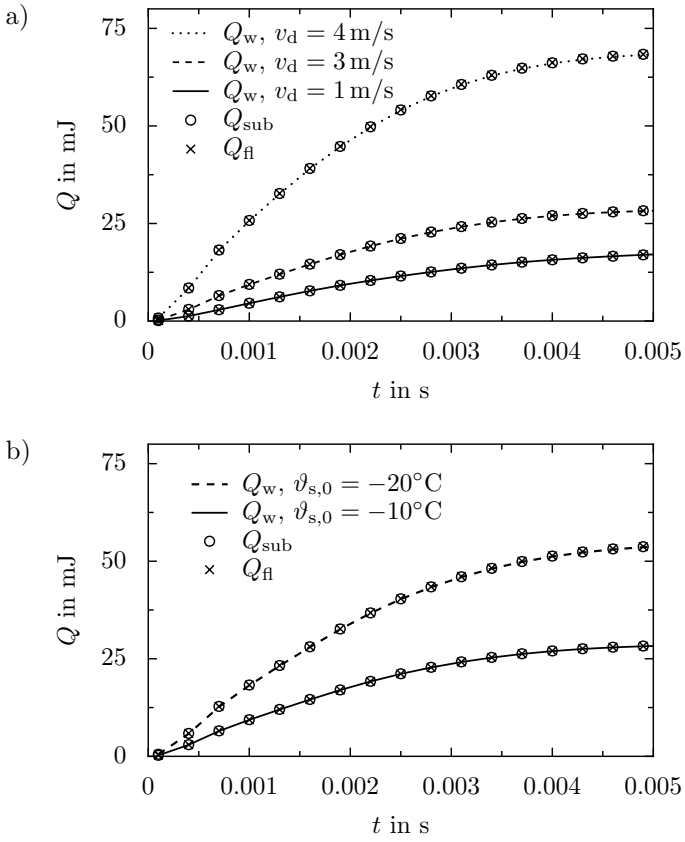

Figure 3.13: Comparison of the change of heat in the fluid, Q_{fl}, and the substrate region, Q_{sub}, with the heat transferred across the coupled boundary, Q_w, for different impact conditions. The drop diameter is $d_d = 0.002\,m$, the advancing and receding contact angles are $\theta_{adv} = 162.6°$ and $\theta_{rec} = 150°$, respectively. a) Varying impact velocity, $\vartheta_{d,0} = 0\,°C$ and $\vartheta_{s,0} = -20.0\,°C$. b) Varying initial substrate temperature, $v_d = 3\,m/s$ and $\vartheta_{d,0} = 0.0\,°C$. (Reprinted with permission from [313]. Copyright 2017 Elsevier.)

where $c_{p,g}$ is the heat capacity of the gaseous phase. The heat transferred across the interface is calculated by spatial and temporal numerical inte-

gration of the wall heat flux over the entire fluid-substrate interface, A_w, until time t as

$$Q_\mathrm{w}(t) = \left| \int_0^t \int_{A_\mathrm{w}} -k_\mathrm{sub} (\nabla T_\mathrm{sub})|_\perp \, \mathrm{d}A \, \mathrm{d}t \right| . \tag{3.19}$$

Figure 3.13 shows a comparison of the temporal evolution of the thermal energy in the fluid and substrate region with the heat transferred across the substrate surface for different impact velocities and initial substrate temperatures. In Fig. 3.13 a), the heat amounts are compared for a varying impact velocity, whereas Fig. 3.13 b) shows the comparison for a varying temperature difference between the drop and the surface. As shown in Fig. 3.13, the heat amounts are in excellent agreement for all impact conditions. Hence, energy is conserved during non-isothermal drop impact under various impact conditions, again attesting correct thermal coupling of the regions occupied by the fluids and the substrate.

Hydrodynamics during non-isothermal drop impact

The overall functionality of the computational model and the numerical solver comprising the account for temperature dependent fluid properties is verified by means of a comparison of computational results with experimental results for non-isothermal drop impact from [215]. The numerical results are quantitatively compared in terms of the evolution of the spreading ratio $\beta_\mathrm{wet} = d_\mathrm{wet}/d_\mathrm{d}$. The initial drop temperature during impact in the experiments, $T_\mathrm{d,0}$, is not explicitly mentioned in [215], but a relation between the measured ambient temperature T_amb and $T_\mathrm{d,0}$ is reported as

$$T_\mathrm{d,0} = T_\mathrm{amb} - 3.4 \exp(0.044\, T_\mathrm{amb,0}). \tag{3.20}$$

The relation accounts for increased evaporative cooling during the fall of a drop, attributed to the low relative humidity in the experimental chamber. It is used to calculate the initial drop temperature $T_\mathrm{d,0}$ used for the simulations.

Figure 3.14 shows a comparison of computational results with experimental data for normal drop impact with varying drop and surface temperatures. As shown in the figure, the agreement between the experimental data and the computed results is very good during the entire phase of drop spreading and the beginning of the receding phase. During later stages of drop receding the simulations slightly overpredict the experimentally observed receding velocity. This may be attributed to the nano-texture of

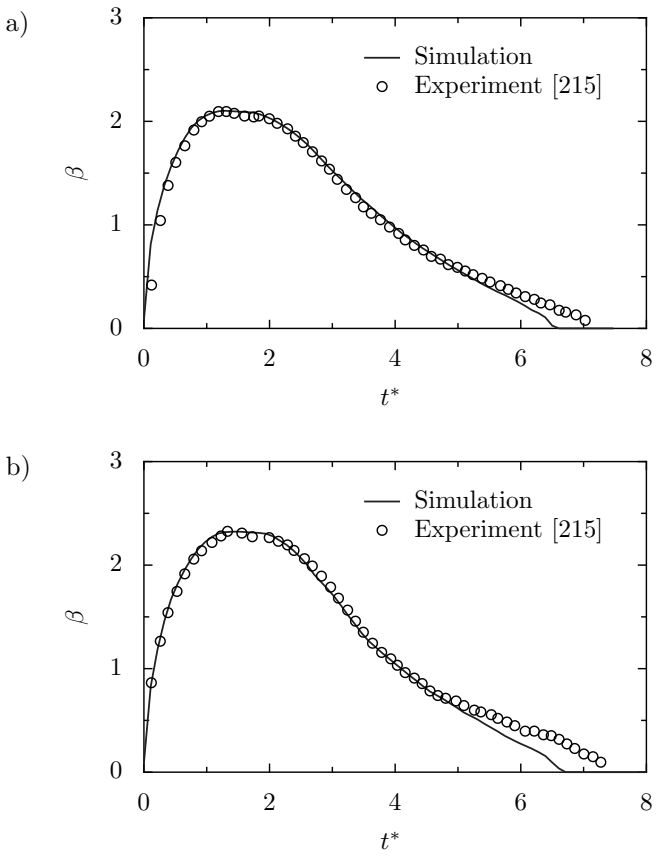

Figure 3.14: Temporal evolution of the spreading ratio during normal drop impact. Comparison of computational results (solid line) and experimental data (circles) from [215], with $v_\mathrm{d} = 1.3\,\mathrm{m/s}$ and $d_\mathrm{d} = 2.4\,\mathrm{mm}$. a) $\vartheta_{\mathrm{d},0} = -17.0\,^\circ\mathrm{C}$, $\vartheta_{\mathrm{sub},0} = \vartheta_{\mathrm{amb},0} = -16.0\,^\circ\mathrm{C}$, $\theta_\mathrm{adv} = 161.3°$, $\theta_\mathrm{rec} = 148.5°$; b) $\vartheta_{\mathrm{d},0} = 14.0\,^\circ\mathrm{C}$, $\vartheta_{\mathrm{sub},0} = \vartheta_{\mathrm{amb},0} = 23.0\,^\circ\mathrm{C}$, $\theta_\mathrm{adv} = 162.6°$, $\theta_\mathrm{rec} = 150°$. (Reprinted with permission from [313]. Copyright 2017 Elsevier.)

the experimentally investigated surfaces, which is not accounted for in the simulations. The surface morphology may cause capillary effects, which

cause an increased deceleration of the receding contact line. However, the overall process of drop impact and receding is accurately predicted with the numerical solver.

Concluding, the computational model is able to accurately capture the physical mechanisms, which are relevant during non-isothermal drop impact, namely conjugate heat transfer, fluid flow, the variation of the material properties with temperature and the mutual influence of these phenomena.

3.1.2.3 Results and discussion

All simulations of drop impact are performed assuming a silicon substrate of 0.5 mm thickness, with $\rho_{\mathrm{sub}} = 2330\,\mathrm{kg/m^3}$, $c_{\mathrm{p,sub}} = 712\,\mathrm{J/(kgK)}$ and $k_{\mathrm{sub}} = 148\,\mathrm{W/(mK)}$ [159]. The surface is characterized with the advancing and receding contact angles of $\theta_{\mathrm{adv}} = 162.6\,^\circ$ and $\theta_{\mathrm{rec}} = 150\,^\circ$, respectively. In all cases, the surrounding air and the substrate are initialized at the same temperature. All impact parameters such as the initial substrate and drop temperature, $\vartheta_{\mathrm{sub},0}$ and $\vartheta_{\mathrm{d},0}$, the impact velocity v_{d} and the drop diameter d_{d} have been varied over a wide range, to study their influence on the hydrodynamics during non-isothermal drop impact, which determine the maximum wetted area potentially iced after a single drop impact. The ranges of the varied parameters and the resulting dimensionless quantities are summarized in Tab. 3.3.

Table 3.3: Ranges of impact conditions and dimensionless quantities used for the numerical parametric study of the hydrodynamics during non-isothermal normal drop impact.

Parameter	Range	Unit
$\vartheta_{\mathrm{d},0}$	$-20 \ldots 20$	°C
$\vartheta_{\mathrm{sub},0}$	$-20 \ldots 20$	°C
v_{d}	$1 \ldots 4$	m/s
d_{d}	$1 \ldots 2$	mm
Re	$230 \ldots 7970$	-
We	$12 \ldots 440$	-
Pr	$7 \ldots 37$	-

Figure 3.15 shows the temporal evolution of the spreading diameter for varying impact velocities, and a drop diameter of $d_\mathrm{d} = 1\,\mathrm{mm}$ and $d_\mathrm{d} = 2\,\mathrm{mm}$. In all cases, the initial substrate and drop temperature are $\vartheta_{\mathrm{s},0} = -20.0\,^\circ\mathrm{C}$ and $\vartheta_{\mathrm{d},0} = 0\,^\circ\mathrm{C}$, respectively. As shown in the figure, the maximum spreading diameter increases with both an increasing drop diameter and an increasing impact velocity. However, the duration of the spreading phase is almost unaffected by the impact velocity. It is finished after $t \approx 0.6\,\mathrm{ms}$ and $t \approx 1.8\,\mathrm{ms}$ for $d_\mathrm{d} = 1\,\mathrm{mm}$ and $d_\mathrm{d} = 2\,\mathrm{mm}$, respectively. Before the drop starts to recede, the spreading diameter remains almost constant for a certain time, corresponding to the decrease of the contact angle from θ_adv to θ_rec, as described in Sec. 2.1. The duration of the period of an almost constant wetted surface area depends on the drop diameter and impact velocity, and is solely attributed to surface tension effects. The time between significant spreading and receding is the shortest for large maximum liquid deformations corresponding to a higher impact velocity. Moreover, a smaller drop diameter which is associated with a larger curvature of the drop surface after spreading leads to a decrease of this time.

Due to the hydrophobicity of the surface, the drop receding can be split into two phases, as already experimentally observed in [215, 216]. Until $t \approx 2\,\mathrm{ms}$ for $d_\mathrm{d} = 1\,\mathrm{mm}$ and $t \approx 5.5\,\mathrm{ms}$ for $d_\mathrm{d} = 2\,\mathrm{mm}$, the drop receding is very fast, followed by a slower further decrease of d_wet. The two regimes of a varying receding velocity have been explained in [215] by a partial penetration of the impinging liquid into the textured surface employed for the experiments, which according to the authors significantly affects liquid recoiling from the surface. Such a penetration behavior is not captured with the present numerical simulations, which assume a smooth surface. Nevertheless, the two regimes of liquid receding are observed, indicating that the behavior is dominantly driven by the drop hydrodynamics without a significant influence of the surface texture. The receding velocity within the first phase increases with increasing impact velocity and drop diameter. However, the receding rate during this stage, which is the receding velocity rationalized with the maximum spreading diameter, is independent of the impact velocity, as also found experimentally in [25]. The beginning of the second phase of receding is almost unaffected by the impact velocity. Moreover, during further recoiling the receding velocity is almost independent from the impact velocity, and it is only weakly influenced by the drop diameter; a larger drop diameter causes a slightly decreased velocity during the second phase of receding. Due

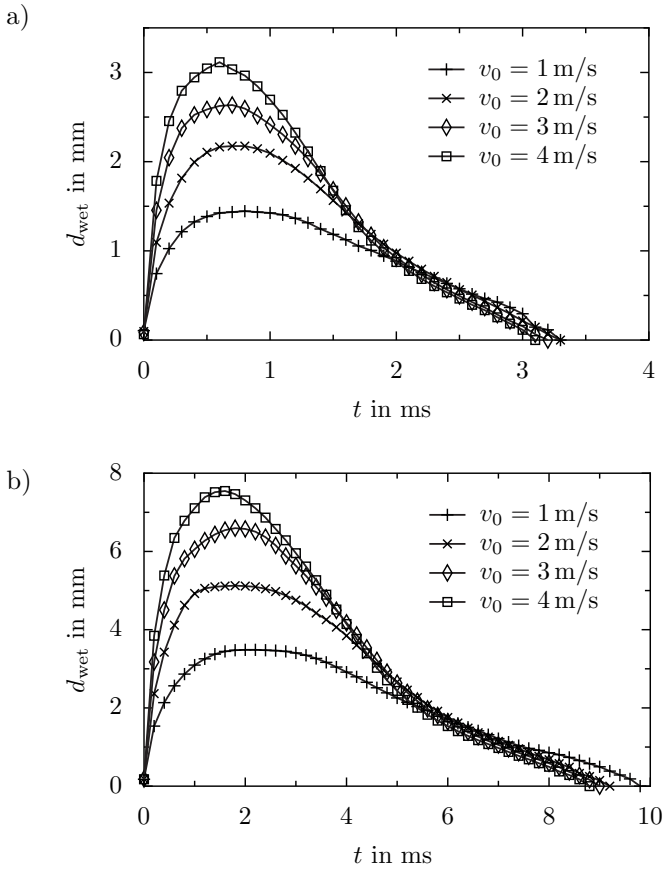

Figure 3.15: Influence of the impact velocity on the temporal evolution of the diameter of the wetted surface area, d_{wet}. The initial temperatures are $\vartheta_{\mathrm{sub},0} = -20.0\,^{\circ}\mathrm{C}$ and $\vartheta_{\mathrm{d},0} = 0\,^{\circ}\mathrm{C}$. The drop diameter is a) $d_{\mathrm{d}} = 1\,\mathrm{mm}$ and b) $d_{\mathrm{d}} = 2\,\mathrm{mm}$. (Reprinted with permission from [313]. Copyright 2017 Elsevier.)

to the hydrophobicity of the impact surface, the drop finally rebounds completely, resulting in $d_{\mathrm{wet}} = 0$. It is noteworthy that, similar to the receding velocity in the second phase, also the moment of detachment from the surface is almost unaffected by the impact velocity. Therefore, the contact time between the surface and the drop is mainly controlled by the

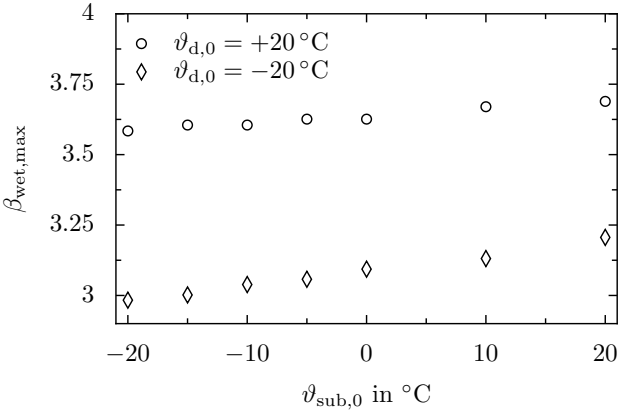

Figure 3.16: Influence of the initial surface temperature on the maximum spread factor $\beta_{\mathrm{wet,max}}$ during non-isothermal drop impact for a varying initial drop temperature. The impact velocity is $v_{\mathrm{d}} = 3\,\mathrm{m/s}$ and the drop diameter is $d_{\mathrm{d}} = 2\,\mathrm{mm}$.

drop diameter and the wettability of the surface, which confirms previous experimental results revealing the scaling between the total contact time t_{c}, and drop diameter as $t_{\mathrm{c}} \sim \sqrt{\rho d_{\mathrm{d}}^3/\sigma}$ [254, 291].

According to the descriptions in Sec. 2.2, the product of the contact time and area controls the rate of heterogeneous nucleus formation at the surface. This rate increases with increasing drop diameter, since both the contact time and the wetted surface area increase. The contact time is almost unaffected by the impact velocity. Nevertheless, a higher impact velocity is expected to causes a larger rate of nucleus formation, since it is associated with an increase of the wetted surface area.

The influence of the initial substrate temperature, $\vartheta_{\mathrm{sub,0}}$, on the maximum spread factor $\beta_{\mathrm{wet,max}}$ is shown in Fig. 3.16 for initial drop temperatures of $\vartheta_{\mathrm{d,0}} = +20.0\,^{\circ}\mathrm{C}$ and $\vartheta_{\mathrm{d,0}} = -20.0\,^{\circ}\mathrm{C}$. The substrate temperature is varied in the range $\vartheta_{\mathrm{sub,0}} = -20 \ldots +20\,^{\circ}\mathrm{C}$. The impact velocity and drop diameter are constant for all simulations, $v_{\mathrm{d}} = 3\,\mathrm{m/s}$ and $d_{\mathrm{d}} = 2\,\mathrm{mm}$, respectively. The maximum spread factor decreases by only approx. 3 % (corresponding to a decrease of the wetted surface area by 6 %) when the initial substrate temperature changes from $\vartheta_{\mathrm{sub,0}} = 20.0\,^{\circ}\mathrm{C}$ to $\vartheta_{\mathrm{sub,0}} = -20.0\,^{\circ}\mathrm{C}$ at an initial drop temperature of $\vartheta_{\mathrm{d,0}} = +20.0\,^{\circ}\mathrm{C}$. In

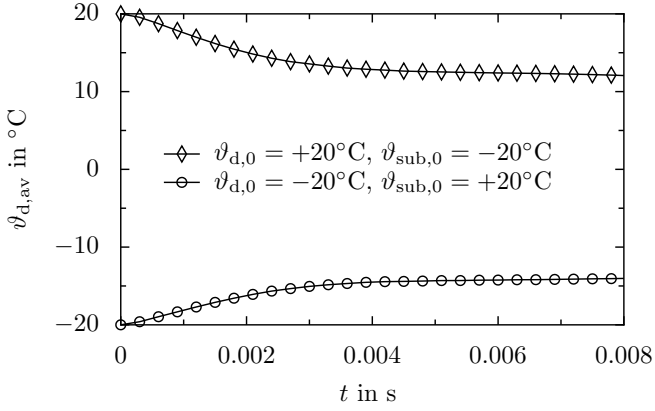

Figure 3.17: Temporal evolution of the mean drop temperature, $\vartheta_{\mathrm{d,av}}$, during non-isothermal drop impact with an initial temperature difference between the drop and the substrate of 40 K, corresponding to the results shown in Fig. 3.16. The impact velocity is $v_{\mathrm{d}} = 3\,\mathrm{m/s}$ and the drop diameter is $d_{\mathrm{d}} = 2\,\mathrm{mm}$.

the same temperature range of $\vartheta_{\mathrm{substrate},0}$, the spread factor decreases by approx. 7 % (about 13.5 % decrease of the wetted surface area) when the drop is initially at $\vartheta_{\mathrm{d},0} = -20.0\,°\mathrm{C}$. Therefore, the influence of a variation of the substrate temperature on the maximum spreading significantly depends on the initial drop temperature. It is larger for a lower initial drop temperature, which may be explained by the temperature dependence of the liquid viscosity as follows.

For a constant impact velocity and drop diameter, the temperature dependent drop viscosity has the greatest influence on the magnitude of $\beta_{\mathrm{wet,max}}$. As shown in Fig. 3.17 for an initial temperature difference of 40 K ($\vartheta_{\mathrm{sub},0} = +20.0\,°\mathrm{C}$ and $\vartheta_{\mathrm{d},0} = -20.0\,°\mathrm{C}$, or $\vartheta_{\mathrm{sub},0} = -20.0\,°\mathrm{C}$ and $\vartheta_{\mathrm{d},0} = +20.0\,°\mathrm{C}$), the absolute change of the mean drop temperature, $\vartheta_{\mathrm{d,av}}$, is only slightly affected by the initial temperatures. Due to a slightly larger wetted surface area causing an increased heat transfer, the change of the mean liquid temperature is increased for a warmer drop. It changes by approx. 7 K during the entire spreading and receding of an impinging drop; after the spreading phase of approx. 2 ms, the mean drop temperature has changed by approx. 5 K. The change of the liquid temperature is accompanied by a change of the liquid viscosity. The dependence of the

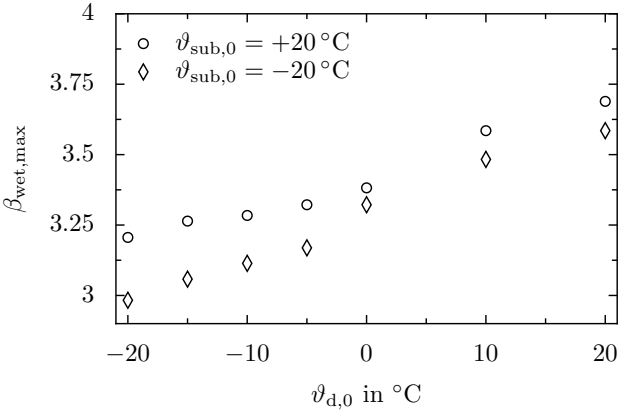

Figure 3.18: Influence of the initial drop temperature on the maximum spread factor $\beta_{\mathrm{wet,max}}$ during non-isothermal drop impact with $v_{\mathrm{d}} = 3\,\mathrm{m/s}$ and $d_{\mathrm{d}} = 2\,\mathrm{mm}$.

liquid viscosity on the liquid temperature depends on the liquid temperature itself; it increases for a decreasing liquid temperature, as shown in App. B. Therefore, for a change of the liquid temperature of 5 K as in the examples shown in Fig. 3.17, the viscosity decreases by 24 % for an initial drop temperature of $\vartheta_{\mathrm{d,0}} = -20.0\,^{\circ}\mathrm{C}$ and increases by only 13 % for an initial drop temperature of $\vartheta_{\mathrm{d,0}} = +20.0\,^{\circ}\mathrm{C}$. By this, the maximum spread factor is generally more sensitive to a varying substrate temperature in the case of lower liquid temperatures, as shown in Fig. 3.16.

As already experimentally shown in the previous section for inclined non-isothermal drop impact, also the numerical results shown in Fig. 3.16 suggest that the heat transfer between the drop and the substrate, and the accompanied change of the material properties are secondary for the maximum spread factor during non-isothermal impact of a warm drop. Figure 3.18 shows the influence of the initial drop temperature $\vartheta_{\mathrm{d,0}}$ on the maximum spread factor $\beta_{\mathrm{wet,max}}$ for initial substrate temperatures of $\vartheta_{\mathrm{sub,0}} = +20.0\,^{\circ}\mathrm{C}$ and $\vartheta_{\mathrm{sub,0}} = -20.0\,^{\circ}\mathrm{C}$. The impact velocity and drop diameter are again constant for all simulations, $v_{\mathrm{d}} = 3\,\mathrm{m/s}$ and $d_{\mathrm{d}} = 2\,\mathrm{mm}$, respectively. As shown in the figure, a variation of the drop temperature has a significantly larger influence on the maximum drop spreading than a variation of the initial substrate temperature. Further-

more, the fact that the influence of the initial substrate temperature on the maximum spreading depends on the initial drop temperature is also shown in Fig. 3.18. The influence of the substrate temperature on the maximum spreading ratio (represented by the vertical distance between the curves) decreases with increasing initial drop temperature. Accordingly, at a substrate temperature of $\vartheta_{s,0} = +20.0\,°C$, the maximum spread factor at an initial drop temperature of $\vartheta_{d,0} = -20.0\,°C$ is about 13 % smaller than at $\vartheta_{d,0} = +20.0\,°C$, and for a substrate at $\vartheta_{s,0} = -20.0\,°C$, the decrease is even about 17 %. These variations are accompanied by a reduction of the wetted surface area of 24 % and 30 %, respectively. The decrease of $\beta_{wet,max}$ for a decreasing drop temperature is clearly due to the more than fourfold increase of the viscosity of water accompanying the decrease of the drop temperature from $\vartheta_{d,0} = +20.0\,°C$ to $\vartheta_{d,0} = -20.0\,°C$. It causes a faster reduction of the drop's kinetic energy, due to a higher viscous dissipation, and finally results in a smaller maximum spreading.

3.1.2.4 Conclusion

The computational model used for the present simulations is based on the volume-of-fluid method for the calculation of the flow of two immiscible phases, namely liquid water and gaseous air, within the fluid region. The model considers temperature-dependent material properties of both fluids, as well as their mixture, and accounts for simultaneous conjugate heat transfer between the fluids and the underlying solid substrate. The functionality of the computational model has been confirmed using validation cases which include different dominating physical mechanisms. Numerical results have been compared to experimental data and analytical solutions, showing that the model is capable of reproducing the physics relevant for the simulation of heat transfer during non-isothermal drop impact.

The influence of varying impact conditions such as the drop diameter and impact velocity, and a varying initial drop and substrate temperature on the drop hydrodynamics during normal impact onto a superhydrophobic surface has been numerically investigated. In particular the influence of the impact parameters on the maximum drop spreading has been focused on. Together with the contact time between the drop and the surface, it is crucial for nucleation of the impinging liquid. Furthermore, the maximum spreading determines the amount of the surface which may be maximally iced after a single drop impact.

It has been shown that in the range of investigated parameters, the duration of drop spreading is almost unaffected by the impact velocity; although the maximum spreading diameter increases with increasing impact velocity. After maximum spreading, the contact angle decreases from θ_{adv} to θ_{rec} without a significant change of the spreading diameter, as already described in Sec. 2.1. The decrease of the contact angle is solely driven by surface tension. Therefore, the duration of the period of constant spreading diameter depends on the maximum deformation of the spread drop which is controlled by the impact velocity, and the typical length scale of the problem, i.e. the drop diameter. It is the shortest for small drop diameters and high impact velocities.

Drop receding on the considered superhydrophobic surface can be subdivided into two phases. The receding velocity during the first phase depends on the impact velocity and increases with increasing impact velocity. The second phase starts at an instant which is almost independent from the impact velocity, and the receding velocity during this phase smaller than in the first receding phase. Moreover, it is almost constant for a varying impact velocity. The receding velocity in the second phase is mainly determined by the wettability of the surface and only slightly affected by the drop diameter. As shown in Sec. 2.2, the wetted surface area and the contact time between the surface and the liquid are crucial parameters in the scope of nucleation. Similar to the receding velocity in the second phase of receding, also the complete contact time between the drop and the surface is almost unaffected by the impact velocity. Nevertheless, an increasing impact velocity increases the probability of drop nucleation, since it causes a larger surface area wetted by the drop.

As already shown experimentally in Sec. 3.1.1, it has been shown numerically that the substrate temperature has only a small influence on drop spreading and the resulting maximum wetted surface area, since the drop temperature only slightly changes during the short phase of drop spreading. Due to the strong dependence of the liquid viscosity on temperature, the initial drop temperature has a much larger influence on the maximum spreading after normal drop impact. However, the dependence of the viscosity on the liquid temperature depends on temperature itself: it increases with decreasing liquid temperature. By this, also the influence of a variation of the initial drop or substrate temperature on the maximum spreading depends on temperature. The influence of a variation of the substrate or drop temperature on the maximum spreading diameter generally decreases with increasing temperature.

Similar to the experimental study of inclined drop impact, the present results indicate a dominating influence of the initial drop temperature and the accompanied material properties on the maximum drop spreading. Therefore, the effect of heat transfer during non-isothermal drop impact on the material properties, and by this also on the maximum spreading, may be neglected. Therefore, using the initial liquid properties is sufficient for estimating the outcome of a drop impact using empirical equations such as Eqs. 2.4 - 2.9. Similarly, it is reasonable to assume the typical contact time between the drop and the surface to be also mainly influenced by the liquid properties which are controlled by the initial drop temperature.

3.2 Thermodynamics

The hydrodynamics during drop impact determine the maximum wetted surface area, and by this they control the surface area which is potentially iced after drop impact. Besides the hydrodynamics, also the thermodynamics during non-isothermal drop impact are influential for ice accretion. They involve the heat transfer between the impinging drop and the substrate, which influences the temperature of the impinging liquid. As shown in Secs. 2.2 and 2.3, the liquid temperature is the dominant influence for both nucleation and subsequent freezing of the impinging liquid. Therefore, also heat transfer is essential in the scope of icing of surfaces, since nucleation and freezing fix the momentary shape of the impinging liquid, which may drastically vary, as shown in Sec. 3.1.1. Heat transfer during drop impact is mainly determined by the initial temperatures and material properties of the impinging liquid and the substrate, but may also be affected by the fluid flow during impact.

The heat transfer between the impinging liquid and the substrate, and the evolution of the minimum liquid temperature are investigated for non-isothermal normal drop impact onto a superhydrophobic surface. The influence of varying impact conditions and initial temperatures on both the evolution of the minimum drop temperature, and on the heat transfer during drop impact are numerically examined. Moreover, based on the numerical results, a semi-empirical model for the heat transferred during the spreading phase of an impinging drop is derived.

3.2.1 Numerical investigation of normal drop impact

Using the computational model thoroughly described in Sec. 3.1.2.1, normal impact of water drops is numerically studied for varying impact conditions, and varying initial drop and substrate temperatures. The influence of the impact parameters on the transient heat transfer and the resulting minimum liquid temperature during non-isothermal drop impact is studied.

3.2.1.1 Results and discussion

Similar to the numerical study concerning the hydrodynamics during non-isothermal drop impact, a silicon substrate of 0.5 mm thickness is considered for the examination of the thermodynamics during non-isothermal drop impact. In the previous sections, it has been shown that the substrate temperature has only a negligible influence on the hydrodynamics during drop spreading which is mainly determined by the impact parameters such as the impact velocity and drop diameter, and the initial drop temperature. Therefore, implicit influences of a varying substrate temperature on the thermodynamics during drop impact by an alteration of the impact hydrodynamics are negligible. Accordingly, in the present study concerning the thermodynamics during non-isothermal drop impact, the drop temperature is kept constant at $\vartheta_{\mathrm{d},0} = 0\,^{\circ}\mathrm{C}$ and a temperature difference between the drop and the substrate is realized by a variation of

Table 3.4: Ranges of impact conditions and dimensionless quantities used for the parametric study of the thermodynamics during non-isothermal normal drop impact.

Parameter	Range	Unit
$\vartheta_{\mathrm{d},0}$	0	°C
$\vartheta_{\mathrm{sub},0}$	$-20 \ldots -5$	°C
v_{d}	$1 \ldots 4$	m/s
d_{d}	$1 \ldots 3$	mm
Re	$560 \ldots 8370$	-
We	$13 \ldots 992$	-
Pr	14	-

the initial substrate temperature. By this, influences of a temperature dependent variation of the material properties on the thermodynamics during impact are negligible. The ranges of the impact parameters used for the present numerical study, and the resulting dimensionless numbers are summarized in Tab. 3.4; the dimensionless numbers are calculated using the material properties corresponding to the initial drop temperature, $\vartheta_{\mathrm{d},0} = 0\,^{\circ}\mathrm{C}$.

Minimum temperature of the drop

Figures 3.19 - 3.21 show the minimum liquid temperature, $\vartheta_{\mathrm{l,min}}$, during the first 5 ms of drop impact for a varying impact velocity, drop diameter and initial substrate temperature, respectively. Since the drop is initially warmer than the surface, the position of the minimum liquid temperature is always located directly at the substrate surface where the liquid starts to cool down during impact. Therefore, the numerically obtained minimum liquid temperature is representative for the contact temperature at the substrate surface. For comparison purposes, the respective theoretical contact temperatures, calculated using Eq. 2.11, are also plotted in Figs. 3.19 - 3.21 as dashed lines.

As shown in Fig. 3.19, the evolution of $\vartheta_{\mathrm{l,min}}$ is only weakly influenced by the impact velocity, which has already been reported in [233]. However, for increasing impact velocities, $\vartheta_{\mathrm{l,min}}$ slightly decreases due to a larger convective heat transfer during spreading. The minimum liquid temperature rapidly decreases after impact until $t \approx 0.4\,\mathrm{ms}$. For $t > 0.4\,\mathrm{ms}$, it further decreases with a much lower cooling rate, and seems to converge to the theoretical contact time. However, depending on the impact velocity, $\vartheta_{\mathrm{l,min}}$ abruptly decreases at varying times between $t \approx 2\,\mathrm{ms}$ and $t \approx 3\,\mathrm{ms}$ to a value smaller than the theoretical contact temperature, and remains constant for later times. The abrupt decrease of $\vartheta_{\mathrm{l,min}}$ may be explained with the thermal boundary layer developing in the spreading drop. As long as the boundary layer thickness is smaller than the liquid film, the heat transfer at the liquid-substrate interface is undisturbed and only affected by the initial temperatures of the drop and the substrate, and eventually by the flow in the spreading drop. When the boundary layer reaches the upper surface of the liquid film, the boundary conditions for the heat transfer at the liquid-substrate interface change, causing a change of the smooth temporal evolution of $\vartheta_{\mathrm{l,min}}$. The residual lamella thickness after drop impact according to Eq. 2.8 can be used as a measure for the lamella thickness depending on the impact conditions. For the conditions

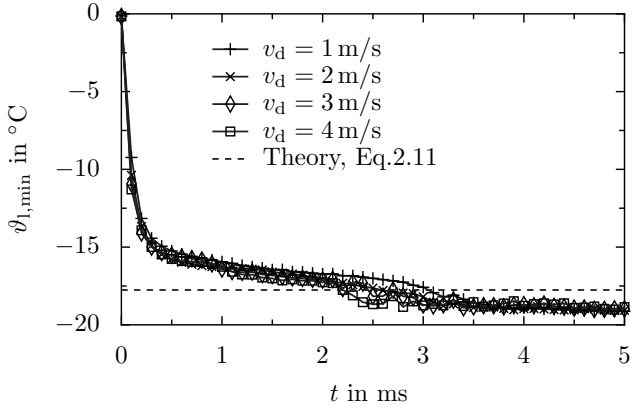

Figure 3.19: Temporal evolution of the minimum liquid temperature in an impinging drop for different impact velocities. The drop diameter is $d_\mathrm{d} = 2\,\mathrm{mm}$ and the initial substrate temperature is $\vartheta_{\mathrm{sub},0} = -20.0\,^\circ\mathrm{C}$. The dashed line represents the theoretical solution according to Eq. 2.11. (Reprinted with permission from [313]. Copyright 2017 Elsevier.)

corresponding to Fig. 3.19, i.e. $d_\mathrm{d} = 2\,\mathrm{mm}$ and $v_\mathrm{d} = 1 \ldots 4\,\mathrm{m/s}$, the residual lamella thickness is in the range of $h_{\mathrm{la,res}} \approx 5.5 \times 10^{-5} \ldots 1 \times 10^{-4}\,\mathrm{m}$. Assuming diffusion normal to the substrate surface as the dominant heat transfer mechanism in the spreading liquid, the thickness of the thermal boundary layer grows as $h_\mathrm{tbl} \approx 2.8\sqrt{a_\mathrm{l} t}$ [20]. For the mentioned impact conditions, the thickness of the thermal boundary layer in the lamella equals the residual lamella thickness at $t \approx 2.9 \ldots 8.7\,\mathrm{ms}$ after impact. The upper bound of this range, corresponding to the smallest impact velocity, is much larger than the experimentally observed time until the abrupt decrease of $\vartheta_{\mathrm{l,min}}$. However, the estimation predicts the correct order of magnitude for this time indicating that the reason for the sudden decrease of $\vartheta_{\mathrm{l,min}}$ is indeed the expansion of the thermal boundary layer up to the free surface of the spread liquid. In accordance with this description, the decrease of the liquid temperature occurs at an earlier instant for an increasing impact velocity which is associated with a thinner lamella thickness.

Also a varying drop diameter only slightly affects the evolution of $\vartheta_{\mathrm{l,min}}$, as shown in Fig. 3.20. Again the minimum liquid temperature seems to

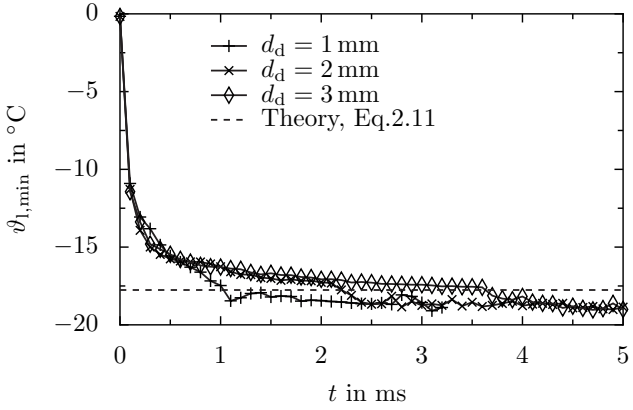

Figure 3.20: Temporal evolution of the minimum liquid temperature in an impinging drop for different drop diameters. The drop impact velocity is $v_\mathrm{d} = 4\,\mathrm{m/s}$ and the initial substrate temperature is $\vartheta_{\mathrm{s},0} = -20.0\,^\circ\mathrm{C}$. The dashed line represents the theoretical solution according to Eq. 2.11. (Reprinted with permission from [313]. Copyright 2017 Elsevier.)

converge to the theoretical contact temperature, until the abrupt decrease of $\vartheta_{\mathrm{l,min}}$ leads to a constant value below the theoretical contact temperature, corresponding to the instant when the thermal boundary layer reaches the upper free liquid surface. In comparison to the previous case of a varying impact velocity, a varying drop diameter has two different effects on the moment of the sudden decrease of the liquid temperature. At first, according to Eq. 2.8 the thickness of the liquid lamella after drop spreading decreases with decreasing drop diameter, resulting in an earlier decrease of the temperature for smaller drops. Moreover, the time until maximum spreading decreases with decreasing drop diameter, as shown in Fig. 3.15. Therefore, also the moment of minimum lamella thickness is reached earlier, finally resulting in a variation of the time of the sudden temperature decrease over a wider range than in the case of a varying impact velocity, for which the moment of maximum spreading and minimum lamella thickness is almost constant. A drop with $d_\mathrm{d} = 1\,\mathrm{mm}$ rebounds from the impact surface at $t \approx 3\,\mathrm{ms}$ (see Fig. 3.15 a)). However, the minimum liquid temperature is rather unaffected by the drop detachment, as indicated in Fig. 3.20.

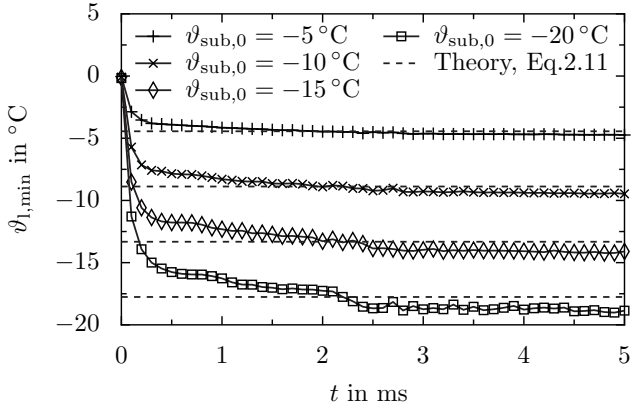

Figure 3.21: Temporal evolution of the minimum liquid temperature in an impinging drop for different initial substrate temperatures. The drop diameter is $d_{\mathrm{d}} = 2\,\mathrm{mm}$ and the impact velocity is $v_{\mathrm{d}} = 4\,\mathrm{m/s}$. The dashed lines represent the theoretical solution according to Eq. 2.11. (Reprinted with permission from [313]. Copyright 2017 Elsevier.)

As shown in Fig. 3.21, the initial surface temperature drastically influences the minimum liquid temperature, since it directly determines the contact temperature (compare Eq. 2.11). Similar to the previous cases, an abrupt decrease of the temperature below the theoretical contact temperature at $t \approx 2.3\,\mathrm{ms}$ is observed for all temperatures. Since the moment of the sudden decrease of the temperature is dominated by the drop hydrodynamics as explained before, it is only slightly affected by the initial substrate temperature. However, the magnitude of the temperature decrease depends on the initial substrate temperature and increases with an increasing initial temperature difference between the drop and the substrate. At an initial substrate temperature of $\vartheta_{\mathrm{sub},0} = -5.0\,^{\circ}\mathrm{C}$, the final minimum liquid temperature is in very good agreement with the theoretically obtained contact temperature. For a decreasing substrate temperature, an increasing deviation between the final minimum liquid temperature and the theoretical contact temperature can be observed.

In analogy to the processes explained before for the thermal boundary layer in the liquid, the boundary conditions for the heat transfer at the

liquid-substrate interface also change when the thermal boundary layer in the substrate is as thick as the substrate itself. The instant when the thermal boundary layer in the substrate reaches the substrate bottom by thermal diffusion can be estimated as $t \approx 0.36\,\mathrm{ms}$. In the case of the present simulations, a constant temperature boundary condition is applied at the bottom of the substrate region. This boundary condition results in a heat flux out of the computational domain, when the thermal boundary layer thickness equals the substrate thickness, which theoretically results in a faster decrease of the minimum liquid temperature for $t > 0.36\,\mathrm{ms}$. However, a faster decrease is not observable in the numerically obtained temperature data shown in Figs. 3.19 - 3.21. In fact, the time of equality between the thermal boundary layer thickness and the substrate thickness even coincides with the moment of a rapid decrease of the rate of change of the minimum liquid temperature, associated with a slower cool down of the liquid. By this, the effect of the finiteness of the substrate on the minimum liquid temperature cannot be clearly identified from the present results.

Heat transfer coefficient during drop impact

Figures 3.22 - 3.23 show the temporal evolution of the surface averaged heat transfer coefficient (HTC) α, for a varying impact velocity, drop diameter and surface temperature, corresponding to the impact conditions shown in Figs. 3.19 - 3.21, respectively. The mean HTC is defined as

$$\alpha = \frac{\dot{Q}_{\mathrm{wet}}}{A_{\mathrm{wet}} \Delta T}, \tag{3.21}$$

where $\dot{Q}_{\mathrm{wet}}$ is the numerically obtained total heat flow across the wetted surface area, A_{wet}, and ΔT is the difference between the initial drop temperature and the theoretical contact temperature, $\vartheta_{\mathrm{c,th}}$, calculated using Eq. 2.11; thus $\Delta T = \vartheta_{\mathrm{d},0} - \vartheta_{\mathrm{c,th}}$.

As shown in Figs. 3.19 and 3.20, the evolution of the contact temperature is almost unaffected by the impact velocity and drop diameter, indicating that the heat transfer at the liquid-substrate interface is not influenced by these quantities. Therefore, also the evolution of α during drop impact is only weakly influenced by a variation of the impact velocity and drop diameter, as shown in Figs. 3.22 a) and b), respectively. The HTC is the highest at the beginning of drop impact, when the thermal boundary layers in the substrate and the liquid start to develop. Corresponding to the decreasing rate of change of the minimum

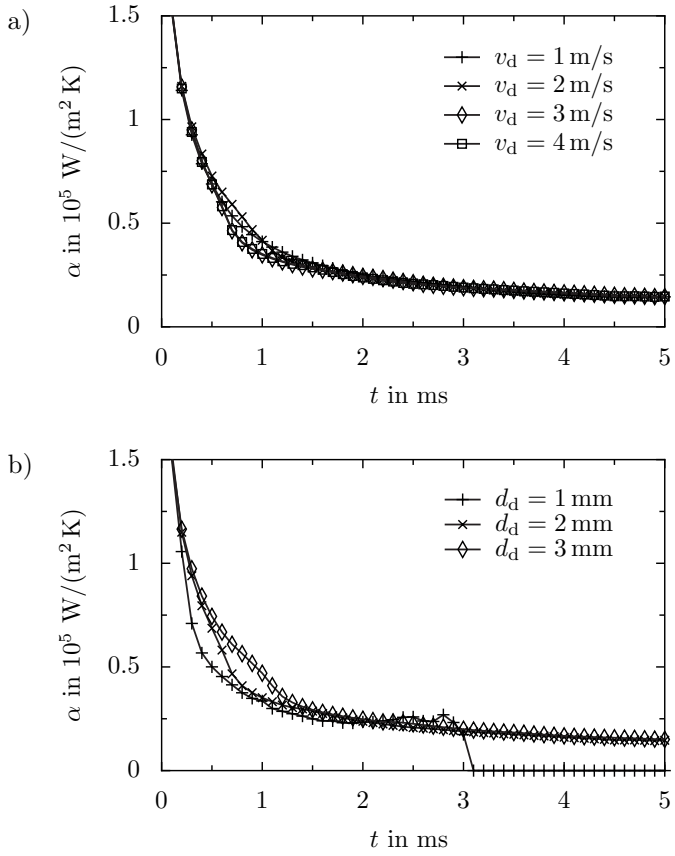

Figure 3.22: Temporal evolution of the heat transfer coefficient α averaged over the surface area wetted during non-isothermal drop impact with $\vartheta_{\mathrm{sub},0} = -20.0\,^{\circ}\mathrm{C}$. a) Varying drop impact velocity and $d_\mathrm{d} = 2\,\mathrm{mm}$. b) Varying drop diameter and $v_\mathrm{d} = 4\,\mathrm{m/s}$. (Reprinted with permission from [313]. Copyright 2017 Elsevier.)

liquid temperature until $t \approx 0.4\,\mathrm{ms}$, also α rapidly decreases during this time. For $t > 0.4\,\mathrm{ms}$, both the minimum liquid temperature and the mean heat transfer coefficient α further decrease with a decreasing rate. While the minimum liquid temperature reaches an almost constant value for all

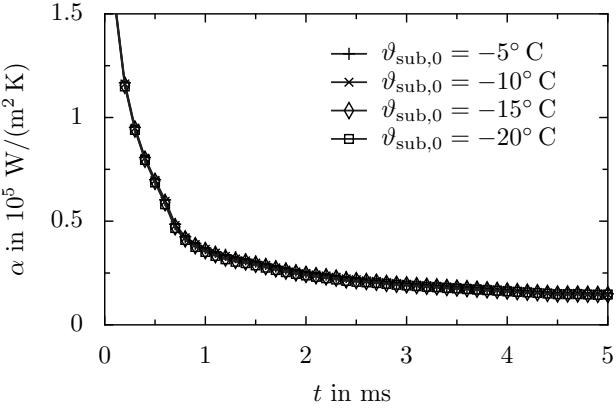

Figure 3.23: Temporal evolution of the mean heat transfer coefficient α at the wetted surface for a varying initial substrate temperature. The drop diameter is $d_\mathrm{d} = 2\,\mathrm{mm}$ and the impact velocity is $v_\mathrm{d} = 4\,\mathrm{m/s}$. (Reprinted with permission from [313]. Copyright 2017 Elsevier.)

impact conditions for $t < 5\,\mathrm{ms}$, the HTC does not converge to a constant value during this time. As shown in Fig. 3.22 b) for a drop diameter $d_\mathrm{d} = 1\,\mathrm{mm}$, the mean HTC abruptly decreases, $\alpha = 0$ at $t \approx 3\,\mathrm{ms}$, corresponding to the moment of drop rebound from the impact surface (see Fig. 3.15 a)). While the drop detachment does not affect the minimum liquid temperature, as shown in Fig. 3.20, the definition of α according to Eq. 3.21 causes $\alpha = 0$ due to $\dot{Q}_\mathrm{wet} = 0$ after dewetting.

The initial surface temperature has no effect on the evolution of α during drop impact, as shown in Fig. 3.23. It is an important parameter for heat transfer between the drop and the substrate, and as seen in Fig. 3.21, the initial substrate temperature significantly affects the minimum liquid temperature during impact, which equals the contact temperature in the present cases. However, according to Eq. 3.21, α is defined as the proportionality factor between the heat flux, and the difference between the theoretical contact temperature ϑ_c and the initial drop temperature. Since the equation for ϑ_c already includes the influence of the substrate temperature, the heat transfer coefficient itself does not further depend on the initial substrate temperature. The indifference of α against the substrate temperature therefore implies a correct estimation of ϑ_c using Eq. 2.11.

3.2.1.2 Conclusion

The thermodynamics during non-isothermal normal drop impact have been numerically examined for a varying drop diameter, impact velocity and initial substrate temperature. The computations have been performed with the solver already used and described in Sec. 3.1.2. In particular the influence of the impact parameters on the evolution of the minimum liquid temperature, $\vartheta_{\mathrm{l,min}}$, and on the evolution of the averaged heat transfer coefficient, α, has been investigated for the varying impact conditions. While the minimum liquid temperature is the most important influential parameter for nucleation and freezing of the impinging drop, the heat transfer coefficient characterizes the heat transfer between the impinging drop and the surface, which in turn determines the evolution of the liquid temperature.

The initial drop temperature has been kept constant at $\vartheta_{\mathrm{d,0}} = 0\,^{\circ}\mathrm{C}$ in all simulations, while the initial substrate temperature has been varied in the range $\vartheta_{\mathrm{sub,0}} = -20 \ldots -5\,^{\circ}\mathrm{C}$. Therefore, the position of $\vartheta_{\mathrm{l,min}}$ is in all cases located at the liquid-substrate interface, where it is representative for the contact temperature during drop impact. The computational results for $\vartheta_{\mathrm{l,min}}$ have been compared to the theoretical contact temperature calculated using Eq. 2.11. It has been shown that the evolution of $\vartheta_{\mathrm{l,min}}$ is only weakly influenced by the drop diameter and impact velocity. Since the initial substrate temperature has a direct influence on the contact temperature, also the minimum liquid temperature is directly affected by this temperature. A thermal boundary layer expands in the spreading liquid. When the boundary layer thickness equals the thickness of the spread liquid itself, the boundary conditions for the heat transfer at the liquid-substrate interface change and cause an abrupt decrease of $\vartheta_{\mathrm{l,min}}$ to a constant value below the theoretical contact temperature. The computationally obtained minimum liquid temperature is only slightly below the theoretical contact temperature for an initial temperature difference between the substrate and the drop of 5 K. However, the magnitude of the abrupt decrease of $\vartheta_{\mathrm{l,min}}$ increases with increasing initial temperature difference between the drop and the substrate, resulting in an increasing deviation between the theoretical contact temperature and $\vartheta_{\mathrm{l,min}}$ after the prompt decrease of the temperature. The drop diameter and impact velocity do not significantly influence the minimum liquid temperature, but they determine the moment of the abrupt decrease of the temperature, since the impact parameters determine the thickness of the spread liquid. A similar effect is expected for the instant when the thickness of the

thermal boundary layer in the substrate equals the substrate thickness. However, this effect cannot be identified from the present results.

In analogy to the independence of the minimum liquid temperature, also the evolution of the heat transfer coefficient averaged over the wetted surface area during drop impact is almost unaffected by any parameter in the investigated range of impact conditions. Due to its definition, the mean heat transfer coefficient is also independent of the initial temperature difference between the drop and the substrate. Therefore, the material properties of both the substrate and the impinging liquid are the only influential parameters for the heat transfer coefficient during drop impact. The HTC characterizes the heat flow per unit area of the wetted surface. Since the evolution of the wetted surface area varies depending on the impact conditions, also the total heat flow during drop impact varies and implicitly depends on the impact conditions. The total heat transferred during drop impact furthermore depends on the time available for heat transfer. Therefore, the heat effectively transferred during drop impact mainly depends on the impact conditions which determine the wetted surface area and the time available for heat transfer.

The present computational results indicate that the minimum liquid temperature is mainly influenced by the initial temperature of the impinging drop and the substrate; it is almost unaffected by the impact conditions. The theoretical contact temperature according to Eq. 2.11 gives a good estimate for the minimum liquid temperature in the case of small initial temperature differences between the drop and the substrate. An increasing deviation between the theory and the computational results can be observed for an increasing initial temperature difference, which is due to the finiteness of the spreading liquid. Until the abrupt decrease of the temperature, the minimum liquid temperature seems to converge to the theoretical contact temperature. Therefore, the theoretical relation for the contact temperature during drop impact is well applicable for the first period of drop impact, i.e. until the thermal boundary layer in the spreading liquid is as thick as the liquid itself.

3.2.2 Mathematical modeling of heat transfer during normal drop impact

Using the previous computational results, a semi-empirical model for the heat transferred during a single non-isothermal drop impact onto a superhydrophobic surface is developed. The model is based on an expression for the heat flux at the surface wetted during drop impact, and semi-empirical expressions for the maximum wetted surface area and the time for wetting during drop impact.

3.2.2.1 Results and discussion

As shown in the previous section, the heat transfer coefficient is almost unaffected by the impact parameters. However, the amount of heat transferred during a single drop impact still depends on these parameters, since the impact parameters determine the contact time and the wetted surface area across which heat is transferred. Due to the fast spreading during drop impact, the thermal boundary layer expansion in the substrate in the direction of drop spreading is much slower than in the direction normal to the liquid-substrate interface. Therefore, the radial component of the heat flux in the substrate is negligibly small in comparison to the component normal to the impact surface. Thus, the heat transferred during drop impact can be described by only considering heat transfer in the z-direction normal to the substrate surface. The heat flux in the z-direction at the substrate surface during drop impact has been obtained in [295] as

$$\dot{q}(t) = \frac{e_\mathrm{d} e_\mathrm{sub} (\vartheta_\mathrm{sub,0} - \vartheta_\mathrm{d,0})}{[e_\mathrm{d} + e_\mathrm{sub} \varphi(\mathrm{Pr})] \sqrt{\pi} \sqrt{t}}, \tag{3.22}$$

where $t = 0$ corresponds to the moment when the liquid makes contact with the substrate. Denote $t_\mathrm{wet}(r)$ as the moment when the surface element $\mathrm{d}A = 2\pi r \mathrm{d}r$ at the radial position r becomes wetted. Then, the heat transferred across the wetted surface area $A_\mathrm{wet}(t)$ until time t is obtained from spatial and temporal integration of Eq. 3.22 as

$$Q_\mathrm{wet}(t) \;=\; \int_0^t \int_{A_\mathrm{wet}(t)} \frac{e_\mathrm{d} e_\mathrm{sub} (\vartheta_\mathrm{sub,0} - \vartheta_\mathrm{d,0})}{[e_\mathrm{d} + e_\mathrm{sub} \varphi(\mathrm{Pr})] \sqrt{\pi} \sqrt{t - t_\mathrm{wet}(r)}} \,\mathrm{d}A \,\mathrm{d}t. \tag{3.23}$$

Exact integration in Eq. 3.23 is impossible, since the expression is singular for $t = t_\mathrm{wet}(r)$ and furthermore, $t_\mathrm{wet}(r)$ and $A_\mathrm{wet}(t)$ depend on the

impact conditions of a specific drop impact. However, to find an engineering solution which allows the estimation of the typical amount of heat transferred during drop spreading, $Q_{\mathrm{spr,th}}$, the time dependence of the wetted surface area, $A_{\mathrm{wet}}(t)$, and the exact instants of wetting, $t_{\mathrm{wet}}(r)$, are neglected for the evaluation of the corresponding integrals in Eq. 3.23. Instead, Eq. 3.23 is approximated using time and area scales which are typical for a single drop impact. Using the squared diameter of the maximum wetted surface area, $d^2_{\mathrm{wet,max}}$, as the area scale and the spreading time until maximum wetting, $t_{\mathrm{wet,max}}$, as the time scale, Eq. 3.23 can be approximated as

$$Q_{\mathrm{spr,th}} \approx 2\,\varphi\,\frac{e_{\mathrm{d}} e_{\mathrm{sub}}(\vartheta_{\mathrm{sub},0} - \vartheta_{\mathrm{d},0})}{[e_{\mathrm{d}} + e_{\mathrm{sub}}\varphi(\mathrm{Pr})]\,\sqrt{\pi}}\,d^2_{\mathrm{wet,max}}\,\sqrt{t_{\mathrm{wet,max}}}, \tag{3.24}$$

where φ is a proportionality factor, which is found by fitting of the numerical results using the model equation.

To obtain a predictive relation for the heat amount transferred during drop impact, which just depends on the initial impact conditions, $d_{\mathrm{wet,max}}$ and $t_{\mathrm{wet,max}}$ are expressed as functions of the impact conditions. According to Eq. 2.9, the maximum spreading diameter can be estimated as

$$d_{\mathrm{wet,max}} = d_{\mathrm{d}}\left(0.87\,\mathrm{Re}^{1/5} - 0.4\,\mathrm{Re}^{2/5}\,\mathrm{We}^{-1/2}\right). \tag{3.25}$$

The relation for the time until maximum spreading, $t_{\mathrm{wet,max}}$, is assumed in a form similar to the relation for $d_{\mathrm{wet,max}}$. The coefficients in the relation for $t_{\mathrm{wet,max}}$ are found by fitting the numerically obtained results, partially presented in Sec. 3.1.2.3, resulting in

$$t_{\mathrm{wet,max}} = \frac{d_{\mathrm{d}}}{v_{\mathrm{d}}}\left(0.746\,\mathrm{Re}^{1/5} - 0.642\,\mathrm{Re}^{2/5}\,\mathrm{We}^{-1/2}\right). \tag{3.26}$$

The Reynolds and Weber number in Eqs. 3.25 and 3.26 are calculated using the liquid properties at the mean temperature $\vartheta_{\mathrm{av}} = (\vartheta_{\mathrm{c,th}} + \vartheta_{\mathrm{d},0})/2$. The prefactor φ in Eq. 3.24 is obtained by a least squares fit of the equation to the numerical results, yielding $\varphi = 0.784$. For fitting, the numerically calculated heat amount $Q_{\mathrm{spr,num}}$ is evaluated at the instant of numerically obtained maximum wetting, while Eqs. 3.25 and 3.26 are used in Eq. 3.24.

Figure 3.24 shows a comparison of the calculated heat, $Q_{\mathrm{spr,th}}$, with the computational results for $Q_{\mathrm{spr,num}}$. As shown in the figure, the theoretical results are in very good agreement with the numerical data over a wide

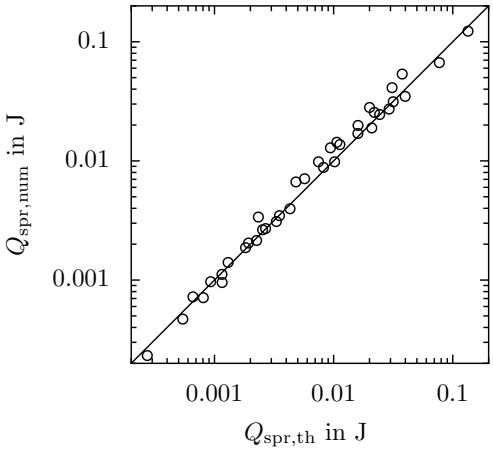

Figure 3.24: Comparison of the heat transferred during drop impact obtained computationally and theoretically utilizing Eq. 3.24. (Reprinted with permission from [313]. Copyright 2017 Elsevier.)

range of parameters corresponding to a variation of the transferred heat over three orders of magnitude. The parameter φ serving as a scaling factor in the theoretical relation, Eq. 3.24 has been obtained by fitting of the found relation to the experimental results. Nevertheless, the good agreement between the theoretical predictions of the model and the numerical results indicates that the model correctly accounts for all influences dominating heat transfer during drop impact, comprising the heat flux at the substrate surface (Eq. 3.22), the wetted surface area (Eq. 3.25), and the contact time between the liquid and the surface (Eq. 3.26).

Note that the theoretical model is based on the numerical results for drop impact onto a superhydrophobic surface. Depending on the impact conditions, a varying surface wettability could in particular influence the maximum wetted surface area and time of wetting during drop impact, which are crucial parameters in the theoretical model. However, it has been shown that the surface wettability has only a minor influence on the maximum wetted surface area in the case of inertia dominated drop impact associated with large Reynolds and Weber numbers [292, 294, 308]. Therefore, it is reasonable to assume also the time for wetting to

be only insignificantly affected by the surface wettability in the case of large Reynolds and Weber numbers. Accordingly, the theoretical model is presumably also applicable for heat transfer during inertia dominated drop impact onto surfaces of varying wettability.

Another aspect related to the surface properties which can significantly affect heat transfer during drop impact, is the morphology of the impact surface. An often used means to control the wettability of a surface is surface texturing. Depending on the impact conditions, a drop may only partially wet such a structured surface, which may significantly reduce the wetted surface area effectively available for heat transfer. Accordingly, the present theoretical model, which assumes a complete wetting of the surface below the liquid, would overpredict the heat transfer during a drop impact involving partial wetting. However, it is very likely that the reduced wetted surface area during partial wetting may be accounted for by means of a scaling factor, depending on the exact surface morphology and impact conditions which determine the resulting effectively wetted surface area.

3.2.2.2 Conclusion

Based on an expression for the substrate heat flux during drop impact, proposed in [295], a theoretical model for the heat amount transferred during the spreading phase of an impacting drop has been derived. The maximum spreading diameter and the time until maximum spreading are used as typical scales for the heat transfer process. These quantities are expressed as functions of the impact conditions, resulting in a final relation for the heat transferred during spreading, which only involves the impact conditions, and the initial temperatures and material properties of the drop and the substrate. A scaling factor arising in the theoretical relation has been found by fitting of the relation to the numerical results of the present study.

A very good agreement of the model with the computational results over three orders of magnitude of the transferred heat attests the model's capability of predicting the heat transferred during the spreading phase of a single drop impact for a wide range of impact conditions. Due to its predictive nature, the model may not only be used for the improvement of ice accretion models but also for the design and optimization of other technical applications such as spray cooling systems.

Parts of the work presented in the following chapter are based on the Master-Thesis of Konstantin Kröll [186], and have already been published and presented in the following publications and conference contributions:

[315] M. Schremb, I. V. Roisman, S. Jakirlić and C. Tropea. Spreading and freezing of a droplet impacting onto an inclined colled surface: Different outcomes for same conditions. In *Book of Abstracts of the SAE 2015 International Conference on Icing of Aircraft, Engines, and Structures*, Prague, Czech Republic, 2015.

[316] M. Schremb, I. V. Roisman, S. Jakirlić and C. Tropea. Freezing behavior of supercooled water drops impacting onto a cold surface. In *Proceedings of the 27th Annual Conference on Liquid Atomization and Spray Systems*, Brighton, UK, 2016.

[317] M. Schremb, I. V. Roisman, S. Jakirlić and C. Tropea. Freezing delay and nucleation rates of supercooled water drops impacting onto a cold surface. In *Book of Abstracts of the 9th International Conference on Multiphase Flow*, Florence, Italy, 2016.

[318] M. Schremb, I. V. Roisman and C. Tropea. Different outcomes after inclined impacts of water drops on a cooled surface. In *Proceedings of the 13th Triennial International Conference on Liquid Atomization and Spray Systems*, Tainan, Taiwan, 2015.

[320] M. Schremb, I. V. Roisman and C. Tropea. Transient effects in ice nucleation of a water drop impacting onto a cold substrate. *Physical Review E*, 95:022805, 2017.

[358] C. Tropea, M. Schremb and I. Roisman. Physics of SLD impact and solidification. In *Proceedings of the 7th European Conference for Aeronautics and Aerospace Sciences*, Milan, Italy, 2017.

4 Nucleation during drop impact

The present chapter is devoted to the statistics of ice nucleation during drop impact of supercooled water, which is in the present work experimentally examined for the first time. As shown in the previous chapter, the wetted surface area significantly varies during the different phases of drop impact comprising spreading, receding and potential rebound from the surface. While the hydrodynamics of drop impact determines the

maximum surface area that may be iced after drop impact, nucleation and subsequent freezing fix the shape of the potentially deformed liquid. Since the wetted surface area may drastically vary over time, the statistics of nucleation is a crucial influence on the surface area ultimately iced after drop impact. Nucleation is a complex process, which still motivates extensive research; even for the case of nucleation in a liquid at rest. Drop impact is accompanied by several mechanisms possibly influential for nucleation, causing nucleation during drop impact to be even more complicated than nucleation in a still liquid. Since the present study is a first attempt to account for nucleation during drop impact, interpretations of the obtained results are first hypotheses rather than definite explanations, which can not be expected after entering a new area of research.

Similar to the case of nucleation in supercooled water at rest, the liquid temperature is expected to be crucial also in the case of nucleation during drop impact. However, several other mechanisms present during drop impact may affect nucleation, as described in Sec. 2.2. During impact, a pressure wave propagates through the impinging drop, eventually influencing nucleation similar to shear in the spreading liquid. Moreover, the impinging drop is in contact with the impact surface which triggers solidification by facilitating heterogeneous nucleation. Due to the dynamics of drop impact, the wetted surface area continuously varies, resulting in a varying surface area active for heterogeneous nucleation which generally has to be accounted for during examination of nucleation during impact.

According to the aforementioned potential influences, the experiments are performed for varying temperatures and impact conditions, comprising a variation of temperature during both isothermal and non-isothermal drop impact, and a variation of the impact velocity and gas content of the impinging liquid. The experiments are repeated multiple times for each set of impact conditions, to allow a statistical analysis of the data.

First the experimental procedure for the examination of nucleation during drop impact is described. Then, the results are qualitatively analyzed based on a comparison of the drop freezing rates observed for varying conditions. Finally, a statistical model accounting for both the variation of the wetted surface area and the nucleation rate during impact is derived. It provides the cumulative number of active nucleation sites per unit area of the wetted substrate surface from the experimentally observed decay of a drop ensemble. The model is employed for a generic analysis of the experimental results for nucleation during isothermal drop impact.

4.1 Experimental method

The experimental setup and high-speed video system used for the examination of nucleation during drop impact has already been described and used in Sec. 3.1.1. The drop hydrodynamics during impact has been investigated using a polished aluminum substrate, which is prone to the development of an oxide layer on the substrate surface. While the influence of this layer on the hydrodynamics during inertia dominated drop impact can be assumed as negligible, its influence on nucleation is not clear. However, due to the altered chemical properties of the surface the influence is assumed as significant. Therefore, nucleation during drop impact is investigated using a glass mirror of 2 mm thickness as the impact surface, whose chemical inertness guarantees constant surface properties for all experiments. The thermophysical properties of the glass impact surface are $\rho_{\mathrm{sub}} = 2500\,\mathrm{kg/m^3}$, $c_{\mathrm{p,sub}} = 750\,\mathrm{J/(kg\,K)}$, and $k_{\mathrm{sub}} = 1.4\,\mathrm{W/(m\,K)}$ [159].

To be able to examine influences on nucleation during drop impact, a sufficiently large nucleation rate for the range of investigated impact parameters is essential, to prevent the need for an excessively large number of repetitions of the experiment. Preliminary experiments using an untreated glass substrate revealed a vanishing nucleation rate for the range of impact conditions in the present study. Moreover, a reliable distinction between an impinging drop and the entirely transparent substrate in the captured high-speed videos is not possible. Therefore, the surface of the glass substrate has been sandblasted which, contrary to previous experimental findings [58], results in a sufficiently increased nucleation rate in the relevant range of impact conditions. Additionally, the surface treatment allows a clear distinction between dry and wetted parts of the surface; dry regions of the surface are matt, while wetted parts appear transparent and thus reflective in the captured high-speed videos.

Sandblasting of the surface is expected to result in a homogeneously rough surface morphology. To ensure the surface homogeneity with respect to the size of the roughness elements, which is assumed crucial for the enhancement of nucleation, the surface morphology has been characterized using a tactile roughness probe (*Mahr, Marsurf GD 25*) over a measurement length of 5.6 mm at three different probe locations on the impact surface. The arithmetic averages of the absolute roughness values for the probe locations is in the range $R_{\mathrm{a}} = 2.6 \ldots 3.0\,\mu\mathrm{m}$, thereby varying by only 14 % between the different probe locations. The size of a roughness element is considered as the crucial parameter characterizing its ability

to promote nucleation. The size of the individual roughness elements on the surface is not constant and follows a certain distribution[1]. Therefore, depending on the size of an impinging drop, and the typical size of the roughness elements, the ability of a surface element to promote nucleation may depend on the exact position on the surface, i.e. on the size of the roughness elements wetted during impact at this position. Assuming the width of the roughness elements to be of the same order of magnitude as the depth of the roughness elements, the measured roughness represents the typical length scale, l_{sur}, characterizing the surface morphology with respect to nucleation. The number of roughness elements wetted during drop impact can be estimated as $d_{\mathrm{d}}^2/l_{\mathrm{sur}}^2 \approx 10^6$, where $d_{\mathrm{d}}^2 \approx 9\,\mathrm{mm}^2$ is used as a scale for the wetted surface area. Due to the large number of roughness elements wetted during drop impact, the impact surface can be considered as homogeneously effective for nucleation, independent of the exact impact position on the surface. In addition to the tactile measurement, the surface morphology has also been optically measured using a 3D confocal white light surface microscope (*NanoFocus, µsurf*) at two different probe locations on a respective area of $0.8 \times 0.8\,\mathrm{mm}^2$, subdivided into 512×512 measurement points. Using this method, the arithmetic average of the absolute roughness values for the probe locations has been obtained without any further data processing as $R_{\mathrm{a},1} = 5.3\,\mu\mathrm{m}$ and $R_{\mathrm{a},2} = 7.2\,\mu\mathrm{m}$, which is comparable to the results of the tactile measurement. Compared to the tactile measurement, the results of the optical measurement are associated with an inaccuracy attributed to the partial transparency of the surface [134]. However, the obtained results may at least be used to qualitatively estimate the homogeneity of the surface morphology. As shown in Fig. 4.1, the surface morphology is very homogeneous with only a few larger deviations from the mean roughness. Therefore, in addition to the previous quantitative estimation, also the optical measurement demonstrates the homogeneity of the surface with respect to the size and distribution of the roughness elements.

Besides the measured roughness of a surface, also small-scale cracks and fractures in a surface may promote heterogeneous nucleation. Sandblasting of a brittle material such as glass possibly causes such surface features, which can additionally promote nucleation on the substrate. Therefore, the number of potential nucleation sites wetted during drop impact further increases, and it is reasonable to assume the substrate to be equally

[1] It is well described by a normal distribution, which has been found by the analysis of results obtained from confocal microscopy, shown in Fig. 4.1.

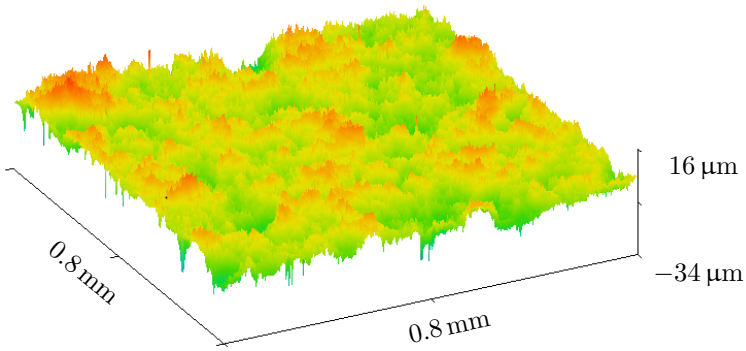

Figure 4.1: Surface morphology of the sandblasted surface, obtained from optical surface measurement using 3D confocal microscopy. Outliers which do not satisfy the 3σ criterion of the height distribution, and disconnected measurement points detected via a median filter with a radius of 2 pixels have been sorted out using a data visualization and analysis software (*Gwyddion, V 2.44*). Note that the image only gives a qualitative estimation of the surface morphology and homogeneity.

effective for nucleation at any part of the surface; at least for nucleation associated with microscopic and sub-microscopic surface features.

Similar to the experiments concerning the hydrodynamics during drop impact, purified de-ionized water (*Millipore, Milli-Q® Type 1*, electrical conductivity $\gamma_{\mathrm{el}} = 5.5 \times 10^{-6}\,\mathrm{S/m}$ at $25\,^{\circ}\mathrm{C}$) is used for the experiments in the present chapter, to minimize the effect of impurities on nucleation. The instant of nucleation is detected from the captured high-speed videos, where the nucleus can be observed as an initially small dark spot radially growing, as already shown in Fig. 2.1.

Nucleation during drop impact is examined for varying impact conditions. First the influence of temperature on nucleation during isothermal drop impact is investigated. Several other impact conditions are varied to examine their influence on nucleation, comprising the impact velocity and gas content of the impinging water drops. Moreover, experiments regarding non-isothermal drop impact are performed. For these experiments, the drop and/or substrate temperature are varied such that either the drop temperature, the substrate temperature, or the contact temperature between the drop and the substrate are constant, while the remaining

Table 4.1: Impact conditions and resulting dimensionless quantities for the parametric study of nucleation during non-isothermal normal drop impact.

Parameter	Value	Unit
$\vartheta_{\mathrm{d},0}$	$-15.8 \ldots -6.5$	°C
$\vartheta_{\mathrm{sub},0}$	$-16.0 \ldots -6.0$	°C
v_{d}	2.17 ± 0.05 & 3.19 ± 0.02	m/s
d_{d}	3.2	mm
Re	2000 ... 4570	-
We	198 ... 428	-
Pr	17 ... 29	-

temperatures vary. The ranges of the impact conditions for the experimental study, and the resulting dimensionless numbers are summarized in Tab. 4.1. For each set of impact conditions concerning isothermal drop impact, the experiments have been repeated at least 99 times, representing the basis for experimental results of a sufficient statistical significance. However, the experiment at $\vartheta_{\mathrm{sub},0} = \vartheta_{\mathrm{d},0} = -6.2\,°\mathrm{C}$ has only been repeated 20 times, since nucleation has not been observed at all for these conditions. The remaining experiments concerning non-isothermal drop impact and the influence of the liquid gas content have been repeated at least 51 times.

The applied settings of the high-speed camera allow capturing of the first 7 s after drop impact. Therefore, the analysis of the experimental data is generally restricted to this period.

4.2 Qualitative analysis

The representation of the experimental data in the form of survival curves over time is used for a first, qualitative analysis of the results concerning nucleation during the impact of supercooled water drops under varying conditions. In this analysis the slope of a survival curve, i.e. the drop freezing rate is assumed to be representative for the nucleation rate causing drop freezing. A survival curve for a set of experiments concerning nucleation during drop impact is obtained as follows.

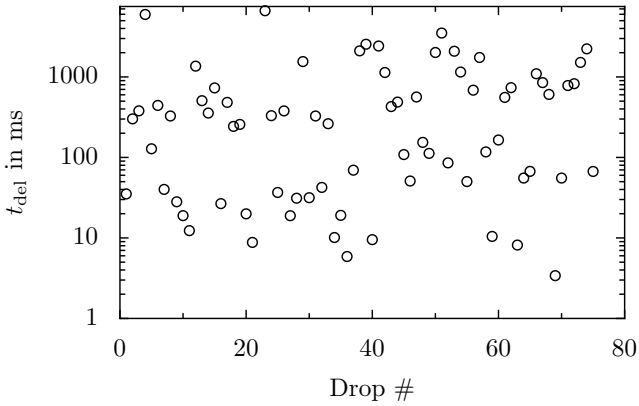

Figure 4.2: Variation of the freezing delay of impinging and nucleating drops, being the typical outcome of a study on nucleation during isothermal impact of supercooled water drops, performed with $\vartheta = -8.6\,^{\circ}\mathrm{C}$, $d_{\mathrm{d}} = 3.2\,\mathrm{mm}$ and $v_{\mathrm{d}} = 2.2\,\mathrm{m/s}$.

Figure 4.2 shows the typical outcome of a set of experiments at constant conditions ($\vartheta_{\mathrm{d},0} = \vartheta_{\mathrm{sub},0} = -8.6\,^{\circ}\mathrm{C}$, $d_{\mathrm{d}} = 3.2\,\mathrm{mm}$, $v_{\mathrm{d}} = 2.2\,\mathrm{m/s}$), being a collection of the freezing delay time observed for each drop of the ensemble. The specific experiment has been repeated 99 times resulting in 74 observed freezing events. As shown in the figure, the freezing delay of the drops varies stochastically over three orders of magnitude, ranging from several milliseconds to several seconds. Since all drops impact at equal conditions, each drop has the same probability of freezing at a certain time. Therefore, the drops can be assumed to be impacted simultaneously. This allows sorting of the freezing delays in an ascending order, and subsequent calculation of the relative number of liquid drops after each observed nucleation event. It results in the survival curve of the drop ensemble, i.e. the relative number of liquid drops as a function of time, $N_{\mathrm{l}}(t)/N_0$, as shown in Fig. 4.3. According to 2.41, this ratio represents the evolution of the average probability of a drop to be liquid until time t.

The experimental data is generally associated with a certain error, which is attributed to the fact that the data is based on a discrete number of experiments. As shown in Sec. 2.2, nucleation is well described as a Poisson process in time. Nevertheless, the probability for nucleation until

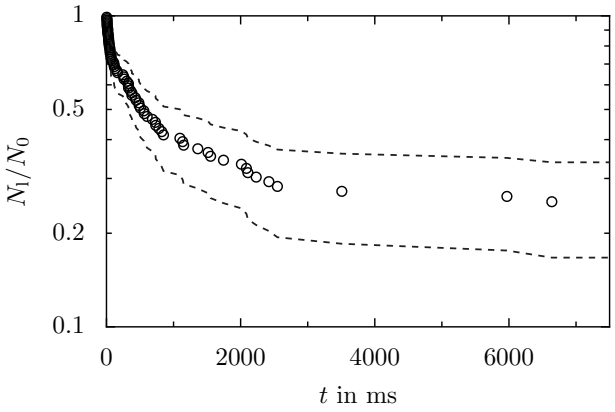

Figure 4.3: Survival curve obtained by sorting of the freezing delays measured during an experiment, and subsequent calculation of the relative number of liquid drops for each freezing event. $N_l(t)/N_0$ represents the average probability of a drop to stay liquid until time t. Dashed lines represent the bounds of the confidence interval containing 95.5 % of all expectable data. The data corresponds to the distribution of freezing delays shown in Fig. 4.2

a certain instant after impact, t, may be also considered as binomially distributed. In the case of constant conditions for each drop in an experiment, every drop has the same probability for nucleation at a certain time. Therefore, a drop being liquid until time t can be considered as the positive event of a Bernoulli trial; drop nucleation at time t is the negative event. In this case, the experimental results for $N_l(t)/N_0 = P_l$ represent the mean probability for a positive event at time t, obtained from N_0 Bernoulli trials. For a large number of independent Bernoulli experiments, a binomial distribution can be approximated as a standard normal distribution [272]. In the present study, where $N_0 \approx 100$, this approximation is adequate for the range $N_l(t)/N_0 = 0.084 \ldots 0.916$ [45]. By making use of the properties of a normal distribution, the upper and lower bound of a confidence interval for the probability of a positive event, i.e. a drop being liquid until time t, can be estimated using the experimental results for $N_l(t)/N_0$. Based on a two-sigma band around the experimentally obtained values for $N_l(t)/N_0$, the upper and lower bounds, $P_{l,\mathrm{low/up}}$,

of the confidence interval containing 95 % of all results which can be expected from an infinitely large number of Bernoulli trials, is estimated as [272]

$$P_{\mathrm{l,low/up}} = P_{\mathrm{l}} \pm 1.96\sqrt{\frac{P_{\mathrm{l}}(1-P_{\mathrm{l}})}{N_0}}. \tag{4.1}$$

The obtained upper and lower bound of this confidence interval are shown for example in Fig. 4.3 as dashed lines. The width of the confidence interval, with respect to the y-coordinate, i.e. $P_{\mathrm{l,up}} - P_{\mathrm{l,low}}$, increases with time for $N_{\mathrm{l}}(t)/N_0 \geq 0.5$, and decreases for $N_{\mathrm{l}}(t)/N_0 \leq 0.5$. Its maximum for the shown example is 0.197, corresponding to $N_{\mathrm{l}}(t)/N_0 = 0.5$.

In the case of nucleation experiments with a liquid at rest, the wetted surface area A_{wet} is constant, and the representation of the data in a semi-logarithmic plot is sufficient for a graphical estimation of the nucleation rate according to Eq. 2.48. In this case, according to $j_{\mathrm{het}} = \omega/A_{\mathrm{wet}}$, the nucleation rate being the physical quantity characterizing the nucleation process is proportional to the drop freezing rate observed for the drop ensemble, which is found as the slope of a survival curve. However, in the case of drop impact, the wetted surface area which is eventually active for heterogeneous nucleation changes over time. Therefore, Eq. 2.48 is not directly applicable to experimental results concerning nucleation during drop impact for the calculation of the nucleation rate from the drop freezing rate, i.e. from the slope of the survival curve. Besides the variable wetted surface area, several other mechanisms, such as the propagation of a pressure wave after impact, or the fluid flow during impact may affect nucleation. However, these mechanisms are equal for each drop in an ensemble. Assuming the wetted surface area to be only slightly affected by a variation of the impact conditions, a comparison of the drop freezing rates for varying conditions is thus appropriate for a qualitative estimation of the influence of a varied parameter on the nucleation process.

In the present study, nucleation is examined for the case of drop impact onto a rough surface. Depending on the impact conditions, the impinging liquid penetrates into the rough surface and wets more or less of the valleys and peaks of the surface, which is associated with a change of the surface area, effectively active for nucleation. Since this effect can not be clearly quantified, it is neglected in the following analysis, and the effectively wetted surface is always assumed proportional to the projected area of the wetted surface area, which is obtained from the high-speed videos captured in top-view.

As already mentioned in Sec. 2.2, the aforementioned relation between the observed drop freezing rate and the underlying nucleation rate is based on the assumption that exactly one nucleation event causes freezing of a drop, and no further nucleation takes place during the freezing process of a drop. Due to the large growth velocity of ice in supercooled water, and the relatively small amounts of water and the corresponding wetted surface area, this assumption is valid in most cases of the present study. Only in some cases more than one nucleation event has been observed in a drop. However, since the majority of drops includes only one active nucleation site, the influence of multiple nucleation sites on the estimation of the actual nucleation behavior is neglected in the present study. Only the first active nucleation site causing freezing of a drop is taken into account for the analysis.

4.2.1 Results and discussion

In the present section, nucleation during drop impact with varying impact conditions is examined based on a comparison of the drop freezing rates obtained from the experimental data without any further modeling. The influence of temperature, a varying impact velocity and a varying gas content of the impinging liquid on nucleation during isothermal drop impact, and varying temperatures during non-isothermal drop impact is studied. For the present qualitative analysis of the different influences, the variation of the wetted surface area during impact is neglected and the drop freezing rate is assumed as representative for the nucleation rate present at the respective conditions.

4.2.1.1 Effect of temperature during isothermal drop impact

Figure 4.4 shows the drop survival curves for varying temperatures during isothermal drop impact with $v_\mathrm{d} = 2.2\,\mathrm{m/s}$ and $d_\mathrm{d} = 3.2\,\mathrm{mm}$. The results are shown for varying periods after impact, $t \leq 7000\,\mathrm{ms}$, $t \leq 700\,\mathrm{ms}$, and $t \leq 70\,\mathrm{ms}$. To increase the statistical significance of the data, each experiment has been repeated at least 99 times, resulting in a minimum of 74 nucleation events for each experiment. The evolution of the relative number of liquids drops is not perfectly smooth, as shown especially for $\vartheta = -13.4\,^\circ\mathrm{C}$ in Fig. 4.4 b) and for $\vartheta = -15.8\,^\circ\mathrm{C}$ in Fig. 4.4 c). Despite the relatively large number of repetitions of the experiments, the

deviations from a perfectly smooth evolution are very unlikely to be justified physically, and are probably attributed to small uncertainties and variations of the experimental conditions; which unfortunately cannot be completely ruled out. Therefore, these deviations are likely to smooth out for an even larger number of repetitions of the experiments, which is indicated by the fact that each data set shows a clear trend. Based on this trend, a distinct analysis of the experimental results is possible despite the observed deviation from a smooth evolution, which is neglected in the following analysis.

As shown in Fig. 4.4, similar to nucleation in a liquid at rest, the nucleation rate generally increases for decreasing temperature. By this, the relative number of liquid drops, i.e. the probability of a drop to be liquid at a certain time decreases with decreasing temperature. However, in contrast to the case of nucleation in a liquid at rest, the drop freezing rate is not constant, indicating that the nucleation rate is influenced by the specific mechanisms associated with drop impact. The drop freezing rate is the largest in the first phase after impact and decreases with increasing time, as clearly shown in Fig. 4.4 a) for $\vartheta = -8.6\,^{\circ}\mathrm{C}$. Drop spreading, which may affect the nucleation rate by a variation of the wetted surface area, takes approx. 3 ms for the impact conditions corresponding to the shown data. Sandblasting of the glass impact surface results in a large hydrophilicity, prohibiting a significant receding of the drops after spreading. Therefore, a variation of the wetted surface area may affect the drop freezing rate only during drop spreading in the first milliseconds after impact. In particular it cannot be the reason for the change of the rate observed for times up to several seconds after impact in the case of $\vartheta = -8.6\,^{\circ}\mathrm{C}$. Moreover, assuming a constant nucleation rate, a smaller wetted surface area during drop spreading would cause a decreased drop freezing rate, which is contrary to the increased drop freezing rate observed in the first phase after impact. This clearly indicates that nucleation is significantly enhanced during the first phase after impact due to specific mechanisms accompanying the impact process.

In the case of $\vartheta < -8.6\,^{\circ}\mathrm{C}$, all drops are frozen after the first 600 ms. In contrast, approx. 25 % of the impinging drops are still liquid at the end of the observation time for a temperature of $\vartheta = -8.6\,^{\circ}\mathrm{C}$. As already mentioned, the drop freezing rate generally decreases with time. In the case of $\vartheta = -8.6\,^{\circ}\mathrm{C}$, the relative number of liquid drops even seems to converge to the constant value of 0.25. This convergence corresponds to a vanishing nucleation rate, and implies that for times $t > 7000$ ms virtually

no further nucleation is expected for this temperature. As indicated by the larger nucleation rate in the first phase after drop impact, some of the mechanisms associated with drop impact promote nucleation; the influence of these mechanisms on nucleation decreases with time, and finally results in a vanishing nucleation rate for $\vartheta = -8.6\,^{\circ}\mathrm{C}$. This means that in the case of a liquid at rest on the impact surface, i.e. in the absence of drop impact, no nucleation would have been observed at all for $\vartheta = -8.6\,^{\circ}\mathrm{C}$, and in particular for $\vartheta > -8.6\,^{\circ}\mathrm{C}$ as already mentioned and confirmed for $\vartheta = -6.2\,^{\circ}\mathrm{C}$. In the experiments only the impact process and the associated influential mechanisms cause nucleation of the impinging liquid after impact at $\vartheta = -8.6\,^{\circ}\mathrm{C}$. These mechanisms promote nucleation but do not guarantee it, as shown for the case of $\vartheta = -6.2\,^{\circ}\mathrm{C}$, where no nucleation has been observed even during drop impact. The drastic difference in the nucleation behavior between the drops at $\vartheta < -8.6\,^{\circ}\mathrm{C}$ and those at $\vartheta > -8.6\,^{\circ}\mathrm{C}$ confirms the rather singular nature of nucleation, described in Sec. 2.2.

According to the previous considerations, the "classic" critical nucleation temperature, introduced in the scope of the singular nucleation model in Sec. 2.2, i.e. for a liquid at rest on the impact surface, is definitely below $-8.6\,^{\circ}\mathrm{C}$, since virtually no nucleation is observed for drops at rest on the surface at $\vartheta \geq -8.6\,^{\circ}\mathrm{C}$. The exact value of this critical nucleation temperature cannot be identified based on the experimental data for drop impact, since the influence of the impact process on the nucleation temperature is not clear. However, with consideration of the mechanisms during drop impact, the critical nucleation temperature during drop impact is in the range between $\vartheta = -8.6\,^{\circ}\mathrm{C}$ and $\vartheta = -6.2\,^{\circ}\mathrm{C}$; at least for the specific impact conditions. The influence of the impact process on the critical nucleation temperature can not be definitely estimated from the experimental results. However, with the assumption that the mechanisms promoting nucleation during drop impact are only related to an energy contribution which helps to overcome the critical energy barrier for heterogeneous nucleation, ΔG^*, the experimental results allow estimation of this energy contribution during drop impact at the specific conditions. While the energy provided during impact is sufficient to overcome the energy barrier at $\vartheta = -8.6\,^{\circ}\mathrm{C}$, it is not sufficient to promote nucleation at $\vartheta = -6.2\,^{\circ}\mathrm{C}$, which is associated with a larger energy barrier than $\vartheta = -8.6\,^{\circ}\mathrm{C}$, being conclusive from the descriptions in Sec. 2.2. Therefore, the energy barriers for heterogeneous nucleation without drop impact at $\vartheta = -8.6\,^{\circ}\mathrm{C}$ and at $\vartheta = -6.2\,^{\circ}\mathrm{C}$ may serve for

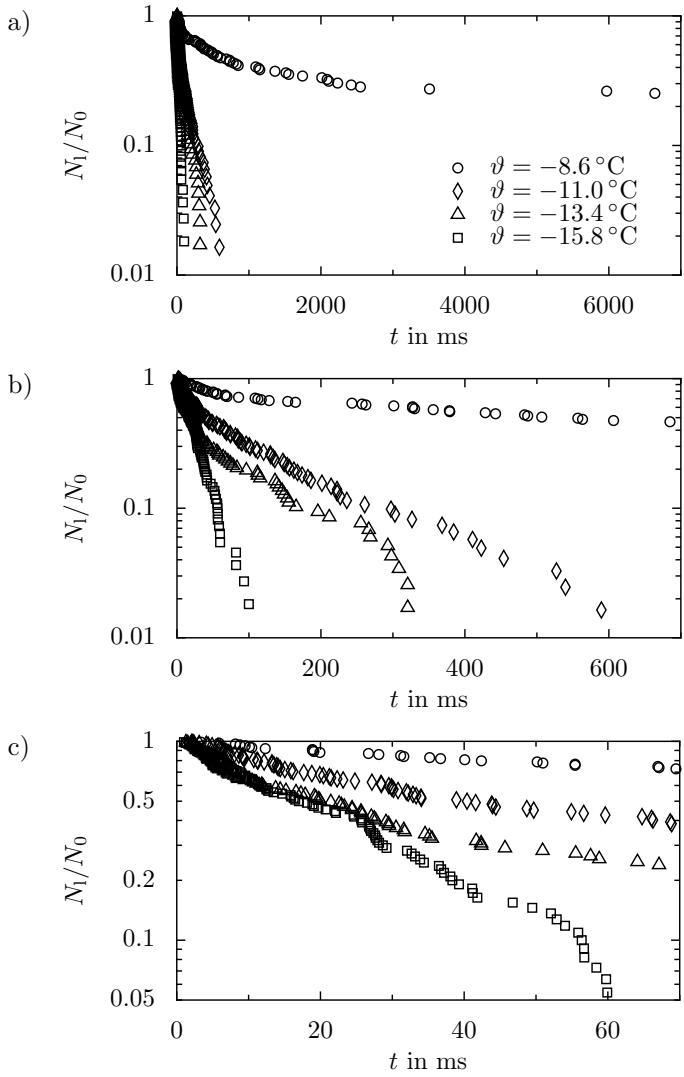

Figure 4.4: Drop survival curves for varying temperature during isothermal drop impact onto sandblasted glass with $d_\mathrm{d} = 3.2\,\mathrm{mm}$ and $v_\mathrm{d} = 2.2\,\mathrm{m/s}$, shown for varying periods after impact.

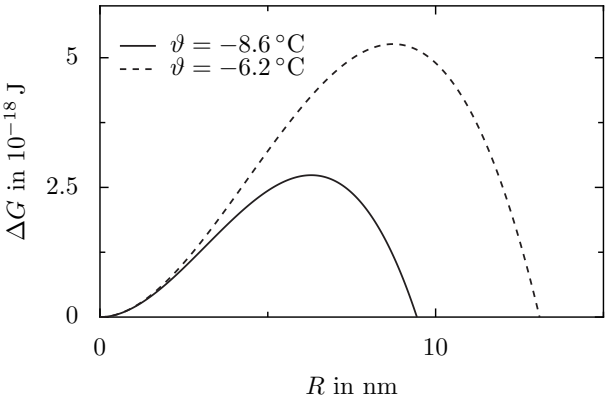

Figure 4.5: Gibbs free energy ΔG for heterogeneous nucleation associated with the formation of a spherical nucleus with radius R for different liquid temperatures.

an estimation of the lower and upper bound of the energy contribution by drop impact to nucleation, respectively.

Figure 4.5 shows the Gibbs free energy ΔG for heterogeneous nucleation at $\vartheta = -8.6\,^\circ\mathrm{C}$ and $\vartheta = -6.2\,^\circ\mathrm{C}$, depending on the nucleus radius R. It is obtained using Eq. 2.29, the properties of water, $\sigma_{\mathrm{sl}} \approx 0.033\,\mathrm{J/m^2}$ [149], $T_{\mathrm{m}} = 273.15\,\mathrm{K}$, $L_{\mathrm{v}} \approx 333.3 \times 10^6\,\mathrm{J/m^3}$, and an assumed shape factor of $S(\Theta) = 0.5$, corresponding to $\Theta = 90°$, i.e. a surface which is indifferent to ice (see Fig. 2.6). The critical energy barrier for heterogeneous nucleation without drop impact is obtained from Eq. 2.33 as $\Delta G^* \approx 2.74 \times 10^{-18}\,\mathrm{J}$ for $\vartheta = -8.6\,^\circ\mathrm{C}$, and $\Delta G^* \approx 5.27 \times 10^{-18}\,\mathrm{J}$ at $\vartheta = -6.2\,^\circ\mathrm{C}$. According to Eq. 2.1, using the speed of sound in water at the melting temperature, $c \approx 1402\,\mathrm{m/s}$ [40, 83], the pressure rise (which may be interpreted as an energy density) associated with drop impact under the present conditions is $\Delta p \approx 3.1 \times 10^6\,\mathrm{J/m^3}$. From Eq. 2.32, the critical nucleus radii at $\vartheta = -8.6\,^\circ\mathrm{C}$ and $\vartheta = -6.2\,^\circ\mathrm{C}$ are obtained as $R^* \approx 6.3\,\mathrm{nm}$ and $R^* \approx 8.7\,\mathrm{nm}$, respectively. Using the mean critical nucleation radius $R^* \approx 7.5\,\mathrm{nm}$ as a typical length scale for the formation of a hemispherical nucleus at the substrate surface with a critical volume, $V^* \approx 8.8 \times 10^{-25}\,\mathrm{m^3}$, the energy provided by the pressure rise during impact can be estimated as $\Delta p V^* \approx 2.74 \times 10^{-18}\,\mathrm{J}$, which is in perfect agreement with the estimated critical energy for heterogeneous nucleation

at $\vartheta = -8.6\,^{\circ}\mathrm{C}$. Therefore, the pressure rise associated with drop impact may be sufficient to enhance nucleation at $\vartheta = -8.6\,^{\circ}\mathrm{C}$, but it is to small to cause nucleation at $\vartheta = -6.2\,^{\circ}\mathrm{C}$, for which the critical energy barrier for nucleation is approx. two times larger than the estimated energy provided by drop impact. In particular, the pressure rise during drop impact may be the reason for the increase of the drop freezing rate during the first phase of drop impact, although the wetted surface area which is active for nucleation is smaller than at later times after impact. However, the propagation of the pressure wave during impact is restricted to a short phase after impact. The typical time associated with the pressure wave generated by drop impact can be estimated as the ratio of the drop diameter, $d_\mathrm{d} \sim 10^{-3}\,\mathrm{m}$, to the speed of sound in water, $c \sim 10^{3}\,\mathrm{m/s}$, as $t^\star = d_\mathrm{d}/c \sim 1\,\mu\mathrm{s}$. Therefore, the propagation of the pressure wave may affect nucleation only in a very short period after impact, and thus it can not be the reason for a change of the drop freezing rate at long times after impact, as observed for $\vartheta = -8.6\,^{\circ}\mathrm{C}$.

Another aspect, which has to be considered as influential for nucleation during drop impact is the flow and the resulting shear in the drop [286]. The typical time of drop spreading, $t^\star = d_\mathrm{d}/v_\mathrm{d}$, is of the order of milliseconds. At the impact instant a viscous boundary layer starts to develop in the spreading drop, whose thickness grows in time as $h_\mathrm{vis} \sim 2\sqrt{\nu t}$ [294]. The liquid film thickness after spreading can be estimated from geometrical considerations as $h_\mathrm{la} \approx 200\,\mu\mathrm{m}$. Using the viscosity of water $\nu \sim 10^{-6}\,\mathrm{m^2/s}$, the characteristic time at which the boundary layer reaches the free surface of the spread liquid can be estimated as $\sim 10^{-2}\,\mathrm{s}$. From this time, viscosity strongly damps the flow in the drop. It can be thus assumed that at times larger than $t \sim 10^{-2}\,\mathrm{s}$ the drops can be considered static, which is in good agreement with the observations from the high-speed videos, where the drop's liquid-gas interface appears to be at rest at $t \approx 40\,\mathrm{ms}$. Therefore, also the shear flow in the impinging drop may not be the reason for the change of the drop freezing rate at long times after impact. A mechanism which may cause the variation of the nucleation rate at later times after impact will be identified and discussed later.

As shown in Fig. 4.4, the time dependence of the drop freezing rate depends on temperature. The drop freezing rate drastically changes over time for $\vartheta = -8.6\,^{\circ}\mathrm{C}$, while it is almost constant at $\vartheta = -15.8\,^{\circ}\mathrm{C}$, which may be explained by the singular nucleation behavior with respect to the typical time scales of potentially influential processes. As described in

Sec. 2.2, the nucleation rate drastically increases in the vicinity of the critical nucleation temperature ϑ_{nuc}. While virtually no nucleation is observed for $\vartheta > \vartheta_{\mathrm{nuc}}$, the rate of nuclei formation explodes for $\vartheta < \vartheta_{\mathrm{nuc}}$. Despite this rather singular behavior with respect to temperature, nucleation is still a stochastic process based on stochastic molecule motion, where the temperature generally determines the typical time scale of the process. Therefore, the liquid temperature can be considered as the primary and fundamental effect having a twofold influence on nucleation. At first it controls the nucleation rate, and moreover, by controlling the nucleation rate the liquid temperature furthermore determines the typical time scale of the nucleation process. For convenience, in the following it is referred to nucleation solely controlled by temperature in the absence of any other influences as primary nucleation. Whether or not other effects such as the mechanisms associated with drop impact are relevant for effective nucleation depends first of all on the typical time scale of primary nucleation determined by the liquid temperature, in comparison to the time scale of a potentially influential mechanism. The typical time scale of primary nucleation is proportional to the inverse of the primary nucleation rate itself. The drop freezing rate attributed to primary nucleation represents the time during which nucleation in the drop may be affected by other influential mechanisms. While this time is very large for high temperatures associated with a small primary nucleation rate, it is small for large rates of primary nucleation corresponding to low temperatures. Due to a drastic increase of the nucleation rate in a small temperature range, also the typical time scale of nucleation drastically varies in a small temperature range. For temperatures below the critical nucleation temperature, nucleation is rather of singular nature, and thus unaffected by external influences which take place on a larger time scale. Nucleation may be significantly affected by these mechanisms in the case of temperatures above the critical nucleation temperature, which are associated with a large time scale of primary nucleation. This explains the drastic difference of the time dependence of the nucleation rate depending on liquid supercooling, observed in Fig. 4.4 a).

In a similar way, the influence of nucleation on other processes may be described as follows. Depending on both the liquid temperature, and the typical time scale of the process for which nucleation is taken into account, nucleation may be described by a rather stochastic, or a rather singular behavior. The singular nature of nucleation increases for decreasing temperature, as shown in Fig. 4.4 a). On the time scale characteristic for

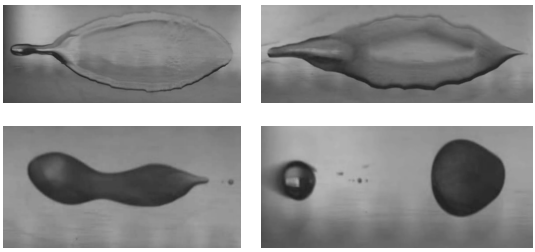

Figure 4.6: Outcomes after impacts of drops initially at room temperature onto an inclined mirror-polished aluminum substrate at $\vartheta_{\mathrm{sub},0} = -17.0\,^{\circ}\mathrm{C}$. The freezing delay resulting from the stochastics of nucleation determines the final shape of the frozen liquid. It is (from left to right and top to bottom) $t_{\mathrm{del}} \approx 30\,\mathrm{ms}$, $t_{\mathrm{del}} \approx 70\,\mathrm{ms}$, $t_{\mathrm{del}} \approx 130\,\mathrm{ms}$, $t_{\mathrm{del}} \approx 600\,\mathrm{ms}$. Note that the figures only serve for illustration and are not in scale.

Fig. 4.4 a), nucleation at $\vartheta = -8.6\,^{\circ}\mathrm{C}$ is clearly stochastic in time, while it may be treated as singular for $\vartheta = -15.8\,^{\circ}\mathrm{C}$. Moreover, the singular nature of nucleation increases with an increasing typical time for which nucleation is taken into account, as seen by a comparison of Figs. 4.4 c) and 4.4 a). While nucleation is rather singular associated with a relatively fast decrease of the relative number of liquid drops at $\vartheta = -15.8\,^{\circ}\mathrm{C}$ on the time scale characteristic for Fig. 4.4 a), the stochastic nature of nucleation gets clear even at this temperature, when considering nucleation with respect to a smaller time scale, as shown in Fig. 4.4 c).

Therefore, whether or not nucleation can be treated as singular or if the stochastic nature has to be considered, depends on the process for which nucleation is taken into account as a potentially influential mechanism. When considering a dynamic process taking place on a small time scale such as drop impact, the stochastic behavior is not negligible, as shown in Fig. 4.6. It illustrates possible resulting outcomes of frozen drops after inclined impact of water drops initially at room temperature on a mirror-polished aluminum surface at $\vartheta_{\mathrm{sub},0} = -17.0\,^{\circ}\mathrm{C}$, corresponding to the experimental results shown in Figs. 3.7 and 5.10. The impact conditions are constant for all shown drops. Therefore, the final shape of the frozen drop, and thus the surface area iced after freezing is only determined by the variation of the freezing delay after impact. Since the typical time scale of the rate of nucleus formation in a drop is well comparable to

the typical time scale of the impact process at the respective conditions, the surface area finally iced after drop impact is significantly affected by the stochastic nature of nucleation. Therefore, the statistics of nucleation definitely has to be taken into account during investigation of nucleation during drop impact with respect to the surface area iced after drop impact. Since the stochastic nature of nucleation also affects several other aspects such as the time available for drop rebound from a superhydrophobic surface, it should even be accounted for in all studies related to icing due to impinging supercooled water drops. In the case of rather static processes, such as cloud glaciation or icing due to sessile supercooled water drops, the stochastics of nucleation are irrelevant, and the critical nucleation temperature is the more important parameter characterizing the nucleation and icing process. In particular an increment or a depression of the nucleation temperature depending on atmospheric dust particles, or surface properties are relevant e.g. for weather forecast and the prevention of ice accretion, respectively. For the examination of these influences, the stochastics of nucleation are irrelevant and thus nucleation may be described using the singular nucleation model as described in Sec. 2.2. Note that also in this case, nucleation may follow certain statistics associated with the distribution of ice nucleating particles in the liquid or nucleation sites on the surface, which cause a spread of the nucleation temperature over a certain range, as shown in Fig. 2.9. Nevertheless, in this case the median nucleation temperature is an appropriate means to characterize the process, as described in Sec. 2.2.

4.2.1.2 Effect of the impact velocity

Figure 4.7 shows the influence of the impact velocity on the drop survival curves for varying temperatures during isothermal drop impact. A drop impact with a larger impact velocity results in a larger wetted surface area active for nucleation. Moreover, the pressure rise during drop impact is proportional to the impact velocity (see Eq. 2.1). Therefore, the energy provided for the nucleation process during drop impact is larger for a higher impact velocity. Similar to the larger wetted surface area, the increased energy during impact is expected to increase the drop freezing rate. However, no increased drop freezing rate for a higher impact velocity can be observed in Fig. 4.7. The drop freezing rate is even smaller for the larger impact velocity for all temperatures at times $t < 960\,\mathrm{ms}$. Until time $t \approx 580\,\mathrm{ms}$, all drops freeze for temperatures $\vartheta < -8.6\,^{\circ}\mathrm{C}$ at the smaller impact velocity, inhibiting a comparison of the drop freezing rate

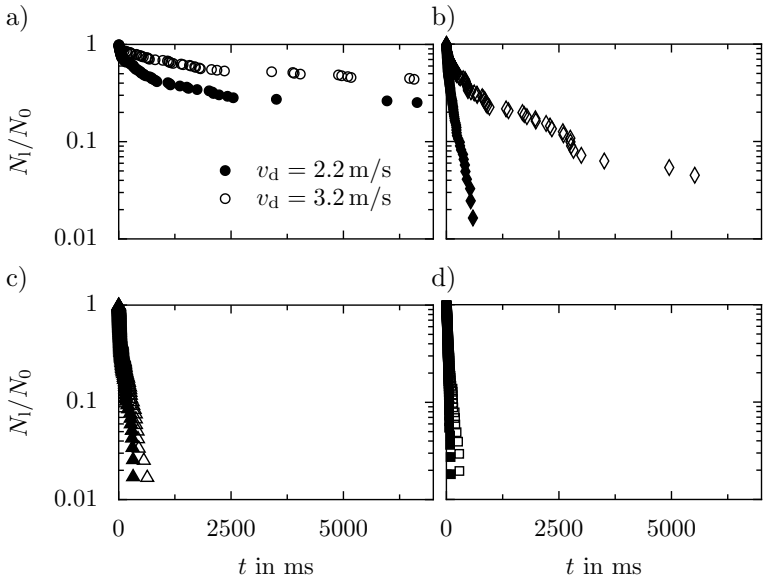

Figure 4.7: Drop survival curves depending on the impact velocity during isothermal drop impact of supercooled water drops for varying temperatures, a) $\vartheta = -8.6\,°C$, b) $\vartheta = -11.0\,°C$, c) $\vartheta = -13.4\,°C$, and d) $\vartheta = -15.8\,°C$. The drop diameter is $d_d = 3.2\,mm$ and the drops impact with $v_d = 2.2\,m/s$, and $v_d = 3.2\,m/s$.

for a varying impact velocity at later times. Similar to the results shown in the previous section, the drop freezing rate is significantly smaller for $\vartheta = -8.6\,°C$ than for lower temperatures, also in the case of the higher impact velocity, allowing a comparison of the drop freezing rate at later times. As shown in the figure, for the highest temperature the drop freezing rate is almost unaffected by the impact velocity for $t > 960\,ms$, indicating that the influence of a varying impact velocity is restricted to a certain phase after impact. If the increase of the drop freezing rate in the first phase after impact was only related to the propagation of a pressure wave and its contribution to overcome the energy barrier for nucleation, the influence of a variation of the impact velocity should be restricted to the phase of the propagation of the pressure wave during a short phase after impact. As shown in Fig. 4.7 a), the impact velocity affects the

drop freezing rate even until $t \approx 960\,\mathrm{ms}$ although the spread liquid is already at rest after $t \approx 35\,\mathrm{ms}$, as observed in the captured high-speed videos. Moreover, if the propagation of the pressure wave was the only mechanism which increases the nucleation rate, a larger nucleation rate is expected for an increasing impact velocity. Therefore, a variation of the impact velocity obviously involves further mechanisms also influential for nucleation, which are not related to the propagation of the pressure wave. While the impact process itself may enable and enhance nucleation by the propagation of a pressure wave, the other mechanisms accompanying drop impact have an opposite effect: they significantly mitigate nucleation for an increasing impact velocity. One of the mechanisms causing this effect will be identified and discussed later.

In accordance with the explanations in the previous section, the influence of the impact velocity on nucleation significantly depends on the twofold effect of the liquid temperature on nucleation. Also for the higher impact velocity, a decreasing temperature consistently results in an increasing drop freezing rate. However, similar to the effect of the impact process itself, also the effect of a varying impact velocity on the drop freezing rate depends on temperature. For $\vartheta = -8.6\,^{\circ}\mathrm{C}$ generally associated with the largest time scale of primary nucleation, also the higher impact velocity causes nucleation in the first phase after impact, while the nucleation rate almost vanishes for later times. However, the enhancement of nucleation is less pronounced for the higher impact velocity. At $\vartheta = -11.0\,^{\circ}\mathrm{C}$ which is first of all associated with a larger primary nucleation rate and thus a smaller time scale of primary nucleation, a fast decrease of the number of liquid drops is observed for the smaller impact velocity. In the case of the higher impact velocity, the nucleation rate is drastically reduced resulting in a significantly slower decrease of the number of liquid drops. Therefore, the time scale of primary nucleation at this temperature is still sufficiently large to cause nucleation to be affected by the processes associated with a variation of the impact conditions. In contrast, for $\vartheta = -13.4\,^{\circ}\mathrm{C}$ and $\vartheta = -15.8\,^{\circ}\mathrm{C}$ associated with an even smaller time scale of primary nucleation, similar to the effect of the drop impact process itself, also a variation of the impact velocity has a vanishing effect on effective nucleation and the observed drop freezing rate, which appear only slightly affected by an increase of the impact velocity.

Concluding, due to an additional effect associated with drop impact, a larger impact velocity generally results in a smaller drop freezing rate at the investigated impact conditions. However, the effect of a varying

impact velocity vanishes for both later times as indicated in Fig. 4.7 a), and lower liquid temperatures as indicated in Fig. 4.7 c) and d).

4.2.1.3 Nucleation during non-isothermal drop impact

Several aspects of a temperature variation during non-isothermal drop impact have to be considered for nucleation. At first, if only the pressure wave during impact is dominant for nucleation, the minimum liquid temperature would be crucial for nucleation, regardless if this temperature is only locally present in the liquid. Secondly, if nucleation is dominated by heterogeneous nucleation at the substrate surface, the contact temperature during impact would be crucial for nucleation. Finally, non-isothermal drop impact is accompanied by a further cool down or a warm up of the impinging liquid. According to Eq. 2.49, the stochastic nucleation model predicts a reduced drop freezing rate for an increasing liquid cooling rate, which may also affect nucleation during non-isothermal drop impact.

Based on these considerations, the initial drop and substrate temperature have been appropriately varied to investigate drop impact for a constant initial drop temperature, substrate temperature, and an almost constant resulting contact temperature, calculated using Eq. 2.11. In all of the aforementioned cases, the temperatures have been varied to allow

Table 4.2: Initial drop and substrate temperatures, and the resulting theoretical contact temperatures calculated using Eq. 2.11, used for the study of nucleation during non-isothermal drop impact.

a)

$\vartheta_{sub,0}$ = const		
$\vartheta_{d,0}$	$\vartheta_{sub,0}$	ϑ_c
in °C		
-6.5	-11.0	-8.5
-11.0	-11.0	-11.0
-15.5	-11.0	-13.5

b)

$\vartheta_{d,0}$ = const		
$\vartheta_{d,0}$	$\vartheta_{sub,0}$	ϑ_c
in °C		
-11.0	-6.0	-8.7
-11.0	-11.0	-11.0
-11.0	-16.0	-13.3

c)

ϑ_c = const		
$\vartheta_{d,0}$	$\vartheta_{sub,0}$	ϑ_c
in °C		
-6.5	-11.0	-8.5
-8.6	-8.6	-8.6
-11.0	-6.0	-8.7
-11.0	-16.0	-13.3
-13.4	-13.4	-13.4
-15.5	-11.0	-13.5

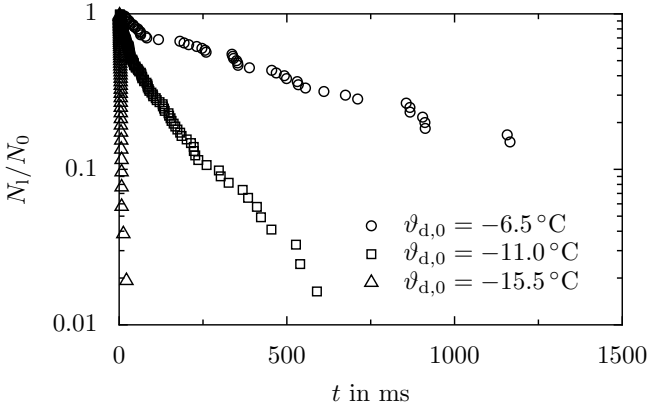

Figure 4.8: Drop survival curves depending on the initial drop temperature during non-isothermal drop impact. The initial substrate temperature is constant at $\vartheta_{sub,0} = -11.0\,°C$, while the initial drop temperature is varied between $\vartheta_{d,0} = -15.5\,°C$ and $\vartheta_{d,0} = -6.5\,°C$. The drop diameter is $d_d = 3.2\,mm$ and the drops impact with $v_d = 2.2\,m/s$.

examination of both a further cooling down, and a warming up of the liquid in the vicinity of the substrate surface, susceptible for heterogeneous nucleation. The experiments have been performed with a drop diameter of $d_d = 3.2\,mm$ and an impact velocity of $v_d = 2.2\,m/s$. The combinations of the initial drop and substrate temperature as well as the calculated theoretical contact temperatures are summarized in Tab. 4.2.

Constant initial substrate temperature

Figure 4.8 shows the drop survival curves for a constant initial substrate temperature and a varying initial drop temperature corresponding to the conditions summarized in Tab. 4.2 a). Note that the survival curve for $\vartheta_{d,0} = -11.0\,°C$ corresponds to isothermal drop impact. A decreasing initial drop temperature which is accompanied by a decreasing contact temperature consistently results in an increasing drop freezing rate.

Therefore, the results clearly indicate that nucleation is significantly affected by either the contact temperature or the minimum liquid temperature. The impact with an initial drop temperature above or below

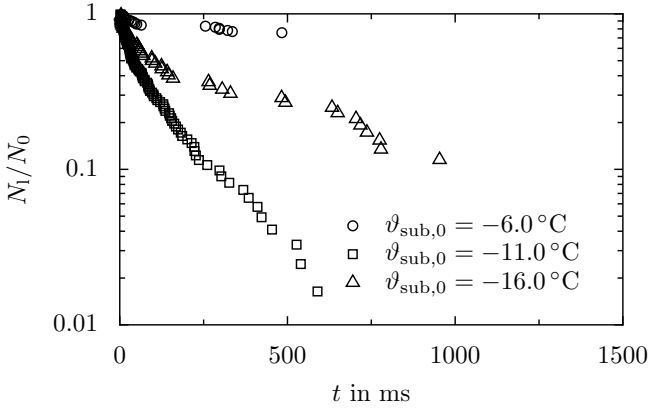

Figure 4.9: Drop survival curves depending on the initial substrate temperature during non-isothermal drop impact. The initial drop temperature is constant at $\vartheta_{\mathrm{d},0} = -11.0\,^\circ\mathrm{C}$, while the initial substrate temperature is varied between $\vartheta_{\mathrm{sub},0} = -16.0\,^\circ\mathrm{C}$ and $\vartheta_{\mathrm{sub},0} = -6.0\,^\circ\mathrm{C}$. The drop diameter is $d_\mathrm{d} = 3.2\,\mathrm{mm}$ and the drops impact with $v_\mathrm{d} = 2.2\,\mathrm{m/s}$.

the initial substrate temperature is associated with a further cool down or warm up of the impinging liquid during impact, respectively. The effect of such a temperature change of the impinging liquid on the nucleation rate cannot be clearly identified from the present results. It may be present but is obviously smaller than the effect of temperature itself, and thus not observable.

Constant initial drop temperature

The drop survival curves for a constant initial drop temperature and a varying initial substrate temperature, corresponding to the conditions summarized in Tab. 4.2 b), are shown in Fig. 4.9. The survival curve for $\vartheta_{\mathrm{sub},0} = -11.0\,^\circ\mathrm{C}$ corresponds to isothermal drop impact. In the case of $\vartheta_{\mathrm{sub},0} = -6.0\,^\circ\mathrm{C}$, the contact temperature, $\vartheta_\mathrm{c} = -8.7\,^\circ\mathrm{C}$, is above the initial drop temperature, $\vartheta_\mathrm{c} > \vartheta_{\mathrm{d},0}$. Consequently, the liquid in the near-wall region warms up, while the minimum drop temperature remains unaffected during drop impact. As shown in the figure, these conditions result in a reduced drop freezing rate in comparison to the isothermal impact at $\vartheta_{\mathrm{sub},0} = -11.0\,^\circ\mathrm{C}$. Since the minimum liquid temperature is

unaffected, the observed reduction of the drop freezing rate indicates a significant influence of the contact temperature on nucleation.

In the case of drop impact onto the substrate with the lowest temperature, $\vartheta_{\mathrm{sub},0} = -16.0\,^{\circ}\mathrm{C}$, the contact temperature which in this case represents the minimum liquid temperature, $\vartheta_{\mathrm{c}} = -13.3\,^{\circ}\mathrm{C}$, is well below the initial drop temperature. In accordance with the previous considerations, it is associated with a larger drop freezing rate than the impact onto the warmer substrate with $\vartheta_{\mathrm{c}} = -8.7\,^{\circ}\mathrm{C}$. Surprisingly, as shown in the figure, the impact onto the substrate with the lowest temperature is associated with a decrease of the drop freezing rate in comparison to the isothermal case $\vartheta_{\mathrm{sub},0} = -11.0\,^{\circ}\mathrm{C}$; although the contact temperature is reduced with respect to the isothermal case, which is expected to cause an increase of the nucleation rate. Therefore, neither the contact temperature at the substrate surface, nor the minimum liquid temperature (which in this case is at the substrate surface) can be the only influential mechanisms for nucleation during non-isothermal drop impact. Obviously, the process is also affected by a temporal change of the liquid temperature during impact, which is the only remaining difference associated with the examined temperature variations. As mentioned above and shown in Sec. 2.2, the statistical nucleation model predicts a decrease of the drop freezing rate for an increasing liquid cooling rate. Drop impact onto the colder substrate is accompanied by a further cool down of the impinging liquid in the near-wall region, which thus may be the reason for a drop freezing rate reduced with respect to the drop freezing rate at isothermal conditions.

Concluding, the influence of the initial substrate temperature on the drop freezing rate during non-isothermal drop impact appears to be twofold: a variation of the substrate temperature affects the drop freezing rate by a change of both the contact temperature, and the rate of change of the liquid temperature in the near-wall region which is susceptible for heterogeneous nucleation.

Constant contact temperature

The experiments in the previous sections revealed two significant influences on nucleation during non-isothermal drop impact: the contact temperature and the temporal change of the liquid temperature in the near-wall region, susceptible for heterogeneous nucleation. So far, the temperature variations in the previous experiments were accompanied by both a

varying contact temperature, and a varying cooling rate of the liquid in the vicinity of the wall, thereby prohibiting investigation of the distinct influences. For a more differentiated examination of nucleation during non-isothermal drop impact, the experimental conditions have been varied to allow study of the influence of a changing liquid temperature in the case of an almost constant contact temperature, corresponding to the conditions summarized in Tab. 4.2 c).

The previous experiments showed no clear trend of the drop freezing rate depending on a variation of the initial substrate temperature (see Fig. 4.9), since these experiments were accompanied by a simultaneous variation of both the contact temperature and the temporal change of the liquid temperature at the substrate. This behavior could not be observed for the experiments with a varying drop temperature, where the initial drop and the resulting contact temperature appeared to be the dominating influence on nucleation.

As shown in Fig. 4.10 for the experiments concerning nucleation at a constant contact temperature, a clear trend of the drop freezing rate is found for a variation of the drop and substrate temperature. However, another surprising result can be observed for these experiments: while a decreasing initial drop temperature results in an increasing drop freezing rate for the lower contact temperature, $\vartheta_c \approx -13.4\,°C$ (Fig. 4.10 b)), it causes a decreasing rate of drop freezing for the higher contact temperature, $\vartheta_c \approx -8.6\,°C$ (Fig. 4.10 a)). Therefore, the drop freezing rate appears to be dominated by the initial drop temperature at lower temperatures, while other effects on nucleation such as the liquid cooling rate gain importance for higher temperatures.

A possible reason for this behavior may be found by means of the statistical nucleation model and the fundamentals of nucleation, described in Sec. 2.2. On the one hand, according to Eq. 2.49 the cooling rate has a linear influence on the drop freezing rate, which is independent of temperature. On the other hand, the drop freezing rate depends on the nucleation rate which, according to Eq. 2.35 and as shown in Fig. 2.7, strongly depends on temperature; it drastically increases in a small temperature range. By this, both the absolute temperature which controls the nucleation rate, and the cooling rate compete in determining the drop freezing rate. The role of temperature in this competition may be explained similar to the temperature dependent effect of further mechanisms on nucleation, explained in the previous section concerning isothermal drop impact. Due

to the drastic increase of the nucleation rate below the critical nucleation temperature, temperature is the dominant influence on nucleation at low temperatures. Due to a significant decrease of the typical time scale of nucleation at higher temperatures, similar to any other potentially influential mechanism, the cooling rate gains influence on nucleation above the critical nucleation temperature. Accordingly, nucleation at $\vartheta_c \approx -13.4\,°C$ is dominated by the liquid temperature, resulting in a larger drop freezing rate for lower initial drop temperatures, as shown in Fig. 4.10 b). At $\vartheta_c \approx -8.6\,°C$, not only the initial drop temperature but also other effects such as a change of the liquid temperature during impact, which accompanies a variation of the initial substrate temperature, may affect nucleation, resulting in a seemingly opposite dependence of the drop freezing rate on the initial drop temperature.

Another effect which may be influential for drop freezing during non-isothermal drop impact, and thus can cause an increasing drop freezing rate for an increasing initial drop temperature is the effective wetting of the rough substrate. As mentioned earlier, depending on the impact conditions the impinging liquid partially penetrates into the roughness elements of the surface. The impalement of the liquid is not only determined by the impact conditions, but may also be affected by the liquid viscosity which significantly depends on temperature, as already discussed, and shown in App. B. Due to an enhanced penetration accompanying a decreased liquid viscosity, the effective wetting of the surface increases for an increasing temperature. By this, the impact of a warmer drop results in a larger effectively wetted surface area, which may increase the drop freezing rate also for higher liquid temperatures.

Based on the present experiments, a definite explanation of the different influences on nucleation during non-isothermal drop impact is unfortunately not possible. Nevertheless, the present experiments constitute a significant contribution to a better understanding since they demonstrate that not only the liquid temperature but also other mechanisms such as a further cool down or a warm up of the impinging liquid are influential for nucleation. Moreover, in accordance with the results in the previous sections, the present results indicate that the influence of further effects on nucleation depends on temperature. For low temperatures of the impinging liquid, the liquid temperature primarily dominates nucleation, while other effects gain importance only for higher temperatures.

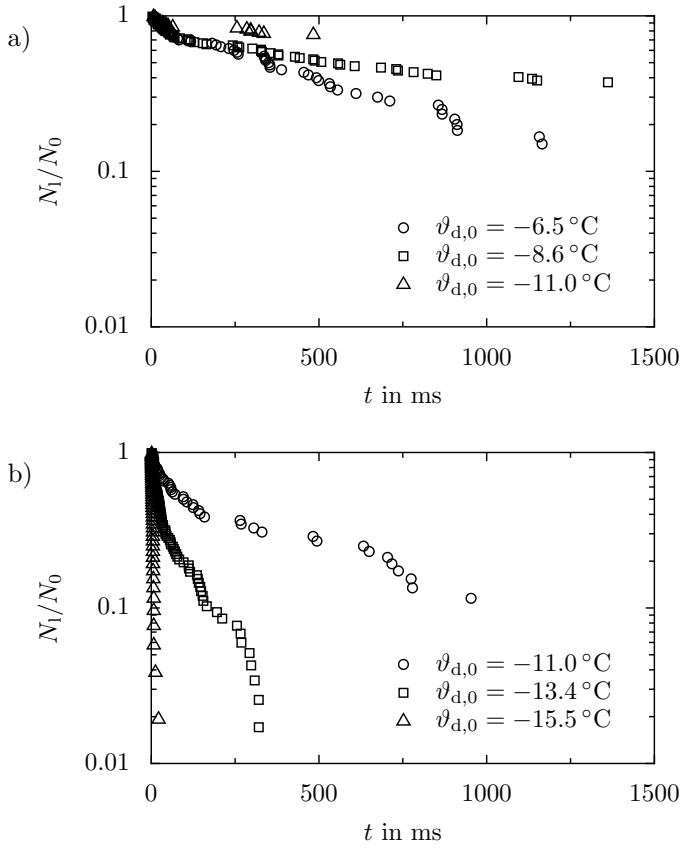

Figure 4.10: Drop survival curves depending on the initial drop and substrate temperature during non-isothermal drop impact. The initial substrate and drop temperature are varied between a) $\vartheta = -11.0\,°C$ and $\vartheta = -6.0\,°C$, and b) $\vartheta = -16.0\,°C$ and $\vartheta = -11.0\,°C$, as summarized in Tab. 4.2 c), resulting in a constant theoretical contact temperature of a) $\vartheta_c = -8.6\,°C$, and b) $\vartheta_c = -13.4\,°C$. The drop diameter is $d_d = 3.2\,mm$ and the drops impact with $v_d = 2.2\,m/s$. Note that the cases with $\vartheta_{d,0} = -8.6\,°C$ and $\vartheta_{d,0} = -13.4\,°C$ correspond to isothermal drop impact.

4.2.1.4 Further effects on nucleation during drop impact

A phenomenon which can significantly influence the nucleation kinetics of drop freezing is associated with the generation of gas bubbles during drop spreading. The effect of air bubbles and bubble cavitation on the intensification of nucleation or on the reduction of the nucleation temperature is well-known [68, 143]. In the case of drop impact, air bubbles may be entrapped within the rough surface during drop impact, especially during drop spreading over the rough sandblasted glass surface used in the present study [22]. As long as these bubbles exist inside and below the spread liquid, they may enhance the rate of nucleus formation in the liquid. Accordingly, dissolving of the bubbles is expected to cause a nucleation rate, decreasing with time.

In order to more explicitly confirm the hypothesis on the influence of bubble formation on the nucleation rate in impinging drops, impact experiments have been performed with water drops of different initial gas content, which has been obtained using vacuum degasification. The gas content in the drops is varied between the saturation gas content at standard pressure of $p \approx 1\,\mathrm{bar}$, and at a pressure of $p \approx 0.1\,\mathrm{bar}$, where the latter gas content is according to Henry's law ten times smaller than at standard pressure [145].

In the experiments both the drop and the substrate temperature is $\vartheta_{\mathrm{d},0} = \vartheta_{\mathrm{sub},0} = -11\,^{\circ}\mathrm{C}$, and the drop diameter and impact velocity are $d_{\mathrm{d}} = 3.2\,\mathrm{mm}$ and $v_{\mathrm{d}} = 2.2\,\mathrm{m/s}$, respectively. Fig 4.11 shows a comparison of the spreads of a non-degassed and a degassed water drop, 40 ms after drop impact. In the case of non-degassed water (left photograph), significantly more air bubbles in the form of small black spots on the wetted surface area can be observed than for the case of degassed water (right photograph). This effect can be explained by the faster dissolving of the bubbles in the degassed liquid, which is undersaturated with respect to the ambient pressure during the experiments. Accordingly, if entrapped air bubbles promote nucleation, a smaller drop freezing rate should be observable in the case of degassed water drops due to a faster dissolving of gas bubbles. The observed survival curves for a varying gas content of the impinging liquid are shown in Fig. 4.12. In consistency to the aforementioned considerations, the drop freezing rate observed for degassed water drops is significantly smaller compared to the freezing rate of non-degassed drops, thus confirming the hypothesis on the enhancement of nucleation by air bubbles entrapped during drop spreading.

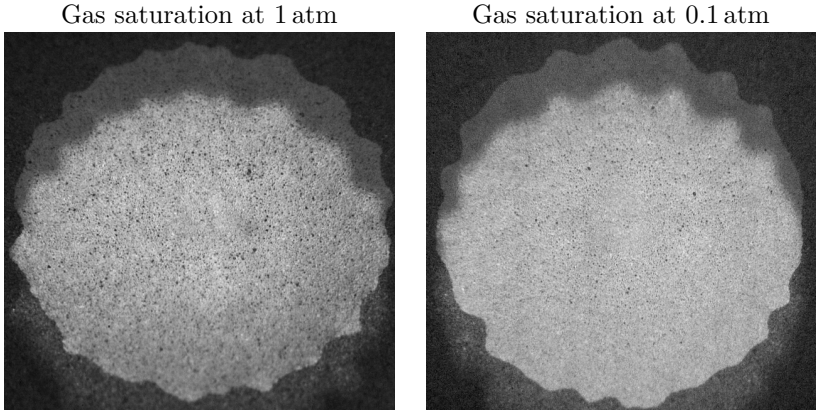

Figure 4.11: Air bubble entrapment during drop spreading, shown 40 ms after isothermal normal drop impact with $d_\mathrm{d} = 3.2\,\mathrm{mm}$ and $v_\mathrm{d} = 2.2\,\mathrm{m/s}$ onto a cold, sandblasted glass substrate at $-11.0\,^\circ\mathrm{C}$. Left photograph: Drop with saturation gas content at a pressure of 1 bar. Right photograph: Drop with saturation gas content at a pressure of 0.1 bar. (Reprinted figure (adapted) with permission from [320]. Copyright 2016 by the American Physical Society.)

The initial size of the gas bubbles entrapped during impact, R_0, is comparable to the roughness of the surface. As mentioned earlier, the average of the absolute roughness values of the sandblasted surface has been measured as $R_\mathrm{a} \approx 3.0\,\mu\mathrm{m}$. The time of the bubble shrinkage in water is determined by the kinematics of diffusion of the dissolved gas in the neighborhood of the bubble. For small bubbles this time is obtained from the Epstein-Plesset theory as $t_\mathrm{life} \approx R_0^2 \rho_\mathrm{g}/(3Dc_\mathrm{s})$ [100, 207]. With the diffusion coefficient for air in water, $D \approx 2 \times 10^{-9}\,\mathrm{m^2/s}$ [27], the air density $\rho_\mathrm{g} \approx 1.2\,\mathrm{kg/m^3}$, and using the solubility of air in water at the melting temperature, $c_\mathrm{s} \approx 3.7 \times 10^{-2}\,\mathrm{kg/m^3}$ [373], the life-time of a bubble with $R_0 \approx 3\,\mu\mathrm{m}$ is estimated as $t_\mathrm{life} \approx 50\,\mathrm{ms}$. This time is well comparable to the instant of the sharp decrease of the drop freezing rate for the degassed drops, observed at $t \approx 35\,\mathrm{ms}$ in Fig. 4.12. While for earlier times, $t < t_\mathrm{life}$, nucleation is supported by the presence of gas bubbles on the substrate surface, in the absence of air bubbles at later times pure heterogeneous nucleation on the wetted substrate dominates the process.

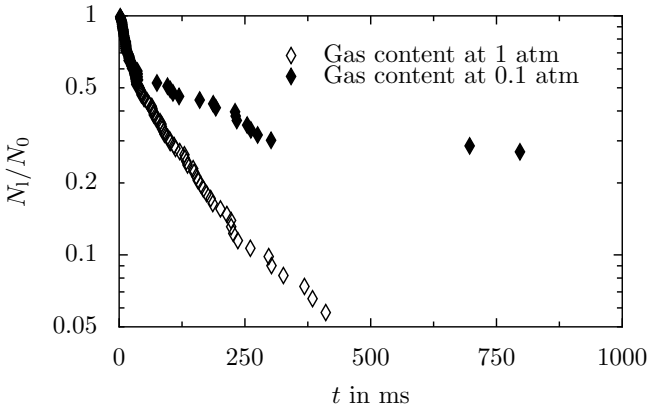

Figure 4.12: Drop survival curves depending on the gas content of the impinging liquid during isothermal drop impact at −11.0 °C. The curves correspond to a saturation gas content at a pressure of 1 bar and 0.1 bar. The drop diameter is 3.2 mm and the impact velocity is 2.2 m/s. (Reprinted figure (adapted) with permission from [320]. Copyright 2016 by the American Physical Society.)

Due to their continuous dissolving until time t_{life}, the influence of gas bubbles on nucleation continuously decreases until t_{life}, which explains the changing nucleation rate also for $t < t_{\text{life}}$, as observed in the previous study of the influence of temperature on nucleation during isothermal drop impact (see Fig. 4.4 c)). It should be noted that for very small bubbles, the lifetime at a wall can be much longer than t_{life} [207], which may lead to a non-constant nucleation rate even at later times $t > t_{\text{life}}$.

Dissolving of the gas bubbles begins immediately after their generation during impact and results in a decreasing nucleation rate from the beginning of drop impact. The air bubbles contribute to an increase of the nucleation rate in the first phase after impact, as it has been observed for all impact conditions. While the propagation of the pressure wave may influence nucleation only in a very short phase after impact, air bubbles exist much longer, and therefore, they also cause a change of the nucleation rate long times after impact. Entrapment of air bubbles during impact, and their effect on nucleation may also explain the decreased drop freezing rate which has been observed for an increasing impact velocity. A

larger impact velocity causes an increased dynamic pressure at the leading edge of an impinging drop, which results in a deeper penetration of the impinging liquid into the rough surface. Therefore, the entrapped air bubbles are smaller from the beginning, and thus are less effective in promoting nucleation, resulting in a decreased drop freezing rate. When the air bubbles are completely dissolved, the impact velocity has no further effect on nucleation, as indicated by the almost constant drop freezing rate observed for $t > 960\,\mathrm{ms}$ in Fig. 4.7 a).

As mentioned earlier, a deeper penetration of the liquid into the surface structure is associated with a larger surface area effectively wetted. Moreover, a higher impact velocity is accompanied by a larger liquid spreading. Both effects result in an increased surface area active for heterogeneous nucleation, theoretically increasing the drop freezing rate. Surprisingly, a smaller drop freezing rate is observed for a higher impact velocity, indicating that the aforementioned effects are secondary, and the effect of a decreased bubble size associated with an increased impact velocity is the dominating influence on the drop freezing rate; at least for the present impact conditions.

The results of the present chapter reveal that nucleation during drop impact is a highly complex process, influenced by a variety of parameters and mechanisms, such as air entrapment during impact, temperature gradients in the liquid, a further cool down or warm up of the impinging liquid, the drop impact velocity and mutual effects of these mechanisms. At this time, it is not clear if, and how even more effects associated with drop impact, such as the shear flow in the drop, affect nucleation during drop impact. For clarification, further experiments with varying impact conditions are required. Although the involved mechanisms and effects are not completely clear at the moment, the present work may serve as a suitable building block for future investigations.

4.2.2 Conclusion

Nucleation during the impact of supercooled water drops onto a sand-blasted glass mirror has been experimentally investigated. Several impact parameters, comprising the temperature, impact velocity and gas content of the impinging liquid during isothermal drop impact, and both the drop and substrate temperature during non-isothermal drop impact have been varied to examine their influence on the drop freezing rate during impact.

Due to the surface morphology in the present experiments, drop impact is not followed by receding of the liquid. Therefore, with neglection of both the drop spreading phase and the influence of varying impact conditions on the surface area effectively wetted during impact, the negative slope of the drop survival curves, which are obtained from the experiments without any modeling, can be assumed proportional to the nucleation rate in the impinging liquid. This allows qualitative examination of the influence of the varied impact conditions on nucleation by a comparison of the drop survival curves and the resulting drop freezing rates obtained from the experiments without any further modeling.

It has been shown that similar to the case of nucleation in a liquid at rest, a lower drop temperature results in a higher nucleation rate also during isothermal drop impact. However, in comparison to nucleation in a liquid at rest, the nucleation rate during drop impact is not constant and varies over time. Due to several effects associated with drop impact it is larger in a short phase after impact and decreases with time. The pressure wave arising during impact, and propagating through the spreading drop could be identified to provide enough energy to overcome the critical energy barrier for heterogeneous nucleation at temperatures where no nucleation is observed in the absence of drop impact. The influence of the pressure wave on nucleation is restricted to a short phase after impact, and at later times after impact it does not affect the drop freezing rate. Gas bubbles which are entrapped during spreading on the rough surface act as additional nucleation sites and promote nucleation from the beginning after drop impact. The gas bubbles continuously dissolve in the impinging liquid causing a decreasing nucleation rate also at long times after impact. A smaller drop freezing rate is observed for the impact of degassed water drops, since entrapped gas bubbles are smaller and dissolve faster in comparison to the impact of non-degassed drops.

Experiments revealed that an increasing impact velocity results in a decreasing drop freezing rate. In the case of an increased impact velocity, a higher dynamic pressure of the impinging drop causes a deeper penetration of the liquid into the rough surface, resulting in smaller gas bubbles entrapped in the surface. Therefore, nucleation is less enhanced by gas bubbles, causing a smaller drop freezing rate; although the larger velocity causes both a larger wetted surface area active for heterogeneous nucleation, and a larger pressure rise after impact, which both should promote drop freezing. Some time after impact, when the gas bubbles are completely dissolved, the freezing rate is almost unaffected by the impact

velocity.

It has been shown that the effect of a variation of the impact conditions on nucleation in general depends on temperature. While the drop freezing rate is almost unaffected by other mechanisms and primarily determined by temperature for lower temperatures, other effects gain importance for the nucleation rate at higher temperatures. This effect may be described by the singular nature of nucleation with consideration of the typical time scales of both nucleation and the potentially influential process. Whether or not any other mechanism besides temperature influences nucleation, depends on the typical time scale of the respective process in comparison to the typical time scale of nucleation. The typical time scale of nucleation is proportional to the inverse of the nucleation rate, and thus it is short for large nucleation rates at low temperatures, and long for smaller rates at higher temperatures. Processes taking place on a time scale which is longer than the typical time scale of nucleation do not affect nucleation. Therefore, at lower temperatures which are associated with a short time scale of nucleation, nucleation is dominated by temperature and other effects only play a minor role; nucleation is rather singular with respect to the slower process. The number of processes which are influential for nucleation increases with a decreasing nucleation rate at higher temperatures, where the stochastic nature of nucleation gains importance.

The influence of temperature on nucleation during non-isothermal drop impact is not completely clear. A variation of the drop temperature during impact with a constant substrate temperature consistently results in an increasing drop freezing rate for a decreasing drop temperature. However, in the case of a constant drop temperature, no clear trend of the drop freezing rate is observed for a varying substrate temperature. For non-isothermal drop impact with a constant contact temperature, clear trends of the drop freezing rate depending on the initial drop temperature are observed. However, these trends depend on the contact temperature itself. Similar to isothermal drop impact, a decreasing drop temperature results in an increase of the drop freezing rate at $\vartheta_c = -13.4\,^{\circ}\mathrm{C}$, whereas an opposite influence has been observed for $\vartheta_c = -8.6\,^{\circ}\mathrm{C}$. At this contact temperature, the drop freezing rate increases with decreasing substrate temperature. The effects on nucleation during non-isothermal drop impact cannot be definitely explained at the moment, but the observed behavior is probably related to the statistics of nucleation and the rather singular nature of nucleation at lower temperatures. According to the stochastic nucleation model, the drop freezing rate is generally de-

termined by the temperature dependent nucleation rate. The nucleation rate drastically increases by several orders of magnitude in a narrow range of temperature, which represents a rather singular nucleation behavior at low temperatures. In addition to its dependence on the nucleation rate, the drop freezing rate is also influenced if a drop ensemble is exposed to a cooling rate; according to the stochastic nucleation model an increasing cooling rate causes a decreasing drop freezing rate. In the case of non-isothermal drop impact, the impact is associated with a further cool down or a warm up of the impinging liquid, which thus may affect the drop freezing rate. However, due to the exponential increase of the nucleation rate with decreasing temperature, a cool down or warm up of the liquid may only affect the drop freezing rate at moderate supercoolings associated with long time scales of nucleation. Thus, at the lower contact temperature, $\vartheta_c = -13.4\,°C$, the singular nature of nucleation is dominant, and mainly the liquid temperature controls the drop freezing rate via an increased nucleation rate. Also a further cooling down or warming up of the liquid affects nucleation at the higher contact temperature, $\vartheta_c = -8.6\,°C$, which is generally associated with a smaller nucleation rate. Besides the heat flow during non-isothermal drop impact, also the liquid properties may affect the drop freezing rate. A change of the liquid viscosity results in an altered impalement of the impinging liquid into the rough surface used for the present experiments. By this, the effectively wetted surface area is implicitly affected by the liquid temperature, which can have an influence on the resulting drop freezing rate. In particular it could explain a decreasing drop freezing rate for a decreasing initial liquid temperature observed for the experiments at $\vartheta_c = -8.6\,°C$, which may be due to a decreasing effectively wetted surface area as a consequence of an increased liquid viscosity.

As shown in the present study, the effect of distinct processes on nucleation may be explained based on an interplay of the stochastic and the singular nature of nucleation. In analogy, both the singular and stochastic nature have to be considered also for the estimation of influences from nucleation on other processes. Also in this case, both the typical temperature and the typical time scale of the considered process determine whether or not nucleation may be assumed as singular, or if the statistics of nucleation are relevant for the specific process. Generally, the singular nature of nucleation increases for decreasing temperature and increasing time scale of the considered process, which is potentially influenced by nucleation. When the typical time scale of the process is much longer than that of nu-

cleation, as in the case of icing due to sessile water drops, the statistics of nucleation are irrelevant for the process and nucleation may be assumed singular. In this case, the median nucleation temperature according to the singular nucleation model is the more relevant parameter determining the nucleation and icing process. When the time scale of the process is comparable to the typical time scale of nucleation such as in the case of drop impact, the stochastic nature of nucleation cannot be neglected since it may significantly influence the considered process. This has been demonstrated for inclined drop impacts onto mirror-polished aluminum, where the stochastic nature of nucleation drastically influences the surface area iced after a single drop impact.

4.3 Quantitative analysis

In the previous section, the experimental results concerning different influences on nucleation during drop impact have been compared in terms of the drop freezing rates observed in the respective experiments. In the case of comparable conditions, in particular for a comparable evolution of the wetted surface area, this qualitative analysis is reasonable to estimate the dependence of the nucleation rate on the varied conditions by a comparison of the respective drop freezing rates; similar to the case of experiments with liquid drops at rest. In the present study of drop impact onto a sandblasted glass surface, no drop receding has been observed and the time of drop spreading is negligibly small compared to the observed freezing delays, justifying estimation of the influences on nucleation by a comparison of drop freezing rates.

However, in general the wetted surface area significantly varies during drop impact, and is moreover affected by a variation of the impact conditions, as shown in Sec. 3. In this case, comparison of the drop freezing rates does not allow estimation of the influences on the nucleation rate, since in addition to the nucleation rate also the variation of the wetted surface area affects the drop freezing rate. In these cases, the temporal evolution of the wetted surface area has to be accounted for during the analysis of influences on nucleation. In the following, a statistical model accounting for both a varying wetted surface area, and a variation of the nucleation rate during the impact process is derived. It enables calculation of the cumulative number of active nucleation sites per unit surface area, and is used for a generic analysis of the experimental results for isothermal drop impact presented in Sec. 4.2.1.1.

4.3.1 Statistical modeling

As thoroughly described in Sec. 2.2 and shown in the previous section, nucleation is a random process following certain statistics, which can be obtained by analysis of multiple experiments at the same operational conditions. However, to allow a distinct quantitative analysis of nucleation during drop impact, the special circumstances accompanying drop impact such as the variability of the wetted surface area and nucleation rate have to be accounted for in the analysis.

Denote $j_{\mathrm{tot}}(t)$ as an instantaneous total rate of nucleus formation per unit area of the wetted surface. It includes a constant rate associated with heterogeneous nucleation at the liquid-solid interface, j_{het}. In the case of drop impact, it furthermore includes a rate associated with the generation of gas bubbles and other transient effects during drop impact, j_{tr}, which is assumed as a rate of nucleus formation per unit area. The observed active nucleation sites in the impinging drops are distributed uniformly over the wetted area of the substrate; i.e. $j_{\mathrm{het}}(t)$ and $j_{\mathrm{tr}}(t)$ can be assumed to be independent of the exact position on the wetted substrate. This result is in agreement with earlier observations of heterogeneous nucleation, where no preference for nucleation at the contact line has been observed [136].

Since the nucleation rate does not depend on the position at the wetted surface, the average number of active nucleation sites on an element of the wetted surface area ΔA, which have accumulated until time t, is $\Delta\Lambda = \int_{t_{\mathrm{wet},\mathrm{d}A}}^{t} j_{\mathrm{tot}}\mathrm{d}t\,\Delta A$, where $t_{\mathrm{wet},\mathrm{d}A}$ is the instant when the given area element is wetted by the spreading drop the first time. Therefore, the total average number of active nucleation sites per drop, accumulated until time t, is obtained as

$$\Lambda(t) = \int_0^{A_{\mathrm{wet}}(t)} \left(\int_{t_{\mathrm{wet},\mathrm{d}A}}^{t} j_{\mathrm{tot}}(t)\,\mathrm{d}t \right) \mathrm{d}A, \tag{4.2}$$

where $A_{\mathrm{wet}}(t)$ is the surface area wetted at time t.

Let us now assume that potential nucleation sites at a given location on the substrate disappear during dewetting. Only the surface area, wetted at the instant of nucleation, controls the number of active nucleation sites accumulated until this time. This corresponds to the previous assumption of a nucleation rate which is indifferent to the exact position on the substrate. For long times after impact, $t \gg t_{\mathrm{wet},\mathrm{d}A}$, the time of drop spreading can be neglected in comparison to the total time until drop

nucleation. In this situation, the average number of accumulated active nucleation sites, Eq. 4.2, can be rewritten as

$$\Lambda(t) \approx A_{\mathrm{wet}}(t) \int_0^t j_{\mathrm{tot}} \mathrm{d}t. \tag{4.3}$$

The assumption of nucleation sites disappearing after dewetting may be incorrect for nucleation sites which are not directly associated with the substrate surface, such as gas bubbles or contaminants on the surface which can be collected by the receding liquid. However, in the present experiments a significant receding of the impinging drop is absent, justifying this assumption. Nevertheless, Eq. 4.3 may also give a good estimate for the case of drop impact, which is accompanied by a varying wetted surface area.

Since the process of nucleation is completely random, the statistics of the number of active nucleation sites follows a Poisson distribution [109], as shown in Sec. 2.2. This means that the probability that a single drop contains exactly N_{nu} active nucleation sites is

$$P(N_{\mathrm{nu}}; \Lambda) = \frac{\Lambda^{N_{\mathrm{nu}}} \exp(-\Lambda)}{N_{\mathrm{nu}}!}. \tag{4.4}$$

For a certain time t, the probability of the absence of active nucleation sites is $P(0; \Lambda) = \exp[-\Lambda]$. This probability can be obtained experimentally as the relative number of drops, remaining liquid until time t, thus

$$N_{\mathrm{l}}(t)/N_0 = \exp(-\Lambda(t)). \tag{4.5}$$

Combining Eqs. 4.3 and 4.5 yields a relation between the experimentally observed decay of a drop ensemble, $N_{\mathrm{l}}(t)/N_0$, the experimentally observed evolution of the wetted surface area, $A_{\mathrm{wet}}(t)$, and the average cumulative number of active nucleation sites per unit surface area, λ(t), as

$$\frac{1}{A_{\mathrm{wet}}(t)} \ln\left[\frac{N_0}{N_{\mathrm{l}}(t)}\right] = \lambda(t), \tag{4.6}$$

$$\lambda(t) \equiv \int_0^t j_{\mathrm{tot}} \mathrm{d}t, \tag{4.7}$$

valid for times much longer than the time of drop spreading, $t \gg t_{\mathrm{spreading}}$.

Calculation of the parameter $\lambda(t)$ from experimental results allows a distinct quantitative analysis of nucleation during drop impact with consideration of the time dependence of both the wetted surface area, and the total nucleation rate. By this it enables comparison of results from experiments involving significantly varying impact conditions.

4.3.2 Generic analysis of nucleation during isothermal drop impact

To demonstrate the capability of the theoretical approach, the proposed model is applied for a generic analysis of the experimental results for nucleation during isothermal drop impact. The evolution of $\lambda(t)$ for the results of isothermal drop impact with varying initial temperature, calculated using Eq. 4.6, are shown in Fig. 4.13. As already explained in the previous section, deviations of the shown data from a smooth evolution are very unlikely to be physical, and are rather attributed to small variations and uncertainties of the experimental conditions. However, in all cases a time-dependent nucleation rate, i.e. a transient rate of increase of λ can be observed, as already indicated in Fig. 4.4. The rate of change of λ is relatively high during the first 35 ms after drop impact and decreases for longer times. In contrast to the qualitative analysis in the previous section, the presented quantitative results allow further analysis, in particular with respect to the time dependence of nucleation induced by air bubbles and other transient effects on nucleation.

For a constant rate of heterogeneous nucleation at the wetted surface, the total number of active nucleation sites per unit surface area, λ, can be decomposed into a part attributed to the rate of heterogeneous nucleus formation at the substrate surface, λ_{het}, and a part attributed to a rate of nucleus formation due to entrapped air bubbles and other transient effects, λ_{tr}. While the rate of nucleus formation per unit area of the substrate surface mainly is a function of temperature, $j_{\mathrm{het}}(T)$ (see Eq. 2.35), the rate of nucleus formation due to transient effects furthermore depends on time, $j_{\mathrm{tr}}(T,t)$. The number of active nucleation sites due to air bubbles is assumed proportional to the number of air bubbles generated during drop impact. Moreover, the number of air bubbles generated during drop impact can be assumed proportional to the wetted surface area. Therefore, similar to the heterogeneous nucleation rate, also the nucleation rate associated with the existence of air bubbles can be expressed as an area specific quantity with units of $\mathrm{m^{-2}s^{-1}}$. Since nothing is known about

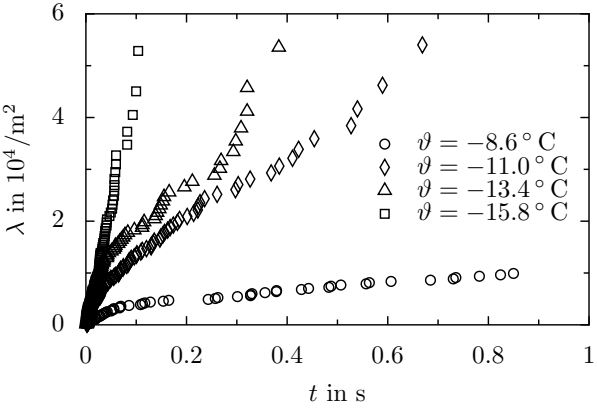

Figure 4.13: Average cumulative number of active nucleation sites per unit area as a function of time for isothermal drop impact with varying temperature. The drop diameter is $d_\mathrm{d} = 3.2\,\mathrm{mm}$ and the impact velocity is $v_\mathrm{d} = 2.2\,\mathrm{m/s}$. (Reprinted figure (adapted) with permission from [320]. Copyright 2016 by the American Physical Society.)

further transient effects in nucleation, also these effects are assumed to be related to the wetted surface area and thus, Eq. 4.7 can be rewritten as

$$\begin{aligned} \lambda = &\quad \lambda_\mathrm{het} \quad + \quad \lambda_\mathrm{tr} \\ = &\; j_\mathrm{het}(T)t \; + \; \int_0^t j_\mathrm{tr}(t,T)\mathrm{d}t. \end{aligned} \tag{4.8}$$

As shown in the previous section, mechanisms accompanying drop impact, which may be influential for nucleation are negligible at long times after impact. In particular after the time of bubble dissolution $t > t_\mathrm{life}$, an influence of gas bubbles on the nucleation rate can be neglected. Therefore, the experimental results of λ for later times may serve for estimating the heterogeneous nucleation rate at the substrate surface from the rate of increase of λ. As shown in Fig. 4.4, the rate of decrease of the relative number of liquid drops for $\vartheta = -8.6\,^\circ\mathrm{C}$ tends to zero for long times after impact. Therefore, also j_het vanishes for long times after impact, and is assumed as zero in the following. In the previous section, the time for dissolving of the gas bubbles has been estimated as $t_\mathrm{life} \approx 50\,\mathrm{ms}$. However,

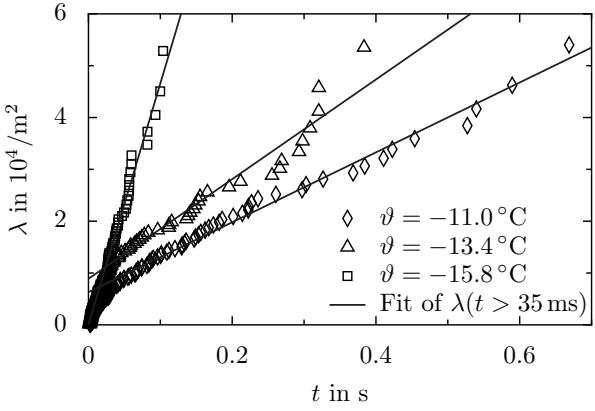

Figure 4.14: Linear fits describing $\lambda(t > 35\,\mathrm{ms})$ during isothermal drop impact for $\vartheta < -8.6\,^{\circ}\mathrm{C}$, where the slope represents j_{het}.

a significant change of the experimental data can be already observed at $t \approx 35\,\mathrm{ms}$, as shown in Fig. 4.13. Therefore, the time during which transient effects have a significant influence on nucleation is assumed as $t_{\mathrm{tr}} < 35\,\mathrm{ms}$ in the following. By this, the heterogeneous nucleation rates for $\vartheta < -8.6\,^{\circ}\mathrm{C}$ can be obtained as the rate of increase of λ for times $t > t_{\mathrm{tr}}$.

A least-squares fit of these data results in linear relations for λ, as shown in Fig. 4.14 in comparison to the experimental data. In particular the data for $\vartheta = -11.0\,^{\circ}\mathrm{C}$ and $\vartheta = -15.8\,^{\circ}\mathrm{C}$ are well described by a linear relation. The uneven evolution of the data for $\vartheta = -13.4\,^{\circ}\mathrm{C}$ causes a larger deviation from a linear increase of λ. However, also in this case, the trend of the data is well described by a linear relation, indicating that the previous procedure is reasonable for the estimation of the rate of heterogeneous nucleation on the substrate surface from the rate of increase of λ for $t > t_{\mathrm{tr}}$.

The obtained nucleation rates, i.e. the rates of increase of λ, as a function of supercooling are shown in Fig. 4.15. Note that the nucleation rates for $\vartheta = 0.0\,^{\circ}\mathrm{C}$, $\vartheta = -6.2\,^{\circ}\mathrm{C}$ and $\vartheta = -8.6\,^{\circ}\mathrm{C}$ can be reasonably assumed zero, and are also shown in the figure. Error bars in the figure correspond to the estimation of the 95 % confidence interval for the evolution of $N_{\mathrm{l}}(t)/N_0$, which results in the lower and upper bounds for

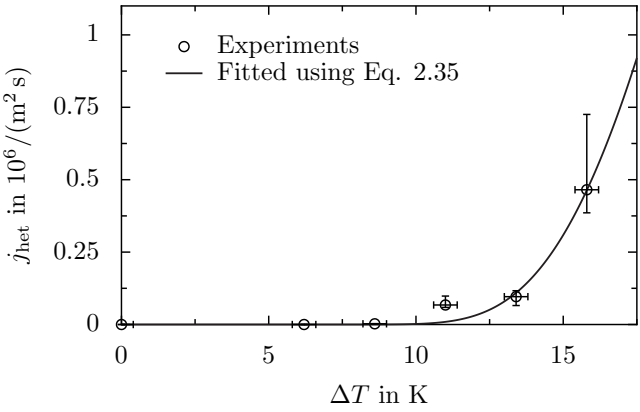

Figure 4.15: Heterogeneous nucleation rates long times after isothermal drop impact, obtained from linear fits to the experimental data $\lambda(t > 35\,\mathrm{ms})$ for $\vartheta < -8.6\,^{\circ}\mathrm{C}$. The solid line represents a least-squares fit of Eq. 2.35 to the obtained data.

the probability of nucleation until a certain time, $P_{\mathrm{l,low}}$ and $P_{\mathrm{l,up}}$, respectively. The upper and lower bound for the calculated nucleation rates, shown in Fig. 4.15, are obtained by fitting the upper and lower limits of λ, which are calculated with Eq. 4.6 using $P_{\mathrm{l,low}}$ and $P_{\mathrm{l,up}}$, respectively. Corresponding to the experimental method (see Sec. 3.1.1) and the estimation of the drop warming during its fall (see App. A), the error accompanying the temperature measurement is estimated as $\pm 0.4\,\mathrm{K}$. In addition to the experimentally obtained data, the dependence of the heterogeneous nucleation rate on supercooling, obtained from classical nucleation theory (see Eq. 2.35) is also shown in the figure. The involved constant $f_1 C_1 = 1.86 \times 10^7\,1/(\mathrm{m}^2\mathrm{s})$ and the shape factor of $\mathrm{S}(\Theta) = 0.0081$ corresponding to $\Theta \approx 22.3°$, have been obtained by a least squares fit of Eq. 2.35 to the calculated nucleation rates. As shown in the figure, the dependence of the nucleation rate on liquid supercooling is well described by Eq. 2.35, indicating that nucleation at long times after impact indeed may be described by means of classical nucleation theory for heterogeneous nucleation, as introduced in Sec. 2.2.

Using the obtained heterogeneous nucleation rates, $j_{\mathrm{het}}(T)$, the cumulative number of active nucleation sites per surface area, attributed to transient nucleation during drop impact, can be estimated from Eq. 4.8

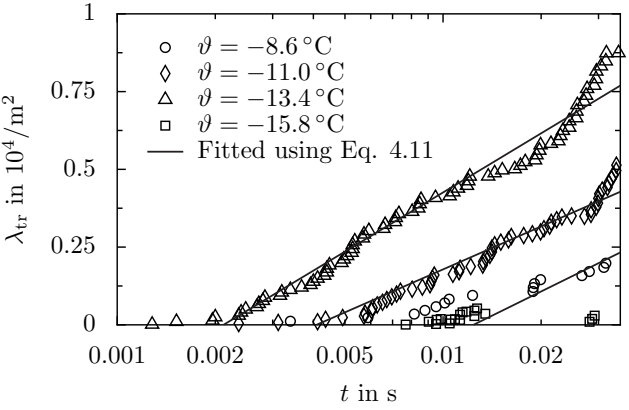

Figure 4.16: Evolution of the number of active nucleation sites per unit surface area, attributed to transient nucleation, obtained from the experimental data for λ using Eq. 4.9 and calculated values of j_{het}. Solid lines represent fit functions in the form $\lambda_{tr}(t) = c_1 \ln(t/s) + c_2$. Note the logarithmic scaling of the abscissa.

as

$$\lambda_{tr}(T,t) = \lambda(T,t) - j_{het}(T)\,t. \tag{4.9}$$

The obtained temporal evolution of λ_{tr} for varying temperature is shown in Fig. 4.16 for $t < t_{life}$; note the logarithmic scaling of the abscissa. The qualitative analysis in the previous section indicated a decreasing influence of transient effects for decreasing temperature: the drop freezing rate for $\vartheta = -8.6\,°C$ drastically varies over time, while it is almost unaffected by drop impact for $\vartheta = -15.8\,°C$. The invariance of the nucleation rate against mechanisms associated with drop impact at $\vartheta = -15.8\,°C$ can also be seen in Fig. 4.16. For that temperature, λ_{tr} does not increase with time, and rather fluctuates around zero (negative values of λ_{tr} exist, but are not shown in the figure since they are not physical). This implies that drop impact does not affect nucleation at $\vartheta = -15.8\,°C$, which is dominated by heterogeneous nucleation, only controlled by temperature; thus $j_{tr} \approx 0$. However, the data for the remaining temperatures reveals a dependence of nucleation on the mechanisms associated with drop impact.

As shown in Fig. 4.16, the curves for λ_{tr} at $\vartheta > -15.8\,°C$ are almost

Table 4.3: Coefficients in Eq. 4.12, describing the temporal evolution of the cumulative number of active nucleation sites during isothermal drop impact, attributed to heterogeneous nucleation at the substrate surface and transient nucleation due to the mechanisms associated with drop impact.

ϑ in °C	j_{het} in $1/(\mathrm{m}^2\ \mathrm{s})$	c_1 in $1/(\mathrm{m}^2)$	c_2 in $1/(\mathrm{m}^2)$
−8.6	0	2.24×10^3	9.85×10^3
−11.0	6.74×10^4	2.00×10^3	10.96×10^3
−13.4	9.61×10^4	2.74×10^3	16.89×10^3
−15.8	46.53×10^4	0	0

parallel, meaning that at a certain time t after impact, the rate of increase of λ_{tr} is almost unaffected by the liquid temperature; it only insignificantly increases for decreasing temperature. This implies that transient nucleation during and after drop impact is mainly controlled by the specific mechanisms during the process, and only weakly affected by temperature. However, the time until formation of a significant number of nucleation sites depends on temperature; it decreases with decreasing temperature.

The temporal evolution of λ_{tr} is well described by a relation in the form

$$\lambda_{\mathrm{tr}}(t) = c_1\ \ln(t/\mathrm{s}) + c_2, \tag{4.10}$$

where the parameters c_1 and c_2 for $\vartheta = -11.0\,^{\circ}\mathrm{C}$ and $\vartheta = -13.4\,^{\circ}\mathrm{C}$ have been obtained by fitting the relation to the experimental data $\lambda_{\mathrm{tr}}(t < t_{life})$. For $\vartheta = -8.6\,^{\circ}\mathrm{C}$, the relation has been fitted in the range $t < 7\,\mathrm{s}$, which corresponds to the fact that the nucleation rate for this temperature continuously changes over almost the entire observation time of 7 s. The obtained relations of Eq. 4.10 for varying temperature are shown in comparison to the calculated values of λ_{tr} in Fig. 4.16. Based on the relation for λ_{tr}, the transient rate of nucleus formation is obtained in the form

$$j_{\mathrm{tr}}(t, T) = \frac{c_1}{t}. \tag{4.11}$$

Using the previously found values for j_{het} and the relation for the transient contribution to the number of active nucleation sites according to

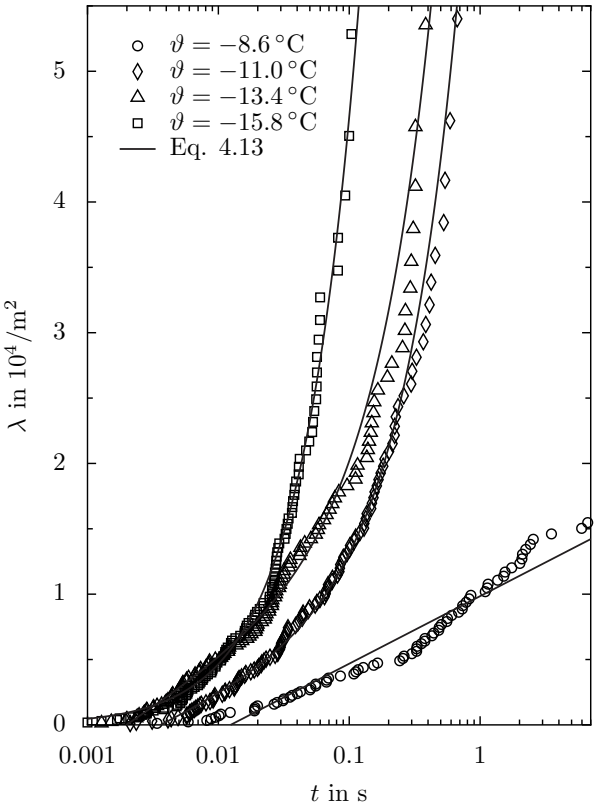

Figure 4.17: Evolution of the total number of active nucleation sites per unit surface area, obtained from the present experimental data (symbols), and described using Eq. 4.12 (solid lines) accounting for heterogeneous nucleation at the substrate surface, and transient nucleation due to mechanisms associated with drop impact.

Eq. 4.10, the evolution of the total number of active nucleation sites can be expressed as

$$\lambda = j_{\mathrm{het}}\, t + c_1 \ln(t/\mathrm{s}) + c_2. \tag{4.12}$$

The coefficients j_{het}, c_1 and c_2 are summarized in Tab. 4.3 for the different temperatures.

Figure 4.17 shows the experimentally obtained temporal evolution of λ in comparison to the values calculated using Eq. 4.12 and the coefficients shown in Tab. 4.3. It is worth to note that the coefficients summarized in Tab. 4.3 are the parameters which have been obtained by fitting the data after decomposition according to Eq. 4.8. As shown in the figure, the experimental data are well described for the entire observation time, indicating that the total nucleation rate during drop impact and the resulting number of active nucleation sites can indeed be expressed as the sum of a constant nucleation rate attributed to heterogeneous nucleus formation at the substrate surface, and a transient part attributed to the specific mechanisms associated with drop impact. The transient part of nucleus formation is only relevant for higher temperatures. At lower temperatures, nucleus formation is mainly controlled by heterogeneous nucleation at the substrate surface, which is only determined by temperature.

4.3.3 Conclusion

Based on the description of nucleation as a Poisson process, a statistical model has been derived to enable quantitative analysis of nucleation during drop impact. The model accounts for the temporal change of the surface area wetted during drop impact, and is furthermore applicable for the case of a non-constant nucleation rate which has been observed in the experiments of the present study. The model enables calculation of the cumulative number of active nucleation sites per unit area of the wetted surface. In comparison to the drop freezing rate, the area specific number of active nucleation sites can be considered as a quantity which allows examination of nucleation for varying impact conditions. The calculated data can be used as the basis for a detailed further analysis of nucleation during drop impact, as carried out for the analysis of the experimental results concerning isothermal drop impact.

It has been shown that the number of active nucleation sites generated during and after drop impact can be decomposed into a part attributed to heterogeneous nucleation at the substrate surface, and a part attributed to nucleation induced by transient effects on nucleation which accompany drop impact. Heterogeneous nucleation is only dependent on temperature and the ability of the surface for promoting nucleation; it is associated with a constant rate of nucleus formation. The transient part of nucleation is furthermore time dependent due to continuous dissolving of air bubbles and the decay of other effects accompanying drop impact. Since

an influence of transient effects on the number of active nucleation sites can be neglected for large times after impact, these experimental data have been used to estimate the linear contribution of heterogeneous nucleation at the substrate surface to the total number of active nucleation sites. The obtained nucleation rates show a temperature dependence which is well described by classical nucleation theory.

Subtraction of the number of active nucleation sites attributed to heterogeneous nucleation from the total number of active sites enabled analysis of the transient rate of nucleus formation due to the mechanisms accompanying drop impact. As already indicated in the previous section, it now has been shown quantitatively that heterogeneous nucleation is the dominating mechanism for the lowest examined temperature, where further effects only play a minor role. For this temperature an almost linear increase of the number of active nucleation sites has been observed, indicating a constant nucleation rate for all times. For the remaining temperatures, a transient nucleation rate due to drop impact has been found. Temperature controls the time until formation of a significant number of active nucleation sites due to transient nucleation. However, after that time temperature only plays a minor role for transient nucleation. The rate of increase of the number of active sites then mainly depends on time; i.e. at a certain time after impact, the transient rate of nucleus formation is constant for all temperatures. This indicates that the transient part of nucleus formation is predominated by the specific mechanisms accompanying drop impact, which do not significantly vary for varying temperature.

The time dependence of the transient nucleation rate is well described by a hyperbolic relation, resulting in a logarithmic relation for the evolution of the number of active nucleation sites attributed to transient nucleation. Combination of the relations found for the number of active nucleation sites, attributed to heterogeneous and transient nucleation, showed very good agreement with the experimentally obtained data. These relations are not of predictive nature and are obtained by fitting of the experimental data. However, they strongly indicate the reasonableness of the decomposition into a heterogeneous nucleation rate only depending on temperature, and a transient nucleation rate which furthermore depends on time. The chosen ansatz function for the description of transient nucleation does not contain any physical meaning. Further experimental work followed by a detailed mathematical modeling is necessary to describe transient nucleation by means of a detailed physical model.

The exact reason for enhanced nucleation due to transient effects associated with drop impact is not completely clear. However, the previous analysis indicates that gas bubbles entrapped during spreading are an important influence on the transient nucleation behavior. Nevertheless, a definite identification of the involved and dominating mechanisms deserves further experiments with a varying surface morphology and impact conditions. The theoretical modeling and the subsequent procedure of analysis, demonstrated in the present section, may serve as a substantial building block for a detailed examination of future experiments aiming at the identification, and in particular the quantification of the distinct mechanisms.

Parts of the work presented in the following chapter are based on the Master-Thesis of Silvia Iannella [158], and have already been published and presented in the following publications and conference contributions:

[314] M. Schremb, J. Campbell, H. Christenson and C. Tropea. Ice layer spreading along a solid substrate during the freezing of supercooled water: Experiments and modeling. *Langmuir*, 33(19):4870-4877, 2017.

[321] M. Schremb and C. Tropea. Solidification of supercooled water in the vicinity of a solid wall. *Physical Review E*, 94(5):052804, 2016.

[358] C. Tropea, M. Schremb and I. Roisman. Physics of SLD impact and solidification. In *Proceedings of the 7th European Conference for Aeronautics and Aerospace Sciences*, Milan, Italy, 2017.

5 Solidification of supercooled sessile water drops

The present chapter is devoted to the solidification of supercooled water, which is experimentally examined and theoretically modeled. Following drop impact and nucleation, which have been examined in the previous sections, liquid solidification is the third major process involved in ice accretion. The freezing velocity of the impinging liquid determines the time-scale of drop freezing, and hence it controls the time available for processes such as drop rebound and flow-induced shedding of water from the surface, after nucleation has initiated freezing. Therefore, solidification of the impinging liquid is an important mechanism in the context of icing of surfaces due to supercooled water drops. In particular the substrate's influence on the freezing velocity of supercooled water drops in contact with a wall is not completely clear, and therefore deserves further examination.

Distinct examination of solidification during drop impact is complicated, or even impossible. Also investigation of the solidification of sessile water drops involves some difficulties such as optical distortions at the curved liquid-gas interface, preventing a detailed analysis of the process. Therefore, the solidification process of supercooled sessile water drops is

studied using a novel experimental approach. Utilizing a Hele-Shaw cell to entrap the supercooled water drops, the experimental facility overcomes optical distortions present due to reflections and refraction of light on the drop surface when observing the freezing of sessile drops. A Hele-Shaw cell has been previously used to examine solidification of sessile water drops without initial supercooling [99, 221]. However, to the author's knowledge the present study is the first in which a Hele-Shaw cell is employed for the examination of freezing of supercooled water drops.

In the following, first the experimental approach is described. In comparison to other approaches, it allows a more detailed examination of the different processes during freezing of a supercooled sessile drop. This justifies a phenomenological description of the entire process comprising the fast evolution of a thin initial ice layer along the substrate surface, dendritic freezing of the supercooled bulk liquid, and planar freezing of the remaining liquid at the melting temperature. These processes observed using the present experimental approach are qualitatively compared to results obtained from the observation of freezing of a free sessile drop. It is qualitatively and quantitatively demonstrated that the freezing behavior is unaffected by the use of the Hele-Shaw cell. Experiments are performed for varying substrate materials and the thermal influence of the substrate on the phase of ice layer spreading is examined. Based on the experimental results, and by employing the analytical solution of the two-phase Stefan problem, a semi-empirical model for the prediction of the ice layer velocity depending on the initial liquid supercooling and the thermal properties of the substrate is derived. Finally, the freezing front velocity measured during dendritic freezing of the bulk liquid is compared to experimental and theoretical results for the tip velocity of a single dendrite growing in supercooled water.

5.1 Experimental method

The experimental facility consists of a cooling system, a vertically oriented Hele-Shaw cell and an observation system; it is schematically shown in Fig. 5.1. A cooling plate (*Fryka, KP281*) capable of maintaining a specified temperature by an external chiller is used for the experiments. It allows plate temperatures down to $\vartheta = -30\,^{\circ}\mathrm{C}$, and is included into the setup being the bottom of a closed styrofoam chamber. To prevent the build-up of frost and condensate on the cold surfaces, the environment within the chamber is kept dry using gaseous nitrogen. Double glassed

side windows provide optical access to the styrofoam chamber.

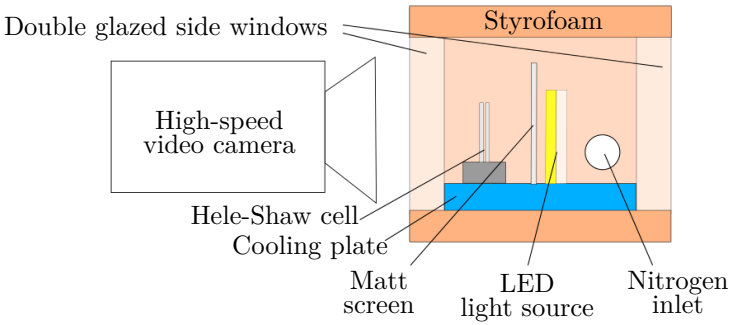

Figure 5.1: Schematic side view of the experimental setup used for the freezing experiments utilizing a Hele-Shaw cell.

The Hele-Shaw cell with an inserted drop is shown in Fig. 5.2. It consists of two sheets of acrylic glass (PMMA), and a spacer at the base, which is made of a variable smoothed material. The spacer maintains a constant distance of 1 mm between the side walls, and furthermore serves as the substrate on which the drop is at rest. The combination of the side walls and the substrate strip are stacked and fixed by screws within an aluminum base. A drop of purified de-ionized water (*Millipore, Milli-Q® Type 1*, electrical conductivity $\gamma_{el} = 5.5 \times 10^{-6}$ S/m at 25 °C) is trapped between the side walls and is in direct contact with the spacer material as depicted in the figure.

A thermocouple with a diameter of 0.5 mm (*ES Electronic Sensor, IKT 05/10*) is immersed into the spacer substrate of the Hele-Shaw cell. During the study of the front velocity of the dendrite cloud, the temperature has been measured in the spacer at a distance of approx. 0.5 mm below the spacer surface. Only copper has been used as the substrate for these experiments. For high thermal conductivity materials like copper, the temperature gradient in the substrate region between the drop and the thermocouple tip is negligible and the drop's base can be assumed to be at the temperature measured in the substrate. The substrate material has been varied during the study of the velocity of the initial ice layer, eventually resulting in a significant temperature gradient in the substrate.

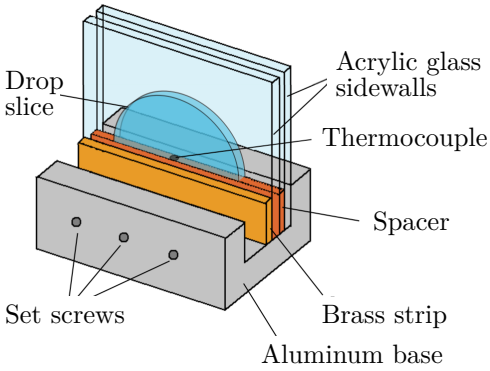

Figure 5.2: Schematic of the Hele-Shaw cell including an entrapped drop. (Reprinted with permission from [314]. Copyright 2017 American Chemical Society.)

Therefore, for these experiments, the temperature measurement has been improved such that the thermocouple does not end in the spacer, but at its surface, as shown in Fig. 5.3. By this, the liquid temperature is measured at the bottom of the drop and the measurement is unaffected by thermal conduction in the spacer.

Nucleation only sometimes occurs at the thermocouple. In the other cases, it occurs at a random position of the wetted substrate and is not preferential at any position. Thus, no significant influence of the thermocouple on the nucleation process has been observed. Anyway, nucleation is not the subject of the present study and therefore, any influence of the thermocouple on the measurements can be neglected. In very few cases, nucleation occurred at the sidewalls of the Hele-Shaw cell. Although the freezing process at the substrate is unaffected by nucleation at the sidewalls and proceeds similar to the process after nucleation at the substrate surface, these experiments have not been used for the analysis in the present study.

The freezing process is observed in a side view using a high-speed video camera (*Photron, Fastcam MC2.1*), operated at a frame rate of 2000 fps with a resolution of 512 px × 256 px. The process is captured with a spatial resolution of approx. 13 µm/pixel. With an illuminated matt screen behind the Hele-Shaw cell, the freezing process is captured using

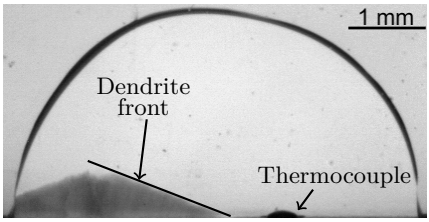

Figure 5.3: Two dimensional side view of dendritic solidification of a water drop at approx. $\vartheta_\mathrm{d} \approx -15\,^\circ\mathrm{C}$ entrapped in the Hele-Shaw cell. The drop temperature is measured with a thermocouple ending at the bottom of the drop. The front velocity of the dendrite cloud is measured in its normal direction. In the case that the initial ice layer is not clearly visible in the high-speed videos, the movement of the intersection point of the substrate and the dendrite front are assumed representative for the ice layer propagation. (Reprinted (adapted) with permission from [314]. Copyright 2017 American Chemical Society.)

backlight shadowgraphy imaging.

At the beginning of an experiment, a drop at room temperature is placed into the Hele-Shaw cell, which is subsequently placed onto the cooling plate precooled to $0\,^\circ\mathrm{C}$. Then the cooling plate and the Hele-Shaw cell containing the water drop are simultaneously cooled down at a moderate maximum cooling rate of approx. $0.2\,\mathrm{K/s}$. For large supercooling, freezing automatically starts due to heterogeneous nucleation at the liquid-substrate interface. To allow observation of the freezing process also for smaller supercooling, in these cases solidification is triggered with a seed crystal of frost, brought into contact with the supercooled drop near the water-air-substrate contact line by means of a thin piece of acrylic glass inserted into the Hele-Shaw cell.

Solidification of the liquid results in a fast warming-up of the drop, as described in Sec. 2.3. Therefore, the drop supercooling at the moment of freezing is obtained from the lowest measured temperature value before the sudden temperature increase. The response time of the thermocouple to detect 90 % of an instantaneous temperature change is approx. 0.13 s. Due to the moderate cooling rate in the experiments, this time is associated with a negligible inaccuracy of the determination of super-

cooling attributed to the thermal inertia of the thermocouple of approx. 0.026 K. The liquid supercooling in the present experiments ranges from $\Delta T \approx 1.4\,\mathrm{K}$ to $\Delta T \approx 20.0\,\mathrm{K}$.

Due to continuous liquid cooling during the experiments, a temperature gradient may be present in the drop at the moment of nucleation. It would be associated with a variation of the solidification velocity depending on the normal distance to the substrate surface. The thickness of the initial ice layer, growing prior to dendritic solidification, is very small, $h_{\mathrm{lay}} \sim 10^{-5}\,\mathrm{m}$ [181], and thus an influence of a temperature gradient on the examination of the ice layer growth is negligible. To also minimize its influence on the correlation between the measured liquid temperature and the measured velocities during dendritic growth, the associated velocity measurements are performed in a distance smaller than approx. 250 µm above the substrate surface.

Drops of varying volumes ranging between $V_{\mathrm{d}} \approx 1.5\,\mu\mathrm{l}$ and $V_{\mathrm{d}} \approx 10\,\mu\mathrm{l}$, and diameters between $d_{\mathrm{d}} \approx 2\,\mathrm{mm}$ and $d_{\mathrm{d}} \approx 5\,\mathrm{mm}$, have been used for the experiments and no significant correlation has been observed between the drop size and the freezing process.

5.2 Phenomenological description

As described in Sec. 2.3, several processes involving different physical mechanisms, time scales and length scales take place during the solidification of a supercooled sessile drop. The entire process is highly complex and therefore it is convenient to split it up and describe the different processes separately.

Solidification of supercooled water in the vicinity of a solid wall comprises three consecutive phases, as shown in Fig. 5.4. The two phases of dendritic (I.) and planar (II.) solidification of a supercooled liquid are well known, as already described in Sec. 2.3. These phases are commonly referred to as the *"first phase"* and *"second phase"* of solidification of supercooled water. However, it is worth to note that this designation is not applicable for the case of freezing of supercooled water in contact with a wall, since a thin initial ice layer forms along the wall prior to dendritic freezing (I.*), as already observed in [181]. All three phases involved in the freezing of a supercooled liquid in contact with a wall are known. However, the present experimental approach allows a more detailed examination of the different processes in comparison to previous

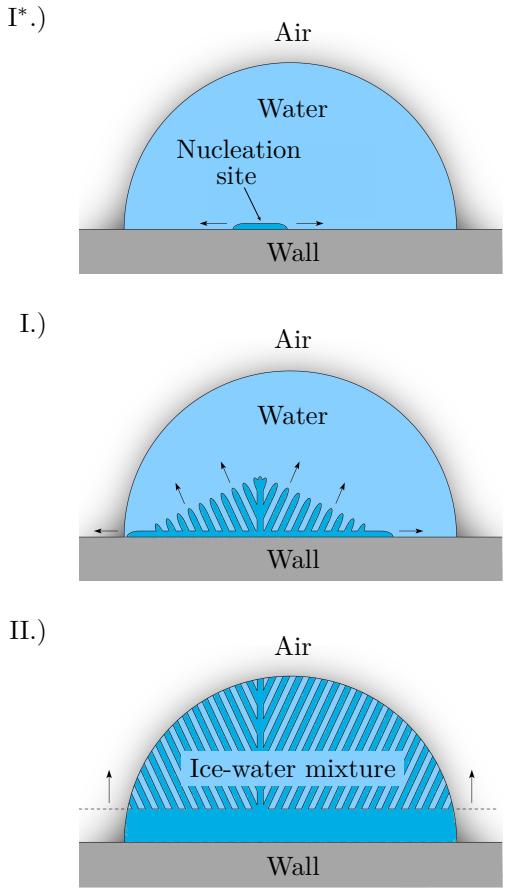

Figure 5.4: The three phases of solidification of a supercooled drop with wall contact: I*.) Heterogeneous nucleation followed by spreading of a thin ice layer at the substrate; I.) Dendritic freezing of the bulk liquid; II.) Isothermal freezing of the remaining water at T_m. Note that the position of the nucleation site in I*., and the orientation of the dendrites in I. and II. are only schematic. (Reprinted (adapted) with permission from [314]. Copyright 2017 American Chemical Society.)

experimental approaches. Therefore, the different phases of solidification captured using the present facility are worth describing again. The observations are compared to the observations of the freezing process in a free sessile water drop, serving for a qualitative estimation of the influence of the Hele-Shaw cell on the freezing process. Since the common designation "first" and "second" phase of solidification may be misleading in the context of the present investigations, in the following they are referred to as the dendritic and planar freezing phase, respectively.

5.2.1 Initial ice layer spreading

Heterogeneous nucleation starts at an arbitrary point of the solid substrate, and is followed by the tangential growth of a thin ice layer spreading over the substrate surface. The spreading ice layer has been observed in [181] for water supercooling down to $\Delta T \approx 7.0\,\mathrm{K}$, revealing that the ice layer grows with a constant tangential speed, which depends on both the liquid temperature and the thermal properties of the wall. Compared to this previous study, the supercooling range in the present work is significantly extended up to $\Delta T \approx 20.0\,\mathrm{K}$.

In the case of a free sessile drop, refraction and reflection at the curved interfaces of the drop significantly affect the observation of the process which takes place in a thin region at the substrate. In [181], the supercooled water has been encapsulated into a transparent box-shaped container. This enabled undisturbed observation of the ice layer spreading in a side view and a top view, since the planar interfaces between the liquid and the container walls do not affect optical observation of the process. Similar to a box-shaped container, also the Hele-Shaw cell employed in the present study suppresses curved interfaces which would affect a side-view observation of the freezing process. Therefore, the initial ice layer can be clearly seen in the captured high-speed videos, as shown for example in the image sequence in Fig. 5.5. The ice layer can be identified as a bright strip propagating along the substrate surface prior to eventual dendritic freezing of the bulk liquid. Due to the aforementioned problems, the initial ice layer cannot be observed in the side view of a freezing sessile drop, as shown in the right column of Fig. 5.6. Therefore, no images of this process are shown for comparison in Fig. 5.5.

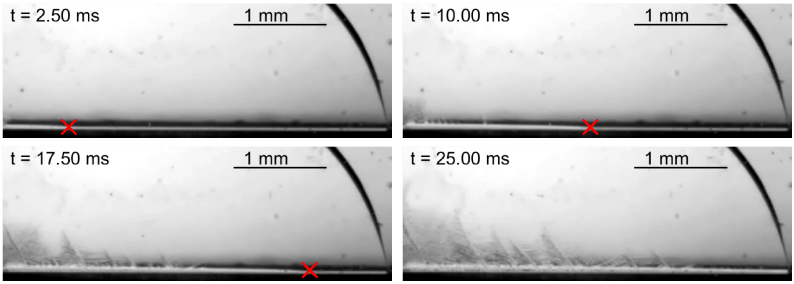

Figure 5.5: Initial ice layer growth along the substrate prior to dendritic solidification of a sessile water drop, supercooled to approx. $\vartheta_d \approx -8.8\,°C$. The ice layer evolves from the left to the right. Red crosses indicate the approximate position of the ice layer tip. At some distance behind the tip, the ice layer becomes unstable resulting in dendritic freezing of the bulk liquid.

5.2.2 Dendritic freezing

For a sufficiently low liquid temperature, the surface of the initial ice layer becomes unstable at a certain position behind the tip of the ice layer, as shown in Fig. 5.5. It results in rapid kinetic crystal growth of single dendrites or a front of numerous dendrites into the bulk liquid, as indicated in Fig. 5.4. The threshold of the initial liquid supercooling, above which unstable growth of the ice layer is observed, has been found as $\Delta T \approx 2.6\,K$ in [181]. For the range of relatively low supercooling up to $\Delta T \approx 7.0\,K$, examined in [181], only single dendrites and hexahedral shapes of ice crystals emerging from the initial ice layer on the substrate have been observed. In the present study, the process is observed for much higher liquid supercooling, and it has been found that there not only exists a transition between the cases of purely planar and dendritic ice growth into the bulk, but also several transitions between different modes of dendritic growth. The number and density of arising dendrites increases with decreasing temperature. Only few single dendrites are observed for higher temperatures, while a cloud of dendrites propagates through the liquid, as shown in Fig. 5.6 for a supercooled water drop at $\vartheta_l \approx -15.8\,°C$. A classification of these modes depending on the liquid temperature will be given later.

Figure 5.6 shows the propagation of a dendrite cloud observed in the

Hele-Shaw cell in the left column, and the same process observed for a free sessile drop in the right column. The direct comparison indicates that the overall process is the same in both cases, differing only in its observability. In the case of the sessile drop, the curved drop interface causes reflections and refraction, resulting in low contrast between the different regions within the drop. In particular in the regions associated with a small angle between the liquid-air interface and the optical axis of the observation system, i.e. in the vicinity of the drop contour in the photographs, refraction prevents any optical access to the processes taking place in the liquid. Moreover, the exact location of nucleation and the direction of propagation of the dendrite cloud cannot be clearly determined from the high-speed videos, prohibiting distinct quantification of the freezing process. In contrast, by employing the Hele-Shaw cell, these optical distortions are suppressed, and the position of nucleation, the subsequent solidification process and the resulting phase distribution are clearly visible.

The initial ice layer growing prior to dendritic freezing cannot be identified in the images shown in Fig. 5.6, since the ice layer becomes unstable very close to its tip, preventing visibility of the ice layer. The arising instability of the initial ice layer is well comparable to the formation of side branches during the growth of a single dendrite. In this case, the distance between a dendrite tip and the first side branch is constant and only depends on temperature [334]. Therefore, it is reasonable to assume also the distance behind the ice layer tip and the position of the first instability as constant, only depending on temperature. As shown in Fig. 5.6, the dendrite cloud is confined by a smooth front, indicating that each of the dendrites grows with almost the same speed. Therefore, the tangential speed of the initial ice layer can be determined from the movement of the point where the line enveloping the dendrite cloud intersects with the substrate surface, as illustrated in Fig. 5.3.

The ice layer being the initiation of the dendrite cloud, grows with a constant horizontal speed. In combination with a constant distance between the ice layer tip and the first dendrite, and a constant speed of all dendrites, this results in the typical triangular shape of the dendrite cloud, as shown in Fig. 5.6. The angle between the dendrite front and the substrate surface only depends on the ratio between the velocities of the ice layer and the dendrite cloud. It decreases with an increasing ice layer speed, and a decreasing dendrite cloud velocity.

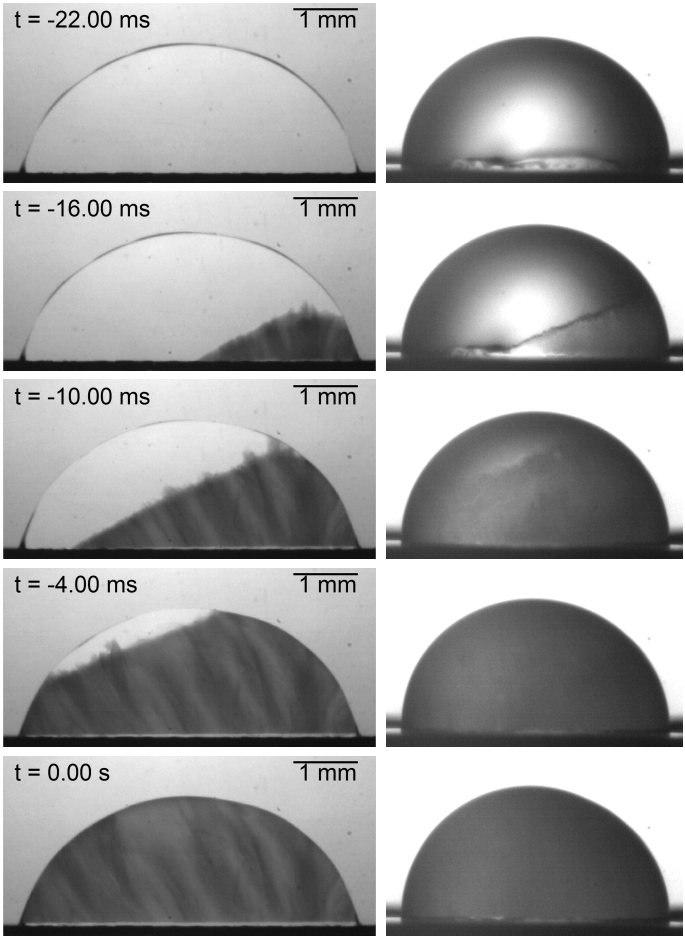

Figure 5.6: Dendritic solidification of a water drop, supercooled to $\vartheta_l \approx -15.8\,°\mathrm{C}$. The initial ice layer becomes unstable at a short distance behind the ice layer tip, leading to the propagation of a cloud of dendrites into the bulk liquid. Qualitative comparison of a drop in the Hele-Shaw cell (left) with a sessile drop (right). (Reprinted figure with permission from [321]. Copyright 2016 by the American Physical Society.)

For the examined drop sizes and liquid temperatures, the entire dendritic freezing takes a few tens of milliseconds. At the end, only a portion of the initially supercooled drop is frozen and a lattice of dendritic ice fills out the entire drop, as indicated in the last images of Figs. 5.4 and 5.6. The latent heat released during solidification has warmed up the water-ice mixture to the melting temperature. Therefore, despite the water-ice mixture in the vicinity of the freezing front of the phase of planar solidification, the remaining water-ice mixture is in a local thermodynamic equilibrium. As described in Sec. 2.3, the degree of liquid supercooling determines the portion γ_f of the liquid which is frozen after dendritic freezing. According to Eq. 2.78, the frozen fraction of the drop shown in Fig. 5.6 can be estimated as $\gamma_\mathrm{f} \approx 19\,\%$.

For temperatures above the threshold for unstable growth, only planar growth of the thin ice layer has been observed, and solidification of the entire liquid proceeds as planar freezing normal to the substrate surface, as described in the following.

5.2.3 Planar freezing

After the dendritic freezing phase, the liquid supercooling is exhausted, and the water-ice mixture, which is not yet affected by planar freezing, is in a local thermodynamic equilibrium at T_m. A further removal of heat results in continued planar freezing of the remaining liquid, which may be described as a one-phase Stefan problem [77]. Planar freezing already starts during the ongoing dendritic freezing of the liquid. It can be observed as the thin layer of changed brightness on the substrate surface in the last three photographs in the left column of Fig. 5.6. In the case of an initial liquid temperature above the threshold for unstable growth of the initial ice layer, dendritic growth is absent, and the liquid is still supercooled during planar freezing. Therefore, the water is not in thermodynamic equilibrium prior to planar freezing, and the freezing process may be described as a two-phase Stefan problem (see Sec. 2.3). However, in both cases, the freezing process is qualitatively the same, as described in the following.

The planar solidification phase of a sessile water drop is shown in Fig. 5.7, again as a comparison of the process observed in the Hele-Shaw cell (left column) and in a free sessile drop (right column). The growth direction at the beginning of planar solidification is normal to the substrate's surface, i.e. in the negative direction of the heat flux into the

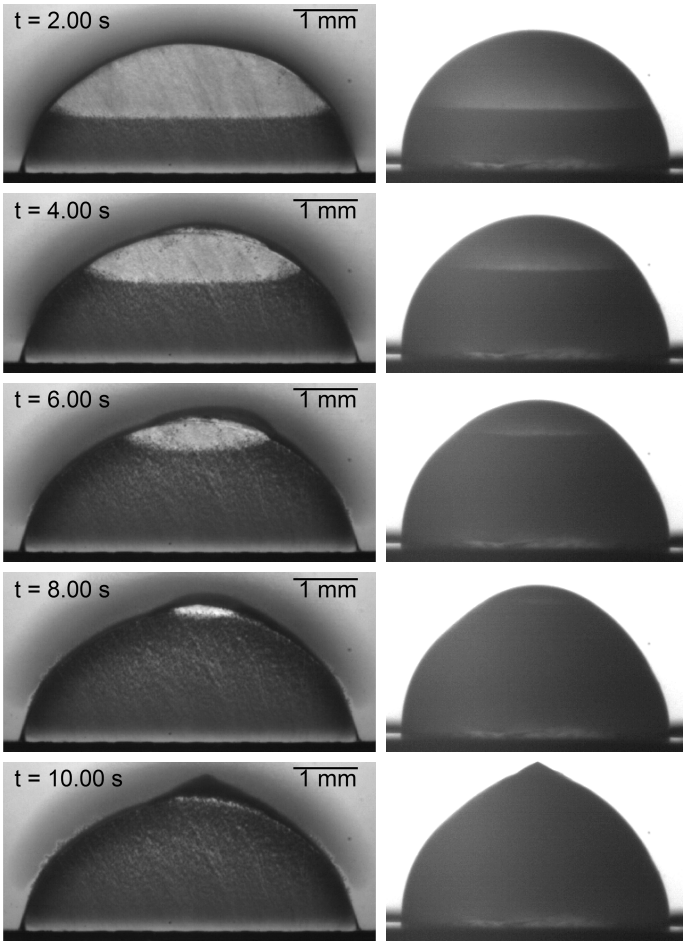

Figure 5.7: Qualitative comparison of the planar solidification after dendritic freezing of a drop entrapped in the Hele-Shaw cell (left), and a sessile drop (right). Both drops are the same as those already shown in Fig. 5.6. (Reprinted figure with permission from [321]. Copyright 2016 by the American Physical Society.)

cooled substrate. Generally, the freezing front in a sessile drop becomes curved due to a boundary constraint at the three phase contact line ice-

water-air [99, 221, 249, 250, 323], namely that the freezing front is perpendicuar to the liquid-gas interface. So far, this effect has been observed in sessile drops, freezing at T_m without any supercooling. As shown in Fig. 5.7, this condition also holds for a drop in which just the liquid remaining after dendritic freezing solidifies. The curved freezing front is difficult to observe in the case of the sessile drop. However, due to the improved optical access it can be clearly identified with the Hele-Shaw setup.

As shown in the figure, for both the sessile drop and the drop in the Hele-Shaw cell, the planar freezing phase results in a cusp shape on top of the frozen drop. This is due to the above-mentioned boundary constraint at the ice-water-air contact line, accompanied by the density decrease and volume expansion during freezing, which finally results in the observable shape. So far, this phenomenon has been explicitly reported and described only for the case of drop freezing without initial supercooling [221, 249, 250]. However, as seen from the present experiments, the same behavior can be observed during the planar freezing phase after dendritic freezing of a supercooled drop; also if the drop is entrapped in the Hele-Shaw cell. During the evolution of the cusp shape, the first qualitative difference between the freezing behavior of a sessile drop and that of a drop in the Hele-Shaw cell can be observed. Since the freezing process and all influential effects are axisymmetric in the case of the sessile drop, the cusp is formed in the middle on top of the drop. In the case of the drop in the Hele-Shaw cell, the cusp does not appear in the symmetry plane of the drop, which is due to additional forces acting between the liquid meniscus and the acrylic glass side walls. An uneven surface of the side walls can lead to local pinning of the contact line, resulting in a non-uniform contact line movement during volume expansion and may finally cause an asymmetric shape of the frozen drop, as observed in Fig. 5.7.

A further qualitative difference of the overall behavior within the Hele-Shaw cell compared to that of the sessile drop can be identified during the planar freezing phase. After dendritic solidification, the solid-liquid mixture is instantaneously at the melting temperature. Due to the low thermal conductivity of the acrylic glass side walls, they remain almost at the initial temperature of the drop after the rapid dendritic solidification is finished. As described in [173] for the freezing of sessile supercooled water drops, the fast recalescence of the drop during the first freezing phase causes the air around the drop to be supersaturated by moisture with respect to the initial drop temperature. Since the acrylic glass side

walls are thermally sluggish and warm up much slower than the dendritic freezing phase is finished, the air is supersaturated also with respect to the temperature of the acrylic glass side walls. This supersaturation leads to a condensation halo on the acrylic glass side walls, observable in the left column of Fig. 5.7 as a darker region around the drop. By continuous cooling of the substrate, the entirely frozen lower part of the drop is cooled down again, resulting in a decreasing supersaturation around the drop. As a consequence the condensation halo dissolves. As shown in the figure, evaporation of the condensate starts from the near-wall region, close to the coldest region of the frozen drop.

5.2.4 Conclusion

A new experimental approach for the investigation of the freezing process of sessile supercooled water drops has been introduced and applied for the phenomenological examination of the distinct freezing phases involved. By making use of a Hele-Shaw cell, into which a drop is inserted, this method allows observation of the process in a quasi two-dimensional manner, without optical distortions arising from the drop's free surface. Thereby, the visibility of the process in terms of contrast and optical distortions is significantly improved. Capturing of the freezing process with a high-speed video system allows accurate examination and description of the freezing phases.

The different freezing phases of a sessile supercooled drop observed in the Hele-Shaw cell have been qualitatively compared with the phases observed in a free sessile drop. It has been shown that the processes observed in the Hele-Shaw cell are generally equal to the processes in a free sessile drop. All known features involved in the freezing of a supercooled sessile drop, comprising the formation of a thin ice layer at the wall, followed by dendritic freezing of the bulk liquid, and the formation of a cusp shape after planar freezing are also observed during freezing of a drop entrapped in the Hele-Shaw. Thus, employing a Hele-Shaw cell for the examination of the freezing process of supercooled sessile drops does not affect the macroscopic appearance of the entire process. In comparison to a free sessile drop, the cusp formation after the planar freezing phase is not axisymmetric, due to capillary forces acting on the meniscus in the Hele-Show cell. Moreover, condensation forms on the side walls of the Hele-Shaw cell after dendritic solidification. However, no further influence of the Hele-Shaw cell on the freezing process can be observed from the high-speed

videos. The aforementioned differences do not affect any measurements in the near-wall region of the drop's bulk, which are the objective of the following quantitative examination. Therefore, the processes taking place in the Hele-Shaw cell can be assumed as a two-dimensional replica of the three-dimensional processes taking place in a free drop.

In the case of a free sessile drop, observation of the processes is significantly affected by reflection and refraction at the curved interfaces of the drop, partially prohibiting any optical access to the processes taking place in the near-wall region. The present experimental approach employing a Hele-Shaw cell overcomes these problems, and allows capturing of all involved mechanisms with a high contrast. When observing a free sessile drop, two-dimensional videos of the process do not contain any information about the processes eventually taking place perpendicular to the image plane, thus preventing accurate measurements of distances and velocities from the videos of a single camera. By means of the Hele-Shaw cell, the processes are reduced to two dimensions, allowing quantification of the distinct processes using the high-speed video of only one camera. Therefore, the present experimental approach is highly effective for the examination of the freezing process of sessile supercooled water drops. In the following, it is used for the examination of the influence of temperature and substrate properties on the characteristic freezing velocities during the ice layer propagation and the dendritic freezing phase.

5.3 Quantitative results

Acrylic glass is used for the side walls of the Hele-Shaw cell. Due to its low thermal conductivity, acrylic glass acts as an isolator for the entrapped liquid, minimizing thermal influences from the ambient on the freezing process. Similarly, influences of the side walls themselves on the freezing process are expected to be negligible. As shown by the comparison in the previous section, no qualitative influence of the Hele-Shaw cell on the freezing process of a sessile drop is observed. By a comparison of the typical length scales involved in the process, the significance of the influence of the side walls on the freezing process may be estimated as follows.

The typical thickness of the initial ice layer is $h_{\mathrm{lay}} \sim 10^{-5}\,\mathrm{m}$ [181], which is very thin compared to the typical length scale of the Hele-Shaw cell, which is $\sim 10^{-3}\,\mathrm{m}$. The diffusion length being the typical length scale of

the ice layer spreading is estimated as $\delta_T \sim a_l / v_{lay,x}$, where $v_{lay,x}$ denotes the horizontal velocity of the ice layer. For ice layer velocities which have been observed in the range $v_{lay,x} \approx 0.01 \ldots 0.4\,\mathrm{m/s}$ and the thermal diffusivity of water, $a_l \approx 10^{-7}\,\mathrm{m^2/s}$, the diffusion length is estimated as $\delta_T \sim 2.5 \times 10^{-7} \ldots 1 \times 10^{-5}\,\mathrm{m}$. Therefore, both the typical thickness of the ice layer and the typical length scale of the ice layer growth are much smaller than the typical length scale of the Hele-Shaw cell, and a thermal influence of the side walls on the growth of the initial ice layer can be neglected. For the experiments concerning the dendritic freezing of the bulk liquid involving front velocities of the dendrite cloud in the approximate range $v_{fro} \approx 0.02 \ldots 0.2\,\mathrm{m/s}$, the typical length scale of the solidification process is in the range $\delta_T \sim a_l / v_{fro} \approx 5 \times 10^{-7} \ldots 5 \times 10^{-6}\,\mathrm{m}$, which is also much smaller than the typical length scale of the Hele-Shaw cell. Therefore, an influence of the Hele-Shaw cell on the dendritic freezing process is also not expected. Nevertheless, the influence of the side walls on the freezing process is examined by a comparison of the front velocities of the expanding dendrite cloud measured for a copper substrate and a varying ambient temperature in the styrofoam chamber. By a variation of the ambient temperature, also the temperature of the side walls of the Hele-Shaw cell varies. If the side walls significantly affect the freezing process, a varying ambient temperature should result in altered freezing front velocities for a varying ambient temperature in the chamber.

The front velocity of the dendrite cloud is always measured normal to the straight envelope of the cloud, a small distance above the substrate surface. In the case of higher temperatures when no cloud of dendrites is observed, the tip velocity of the single dendrites is measured instead of the normal front velocity. Figure 5.8 shows the obtained front velocities for an ambient temperature in the styrofoam chamber varying between $\vartheta_{amb} \approx +3.8\,^\circ\mathrm{C}$ and $\vartheta_{amb} \approx +17.4\,^\circ\mathrm{C}$; the initial liquid supercooling ranges from $\Delta T \approx 7.8\,\mathrm{K}$ to $\Delta T \approx 19.5\,\mathrm{K}$. As shown in the figure, the measured front velocities compare very well for almost the entire range of supercooling. However, in the range between $\Delta T \approx 12.5\,\mathrm{K}$ and $\Delta T \approx 15.0\,\mathrm{K}$, a slightly larger spread of the data can be observed. This spread may be attributed to a variation of the freezing morphology of the dendrites constituting the dendrite cloud. As reported in [332], in the case of dendritic freezing of a supercooled water film, a certain liquid temperature is not necessarily associated with a distinct dendrite tip velocity. The tip velocity also depends on the morphology of the growing dendrite, which changes with temperature. Similar variations of the dendrite mor-

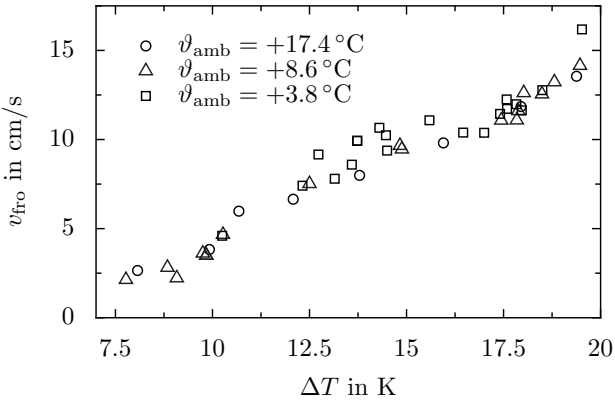

Figure 5.8: Normal velocity of the front of a dendrite cloud depending on liquid supercooling, shown for varying ambient temperature around the Hele-Shaw cell in the styrofoam chamber, ϑ_{amb}.

phology may cause the spread data in the case of simultaneous growth of multiple dendrites in a dendrite cloud. As will be shown and discussed later in this section, the spread of the data in this range of supercooling is observed for all experiments of the present study. Therefore, the obtained dependency of the front velocity on liquid supercooling is well comparable for all ambient temperatures in the styrofoam chamber, indicating that the Hele-Shaw cell does not significantly influence the freezing process.

Due to smaller front velocities involved in dendritic freezing of the bulk liquid in comparison to the ice layer growth, and due to the fact that dendritic freezing takes place a certain distance from the cooling substrate, this freezing phase is much more prone to a thermal influence of the side walls compared to the initial ice layer propagation on the substrate. Since an effect of the side walls on the freezing front velocity during dendritic freezing is not observed, it is reasonable to assume the side walls also negligible for the propagation of the initial ice layer.

As shown above and in the previous section, any qualitative or quantitative influences of the Hele-Shaw cell on the different phases of solidification of a supercooled sessile drop can be neglected. Therefore, the Hele-Shaw cell provides a realistic two-dimensional replica of the three-dimensional processes in the drop, allowing quantitative examination of the processes involved during freezing of a sessile supercooled water drop.

Since the planar freezing phase is rather related to the freezing of a non-supercooled water drop, which has already been examined in detail in previous studies, the following investigations are focused on separate examination of the growth of the initial ice layer, and subsequent dendritic freezing of the bulk liquid.

5.3.1 Initial ice layer spreading

As shown in [181], the growth velocity of the initial ice layer is drastically enhanced by the presence of a metallic substrate in comparison to the velocity of a single dendrite. Furthermore, a strong dependence of the ice layer velocity on the substrate material has been reported for liquid supercooling up to $\Delta T = 7\,\mathrm{K}$. However, it has already been suggested that the dependence of the ice layer velocity on the substrate material decreases for larger liquid supercooling.

Therefore, in the following the growth of the initial ice layer is experimentally examined and theoretically modeled for a significantly larger range of liquid supercooling than in previous studies. It is examined for different substrate materials with thermal properties varying in a wide range, which are summarized in Table 5.1.

Table 5.1: Density ρ, heat capacity c_p, thermal conductivity k, thermal diffusivity a and thermal effusivity $e = \sqrt{\rho c_\mathrm{p} k}$, of ice, water and the substrates used in the present study of ice layer formation on the solid substrate. The data are taken from [203, 367].

	ρ in $\frac{\mathrm{kg}}{\mathrm{m}^3}$	c_p in $\frac{\mathrm{J}}{\mathrm{kgK}}$	k in $\frac{\mathrm{W}}{\mathrm{mK}}$	a in $10^{-6}\,\frac{\mathrm{m}^2}{\mathrm{s}}$	e in $\frac{\mathrm{Ws}^{0.5}}{\mathrm{m}^2\mathrm{K}}$
Copper	8954	384	398	115.75	37000
Aluminum	2707	905	237	96.74	24100
Brass	8522	385	109	33.22	18900
Stainless steel	8000	400	14	4.38	6700
Ice (0 °C)	917	2100	2.215	1.15	2065
Water (0 °C)	1000	4219	0.562	0.133	1540
Acrylic glass	1180	1260	0.19	0.128	531

5.3.1.1 Experiments

Figure 5.9 shows the experimentally measured horizontal ice layer velocities, $v_{\mathrm{lay,x}}$, for varying supercooling and substrate material. For comparison, experimental data from [332] for the velocity of a single dendrite growing freely in supercooled water is also shown. In contrast to solidification on the metallic surfaces, in the case of the acrylic glass substrate no explicit growth of a thin ice layer has been observed. Therefore, the movement of the intersection point of the front of the dendrite cloud with the substrate surface (see Fig. 5.3) has been assumed to be comparable to the ice layer propagation. The horizontal velocity of this point is shown for the acrylic glass substrate in Fig. 5.9. As shown in the figure, the solidification velocity on the acrylic glass substrate is well comparable to the tip velocity of a single dendrite. Thus, the acrylic glass substrate acts similar to an adiabatic wall and does not thermally influence the solidification process in the near wall region. This result confirms the previous indication of a generally negligible influence of the acrylic glass side walls on the freezing process in the Hele-Shaw cell.

In contrast, on the metallic surfaces the ice layer velocity is increased by a factor of more than three in comparison to the velocity of a single dendrite. However, for the extended range of supercooling, examined in the present study, no significant dependence of the ice layer velocity on the substrate material can be observed for the metallic substrates. The ice layer velocity only slightly increases on the copper substrate in comparison to the steel substrate, which are associated with the largest and the smallest effect on the ice layer growth, respectively. As shown in Tab. 5.1, both the densities and heat capacities of steel and copper are well comparable. Therefore, the thermal conductivity and the resulting diffusivity and effusivity are the only thermophysical properties which may be relevant for the phase change process. The thermal conductivity is approx. 28 times larger for copper than for steel, indicating that it is the crucial property of a substrate which determines its effect on the ice layer propagation. The higher the thermal conductivity, the faster latent heat is dissipated away from the solid-liquid interface of the ice layer into the substrate, which in turn increases the ice layer growth rate. This correlation also explains the vanishing effect of the acrylic glass substrate whose thermal conductivity is approx. 73 times smaller than that of steel, thus more than 2000 times smaller than that of copper; and even more than two times smaller than that of water.

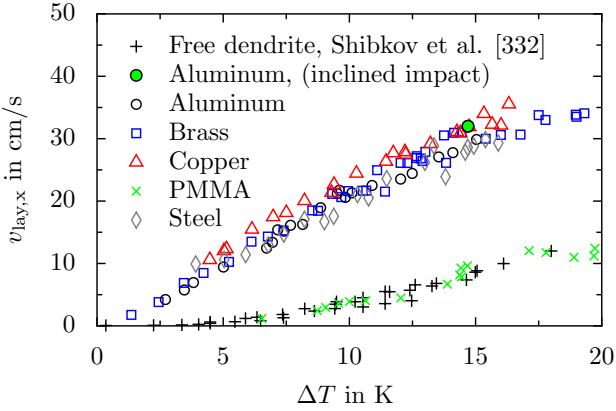

Figure 5.9: Initial ice layer velocity parallel to the substrate surface as a function of the liquid supercooling for varying substrate materials. For comparison the tip velocity of a single dendrite is also shown [332]. (Reprinted (adapted) with permission from [314]. Copyright 2017 American Chemical Society.)

Besides the velocity data obtained from the present experiments and the data for a single dendrite, Fig. 5.9 also shows the layer velocity measured after inclined drop impact onto smoothed aluminum, which has been examined in Sec. 3.1.1.

The propagating dendrite cloud after such an impact is shown in Fig. 5.10. Due to the top view observation of drop impact, the rate of the radial expansion of the dark dendrite cloud in the high-speed videos does not represent the normal front velocity of the dendrite cloud. It rather represents the velocity of the intersection line of the envelope of the dendrite cloud with the impact surface, which can reasonably be assumed as the ice layer velocity, as explained before. The initial ice layer is not visible in the top-view photographs shown in Fig. 5.10, since its visibility strongly depends on the illumination of the process and the morphology of the water-air interface. However, to demonstrate the existence of the initial ice layer also in the case of drop impact, Fig. 5.11 shows a detail of the solidification process of a supercooled water drop after its normal impact onto a polymer coated aluminum substrate. The ice layer is clearly visible as a brighter region surrounding the dark dendritic structure with an almost constant offset at the left side in the shown photographs.

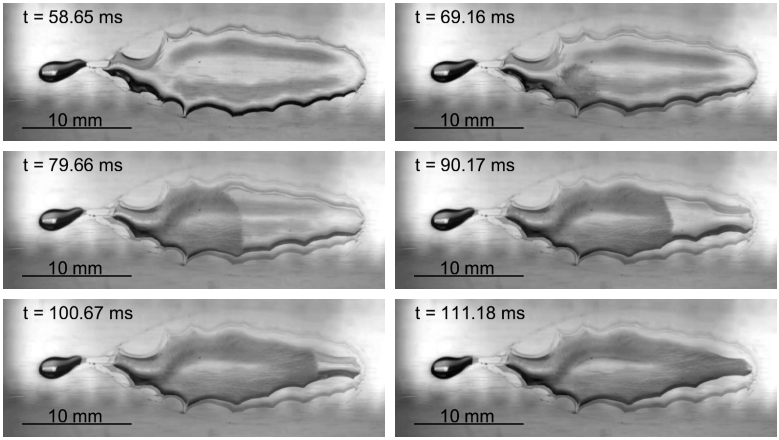

Figure 5.10: Dendritic freezing of a receding drop after oblique impact onto polished aluminum. The drop and the substrate are initially at +14.3 °C and −17.0 °C, respectively. The solidifying liquid in the vicinity of the substrate is significantly supercooled, and solidification proceeds in the stages described before. To illustrate further receding after nucleation, every frame is superposed with the frame at $t = 58.65\,\mathrm{ms}$, being the last frame, before the nucleus is visible in the high-speed video. (Reprinted figure with permission from [320]. Copyright 2016 by the American Physical Society.

As described in Sec. 3.1.1, the freezing delay during the experiments concerning inclined drop impact significantly varies. Until freezing the wetted surface area continuously decreases, which is accompanied by an increase of the curvature of the upper drop surface. Due to the increasing curvature of the drop surface during liquid receding, optical measurement of the dendrite cloud velocity is increasingly affected by refraction at the liquid-air interface. Therefore, the velocity has been only measured up to a certain freezing delay time, $t_{\mathrm{del}} \approx 150\,\mathrm{ms}$, for which refractive effects at the interface are negligible for the velocity measurement. The horizontal ice layer velocity averaged for all high-speed videos, which allow a velocity measurement, has been obtained as $v_{\mathrm{lay,x}} = 0.32\,\mathrm{m/s}$. The contact temperature for the respective impact conditions has been estimated in Sec. 3.1.1 as $\vartheta_{\mathrm{c}} = -14.7\,^{\circ}\mathrm{C}$. As shown in Fig. 5.9, these data are well

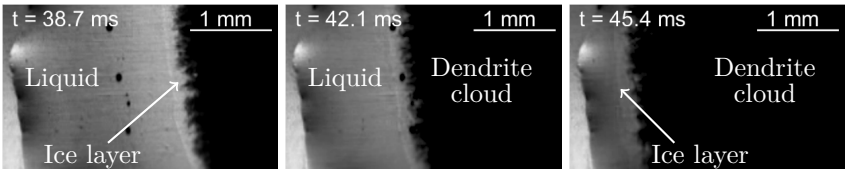

Figure 5.11: Top-view image sequence showing the growth of the initial ice layer prior to dendritic solidification of a supercooled water drop after its normal impact onto a polymer coated aluminum substrate. The initial ice layer is identified as the bright region surrounding the dark dendrite cloud (in the right part of the photographs) with an almost constant offset.

comparable to the results obtained in the Hele-Shaw cell for liquid drops at rest, indicating that the growth of the initial ice layer is unaffected by fluid flow during and after drop impact. Moreover, it is worth noting that the impinging liquid is initially at $\vartheta_{\mathrm{d},0} = +14.3\,^{\circ}\mathrm{C}$, while the substrate is initially at $\vartheta_{\mathrm{sub},0} = -17.0\,^{\circ}\mathrm{C}$. Therefore, a thermal boundary layer develops in the spreading drop, and only the liquid in direct contact with the substrate is at $\vartheta_{\mathrm{c}} = -14.7\,^{\circ}\mathrm{C}$, while the remaining impinging liquid is warmer. The thickness of the thermal boundary layer increases with time as $h_{\mathrm{tbl}} \sim \sqrt{a_{\mathrm{l}} t}$. The freezing delays in the experiments concerning inclined drop impact, for which a distinct ice layer velocity could be measured, varies by a factor of 10 between $t_{\mathrm{del}} \approx 15\,\mathrm{ms}$ and $t_{\mathrm{del}} \approx 150\,\mathrm{ms}$, which corresponds to a triplication of the thermal boundary layer thickness between the first and the last examined drop freezing. Nevertheless, in this range of freezing delays the measured ice layer velocity varies by only approx. 5 % with respect to the averaged value of $v_{\mathrm{lay,x}} = 0.32\,\mathrm{m/s}$; it increases for an increasing freezing delay. The negligible increase of the ice layer velocity for an increasing freezing delay indicates that the surrounding warmer water does not significantly affect the ice layer growth, and that only the liquid temperature in a very thin region above the substrate surface is of relevance for the ice layer velocity. As shown by the comparison in Fig. 5.9, the contact temperature during impact estimated using Eq. 2.11 gives an appropriate estimation of the temperature relevant for the ice layer growth. The exclusive dependence of the ice layer growth on the contact temperature, and its indifference to other influences such as the fluid flow of the surrounding warmer liquid, implicitly confirm the negligible effect of the Hele-Shaw cell on ice layer spreading.

Figure 5.12 separately shows the ice layer velocities measured on copper, brass and steel. They are shown in comparison to previous results presented in [181]. The investigated temperature ranges in the present study and in [181] vary for the different substrate materials. However, the temperature ranges overlap allowing comparison of the results. Both the present results, and the results from [181] respectively show a clear trend of the ice layer velocity depending on temperature. However, as shown in the figure, the velocities and their dependence on temperature, obtained in the present study, are generally higher than those reported in [181]. A definite reason for the observed deviation between the shown data is hard to identify. According to the experimental setups used in the present study and in [181], the measurement of the substrate temperature is accompanied by a minor inaccuracy which is of the order of the measurement accuracy of the respective temperature sensor. Therefore, inaccuracies of the temperature measurement can be excluded as the reason for the significant deviations, which thus may rather be found in the measurement of the layer velocity. A possible reason for the deviation between the two data sets could be an error during calibration of the optical resolution of the captured videos in both experiments. A wrong calibration would cause all measured velocities to deviate by a constant factor, which would also result in an altered slope of the data, as it is observed in Fig. 5.12. Using the experimental results on brass, which show the largest overlap with respect to temperature, the ratio between the velocities obtained in the present study and the results from [181] is found as ≈ 1.77. As shown in Fig. 5.13, a correction of the data with this factor results in a very good agreement of the data sets for all investigated substrate materials.

Since the shown deviation between the data has already been observed during conduction of the experiments in the present study, the spatial calibration for the present study has been repeated several times. Moreover, the analysis tool has been checked several times, and thus both a wrong spatial calibration and an error during the analysis of the captured high-speed videos can be excluded as the reason for the deviation between the shown data. In addition, the good agreement between the results obtained in the Hele-Shaw cell and those measured during inclined drop impact indicates correctness of the present results. After extended private communication with the authors of [181], a wrong calibration and an error during the video analysis can be ruled out also for their experiments. Therefore, so far the reason for the deviations could unfortunately not be

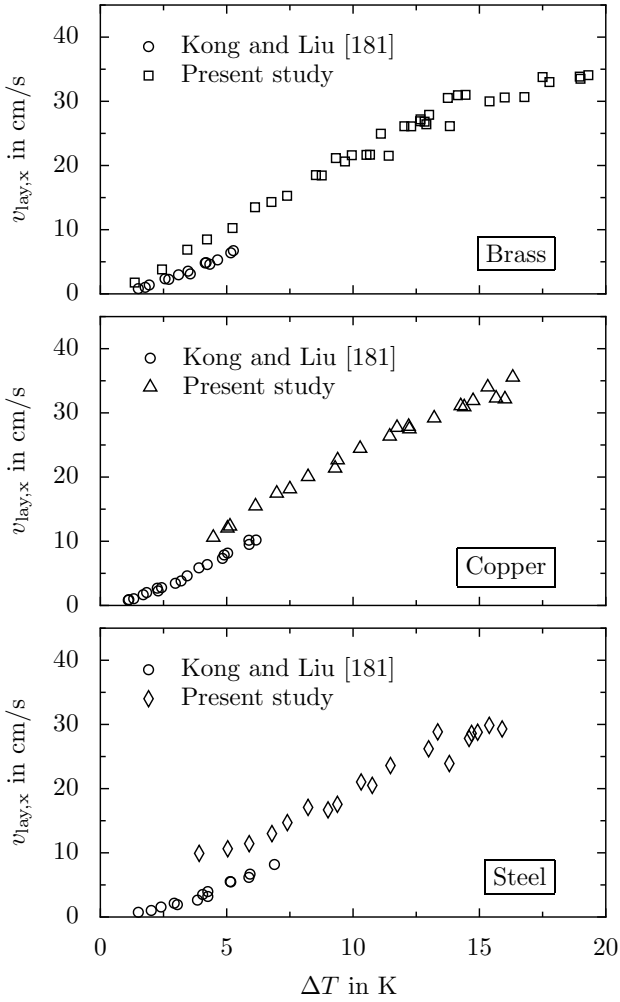

Figure 5.12: Ice layer velocity as a function of supercooling for varying substrate materials. Comparison of present results with data from [181]. (Reprinted (adapted) with permission from [314]. Copyright 2017 American Chemical Society.)

clearly identified. Further experiments are necessary for clarification of the observed deviation.

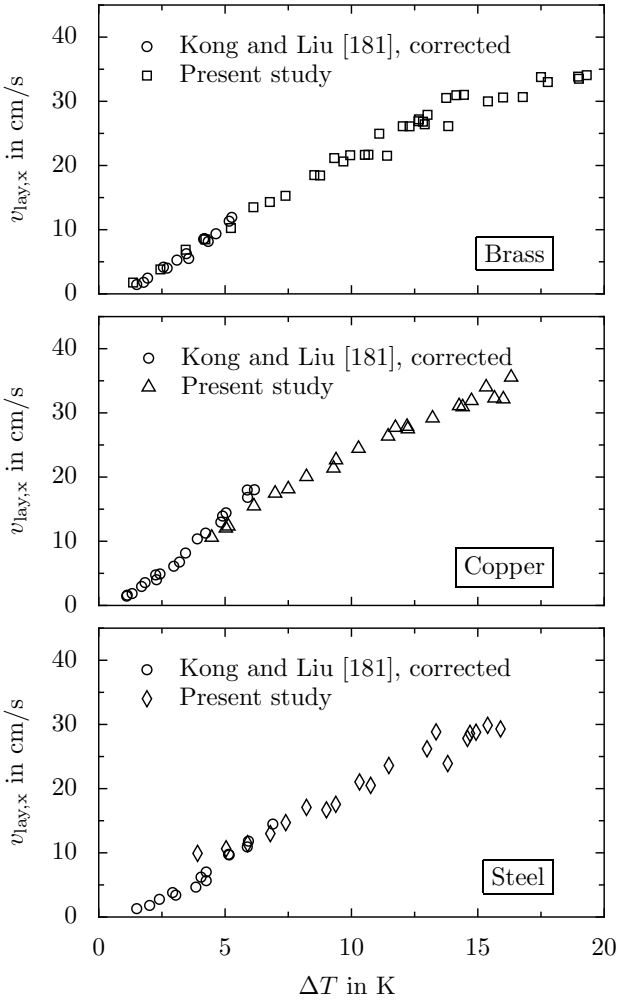

Figure 5.13: Ice layer velocity as a function of supercooling for varying substrate materials. Comparison of present results with data from [181] which are corrected with a constant factor of 1.77. (Reprinted (adapted) with permission from [314]. Copyright 2017 American Chemical Society.)

5.3.1.2 Mathematical modeling

Solidification of supercooled water at a solid substrate has been mathematically described in [181]. They modeled the propagation of the initial ice layer by considering heat conduction in the supercooled liquid and the neighboring solid substrate, and derived the ice layer velocity using a parabolic coordinate system, a moving reference frame and a length parameter to characterize the ice layer thickness. In the present study a simple model is proposed based on the analytic solution of the two-phase Stefan problem, which has been described in Sec. 2.3.

For the model's derivation, let us first recap the one-dimensional case of ice layer growth, where solidification starts at the same time at each point of a substrate. Supercooled water initially at $T_{\mathrm{l},0}$ occupies a semi-infinite slab, $0 < y < \infty$, and is in contact with a substrate at $y = 0$. At time $t = 0$, a constant temperature T_{c} is imposed at the substrate surface, $y = 0$, and a planar freezing front being parallel to the plane $y = 0$ moves into the supercooled liquid $y > 0$. In the case of $T_{\mathrm{l},0} < T_{\mathrm{m}}$ and $T_{\mathrm{c}} < T_{\mathrm{m}}$, the latent heat of fusion is dissipated through both the liquid and the solid phase, and the solidification process is described as a two-phase Stefan problem. The resulting temperature profiles in the liquid phase and the growing solid layer have been shown in Fig. 2.12. As described in Sec. 2.3, the temporal evolution of the ice layer thickness for the two-phase Stefan problem is

$$h(t) = 2\lambda_{\mathrm{s}}\sqrt{a_{\mathrm{s}}t}, \tag{5.1}$$

where the parameter λ_{s} is the root of a transcendental equation, which for the present case reads

$$\frac{\mathrm{St_c}}{\lambda_{\mathrm{s}}\sqrt{\pi}\exp(\lambda_{\mathrm{s}}^2)\,\mathrm{erf}(\lambda_{\mathrm{s}})} + \frac{\mathrm{St_l}}{a^*\lambda_{\mathrm{s}}\sqrt{\pi}\exp[(a^*\lambda_{\mathrm{s}})^2]\,\mathrm{erfc}(a^*\lambda_{\mathrm{s}})} = 1, \tag{5.2}$$

with $a^* = (a_{\mathrm{s}}/a_{\mathrm{l}})^{0.5}$, and the Stefan numbers for the substrate at $y = 0$ and for the liquid, being defined as

$$\mathrm{St_c} = \frac{c_{\mathrm{s}}(T_{\mathrm{m}} - T_{\mathrm{c}})}{L} \qquad \text{and} \qquad \mathrm{St_l} = \frac{c_{\mathrm{l}}(T_{\mathrm{m}} - T_{\mathrm{l},0})}{L}. \tag{5.3}$$

As shown in the previous section, in reality solidification does not start at the same time over the entire substrate surface; it is initiated at a single nucleation site on the surface. Nucleation at time $t = 0$ and position

$\mathbf{x}' = 0$ is followed by the radial spreading of a thin ice layer over the substrate with a constant velocity $v_{\mathrm{lay,x}}$. Therefore, solidification at an arbitrary point $\mathbf{x}'$ on the surface is initiated at time

$$t_{\mathrm{ice}}(\mathbf{x}') = |\mathbf{x}'|/v_{\mathrm{lay,x}}. \tag{5.4}$$

Due to the constant ice layer velocity, the problem is axisymmetric around the position of nucleation. During the initial phase of the ice layer growth which is associated with small ice layer radii and large curvatures of the ice-water interface, the three-dimensionality of the heat transfer problem around the ice layer may lead to an ice layer velocity decreasing with time. For later times associated with a larger ice layer radius and decreasing curvature in the plane parallel to the substrate surface, the three dimensionality of the heat transfer problem becomes increasingly unimportant, resulting in a constant ice layer velocity. The constant ice layer velocity observed in the present experiments indicates that the phase in which the three dimensionality of the problem may lead to a transient ice layer growth is negligibly short. Therefore, it is sufficient and convenient to reduce the problem to two dimensions and to examine the ice layer growth in a plane, normal to the substrate surface and normal to the contact line between the ice, the surrounding water and the substrate, resulting in a cross-sectional view of the ice layer as schematically shown in Fig. 5.14.

Consider a coordinate system moving with the spreading ice layer, with its origin at the tip of the ice layer as shown in the figure. The horizontal coordinate in this moving local system, $\mathbf{x}$, is obtained from the horizontal coordinate in the stationary global system, $\mathbf{x}'$, by the transformation $\mathbf{x} = \mathbf{x}'_{\mathrm{tip}}(t) - \mathbf{x}'$, where $\mathbf{x}'_{\mathrm{tip}}(t)$ is the position of the ice-water-substrate contact line in the global system.

Solidification at the tip of the ice layer is determined by two-dimensional heat conduction in the supercooled liquid, the ice layer and the neighboring substrate. However, far behind the tip of the ice layer where $\mathrm{d}h_{\mathrm{lay}}/\mathrm{d}\mathbf{x} \ll 1$, the movement of the ice-water interface is dominated by one-dimensional heat conduction in the y-direction normal to the substrate's surface, i.e. by the vertical growth velocity of the ice layer, $v_{\mathrm{lay,y}}$ [181]. Therefore, the ice layer thickness far behind the tip can be estimated from the solution of the two-phase Stefan problem, Eq. 5.1. The local time of ice layer growth at an arbitrary position in the laboratory coordinate system as a function of the current position of the ice layer tip

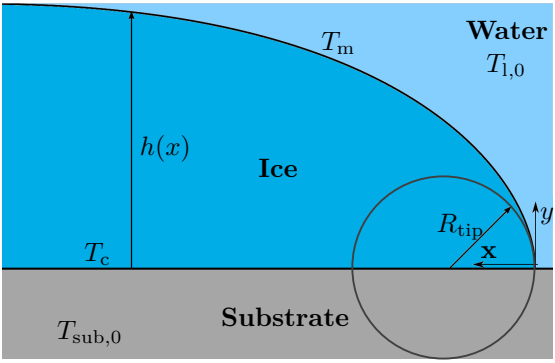

Figure 5.14: Cross-sectional view of the modeled ice layer, spreading from left to right.

in this system is obtained as

$$t_\mathrm{loc}(\mathbf{x}') = t - t_\mathrm{ice}(\mathbf{x}') = \frac{\mathbf{x}'_\mathrm{tip}(t) - \mathbf{x}'}{v_\mathrm{lay,x}} \widehat{=} \frac{\mathbf{x}}{v_\mathrm{lay,x}}. \tag{5.5}$$

Using this relation and the solution of the two-phase Stefan problem, Eq. 5.1, the ice layer thickness in the moving coordinate system at a position $\mathbf{x}$ behind the ice layer tip is obtained as

$$h_\mathrm{lay} = 2\lambda_\mathrm{s}\sqrt{a_\mathrm{s}\frac{\mathbf{x}}{v_\mathrm{lay,x}}}. \tag{5.6}$$

The underlying physical mechanisms involved in ice layer growth are comparable to those during the growth of a single dendrite. Therefore, it is reasonable to assume the temperature profile around the ice layer, and the ice layer itself, to be of parabolic shape [161, 181]. Using this assumption, a second relation for the ice layer thickness in the moving coordinate system is obtained from the general equation of a parabola

$$h_\mathrm{lay} = \sqrt{2R_\mathrm{tip}\mathbf{x}}, \tag{5.7}$$

where R_tip is the tip radius of the ice layer, as illustrated in Fig. 5.14. By equating Eq. 5.6 and 5.7, the horizontal velocity of the ice layer is obtained as

$$v_\mathrm{lay,x} = \frac{2\lambda_\mathrm{s}^2 a_\mathrm{s}}{R_\mathrm{tip}}, \tag{5.8}$$

where λ_s can be calculated using Eq. 5.2. Derivation of Eq. 5.1, transformation into the moving reference frame, and substitution of $v_{lay,x}$ with Eq. 5.8 yields the vertical growth velocity of the initial ice layer depending on the horizontal position in the moving reference frame as

$$v_{lay,y} = \lambda_s^2 a_s \sqrt{\frac{2}{R_{tip}\mathbf{x}}}. \tag{5.9}$$

The temperature at the substrate surface, T_c, is incorporated in the model through Eq. 5.2 which is used for calculation of the parameter λ_s. While the initial substrate temperature equals the initial liquid temperature, the temperature between the ice layer and the substrate, i.e. T_c, is unknown. Depending on the substrate properties, it may change due to the ice layer growth. In the limit of an infinite thermal conductivity of the substrate, the temperature of the substrate surface would be unaffected by ice layer spreading, hence $T_c = T_{sub,0}$. In the other limit of an adiabatic substrate, characterized by a vanishing thermal conductivity, the substrate would not affect the solidification process, as indicated in the previous section by the experimental results obtained for acrylic glass as a low-conductivity substrate (see Fig. 5.9). In this case, the substrate surface would take the temperature of the spreading ice layer, $T_c = T_m$. For a substrate with a finite conductivity, the substrate surface temperature below the ice layer is somewhere in between the previous limits, thus $T_{sub,0} < T_c < T_m$.

With neglect of the thermal boundary layer in the horizontal direction in front of the ice layer, during the horizontal spreading of the ice layer a surface element, initially being at $T_{sub,0}$, is suddenly covered by ice, being at T_m. This process is well comparable to the case of two semi-infinite solid slabs (initially being at $T_{sub,0}$ and T_m, respectively), suddenly brought into contact with each other. Due to the analogy to this process, the substrate surface temperature for the present case of ice layer spreading can be estimated as [20]

$$T_c = \frac{e_{ice} T_m + e_{sub} T_{sub,0}}{e_{ice} + e_{sub}}, \tag{5.10}$$

where $T_{sub,0} = T_{l,0}$, and e_{ice} and e_{sub} are the thermal effusivities of ice and the substrate, respectively. Note that by this approach, the fact that the thermal boundary layer expansion in the ice layer may be faster than the increase of the ice layer thickness itself is neglected. Nevertheless, Eq. 5.10

gives a reasonable estimate of the substrate warm up during spreading of the ice layer.

Equation 5.10 completes the system of equations of the theoretical model. The calculation of the horizontal ice layer velocity for a given supercooling and substrate material comprises estimation of the interface temperature, T_c, using the initial temperatures and material properties in Eq. 5.10, calculation of the parameter λ_s using Eq. 5.2, and finally, calculation of the ice layer velocity using Eq. 5.8. The material properties for the following calculations are all taken from Tab. 5.1, i.e. corresponding to a temperature of 0 °C.

As seen from the previous relations, the substrate thermal properties are incorporated in the theoretical model through Eq. 5.10. They implicitly influence the speed of the ice layer by affecting the temperature T_c of the substrate surface below the ice layer, which is incorporated by Eq. 5.2. According to Eq. 5.10, the larger the thermal effusivity of the substrate material, the smaller is the warming up of the substrate surface below the ice layer. Consequently, the larger is the enhancement of the speed of solidification through the presence of the substrate, due to enhanced dissipation of latent heat arising at the ice-water interface, which is incorporated via Eq. 5.2. The temperature rise of the substrate, $T_c - T_{sub}$, calculated using Eq. 5.10 for an initial substrate temperature $\vartheta_{sub} = -10\,°C$ and the examined substrate materials is shown in Tab. 5.2 as an example. As shown in the table, the estimated change of the surface temperature due to ice layer growth increases significantly from only 0.5 K for copper, to almost 8 K in the case of the acrylic glass substrate, which explains the significant difference between the influence of copper and acrylic glass on the ice layer velocity, shown in Fig. 5.9. Aside from the steel substrate, all other metal substrates are characterized by an only small warm up of less than 1 K, explaining the rather small variation of the ice layer velocity for these substrates.

The ice layer tip radius R_{tip} is the only free parameter in the theoretical model. It is obtained by a least-squares fit of Eq. 5.8 to the experimental data, shown in the previous section. As explained in Sec. 2.3, and found by Shibkov et al. [332, 335] for a single dendrite growing freely in supercooled water, up to a certain liquid supercooling, the freezing process is well modeled by only considering heat diffusion. At greater supercooling the solidification process is furthermore affected by kinetic effects of molecular attachment at the ice-water interface, attributed to the increas-

Table 5.2: Estimated temperature rise of the substrate surface, $T_c - T_{sub,0}$, due to solidification along the surface, calculated with Eq. 5.10 for varying substrate materials and an initial substrate temperature $\vartheta_{sub} = -10\,°C$.

Substrate material	$T_c - T_{sub,0}$ in K
Copper	0.53
Aluminum	0.79
Brass	0.98
Stainless steel	2.36
Acrylic glass	7.95

ing sluggishness of molecules for decreasing temperature. The threshold for kinetic effects in the case of a single dendrite was found at a liquid temperature of $\vartheta_l \approx -5 \ldots -4\,°C$ [332]. As shown in Sec. 2.3, kinetic effects cause both a decreasing dependency of the dendrite tip velocity on temperature, and a wider spread of the velocity data in the transition region between the purely diffusion dominated growth regime, and the regime in which also kinetic effects are of relevance. Both effects of the influence of molecule kinetics are also found in the velocity data of the present study, shown in Fig. 5.12. In particular the data obtained on brass for $\Delta T < 10\,K$ are well described by an almost linear dependency accompanied by an only negligible spread of the data. However, for $\Delta T > 10\,K$ the measured velocities spread significantly, finally resulting in a decreased dependency of the velocity on temperature, indicating an increase of kinetic effects. The present theoretical model only accounts for heat conduction and neglects kinetic effects. Therefore, an increasing deviation of the theoretically predicted ice layer velocities from the experimentally observed velocities can be expected for higher supercooling. To account for this, the ice layer tip radius is obtained by fitting Eq. 5.8 to the experimental data only in the expected diffusion-limited growth regime, up to the indicated threshold of $\Delta T = 10\,K$. No ice layer growth has been observed for solidification on the acrylic glass substrate, and the ice growth velocity along the interface was not noticeably greater than that through the bulk of the drop. Therefore, fitting is not applied to the

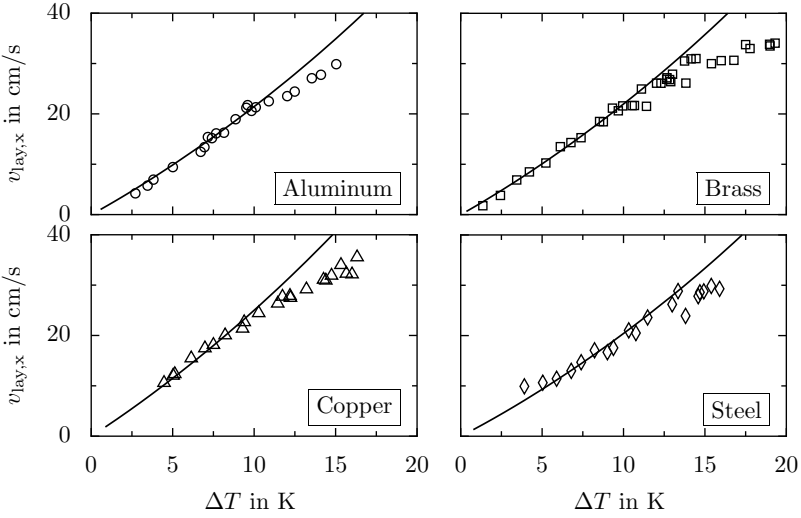

Figure 5.15: Ice layer velocity as a function of supercooling for different substrate materials. Comparison of experimental data (symbols) and the tip velocities calculated using the tip radii summarized in Tab. 5.3 (lines). (Reprinted (adapted) with permission from [314]. Copyright 2017 American Chemical Society.)

data obtained with the acrylic glass substrate.

Figure 5.15 shows a comparison of the ice layer velocities calculated with the obtained tip radii, which are summarized in Tab. 5.3, and the measured velocities for the metallic substrates. As shown in the figure, the experimental data are well described by the theoretical model for all substrate materials in the supercooling range $\Delta T \leq 10\,\mathrm{K}$. The present model is a scaling law, involving only one free parameter, R_{tip}, which is incorporated into the model through Eq. 5.8 as a scaling factor for the horizontal velocity. The parameter does not affect the temperature dependence of the layer velocity, predicted by the model. Therefore, a single experimentally obtained data pair in the range $\Delta T \leq 10\,\mathrm{K}$ would be sufficient to calibrate the model by calculating the tip radius R_{tip}. However, a least squares fit of Eq. 5.8 to multiple data points accounts for a potential spread of the experimental data, and maximizes the coefficient

Table 5.3: Tip radius of the initial ice layer (see Fig. 5.14) for varying substrate materials, obtained by fitting Eq. 5.8 to the experimental data for the supercooling range $\Delta T \leq 10\,\mathrm{K}$.

Substrate material	R_{tip} in nm
Copper	330
Aluminum	374
Brass	358
Stainless steel	329

of determination of the final equation with respect to all data points. As shown in the figure, the temperature dependence of the layer velocity is correctly predicted by the theoretical model, which is not attributed to the scaling factor but to the correct account for the physical mechanisms involved. Therefore, the increasing deviation between the model and the experimental results for $\Delta T > 10\,\mathrm{K}$ indicates that kinetic effects indeed gain relevance for this range of supercooling.

It is worth to note that as already found in [181], the tip radius of the spreading ice layer is a constant which is independent of the liquid supercooling. In the case of a single dendrite growing freely in a supercooled melt, the tip radius depends on the liquid supercooling. As described in Sec. 2.3, it can be calculated using the marginal stability theory [190, 191, 241]. In the range of supercooling examined in the present study, the tip radius of a freely growing dendrite varies over two orders of magnitude between approx. 80 nm and 3 µm. According to the theory, an ice layer tip radius of $R_{\mathrm{tip}} = 350\,\mathrm{nm}$ corresponds to a single dendrite growing in a supercooled melt at approx. $\vartheta = -7.7\,^{\circ}\mathrm{C}$. All tip radii, obtained in the present study and summarized in Tab. 5.3, are in the aforementioned range of tip radii calculated using the marginal stability theory. However, the reason for the constant tip radius in the case of a spreading ice layer in contrast to a temperature dependent dendrite tip radius is not clear.

As shown in Tab. 5.3, the tip radii for the different substrate materials vary by only 14 %. Moreover, no correlation can be observed with any of the material properties shown in Tab. 5.1, indicating the variation of the tip radii to be not physically caused. Therefore, the tip radius is as-

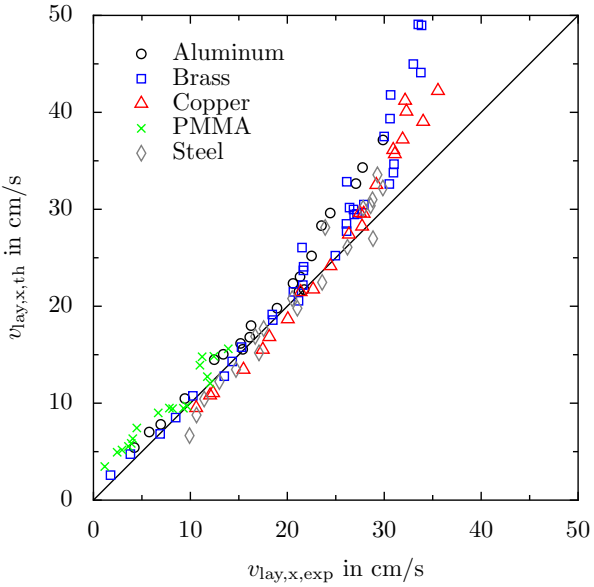

Figure 5.16: Comparison of the theoretically modeled and experimentally measured layer velocity for all investigated substrate materials. A constant tip radius of $R_{\mathrm{tip}} = 352\,\mathrm{nm}$ was used for the calculation of $v_{\mathrm{lay,x,th}}$. (Reprinted (adapted) with permission from [314]. Copyright 2017 American Chemical Society.)

sumed constant, i.e. not only independent of the supercooling, but also of the substrate material. Using the experimental data for all substrate materials (again excluding acrylic glass) for fitting of Eq. 5.8, a tip radius of $R_{\mathrm{tip}} = 352\,\mathrm{nm}$ is obtained for the metallic substrates. Figure 5.16 shows a direct comparison of the experimentally measured layer velocities, $v_{\mathrm{lay,x,exp}}$, and the theoretical predictions, $v_{\mathrm{lay,x,th}}$, calculated with a constant tip radius of $R_{\mathrm{tip}} = 352\,\mathrm{nm}$ for all substrate materials. The solid line represents perfect agreement between the calculated and the measured values. As shown in the figure, even with the constraint of a substrate-independent tip radius, the theoretical model remains in very good agreement with the experimental data in the diffusion-limited growth regime. For layer velocities larger than 0.2 m/s, an increasing deviation between the theoretical and experimental data is observable. Attributed to kinetic effects which are not taken into account, the model overpre-

dicts the layer velocity. These effects are controlled by the kinetics of water molecules at the solidification front, and only depend on temperature; they are indifferent to the substrate material. The latter fact is indicated in Fig. 5.16 by a deviation of the predicted velocities from the line of perfect agreement, which is almost independent of the substrate material.

Figure 5.16 also shows a comparison for the data obtained on the acrylic glass substrate. The experimental data for acrylic glass are not used for the calculation of the tip radius R_{tip}, and no distinct ice layer growth is observable on acrylic glass. Nevertheless, the agreement between the calculated growth velocity and the experimentally measured solidification velocity close to the substrate is very good, indicating that the model accounts for all physical mechanisms relevant for the process and that the tip radius is indeed constant for varying substrate materials.

5.3.1.3 Conclusion

The previously introduced experimental approach employing a Hele-Shaw cell has been used to examine the growth of the initial ice layer prior to dendritic freezing of the bulk liquid of a supercooled sessile water drop. The ice layer velocity has been experimentally investigated and theoretically modeled for both varying supercooling and substrate material.

The initial ice layer has only been observed in the case of metallic substrate materials. In the case of an acrylic glass substrate, the ice layer propagation has not been observed and moreover, the solidification process is not at all affected by the presence of the substrate. The dendritic front close to the substrate propagates with the same velocity as a single dendrite in the bulk liquid. However, in the case of a metallic substrate, the solidification velocity is drastically increased at the substrate surface. For a liquid supercooling up to $\Delta T = 7.0\,\mathrm{K}$, a strong influence of the substrate material properties on the velocity of the initial ice layer has been observed in [181]. Compared to that study, in the present work the range of supercooling has been significantly extended up to $\Delta T \approx 20\,\mathrm{K}$. As already suggested in [181], it has been shown in the present study that for a larger liquid supercooling the substrate thermal properties only slightly affect the ice layer velocity for the case of metallic substrates. A comparison of the present results obtained in the Hele-Shaw cell with the ice layer velocity measured during inclined non-isothermal drop impact, revealed that the fluid flow during drop impact does not influence the ice layer

growth rate. Moreover, based on this comparison it could be shown that only the temperature in a very thin region above the substrate surface is of relevance for the ice layer growth. Due to the small typical length scale of the ice layer growth, other influences on the freezing process, in particular an influence of the Hele-Shaw cell can be excluded. The comparison revealed that the contact temperature during non-isothermal drop impact is an appropriate means for estimating the characteristic temperature, relevant for the ice layer growth during drop impact. Despite the good agreement of the present results with the ice layer velocity measured during inclined drop impact, the present results significantly deviate from experimental results reported in [181]. The ice layer velocities obtained in the present study are consistently higher than the velocities obtained in [181], seemingly deviating by a constant factor of approx. 1.77. Despite an extensive correspondence with the authors of [181], a reason for the deviation of the experimental results could not be found so far.

The propagation of the initial ice layer in the diffusion-limited growth regime has been theoretically modeled. Based on the analytic solution of the two-phase Stefan problem, the model explicitly incorporates heat conduction in the supercooled liquid and in the growing ice layer. Heat conduction in the substrate, which is the origin of an increased velocity in the case of metallic substrates, is implicitly incorporated by the estimation of the substrate surface temperature below the ice layer. It is calculated using the equation for the contact temperature between two semi-infinite slabs of different temperature suddenly brought into contact. The only free parameter in the theoretical model is a length scale characterizing the tip radius of the propagating ice layer. It turns out as a scaling factor for the horizontal ice layer velocity in the model and has been found by a least-squares fit of the theoretical model to the experimental data. This parameter does not significantly depend on the substrate material and is furthermore constant for the entire diffusion limited growth regime. The reason for the constancy of the ice layer tip radius in comparison to the temperature dependence of a dendrite's tip radius is not clear so far. However, this finding is in agreement with previous results reported in the literature. The experimental data for the ice layer velocity in the range of supercooling $\Delta T \leq 10\,\mathrm{K}$ is well described by the semi-empirical model. For higher supercooling, kinetic effects which are not accounted for in the model become important. These effects involve an increasing sluggishness of molecules, and cause smaller ice layer velocities than predicted with the diffusion-based model employed.

5.3.2 Dendritic solidification

As shown before, the typical length scale of dendritic freezing of the bulk liquid is in the range $\delta_T \sim 5 \times 10^{-7} \ldots 5 \times 10^{-6}\,\mathrm{m}$ which is much smaller than the typical length scale of the Hele-Shaw cell. In contrast to the initial ice layer growth, an influence of the substrate material on dendritic freezing of the bulk is therefore not expected. Accordingly, the examination of dendritic freezing is restricted to copper as the substrate material. In the following, the freezing morphologies depending on the liquid supercooling are presented and discussed with respect to freezing morphologies described for dendritic freezing in a liquid film of supercooled water, freely suspended. Moreover, measured front velocities are discussed with respect to experimental data for the tip velocity of a single dendrite and the theoretical predictions of the marginal stability theory.

5.3.2.1 Morphology classification

According to [181], for a water supercooling $\Delta T < 2.7\,\mathrm{K}$ dendritic freezing is absent, and the ice layer growth parallel to the substrate surface is followed by the growth of ice normal to the surface, representing an increase of the thickness of the initial ice layer. However, in the case of a supercooling $\Delta T > 2.7\,\mathrm{K}$, they observed that the thin ice layer on top of the substrate becomes unstable at a certain position behind the tip of the propagating ice layer, resulting in the growth of dendritic ice into the bulk liquid. For the range of relatively low supercooling, they observed single dendrites and hexahedral shapes of ice crystals emerging from the initial ice layer on the substrate. In the present study, the freezing process is observed for a significantly wider range of liquid supercooling up to $\Delta T \approx 20.0\,\mathrm{K}$. It has been found that not only a transition between the cases of purely planar and dendritic ice growth within the bulk, but also several further transitions between different modes of dendritic growth occur at larger supercooling.

The different growth modes are categorized in Tab. 5.4. Vertical lines in the shown photographs indicate the position of the first observable instability of the ice layer, whose tip is on the left boundary of each photograph. As already observed in [181] and described above, for low supercoolings the initial ice layer remains stable and its thickness increases by planar growth normal to the substrate's surface. In this case, the dendritic freezing phase is not observable. While [181] reported a threshold for unstable growth at $\Delta T \approx 2.7\,\mathrm{K}$, the transition has been found in the present study

Table 5.4: Different freezing regimes during dendritic solidification depending on the liquid supercooling. The ice layer propagates from the right to the left and its tip is at the left side of each photograph. The inserted vertical lines mark the position of first visible instabilities of the ice layer. (Reprinted table (adapted) with permission from [321]. Copyright 2016 by the American Physical Society.)

Description	ΔT in K	Detail
Planar	0 ... 4.7	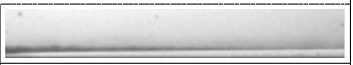
Late dendrites	4.7 ... 7.2	
Single dendrites	7.2 ... 9.9	
Inhomogeneous front	9.9 ... 12.0	
Homogeneous front	12.0 ...	

to occur at $\Delta T \approx 4.7\,\mathrm{K}$. For larger supercooling between $\Delta T \approx 4.7\,\mathrm{K}$ and $\Delta T \approx 7.2\,\mathrm{K}$, the ice layer becomes unstable long time after the growth of the initial ice layer, when the layer has already covered a large part of the wetted substrate surface. As also observed in [181], this instability results in the growth of single dendrites. For a supercooling in the range of approx. $\Delta T = 7.2 \ldots 9.9\,\mathrm{K}$, many more single dendrites and hexahedral ice crystals emerge from the ice layer than in the case of lower supercooling. Moreover, the time of their appearance after the initial ice layer growth is much shorter, i.e. they appear closer behind the tip of the initial ice layer, as shown in Tab. 5.4. In the range between $\Delta T \approx 9.9\,\mathrm{K}$ and $\Delta T \approx 12.0\,\mathrm{K}$, not only single dendrites but a mesh of dendrites evolves at a small distance behind the moving ice layer tip. In this case, the individual dendrites can no longer be identified in the high-speed videos. Their orientation seems random, resulting in an inhomogeneous distribution of ice, as shown in the respective photograph in Tab. 5.4. If the supercooling is even higher, $\Delta T > 12.0\,\mathrm{K}$, the dendrites all seem to be oriented parallel, resulting in a homogeneous ice distribution after dendritic solidification.

All dendrites grow at the same speed, resulting in the parallel propagation of a relatively smooth envelope of the mushy ice-water region, as already shown in Fig. 5.6. The position of the first instability behind the tip generally depends on the supercooling. The higher the supercooling, the closer to the ice layer tip is the position of the first instability of the initial ice layer's surface. Only a small mutual influence of the dendrites can be observed for small supercoolings. Accordingly, all dendrites propagate at approx. the same speed as a single dendrite. Mutual effects between the dendrites in a dendrite cloud increase with increasing supercooling, as will be shown in the following section.

As already mentioned in the previous section, several growth morphologies during dendritic freezing of a supercooled water film have been reported in [332]; they are illustrated in Fig. 5.17. For very small supercooling $\Delta T < 0.5\,\mathrm{K}$, a quasi-isotropic dense-branching structure without a preferred growth direction is observed (a). For increasing supercooling $\Delta T \approx 0.5 \ldots 4.5\,\mathrm{K}$, only well defined individual dendrites with typical thicknesses of a few hundreds of micrometers are reported (b). For $\Delta T \approx 4.5 \ldots 7.5\,\mathrm{K}$ two different morphologies have been observed: a single needle-like dendrite (c), and a tree-like *"fractal needled branch"* consisting of up to hundred needles (d), in which an individual needle grows with an approx. 1.5 times larger average tip velocity compared to a single needle-like dendrite. In the range $\Delta T \approx 7.5 \ldots 12.5\,\mathrm{K}$, three morphologies namely the *"fractal needled branch"* (d), the *"compact needled branch"* (e), and the *"platelet"* (f) exist. The first two morphologies are characterized by a dense packing of small dendrites with an individual size of a few tens of micrometers. The platelet morphology is well known appearing for example in staggered form in frozen aqueous food such as soups. Depending on the direction of observation, these platelets either appear as a needle-like dendrite (in a side-view), or a thin homogeneous ice layer (in a top view). In the case of the fractal needled branch, the orientation of the individual dendrite branches is ordered in several growth directions, while the dendrites all appear parallel in the case of the compact needled branch. For $\Delta T > 12.5\,\mathrm{K}$, only the compact needled branch, and platelet morphologies have been observed, whereas platelet is the only morphology reported for $\Delta T > 16.0\,\mathrm{K}$.

Most of the transition temperatures, and morphologies reported in [332] can be related to the morphological transitions observed in the present study. For $\Delta T > 12.5\,\mathrm{K}$, only the compact needled branch, and platelet morphologies are reported, which both are characterized by a homoge-

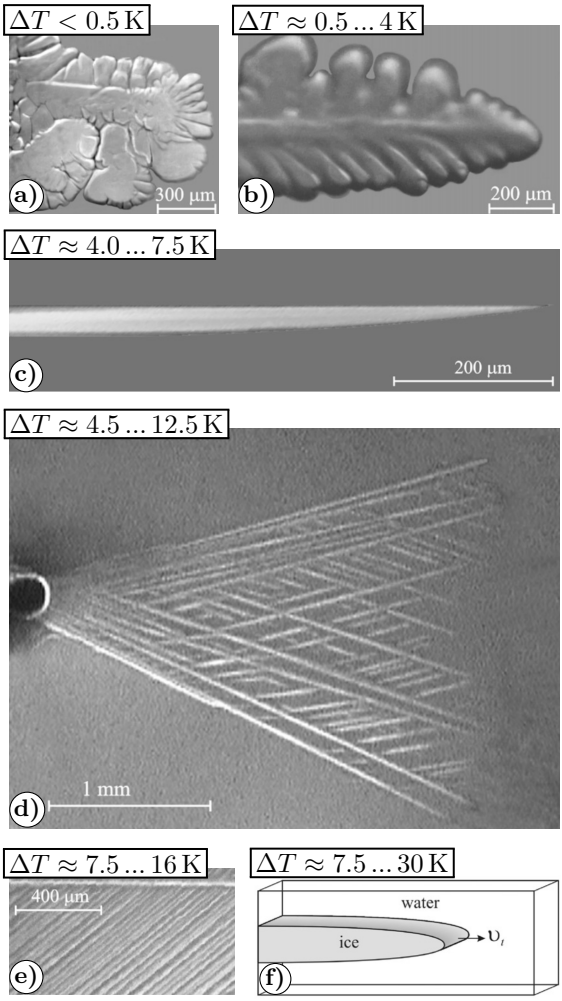

Figure 5.17: Photographs of the freezing morphologies of supercooled water as a function of supercooling reported in [332]: a) fragment of a dense-branching structure, b) dendrite, c) neddle-like crystal, d) fractal needled branch, e) compact needled branch, and f) platelet. (Reprinted from [332], with permission from Elsevier.)

neous ordering of the growing ice. This explains the present observation of a homogeneous front of dendrites for $\Delta T > 12.0\,\mathrm{K}$. The more inhomogeneous appearance of the dendrite front observed for $\Delta T \approx 7.2 \ldots 12.0\,\mathrm{K}$ may be explained by the possible co-existence of the fractal needled branch reported for the range $\Delta T \approx 7.5 \ldots 12.5\,\mathrm{K}$, which is characterized by a more disordered arrangement of dendrites. However, in both cases of front propagation for $\Delta T > 7.2\,\mathrm{K}$, no individual dendrites are observed in the present study due to a limited optical resolution of the high-speed videos, which does not allow resolving of the filigree dendrite structure. For $\Delta T \approx 4.7 \ldots 7.2\,\mathrm{K}$, where larger individual dendrites and needle like crystals have been reported, the optical resolution of the present high-speed videos is sufficient to identify the individual dendrites. In the present study, no dendritic growth is observed for $\Delta T < 4.7\,\mathrm{K}$, while the growth of individual dendrites is reported in [332] also for $\Delta T < 4.0\,\mathrm{K}$. Unfortunately, this discrepancy can not be explained. However, the present observation of the absence of dendrites for low supercooling is in agreement with the observations reported in [181]; even though the found thresholds deviate from each other.

5.3.2.2 Front velocity

The front velocity of the dendrite cloud propagating through the drop's bulk, v_{fro}, is shown as a function of supercooling in Fig. 5.18. Depending on the liquid supercooling and according to the categorization in Tab. 5.4, it represents the velocity of the dendrite tips, or the normal velocity of the envelope of the dendrite cloud, measured close to the substrate surface. For comparison, the tip velocity of a freely growing single dendrite, experimentally obtained in [332] and [121], and the theoretical predictions for the tip velocity of a single dendrite according to the marginal stability theory [190, 191, 241] are also shown in the figure. For a supercooling of up to $\Delta T \approx 10.0\,\mathrm{K}$, the front velocity obtained from the present experiments compares well with the tip velocity of a single dendrite. Due to the relatively large spacing between the dendrites in this temperature range (see Tab. 5.4), the influence of neighboring dendrites on the growth velocity of an individual dendrite is negligible, as already shown numerically in [77]. For a larger supercooling, the velocity of a single dendrite tip and the front velocity of a dendrite cloud increasingly deviate. It is worth to note that the supercooling associated with an increasing deviation between the velocity of a single dendrite and a dendrite cloud, $\Delta T \approx 10\,\mathrm{K}$, well coincides with the previously found threshold subdividing the growth of single

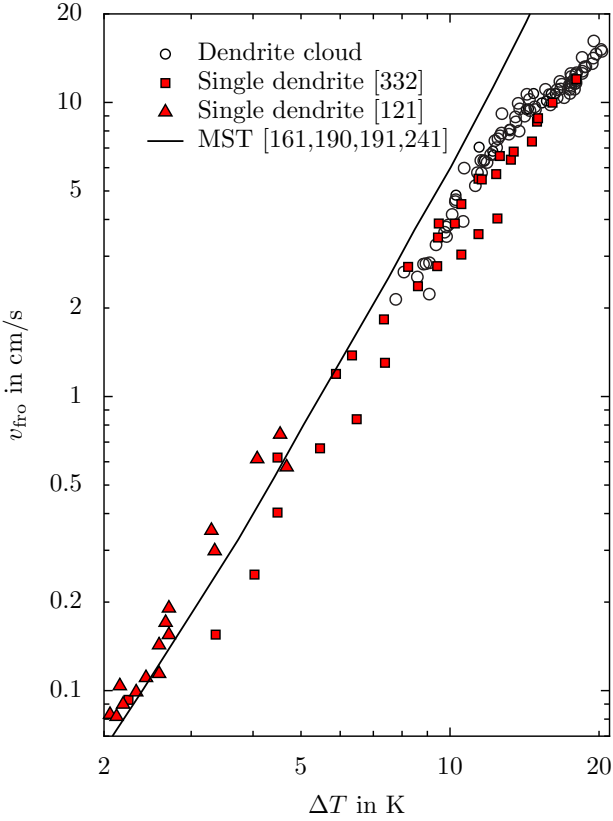

Figure 5.18: Normal front velocity of a dendrite cloud propagating through the bulk liquid as a function of liquid supercooling. Depending on supercooling, this velocity represents the dendrite tip velocity, or the normal velocity of the envelope of the dendrite cloud. Comparison with results for a single dendrite tip from [121, 332], and the theoretical predictions for the dendrite tip velocity according to the marginal stability theory [161, 190, 191, 241].

dendrites from inhomogeneous front propagation in the bulk liquid (see Tab. 5.4).

Due to kinetic effects, for $\Delta T > 5\,\mathrm{K}$ the tip velocity of a single dendrite

significantly spreads and is reduced with respect to the theoretical prediction. The deviation between the theory and the experimentally obtained tip velocity increases for increasing supercooling. Similar to the tip velocity of a single dendrite, also the experimentally obtained front velocity of a dendrite cloud is generally smaller than the velocity calculated using the marginal stability theory. However, the measured front velocity of a dendrite cloud only slightly spreads, and is larger than that of a single dendrite. Therefore, its deviation from the theory is smaller than that of a single dendrite velocity. As a consequence, the measured front velocity remains in rather good agreement with the theoretical predictions up to a supercooling of $\Delta T \approx 12\,\mathrm{K}$. This indicates a mutual thermal influence between the individual dendrites in the cloud, which seems to compensate kinetic effects. This observation is well comparable to the increased tip velocity of the dendrites in a fractal needled branch compared to the tip velocity of an individual dendrite, as reported in [332] and mentioned in the previous section.

For larger supercooling of approx. $\Delta T > 12\,\mathrm{K}$, the front velocity of a dendrite cloud significantly deviates from the theory. Moreover, in the range $\Delta T \approx 14.0 \ldots 17.5\,\mathrm{K}$ virtually no increase of the front velocity is observed for increasing supercooling, which is probably attributed to kinetic effects and an increased mutual influence between the dendrites in the dendrite cloud. However, for $\Delta T > 17.5\,\mathrm{K}$, the front velocity again increases with increasing supercooling, and also compares well again with the tip velocity of a single dendrite.

5.3.2.3 Conclusion

The dendritic freezing of supercooled water in contact with a solid substrate has been experimentally investigated for a liquid supercooling up to $\Delta T \approx 20\,\mathrm{K}$, and the results have been discussed with respect to theoretical and experimental results available in the literature. After heterogeneous nucleation at the substrate, an ice layer forms on the substrate's surface. Depending on the liquid supercooling, the ice layer eventually becomes unstable resulting in delayed growth of single dendrites, or a heterogeneous or homogeneous cloud of dendrites into the bulk liquid. The threshold for stable ice layer growth has been found as $\Delta T \approx 4.7\,\mathrm{K}$. Furthermore, it has been shown that the aforementioned growth morphologies can be categorized with respect to the liquid supercooling. For moderate supercooling, $\Delta T \approx 4.7 \ldots 7.7\,\mathrm{K}$, only few dendrites grow into the liquid.

They arise delayed with respect to the beginning of ice layer growth. For larger supercooling, $\Delta T \approx 7.7 \ldots 9.9\,\mathrm{K}$, much more dendrites form with a significantly decreased delay after ice layer formation. For both regimes, the velocity of the growing dendrites is well comparable with the velocity of a single dendrite growing in supercooled water. Thus, neighboring dendrites do not affect the growth rate of an individual dendrite in this regime. For larger supercooling, $\Delta T \approx 9.9 \ldots 12.0\,\mathrm{K}$, a heterogeneous cloud of dendrites is observed, where individual dendrites could not be identified with the present experimental setup. The growth velocity of a single dendrite is significantly decreased and spread due to kinetic effects in this supercooling range, while the front velocity of the dendrite cloud is larger than the tip velocity of an individual dendrite, which is in accordance with observations in [332]. Therefore, the front velocity of the dendrite cloud is still comparable to the theoretical predictions of the marginal stability theory, indicating that mutual thermal influences between the individual dendrites compensate kinetic effects. For even larger supercooling, $\Delta T > 12.0\,\mathrm{K}$, the dendrite cloud appears as a homogeneous cloud whose front velocity increasingly deviates from the theoretical dendrite velocity up to a supercooling of $\Delta T \approx 14.0\,\mathrm{K}$. As indicated by the present results, kinetic effects during the propagation of a cloud of dendrites gain importance at a different temperature in comparison to the case of a single dendrite, or an ice layer growing along a solid substrate. While these effects play an important role for a supercooling greater than approx. $\Delta T = 4 \ldots 5\,\mathrm{K}$ in the case of a single dendrite [332], and for a supercooling greater than $\Delta T \approx 10\,\mathrm{K}$ in the case of an ice layer forming on a solid substrate, they seem to be significant above a supercooling of $\Delta T \approx 14\,\mathrm{K}$ for the case of the propagation of a cloud of dendrites. For a larger supercooling at first the front velocity of the dendrite cloud virtually does not increase with increasing supercooling. It increases again for an even higher supercooling above, $\Delta T \approx 17.5\,\mathrm{K}$. For these supercoolings the process appears to be entirely dominated by kinetic effects, since no mutual influence of the dendrites is observed, and as a consequence the normal growth velocity of the dendrite cloud again equals that of a single dendrite.

Parts of the work presented in the following chapter are based on the Bachelor-Thesis of Thoren Webert [374], and have already been published and presented in the following publications and conference contributions:

[319] M. Schremb, I.V. Roisman and C. Tropea. Normal impact of supercooled water drops onto a smooth ice surface: Experiments and modeling. *Journal of Fluid Mechanics*, 835:1087-1107, 2018.

[322] M. Schremb and C. Tropea. Experimental investigation of supercooled water drops impacting onto a smooth ice surface: Interaction of fluid flow and phase change. In *Proceedings of the 9^{th} World Conference on Experimental Heat Transfer, Fluid Mechanics and Thermodynamics*, Foz do Iguaçu, Brazil, 2017.

[358] C. Tropea, M. Schremb and I. Roisman. Physics of SLD impact and solidification. In *Proceedings of the 7^{th} European Conference for Aeronautics and Aerospace Sciences*, Milan, Italy, 2017.

6 Fluid flow and phase change during drop impact onto ice

The present chapter is devoted to the impact of supercooled water drops onto an ice surface, which is experimentally examined, and theoretically modeled. While a rather separate examination of the processes involved in ice accretion was the focus of the previous chapters, the present chapter in particular aims on the interaction of fluid flow and solidification during ice accretion due to impinging supercooled water drops.

As shown in the previous chapters, solidification fixes the shape of an impinging drop, and determines the surface area finally iced after drop impact. Stochastic nucleation during drop impact onto a dry surface results in a significantly varying freezing delay after impact; drop impact and solidification do not necessarily start at the same time. As a consequence, also the final outcome in terms of the iced surface area after a single drop impact drastically varies. So far, only the tangential extent of the ice splat on the impact surface has been considered. Contrary, the focus of the present chapter is on the influence of the impact conditions, and initial temperatures on the residual ice layer thickness resulting from the impact

of an individual supercooled water drop. The experiments are performed using an ice impact surface which acts as a uniform and immediate nucleator. By this, stochastic nucleation is suppressed, and drop spreading and freezing of the liquid begin simultaneously, resulting in repeatable experiments and an unique outcome for certain impact conditions.

The impact and solidification of water drops, initially being at room temperature, onto an ice surface have already been investigated in [166]. However, to the author's knowledge the impact of individual supercooled water drops onto a smooth ice surface, resulting in immediate solidification of the impacting supercooled drop, has never been studied before. In the present study, the influence of varying drop and surface temperatures, and a varying impact velocity on the lamella thinning and the residual ice layer thickness after a single drop impact at subfreezing conditions is experimentally examined. Using a high-speed video system and backlight shadowgraphy imaging, the impact process is captured with a high spatial and temporal resolution in a side-view. The lamella thinning and residual ice layer thickness are determined from the captured high-speed videos.

In the following, at first the experimental method is introduced. To understand the results of the present study, the involved mechanisms and mutual influences during drop impact onto an ice surface are phenomenologically described. Quantitative results for the lamella thinning and residual ice layer thickness are presented for varying impact conditions for both isothermal and non-isothermal drop impact. Based on a postulated flow in the spreading lamella, the upper limit for the residual ice layer thickness after a single drop impact is theoretically modeled, considering both dendritic solidification of the supercooled drop and the expansion of the viscous boundary layer in the spreading lamella. Using the derived scaling law, a semi-empirical relation is proposed which allows an accurate a-priori prediction of the final ice layer thickness resulting from a single drop impact, knowing the impact conditions.

6.1 Experimental method

The experimental setup used for the present study has already been described in Chap. 3. It has been used for all studies of drop impact in the present work, and is modified for the present study to allow observation of the impact process in a side-view. In comparison to the previous studies, no flat impact surface, but a cylindrical aluminum impact target is placed

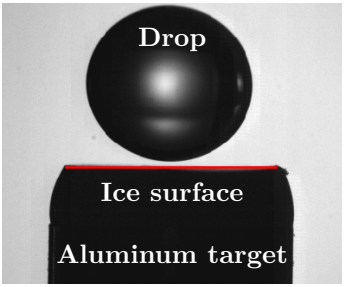

Figure 6.1: A falling drop prior to impact onto the ice impact surface prepared on a cylindrical aluminum target.

on the cooling plate. Water drops impact onto a smooth ice surface, existing at the hollow upper end of the impact target, as illustrated in Fig. 6.1. The ice surface is generated by freezing a water drop placed in the cavity of the impact target inside of the lower styrofoam chamber of the experimental setup. Afterwards, the hemispherical frozen drop is horizontally cut using a razor blade outside of the chamber. After cutting the frozen drop, the impact target comprising the ice surface is reinserted into the chamber. Ice which eventually melted during cutting refreezes again in the chamber, and may lead to a bumpy surface attributed to the volume expansion of water during freezing (see Sec. 5). To smooth the ice surface, the previous procedure comprising cutting outside of the chamber and reinserting of the target into the chamber is repeated until the surface is identified as reasonably flat in the live view of the high-speed camera. The temperature of the ice impact surface is measured with a thermocouple immersed into the impact target, ending in the ice surface.

With a diameter of approx. 5 mm, the size of the ice impact surface is comparable to the drop diameter and therefore, it is smaller than the maximum spread of the impacting drop. Liquid is ejected from the edges of the impact surface during spreading, and the formation of a pronounced rim around the center of impact, which would prevent the observation of the entire process of lamella thinning, is suppressed. Therefore, the lamella thinning and the resulting ice layer thickness in the center of drop impact can be observed undisturbed. This method has been used in several previous studies [299, 300], and an influence of the ejection of the lamella on the measurement of the lamella thickness in the center of drop impact is not expected.

Table 6.1: Summary of the impact conditions and temperatures used for the study of drop impact onto an ice surface.

Parameter	Value	Unit
d_d	3.4 ± 0.1	mm
v_d	2.2 ± 0.02 & 3.2 ± 0.02	m/s
ϑ_d	$-16.0 \ldots -6.0$	°C
ϑ_w	$-16.0 \ldots -6.0$	°C
Re	2130 ... 4860	-
We	210 ... 454	-
Pr	17 ... 29	-

Similar to the previous studies in the present work, purified deionized water (*Millipore, Milli-Q® Type 1*, electrical conductivity $\gamma_\mathrm{el} = 5.5 \times 10^{-6}\,\mathrm{S/m}$ at 25 °C) is used to generate the drops and the ice surface. The drop diameter d_d is kept constant and has been measured for all investigated temperatures from multiple separate calibration videos as $d_\mathrm{d} = 3.4 \pm 0.1\,\mathrm{mm}$. The impact velocity v_d is varied between $v_\mathrm{d} = 2.2 \pm 0.02\,\mathrm{m/s}$ and $v_\mathrm{d} = 3.2 \pm 0.02\,\mathrm{m/s}$; it has also been determined from separate calibration videos for each temperature. The drop and surface temperature are varied between $\vartheta = -16\,^\circ\mathrm{C}$ and $\vartheta = -6\,^\circ\mathrm{C}$. Experiments are performed for both isothermal and non-isothermal impact conditions. With consideration of the temperature dependence of the liquid properties, the impact Reynolds and Weber numbers in the present study are in the range Re = 2130 ... 4860 and We = 210 ... 454, respectively. The experimental conditions are summarized in Tab. 6.1.

The impact process is captured in a side view using a high-speed video camera (*Photron, Fastcam SA 1*), a long distance microscope (*Navitar, 6000 Zoom lens*) and LED backlight illumination. To increase the temporal and spatial resolution of the high-speed videos captured during the experiments, the field of view is reduced and only the lower half of a drop is visible at the moment of its first contact with the ice surface. The impact process is recorded with 10000 fps and an optical resolution of approx. 5.5 µm/pixel to allow an accurate measurement of the transient lamella thinning and the residual ice layer thickness.

6.2 Qualitative description

In the previous Chaps. 3 and 5, both the impact and freezing process have been examined separately, depending on the impact conditions and temperatures. As shown in Chap. 4, due to stochastic nucleation, the impact and freezing process do not necessarily start simultaneously in the case of drop impact onto a dry surface, and therefore also their mutual interaction is subject to the stochastic freezing delay. To prevent stochastic nucleation and guarantee fluid flow and liquid freezing to begin simultaneously during drop spreading, the experiments regarding solidification during drop impact are performed using an ice impact surface. It acts as an uniform and immediate nucleator resulting in a high repeatability of the experiments due to the absence of any stochastics during phase change. As a consequence, the processes taking place during the impact of a supercooled water drop onto an iced surface are very different from the processes during the impact onto a dry solid surface. Therefore, they are qualitatively compared with each other in the following, using the previous findings of the present work.

As shown in Chap. 4, in the case of drop impact onto a dry substrate, stochastic nucleation results in strongly varying freezing delay times after impact, which in turn causes a varying final outcome after drop impact. Nucleation occurs at a discrete number of nucleation sites on the wetted solid substrate. As shown in Chap. 5, nucleation is followed by the spreading of a thin ice layer along the solid surface. Its velocity is constant in time but depends on the liquid supercooling and the thermal properties of the substrate. Depending on the supercooling of the liquid, the ice layer becomes unstable and results in dendritic solidification of the bulk liquid. The dendrite cloud can be identified as the dark region radially expanding in the top-view photographs of a supercooled water drop impacting onto a sandblasted aluminum surface, shown in Fig. 6.2. As shown in Chap. 5, the rate of expansion of the dark region in the top-view photographs does not represent the front velocity of the dendrite cloud, but the horizontal velocity of the initial ice layer spreading along the substrate, which is unaffected by the fluid flow during drop impact.

When the thickness of the dendrite cloud equals the thickness of the liquid film on the substrate, the current shape of the deformed liquid is fixed, as shown in Fig. 6.2 for $t > 8.0\,\mathrm{ms}$. For the illustrated case, the thin liquid lamella at the position of nucleation is fixed at first. The remainder of the liquid is almost unaffected by freezing, as indicated by the further

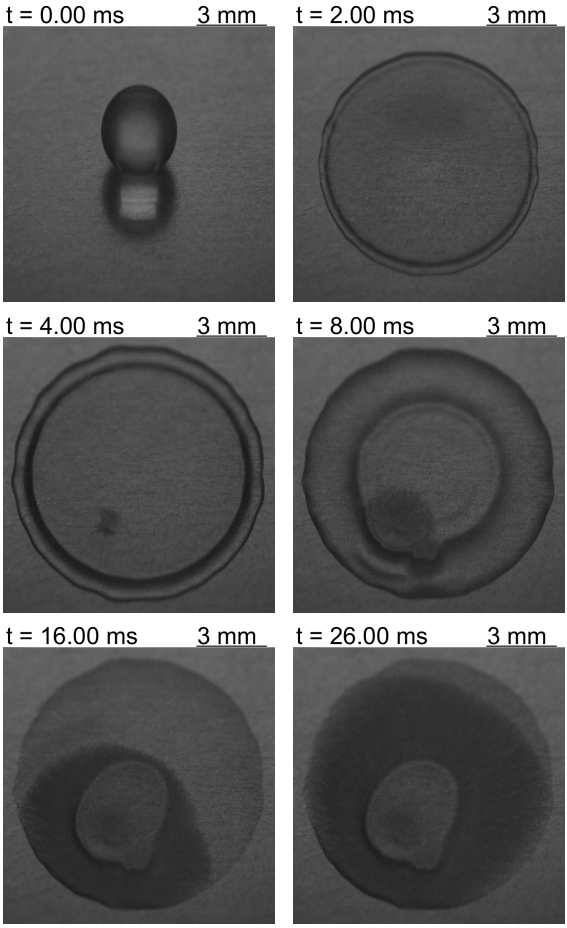

Figure 6.2: Top view observation of a normal impact of a water drop onto a sandblasted aluminum surface, both being at $\vartheta = -16.6\,^{\circ}\mathrm{C}$. Nucleation at a single nucleation site is followed by the radial expansion of a thin ice layer along the substrate (not visible in the images) and dendritic freezing of the bulk liquid above the ice layer (expanding dark region in the images), fixing the shape of the deformed drop. (Reproduced with permission from [319]. Copyright 2018 by Cambridge University Press.)

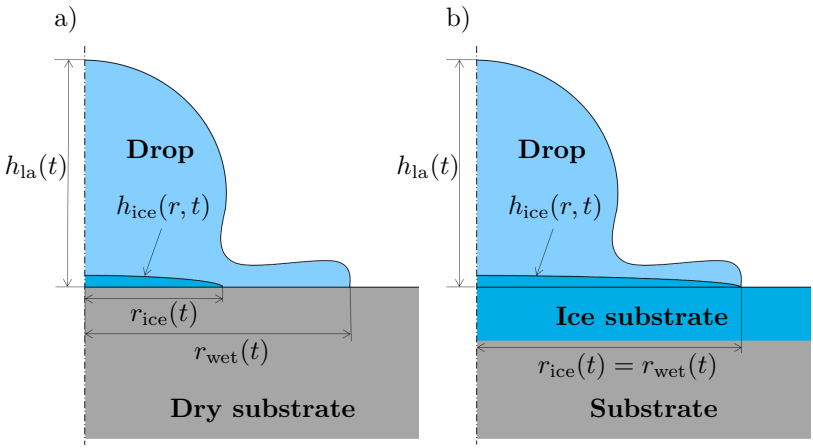

Figure 6.3: Two-dimensional schematic of solidification during impact of a supercooled drop onto a) a dry surface, and b) onto an ice surface. (Reproduced (adapted) with permission from [319]. Copyright 2017 by Cambridge University Press.)

decrease of the thin lamella region from $t = 8.0\,\mathrm{ms}$ to its form, ultimately fixed at $t = 16.0\,\mathrm{ms}$. Solidification of the liquid remaining after dendritic freezing is accompanied by an increase of the final ice layer thickness due to the volume expansion during further freezing (not shown in the figure).

Nucleation does not necessarily take place at the impact position, as shown in Fig. 6.2. However, for simplicity the radial spreading of both the spreading initial ice layer and the drop are assumed axisymmetric in the schematic illustration of the process in Fig. 6.3 a). As indicated in Figs. 6.2 and 6.3 a), the tangential expansion of the initial ice layer along the solid substrate, $r_{\mathrm{ice}}(t)$, is independent of the radial extent of the impinging drop, $r_{\mathrm{wet}}(t)$. Only the initial temperatures and thermal properties of both the drop and the substrate determine the contact temperature at the wetted surface, which is the characteristic temperature for heterogeneous nucleation and subsequent ice layer spreading, as demonstrated in Chap. 5. The ice layer spreading and dendritic freezing appeared to be independent of drop impact. Contrary, their influence on drop impact and its final outcome is significant, and depends on the instant of nucleation.

Bringing an ice crystal into contact with supercooled water results in immediate freezing of the supercooled water. A solid-liquid interface to

which water molecules may attach already exists; thus the energy barrier for nucleation is absent. Accordingly, when a supercooled water drop impacts onto an ice surface, the ice impact surface induces immediate freezing of the impinging liquid. The formation of the new ice layer does not start at a single nucleation site, but immediately when the supercooled liquid makes contact with the ice surface; i.e. at the moving three phase contact line of the spreading drop, where liquid gets into contact with the impact surface by a rolling motion [290]. Therefore, a distinct horizontal spreading of an ice layer is absent, and the radial expansion of the newly formed ice layer and the spreading of the drop are directly connected to each other: the radius of the new ice layer equals the spreading radius of the drop at every moment, $r_{\mathrm{ice}}(t) = r_{\mathrm{wet}}(t)$, as illustrated in Fig. 6.3 b). Hence, in contrast to a drop impact onto a dry solid surface, the radial expansion of the new ice layer during drop impact onto an ice surface mainly depends on the spreading of the impacting drop. It only indirectly depends on the initial temperatures and thermal properties, which may affect the hydrodynamics of drop spreading. Similar as in the case of drop impact onto a dry solid substrate, the propagation of the dendrite cloud through the spreading drop after the initial ice layer became unstable, mainly depends on the liquid temperature.

Figure 6.4 shows the impact process of a supercooled water drop at $\vartheta_{\mathrm{d},0} = -14.0\,^{\circ}\mathrm{C}$ onto the ice impact target at $\vartheta_{\mathrm{sub},0} = -14.0\,^{\circ}\mathrm{C}$ [1]. At time $t = 0$ the drop makes contact with the ice impact surface and begins to spread over the surface. Simultaneously, freezing of the supercooled liquid starts at the solid-liquid interface. The moving contact line reaches the edge of the ice surface at $t \approx 0.36\,\mathrm{ms}$ and for $t > 0.36\,\mathrm{ms}$, the spreading liquid is ejected from the edge of the ice surface. It forms a free expanding liquid sheet around the impact target while the lamella continues thinning above the impact surface. Since the drop diameter is comparable to the diameter of the ice impact target, the liquid sheet is not ejected horizontally but under a certain angle to the horizontal, as already reported in [299]. For the illustrated case, the minimum thickness of the lamella is reached at $t \approx 3.36\,\mathrm{ms}$, when the dendrite cloud fills out the entire lamella. The new layer on top of the ice impact surface consists of an array of dendrites surrounded by liquid water, both at the melting temperature T_{m}.

[1] Note that the photographs in Fig. 6.4 only serve for illustration of the entire impact process. The measurements shown in the present study have been obtained based on a spatial resolution approx. three times higher, as can be seen in Fig. 6.6.

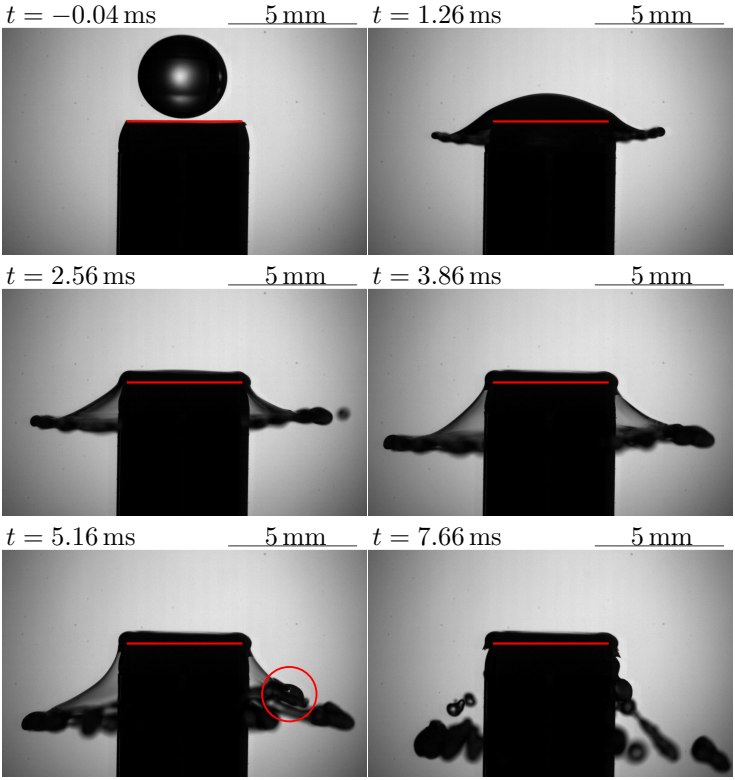

Figure 6.4: Dynamics during impact of a water drop supercooled to $\vartheta_{\mathrm{d},0} = -14.0\,^{\circ}\mathrm{C}$ onto a small ice impact target at $\vartheta_{\mathrm{sub},0} = -14.0\,^{\circ}\mathrm{C}$. The red horizontal lines indicate the surface of the ice impact surface. The red circle in the fifth frame marks a position of freezing in the free liquid lamella, causing rupturing of the thin liquid film. (Reproduced with permission from [319]. Copyright 2018 by Cambridge University Press.)

At $t \approx 5.16\,\mathrm{ms}$, the ejected liquid sheet ruptures and consequently detaches from the newly formed layer. Rupturing begins at the location marked with a red circle in the fifth frame of Fig. 6.4, which was previously located at the rim surrounding the lamella. At this position freezing of the free liquid film can be observed in the high-speed video. It is probably

caused by a seeding ice crystal transported from the ice impact surface into the ejected lamella. As shown in the last photograph in the figure, freezing is not only observed at the position marked in the fifth frame, but in almost every fragment of the rim around the free liquid sheet. While most of the secondary droplets generated from the rupturing sheet are liquid, the major part of the rim in the last frame of Fig. 6.4 is frozen, which can be identified by means of the shape, clarity and translucence of the different fragments. A reason for the predominance of freezing in the rim may be seeding ice crystals which are detached from the ice impact surface by the high shear rate, especially during the beginning of the spreading process. The process of triggering solidification with a crystal of the same material is often referred to as secondary nucleation [242]. In the present special case it is related to the Hallet-Mossop process, which is well known in the scope of cloud glaciation. The Hallet-Mossop process describes an increased drop freezing rate in glaciating clouds (commonly referred to as ice multiplication or secondary ice production) due to riming ice particles, from which ice splinters detach; e.g. due to drop impact onto rimed particles [137, 247, 280]. In the present case, due to larger shear during the first stage of drop spreading, relatively more seeding crystals are detached and carried away from the ice impact surface than in later stages of spreading. The liquid spreading during the beginning of drop impact later forms the rim surrounding the free lamella, whose freezing is presumably initiated by the seeding crystals detached from the surface during early stages of drop spreading. Since the seeding crystals can unfortunately not be observed in the high-speed videos, this is only a hypothetical explanation of the reason for the predominance of freezing in the rim.

For small propagation velocities of the dendrite cloud, i.e. for high liquid temperatures, the lamella reaches its minimum thickness without being filled out completely by the dendrite cloud. The minimum lamella thickness in this situation is mainly determined by the impact conditions such as for drop impact without phase change. In this case, a capillary wave propagates along the upper free surface of the liquid lamella after the temporary minimum of the lamella thickness is reached. The wave affects the measurement of the lamella thickness in the center of drop impact, as will be shown later. However, for increasing growth rates of the dendrite cloud, i.e. for lower temperatures, a significant influence of a capillary wave on the thickness measurement is absent. In these cases, thinning of the lamella is stopped when it is completely filled out by dendrites.

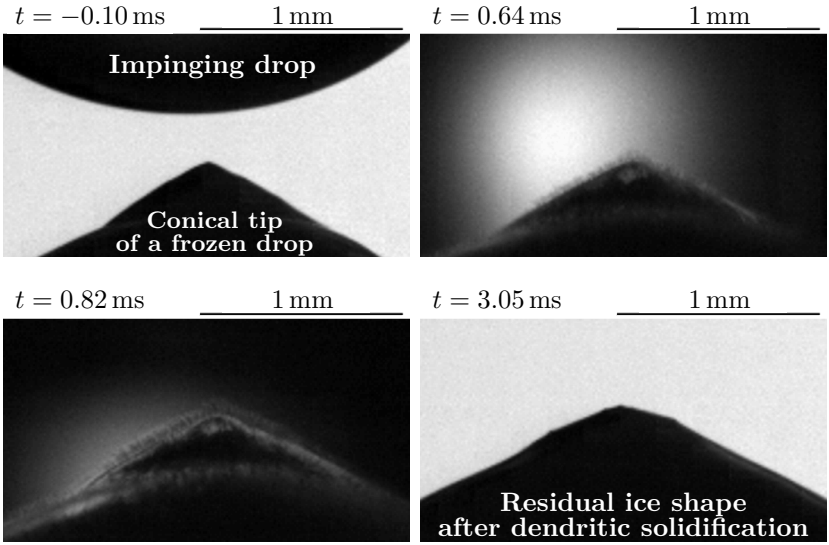

Figure 6.5: Detail of an isothermal impact ($d_\mathrm{d} = 3.4\,\mathrm{mm}$, $v_\mathrm{d} = 3.2\,\mathrm{m/s}$, $\vartheta = -14.0\,^\circ\mathrm{C}$) of a supercooled water drop onto a frozen drop, which exhibited the typical conical cusp shape after freezing (see Chap. 5). After first contact with the frozen drop, the impinging liquid freezes dendritically, which is clearly visible at times $t > 0.64\,\mathrm{ms}$, where the dendrite cloud appears as a hairy fuzz on the surface of the conical impact surface. Note that the curved drop surface causes significant refraction, preventing quantification of the dendrite propagation during impact.

Due to bad optical access into the impinging drop, the dendrite cloud propagation can not be observed in side-view photographs of normal drop impact onto a flat ice surface, as shown in Fig. 6.4. Therefore, the evolution of the dendrite cloud during an isothermal impact ($d_\mathrm{d} = 3.4\,\mathrm{mm}$, $v_\mathrm{d} = 3.2\,\mathrm{m/s}$, $\vartheta = -14.0\,^\circ\mathrm{C}$) of a supercooled water drop onto a frozen drop, which exhibited the typical conical cusp shape after freezing (see Chap. 5), is shown for demonstration in Fig. 6.5. The drop's conical cusp penetrates into the impinging liquid and by this, observation of the freezing process at the top of the frozen drop is possible through the side of the impinging drop; i.e. almost perpendicular to the drop surface without total reflection at the drop surface, which prevents observation during

impact onto a flat surface. As shown in the photographs, in particular for $t > 0.64\,\mathrm{ms}$ the propagation of the dendrite cloud is clearly visible. The dendrite cloud appears as a hairy fuzz on the surface of the conically frozen drop. Refraction at the curved drop surface prevents detailed quantification of the dendrite cloud propagation during drop impact. Nevertheless, a significant increase of the dendrite cloud thickness can be clearly observed from $t = 0.64\,\mathrm{ms}$ to $t = 0.82\,\mathrm{ms}$. Moreover, comparison of the resulting ice layer in the last frame, with the shape of the conically impact surface in the first frame, allows estimation of the mean dendrite cloud velocity during drop impact. Lamella thinning is finished after $t \approx 3.05\,\mathrm{ms}$ (i.e. in the last photograph in the figure) at all positions in the depicted detail of the process. However, the residual ice layer thickness above the tip of the conical impact surface is already reached approx. 2.21 ms after impact. The ice layer thickness at this position can be estimated from the high-speed video as $h_{\mathrm{lay,res}} \approx 200\,\mu\mathrm{m}$. Using the time required for reaching this thickness, the mean front velocity of the dendrite cloud during drop impact can be estimated as $v_{\mathrm{fro}} \approx 9.47\,\mathrm{cm/s}$, which is in very good agreement with the front velocity of the dendrite cloud in a sessile water drop. For a liquid temperature of $\vartheta = -14.0\,^{\circ}\mathrm{C}$, the mean measured front velocity has been obtained as $v_{\mathrm{fro}} \approx 9.33\,\mathrm{cm/s}$ (see Fig. 5.18). Concluding, both the shown photographs and the estimation of the front velocity of the dendrite cloud confirm the previous explanations of the processes involved in drop impact onto ice, which later are the basis for mathematical modeling.

After partial dendritic solidification of an impinging drop, the remaining liquid water freezes on a time scale several orders of magnitude longer than that of the dendritic freezing phase, as shown in Chap. 5. It results in an increasing ice layer thickness due to the volume expansion during solidification. Although the ultimate residual ice layer thickness is reached just after this second phase of solidification, the processes during the first dendritic phase of solidification ($t < 3.36\,\mathrm{ms}$ for the case shown in Fig. 6.4) are the focus of the present study. Moreover, in all following considerations, the thin initial ice layer, which eventually grows into the bulk liquid prior to dendritic freezing, is neglected. As already mentioned in Chap. 5, the typical thickness of this layer is $\sim 10^{-5}\,\mathrm{m}$ [181]. Therefore, the ice layer is very thin compared to both the drop size in the present experiments, and the measured thickness of the residual ice layer after drop impact. Hence, its contribution to the resulting ice layer thickness is negligible, and dendritic solidification is assumed as the dominating mechanism for

the lamella freezing, which is assumed to begin immediately after first contact between the liquid and the ice impact surface.

6.3 Quantitative results

Post-processing of the experimental video data yields the temporal evolution of the entire drop and lamella profile, as illustrated in Fig. 6.6 for isothermal drop impact at $\vartheta = -16.0\,^{\circ}\mathrm{C}$, and an impact velocity of $v_\mathrm{d} = 3.2\,\mathrm{m/s}$. However, all following data concerning the lamella thinning refer to the lamella thickness in the center of drop impact, extracted from the obtained lamella profile at $r = 0$. The evolution of the lamella thickness and the residual ice layer thickness at this position is considered as a characteristic measure for the entire process. As shown in the figure, which can be assumed representative for all experiments of the present study, the initial ice layer is not perfectly smooth; the unevenness varies between the different experiments. Nevertheless, the experimental data are highly reproducible as will be shown in the following. Concluding, deviations from a perfectly smooth ice layer surface are negligible for the lamella thinning in the center of drop impact.

For each set of impact conditions, the experiment has been repeated at least six times to verify the repeatability, and to increase the statistical significance of the experimental results. Figure 6.7 shows the temporal evolution of the lamella thickness measured for the eight repetitions of isothermal drop impact with $\vartheta = -14.0\,^{\circ}\mathrm{C}$ (Fig. 6.7 a)) and $\vartheta = -6.0\,^{\circ}\mathrm{C}$ (Fig. 6.7 b)) as dashed lines; in both cases for an impact velocity of $v_\mathrm{d} = 2.2\,\mathrm{m/s}$. The averaged data of the repetitions is shown in the figure as solid lines. As mentioned earlier and shown in Fig. 6.6, to increase the spatial resolution in the captured high-speed videos, only a portion of an impacting drop is visible at the instant of first contact between the drop and the surface. Hence, the measurement of the lamella thickness for $v_\mathrm{d} = 2.2\,\mathrm{m/s}$ is only possible for $t > 0.81\,\mathrm{ms}$, when the north pole of the impacting drop is in the field of view of the camera. The averaged data shown in Fig. 6.7 for $0 < t < 0.81\,\mathrm{ms}$ are obtained from cubic interpolation of the measured data for $t > 0.81\,\mathrm{ms}$ and $h_\mathrm{la}(t{=}0) = d_\mathrm{d}$.

As shown in Fig. 6.7 a) for the case of $\vartheta = -14.0\,^{\circ}\mathrm{C}$, the lamella thickness is in very good agreement for all experiments during the entire time of lamella thinning. The variation between the largest and the smallest measured lamella thickness with respect to the mean thickness is below

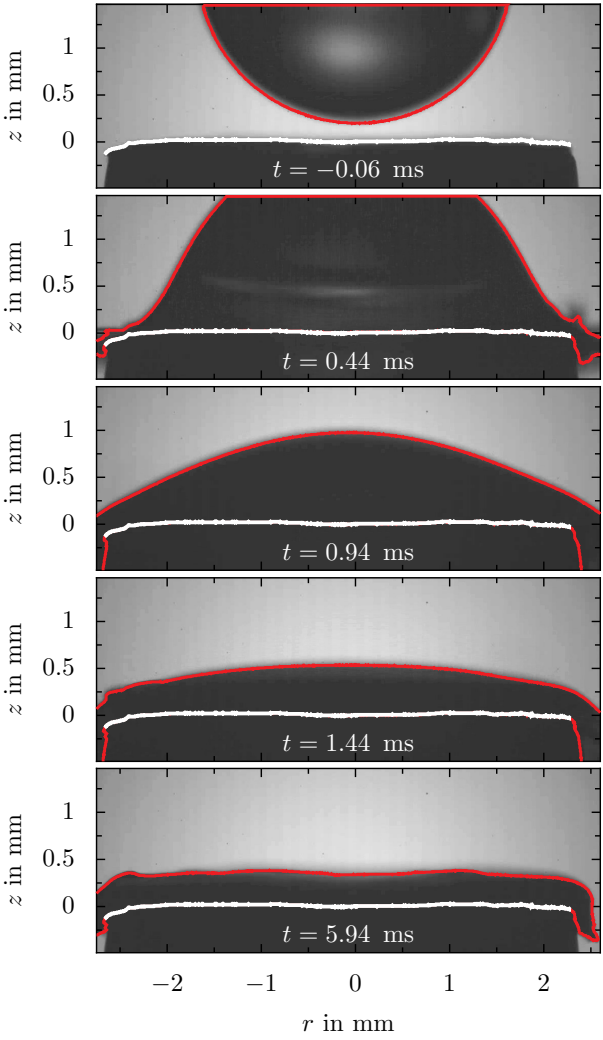

Figure 6.6: Evolution of the lamella profile during isothermal drop impact at $\vartheta = -16.0\,^{\circ}\mathrm{C}$ with $v_\mathrm{d} = 3.2\,\mathrm{m/s}$. The drop and upper lamella surface detected during post-processing are shown in red, the ice layer surface is emphasized as a white line.

a) Repeated isothermal drop impacts with $\vartheta = -14.0\,°\mathrm{C}$.

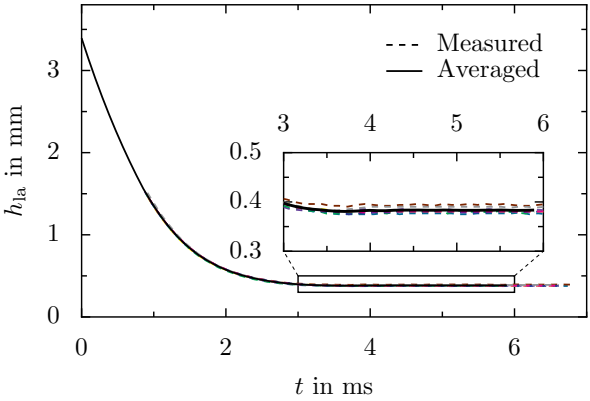

b) Repeated isothermal drop impacts with $\vartheta = -6.0\,°\mathrm{C}$.

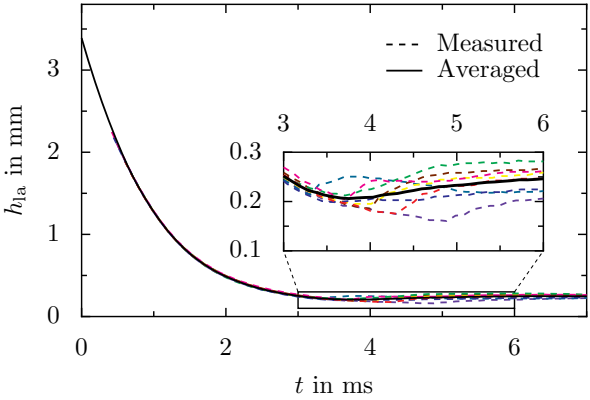

Figure 6.7: Measurement and averaging of the temporal evolution of the lamella thickness in the center of drop impact, $r = 0$. The data is shown for eight repetitions of isothermal impact at a) $\vartheta = -14.0\,°\mathrm{C}$ and b) $\vartheta = -6.0\,°\mathrm{C}$, both with $v_{\mathrm{d}} = 2.2\,\mathrm{m/s}$. Measurement and averaging begin at $t \approx 0.81\,\mathrm{ms}$. The averaged data for $t < 0.81\,\mathrm{ms}$ is based on cubic interpolation. (Reproduced (adapted) with permission from [319]. Copyright 2017 by Cambridge University Press.)

4.6 % at all times. Thus, the experimental results are in general highly reproducible, and obviously unaffected by any variations which would result from stochastic nucleation.

In the case of a smaller liquid supercooling, $\Delta T < 8\,\mathrm{K}$, the small propagation velocity of the dendrite cloud, and the resulting capillary waves along the drop surface cause a significantly higher variation of the lamella thickness. Due to small variations of the morphology of the ice impact surface, the propagation of the capillary wave is not reproducible, and in turn the measured lamella thickness varies between the different experiments, as indicated in Fig. 6.7 b). The largest difference between the maximum and minimum measured lamella thickness of two different experiments during the propagation of the capillary wave is observed for the smallest investigated supercooling of $\Delta T = 6\,\mathrm{K}$; with respect to the mean value it is approx. 56 %. However, with respect to its averaged value, the measurement of the final ice layer thickness varies by only 17.4 % for these conditions, which is the maximum relative variation of the final ice layer thickness observed for all experiments. The absolute variation of the measurement of the final thickness is almost constant and in all cases below $\pm 21.5\,\mu\mathrm{m}$. Therefore, the measurement of the final ice layer thickness is highly repeatable for all temperatures, and the averaged data can be considered as representative for the respective conditions.

6.3.1 Isothermal drop impact

Without consideration of phase change, the evolution of the lamella thickness of an impacting drop for impact Reynolds and Weber numbers of $\mathrm{Re} \gg 25$ and $\mathrm{We} \gg 2.5$ can be described using Eqs. 2.4 - 2.7 (see Sec. 2.1). Both the Reynolds and Weber number in the present study are well above these thresholds. Therefore, in particular the inviscid solution, Eqs. 2.4 and 2.5, may serve as a reference for the experimental results concerning lamella thinning during the initial stages of drop impact.

Figures 6.8 a) and b) show the temporal evolution of the lamella thickness for varying temperatures during isothermal drop impact with $v_\mathrm{d} = 2.2\,\mathrm{m/s}$ and $v_\mathrm{d} = 3.2\,\mathrm{m/s}$, respectively. For comparison, the evolution of the lamella thickness calculated with Eqs. 2.4 and 2.5 is also shown in the figures. These relations are respectively valid in the ranges $t < 0.62\,\mathrm{ms}$ and $t > 1.08\,\mathrm{ms}$ for the small impact velocity, and $t < 0.43\,\mathrm{ms}$ and $t > 0.74\,\mathrm{ms}$ for the high impact velocity, which is indicated by dashed vertical lines illustrating the limits of validity in the figures. It should

a) Varying temperature during isothermal impact with $v_\mathrm{d} = 2.2\,\mathrm{m/s}$.

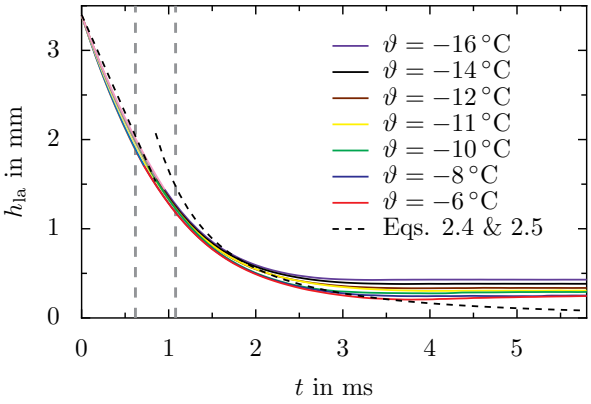

b) Varying temperature during isothermal impact with $v_\mathrm{d} = 3.2\,\mathrm{m/s}$.

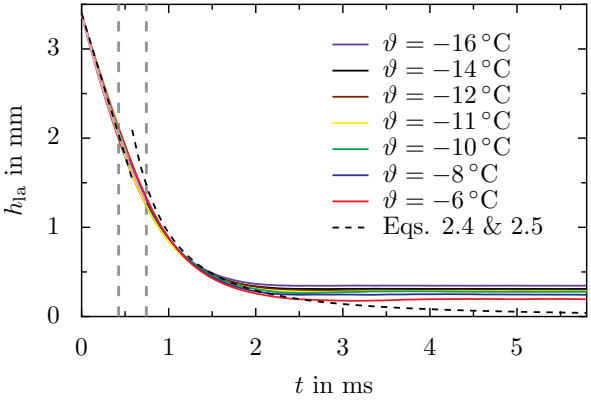

Figure 6.8: Lamella thinning during isothermal drop impact, depending on the drop impact velocity and initial temperature. The dashed black lines are theoretical predictions according to Eqs. 2.4 and 2.5. Vertical dashed gray lines represent the corresponding limits of validity. (Reproduced with permission from [319]. Copyright 2018 by Cambridge University Press.)

be mentioned again that the data shown for the early phase of drop impact has been interpolated from the measured data using a cubic polynomial. Nevertheless, the model assuming a constant decrease of the lamella

thickness, Eq. 2.4, is in very good agreement with the interpolated data, indicating that the velocity of the rear part of an impacting drops indeed does not significantly change during the initial phase of drop impact.

In the investigated temperature range, the kinematic viscosity of water significantly varies, $\nu \approx 2.25 \ldots 3.51\,\mathrm{m^2/s}$, which potentially could influence the impact process. However, for the ranges of the Reynolds and Weber numbers in the present study, inertia dominates the impact process; viscous and surface tension effects can be neglected. Accordingly, the lamella thickness is only slightly influenced by the different temperatures for $t < 1.5\,\mathrm{ms}$. Moreover, up to $t \approx 3.5\,\mathrm{ms}$ for the small impact velocity, and up to $t \approx 2.5\,\mathrm{ms}$ for the high impact velocity, the theoretical predictions are in very good agreement with the experimental data for the smallest supercooling. This agreement confirms the irrelevance of viscosity effects, since these are not accounted for in the theoretical model, Eqs. 2.4 and 2.5. As shown in Chap. 5, for the highest temperature $\vartheta = -6.0\,^\circ\mathrm{C}$ no propagation of a cloud of dendrites, but the growth of single dendrites is observed during dendritic freezing. The number of dendrites and their growth rate are relatively small and therefore, the lamella thinning is almost unaffected by the growing dendrites as implied by the good agreement between the theory and the experimental results. For the smallest supercooling, the capillary wave propagating along the upper lamella interface leads to a temporary rise of the measured lamella thickness for $t > 3.7\,\mathrm{ms}$ in the case of the small impact velocity, and for $t > 3.0\,\mathrm{ms}$ in the case of the high impact velocity. Due to an increased rate of lamella thinning for the higher impact velocity, the increase of the lamella thickness due to the capillary wave is less pronounced than for the lower impact velocity.

For long times after impact when the thickness of the lamella is of the order of the viscous boundary layer thickness, Eq. 2.5 for the flow in a spreading drop without phase change is no longer valid since viscosity damps the flow in the lamella. In the absence of solidification, the residual lamella thickness after drop impact for this case can be estimated using Eq. 2.8, yielding a residual lamella thickness of approx. $100\,\mu\mathrm{m}$ for the present study. This is much smaller than the residual thicknesses experimentally observed for all shown conditions, indicating the dominant influence of solidification on the flow in the spreading lamella. As shown in Fig. 6.8 for both impact velocities, a decreasing temperature causes a decreasing speed of lamella thinning, finally resulting in a larger residual ice layer thickness. The growth rate and number of the dendrites, consti-

tuting the dendrite cloud, increases with lower temperatures and causes an increasing influence of phase change on the flow in the spreading drop. Due to a faster decrease of the flow cross section in the lamella, the rate of lamella thinning is reduced. Moreover, the shape of the thinning lamella is fixed earlier, which finally results in a larger residual lamella thickness.

6.3.2 Non-isothermal drop impact

During non-isothermal drop impact, heat is transferred between the impinging liquid and the impact surface. It results in a temporal change of the liquid temperature during impact, which may cause an altered speed of solidification. Thus, by affecting the solidification process, the heat transfer during non-isothermal drop impact could also influence the fluid flow in the thinning lamella, eventually resulting in an altered residual ice layer thickness.

The temporal evolution of the lamella thickness depending on the initial drop and surface temperature is shown in Fig. 6.9. While Fig. 6.9 a) shows the influence of a varying drop temperature for the case of a constant surface temperature, $\vartheta_{\mathrm{sub},0} = -11.0\,^{\circ}\mathrm{C}$, the influence of a varying surface temperature in the case of a constant drop temperature, $\vartheta_{\mathrm{d},0} = -11.0\,^{\circ}\mathrm{C}$, is shown in Fig. 6.9 b). For comparison, the results obtained for isothermal drop impact at $\vartheta = -16.0\,^{\circ}\mathrm{C}$ and $\vartheta = -6.0\,^{\circ}\mathrm{C}$ are shown in the figures as gray solid lines.

As shown in Fig. 6.9 a), the initial drop temperature has a strong influence on the lamella thinning. Similar to the isothermal case, the residual ice layer thickness significantly increases for decreasing liquid temperature. Both the evolution of the lamella thickness and the resulting ice layer thickness are well comparable with the results of the isothermal experiments at the respective drop temperature. A capillary wave results in a pronounced increase of the lamella thickness for non-isothermal drop impact with $\vartheta_{\mathrm{d},0} = -6.0\,^{\circ}\mathrm{C}$, as already observed for isothermal drop impact. However, the increase of the lamella thickness in the non-isothermal case is more pronounced than in the isothermal case.

As indicated in Fig. 6.9 b), no clear correlation can be observed between the temperature of the ice impact surface and the resulting lamella thinning. Moreover, the variation of the lamella thinning is of the order of the measurement accuracy in the present experiments. Therefore, the results for non-isothermal drop impact at $\vartheta_{\mathrm{d},0} = -11.0\,^{\circ}\mathrm{C}$ are almost unaffected

a) Varying initial drop temperature with $\vartheta_{\mathrm{sub},0} = -11.0\,^{\circ}\mathrm{C}$.

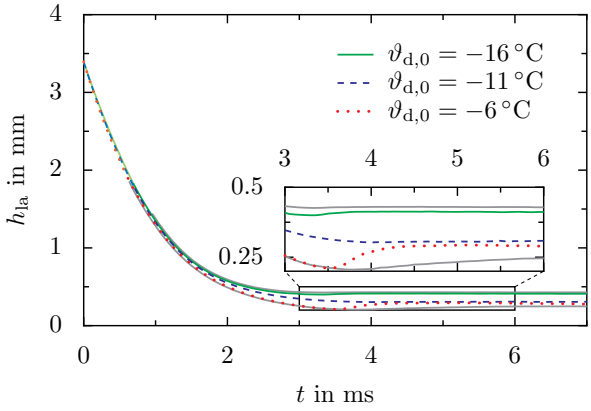

b) Varying initial substrate temperature with $\vartheta_{\mathrm{d},0} = -11.0\,^{\circ}\mathrm{C}$.

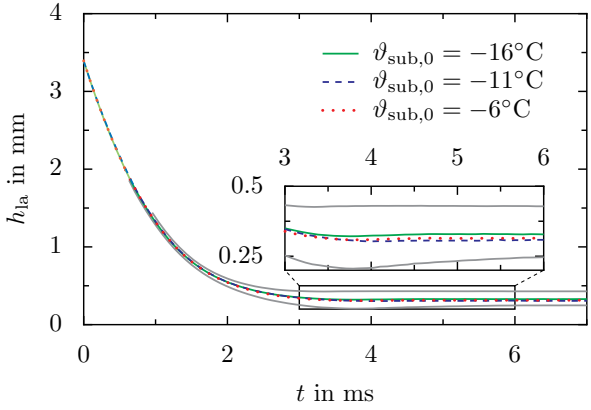

Figure 6.9: Temporal evolution of the lamella thickness during non-isothermal drop impact with $v_{\mathrm{d}} = 2.2\,\mathrm{m/s}$, depending on the initial drop and surface temperature. Either the drop (a)) or substrate (b)) temperature is varied while the remaining temperature is $\vartheta = -11.0\,^{\circ}\mathrm{C}$. For comparison, gray solid lines show the results of isothermal impact at $\vartheta = -16.0\,^{\circ}\mathrm{C}$ (upper curve) and $\vartheta = -6.0\,^{\circ}\mathrm{C}$ (lower curve). (Reproduced (adapted) with permission from [319]. Copyright 2017 by Cambridge University Press.)

by the temperature of the ice impact surface, which implicitly confirms the estimations and descriptions in Chap. 5 regarding the irrelevance of a substrate on dendritic freezing of the bulk liquid. During dendritic solidification of the bulk liquid, only the liquid temperature is relevant for the freezing process. Neither the substrate thermal properties, nor its temperature affect dendritic freezing of the bulk. Concluding, a variation of the temperature of the ice impact surface is negligible for the propagation of the dendrite cloud and, if at all, it has a minor influence on the temporal lamella thinning and the resulting ice layer thickness after drop impact.

The observed indifference of dendritic bulk freezing to the substrate temperature becomes clearer by a description of the physics during non-isothermal drop impact. Thermal boundary layers develop in both the ice impact surface and the impinging liquid. Solidification of the supercooled liquid may only be affected by the substrate when the thickness of the dendrite cloud is smaller than the thickness of the thermal boundary layer in the spreading drop. When the dendrite cloud is thicker than the thermal boundary layer, propagation of the front of the dendrite cloud is unaffected by the substrate. The thickness of the dendrite cloud can be estimated as $h_{\mathrm{ice}} \sim v_{\mathrm{fro}} t$, i.e. it linearly increases with time. The thickness of the thermal boundary layer in the liquid can be estimated as $h_{\mathrm{tbl}} \sim \sqrt{at}$. The boundary layer expansion is associated with an infinite velocity at $t = 0$, which decreases with time as $\sim t^{-0.5}$. Therefore, at the beginning of drop impact, the thermal boundary layer is thicker than the expanding dendrite cloud. However, after a certain time the dendrite cloud thickness overcomes the thermal boundary layer thickness; i.e. the influence of the substrate on dendritic bulk freezing decreases with time. With the propagation velocity of the front of dendrites, $v_{\mathrm{fro}} \sim 10^{-1}\,\mathrm{m/s}$ (see Chap. 5), and the thermal diffusivity of water, $a \sim 10^{-7}\,\mathrm{m^2/s}$, the instant after impact, when the dendrite cloud thickness equals the thermal boundary layer thickness, is estimated as $t \sim 10^{-2}\,\mathrm{ms}$. This time is very small, and thus a thermal influence of the impact surface on dendritic solidification of the spreading drop is negligible over a wide range of impact conditions; in particular for those of the present study, where the typical time of drop impact is $t_{\mathrm{imp}} = d_{\mathrm{d}}/v_{\mathrm{d}} \sim 1\,\mathrm{ms}$. Therefore, the liquid temperature dominates dendritic solidification of the impinging liquid and a thermal influence of the impact surface on the propagation of the dendrite cloud is negligible. Thus, also the lamella thinning and the resulting ice layer thickness are unaffected by the temperature of the ice impact surface, as demonstrated in Fig. 6.9.

6.4 Mathematical modeling

As shown in the previous section, solidification of the spreading liquid, which primarily depends on the liquid temperature, significantly influences lamella thinning and the residual ice layer thickness resulting from a single drop impact. Taking into account the propagation of the dendrite cloud and the viscous boundary layer developing in the spreading lamella, the influence of solidification on fluid flow during normal drop impact onto a flat surface is theoretically modeled. Utilizing the axisymmetry of the problem, an upper bound for the final ice layer thickness after the first phase of solidification is derived.

The model is based on the assumption that the dendrites in the cloud are strong enough, not to be damaged by the flow in the lamella. This assumption is supported by the fact that the yield stress of ice ($Y \sim 10\,\mathrm{MPa}$ [329]) is much higher than the stresses associated with drop impact ($p \sim \rho v_\mathrm{d}^2 \sim 10^{-3} \ldots 10^{-1}\,\mathrm{MPa}$). In addition, estimation of the front velocity of a dendrite cloud emerging during drop impact onto a conically frozen drop, shown in Fig. 6.5, revealed that the dendrite cloud propagation is not significantly affected by fluid flow during drop impact. The estimated front velocity during drop impact is well comparable to the front velocity in a sessile drop obtained in Chap. 5.

The upper bound for the residual ice layer thickness after normal drop impact onto a flat ice surface can be evaluated assuming that the velocity of the liquid flow in the porous dendrite/liquid cloud is much smaller than the flow velocity in the lamella above the cloud. A viscous boundary layer develops above the upper envelope of the expanding dendrite cloud whose position is $z_\mathrm{env} = v_\mathrm{fro,z}(t - t'(r))$, where $v_\mathrm{fro,z}$ is the z-component of the front velocity of the dendrite cloud and $t'(r)$ denotes the instant when freezing begins at the radial coordinate r, i.e. when the contact line reaches position r. As shown in Chap. 5, for the case of heterogeneous nucleation on a solid substrate, the front of the dendrite cloud forms a certain angle with the substrate surface during propagation through the supercooled liquid. According to the explanations in Chap. 5, this angle depends on the ratio between the normal propagation velocity of the dendrite cloud, v_fro, and the horizontal velocity of the initial ice layer, $v_\mathrm{lay,x}$, which initiates freezing of the bulk liquid; it can be estimated as $\sin^{-1}(v_\mathrm{fro}/v_\mathrm{lay,x})$. In the case of the present experiments, nucleation is absent and solidification is not triggered at a single nucleation site. Freezing of the bulk liquid is not initiated by a spreading initial ice layer but

by spreading of the liquid itself, as described in one of the previous sections. Therefore, the angle between the front of dendrites and the ice impact surface depends on the ratio between the normal propagation velocity of the dendrite cloud and the contact line velocity of the spreading drop, v_{cl}. The mean contact line velocity during spreading on the ice impact target, is estimated from Fig. 6.4 to be of the order of 10^1 m/s, and the front velocity of the dendrite cloud is of the order of 10^{-1} m/s (see Chap. 5). Accordingly, the spreading velocity of the impinging drop is much higher than the dendrite cloud velocity. As a consequence, the angle between the dendrite front and the impact surface is negligible small, $\sin^{-1}(v_{\mathrm{fro}}/v_{\mathrm{cl}}) \approx 0.57\,^\circ$. This justifies neglect of the exact orientation of the dendrite cloud and to assume that the cloud propagates in the z-direction normal to the impact surface, thus $v_{\mathrm{fro,z}} \approx v_{\mathrm{fro}}$. It is worth noting that this assumption is supported by the photographs in Fig. 6.5, where the thickness of the dendrite cloud is equal at each position of the conical ice impact surface.

The velocity field in the liquid lamella above the dendrite cloud fulfills the continuity equation and momentum equation

$$\frac{\partial}{\partial r}(ru_{\mathrm{r}}) + \frac{\partial}{\partial y}(ru_{\mathrm{y}}) = 0 \tag{6.1}$$

$$r\frac{\partial u_{\mathrm{r}}(r,y,t)}{\partial t} + \frac{\partial}{\partial r}(ru_{\mathrm{r}}^2) + \frac{\partial}{\partial y}(ru_{\mathrm{r}}u_{\mathrm{y}}) = r\nu\frac{\partial^2 u_{\mathrm{r}}}{\partial y^2}, \tag{6.2}$$

and satisfies the boundary conditions

$$u_{\mathrm{r}} = 0 \quad \text{and} \quad u_{\mathrm{y}} = -v_{\mathrm{fro}}, \quad \text{for} \quad y = 0, \tag{6.3}$$

where $y = z - v_{\mathrm{fro}}(t - t'(r))$ is the vertical coordinate in a moving coordinate system fixed at the envelope of the dendrite cloud, and $u_{\mathrm{y}} = u_{\mathrm{z}} - v_{\mathrm{fro}}$ is the vertical component of the fluid velocity in this moving system; i.e. relative to the propagating dendrite front. The situation is pictured in Fig. 6.10, showing also the y-coordinate with respect to the laboratory coordinate system fixed at the surface of the initial ice layer, (r, z).

The momentum equation, Eq. 6.2, in the integral form reads

$$\lim_{\chi\to\infty}\left\{\int_0^{\chi}\left[r\frac{\partial u_{\mathrm{r}}(r,y,t)}{\partial t} + \frac{\partial}{\partial r}(ru_{\mathrm{r}}^2)\right]\mathrm{d}y + ru_{\mathrm{r}}(r,\chi,t)u_y(r,\chi,t)\right\} = -r\nu\frac{\partial u_{\mathrm{r}}}{\partial y}_{|y\to 0}. \tag{6.4}$$

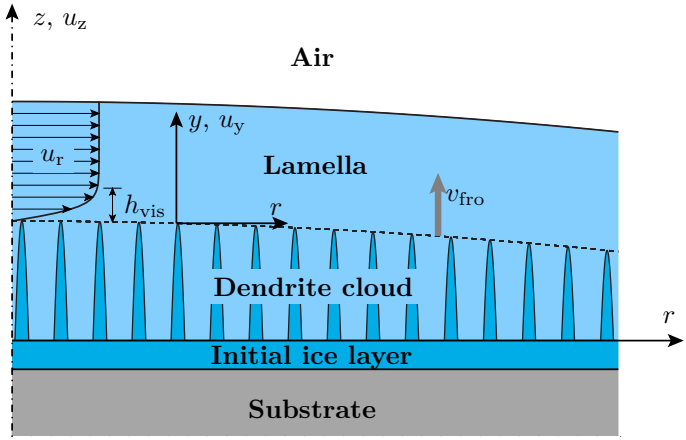

Figure 6.10: Schematic illustration of axisymmetric lamella spreading and dendrite cloud propagation during normal drop impact onto a flat ice surface.

In order to find an approximate solution for the flow in the spreading lamella, which satisfies the momentum equation in integral sense, the radial component of the flow velocity is assumed to take the form

$$u_\mathrm{r} = \frac{r}{t}\left\{1 - \exp\left[-\frac{y}{s(t)}\right]\right\}, \tag{6.5}$$

which satisfies the no-slip condition at the envelope of the cloud of dendrites, $y = 0$, and approaches the inviscid solution, Eq. 2.5, (with neglect of the parameter τ_1 involved in Eq. 2.5, which is reasonable for large times after impact) at large distances above the dendrite cloud, $y \gg s(t)$. The function $s(t)$ is associated with the temporal evolution of the viscous boundary layer thickness h_vis, and is determined in the following.

The axial component of the relative velocity, corresponding to the radial component Eq. 6.5, is found from the continuity equation, Eq. 6.1, as

$$u_\mathrm{y} = 2\frac{s(t)}{t}\left\{-\frac{y}{s(t)} + 1 - \exp\left[-\frac{y}{s(t)}\right]\right\} - v_\mathrm{fro}. \tag{6.6}$$

Substituting the assumed components of the velocity field, Eqs. 6.5 and 6.6, into the integral form of the momentum equation, Eq. 6.4, yields an

ordinary differential equation for the function $s(t)$ as

$$2ts(s' + v_{\mathrm{fro}}) + 3s^2 - 2\nu t = 0. \tag{6.7}$$

In dimensionless form it reads

$$2\xi\delta\,(\delta' + 1) + 3\delta^2 - 2\xi = 0, \tag{6.8}$$

where the dimensionless time and dimensionless boundary layer thickness are defined as

$$\xi = \frac{t v_{\mathrm{fro}}^2}{\nu} \quad \text{and} \quad \delta(\xi) = \frac{s v_{\mathrm{fro}}}{\nu}, \tag{6.9}$$

respectively. The ordinary differential equation, Eq. 6.8, can be solved numerically to obtain $s(t)$. The solution is then used for the description of the flow field in the spreading lamella according to Eqs. 6.5 and 6.6, and the derivation of the expression for the evolution of the lamella height above the rising dendrite cloud.

As shown before, the spreading velocity of a drop is much larger than the velocity of solidification. Therefore, the time for wetting $t'(r)$, which is the inverse function of the spreading radius $r_{\mathrm{wet}}(t)$, influences the solution for the flow in the lamella only in a small region near the spreading rim. This assumption is confirmed by a nearly flat ice layer, observed in the experiments. Therefore, in the major area of the wetted impact surface, $r \ll r_{\mathrm{wet}}$, the time $t'(r)$ can be neglected and the axial flow velocity can be assumed to be only a function of the axial coordinate.

Using Eq. 6.6, the axial velocity of the liquid outside the boundary layer (in the limit $y \gg s$), excluding the region in the vicinity of the rim, is obtained in the reference frame fixed at the wall, as

$$u_{\mathrm{z}} = 2\frac{s(t)}{t}\left[-\frac{z - v_{\mathrm{fro}} t}{s(t)} + 1\right]. \tag{6.10}$$

The temporal evolution of the lamella thickness in the presence of the growing ice layer is obtained as the root of the ordinary differential equation

$$\frac{\mathrm{d}h_{\mathrm{la}}}{\mathrm{d}t} = u_{\mathrm{z}}. \tag{6.11}$$

Using the solution of Eq. 6.8, the lamella thickness is finally obtained from Eqs. 6.10 and 6.11 as

$$h_{\mathrm{la}} = \frac{\tau_2 d_{\mathrm{d}}^3}{v_{\mathrm{d}}^2 t^2} + \frac{2 v_{\mathrm{fro}} t}{3} + \frac{2}{t^2}\int_0^t \zeta s(\zeta)\mathrm{d}\zeta, \tag{6.12}$$

where the first term in this relation is an integration constant, corresponding to the inviscid solution for the lamella evolution, Eq. 2.5. This solution is re-obtained from Eq. 6.12 in the inviscid limit, i.e. $s(t) \to 0$, and $v_{\mathrm{fro}} \to 0$.

An upper bound for the residual ice layer thickness can be estimated from the instant t^*, at which the viscous boundary layer of thickness $y \sim 3s$ reaches the upper free surface of the lamella. It is determined from the condition

$$h_{\mathrm{la}}(t^*) = v_{\mathrm{fro}} t^* + 3s(t^*). \tag{6.13}$$

Using the dimensionless quantities defined in Eq. 6.9, substitution of Eq. 6.13 into Eq. 6.12 results in the dimensionless form

$$\frac{\xi^{*3}}{3} + 3\xi^{*2}\delta(\xi^*) - 2\int_0^{\xi^*} \xi\delta(\xi)\mathrm{d}\xi = \mathrm{P}, \quad \mathrm{P} \equiv \frac{\tau_2 d_{\mathrm{d}}^3 v_{\mathrm{fro}}^5}{\nu^3 v_{\mathrm{d}}^2}, \tag{6.14}$$

where P is a dimensionless scaling of the impact conditions, the temperature dependent dendrite cloud velocity, and the liquid properties. The factor $y/s \approx 3$, chosen for the condition to obtain t^*, corresponds to the y-position in the viscous boundary layer where the radial velocity attains $1 - \exp(-3) \approx 0.95$ of the outer flow velocity. Equation 6.13, i.e. $h^* = h_{\mathrm{la}}(t^*)$ represents an upper bound for the residual ice layer thickness. At times $t > t^*$ the viscous boundary layer is as thick as the liquid lamella above the dendrite cloud, and consequently the flow in the lamella is quickly damped by viscosity, resulting in only minor further lamella thinning. Using the dimensionless quantities defined in Eq. 6.9, the relation for the residual lamella thickness is obtained from Eq. 6.13 as

$$h^* \approx [\xi^* + 3\delta(\xi^*)] \frac{\nu}{v_{\mathrm{fro}}}, \tag{6.15}$$

where $\xi^*(\mathrm{P})$ can be computed from Eq. 6.14 using the solution for $\delta(\xi)$ obtained from Eq. 6.8.

For calculating the parameter P for the present impact experiments, the temperature dependence of the kinematic viscosity is generally taken into account, using literature values [367]. When the drop makes contact with the ice layer, dendritic freezing of the impinging liquid results in a warm up of the dendrite cloud to T_{m}. Consequently, besides the viscous boundary layer, also a thermal boundary layer expands in the spreading liquid above the dendrite cloud. The thickness of the viscous and the thermal boundary layers in the spreading drop can be estimated as

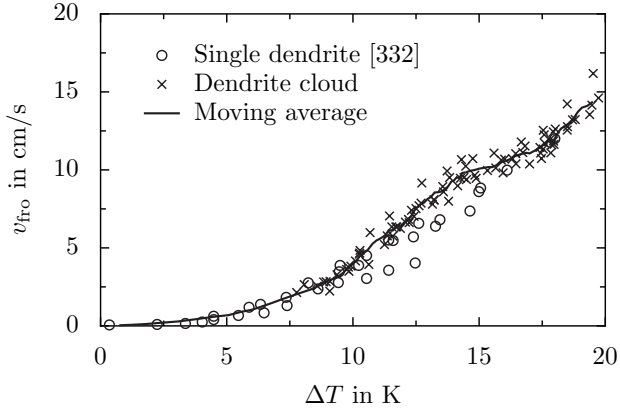

Figure 6.11: Freezing velocity of water depending on supercooling, for a single dendrite tip from [332] (circles), and a cloud of dendrites from the present work (crosses). The solid line is the moving average of the dendrite data for $\Delta T < 9.9\,\mathrm{K}$, and a dendrite cloud for $\Delta T > 9.9\,\mathrm{K}$. (Reproduced with permission from [319]. Copyright 2018 by Cambridge University Press.)

$\sim\sqrt{\nu t}$ and $\sim\sqrt{at}$, respectively. Their ratio $\mathrm{Pr}^{0.5} = \sqrt{\nu/a}$ is much larger than unity for all impact conditions in the present study, meaning that the viscous boundary layer thickness is larger than the thickness of the thermal boundary layer at any time during drop spreading. Therefore, the warm up of the dendrite cloud does not significantly affect the flow in the spreading liquid, and therefore the initial drop temperature is used to determine the liquid viscosity for the calculation of the parameter P.

Experimental data for the front velocity of the expanding dendrite cloud, v_{fro}, which have been obtained in Chap. 5, are used for the calculation of P. They are shown in Fig. 6.11 together with experimental data for the tip velocity of a single dendrite from [332]. Since no functional relation for an adequate description of the velocity data can be found, the calculations are performed using an interpolation of the moving average of the experimental data for v_{fro}. The moving average is obtained from the data for the velocity of a single dendrite for $\Delta T < 9.9\,\mathrm{K}$, and the front velocity of a dendrite cloud for $\Delta T > 9.9\,\mathrm{K}$, using a window size containing eight data pairs. The chosen threshold, $\Delta T = 9.9\,\mathrm{K}$, corresponds to the threshold subdividing the growth regime of single dendrites from

the regime of an inhomogeneous cloud of dendrites, found in Chap. 5. For $\Delta T < 9.9\,\mathrm{K}$, the dendrite velocity obtained in the present study compares very well with the velocity reported in [332]. However, an increasing deviation can be observed for greater supercooling, where the front velocity of a dendrite cloud is significantly increased compared to the velocity of a single dendrite, as shown in Fig. 6.11. The obtained moving average yields a smooth function which well describes the experimental data for the tip and front velocity in the entire temperature range.

The computed values of the dimensionless thickness, $h^* v_{\mathrm{fro}}/\nu$, as a function of the parameter P are shown in Fig. 6.12 as a dashed line. For comparison, the results for the final ice layer thickness, experimentally obtained in the present study, are shown in the figure as symbols. The theoretical prediction for the upper bound of the ice layer thickness is in very good agreement with the experimental results for all impact conditions. For larger P, representative for larger d_{d} and v_{fro}, and smaller v_{d}, an increasing overestimation of the experimental data can be observed. However, more important is the fact that the functional scaling of the model is correct, implying that the model accounts for the dominant physical mechanisms taking place during the process. Therefore, as already indicated for drop impact onto a conically frozen drop, it can be concluded that the fluid flow does not affect the propagation of the dendrite cloud; neither by means of breaking of the dendrites due to shear, nor by any other influence on the solidification process. As shown in Fig. 6.11, the temperature variation in the present study is accompanied by a variation of the dendrite front velocity over an order of magnitude between $10^{-2} \ldots 10^{-1}\,\mathrm{m/s}$, while the impact velocity in the present experiments varies between $2.2 \ldots 3.2\,\mathrm{m/s}$. Nevertheless, all experimental data in Fig. 6.12 follow a clear trend, which is in particular attributed to a correct scaling of the impact conditions in the parameter P.

Therefore, the experimental data, scaled in the proposed way, represents a *master-curve*, which may be used for the derivation of a semi-empirical relation for the resulting ice layer thickness depending on the impact conditions. Using a power function as the ansatz function for the relation between the dimensionless residual lamella thickness, $h_{\mathrm{lay,res}} v_{\mathrm{fro}}/\nu$, and the parameter P, a least squares fit of the experimental data, shown in Fig. 6.12, results in

$$h_{\mathrm{lay,res}} \frac{v_{\mathrm{fro}}}{\nu} = 2.26\mathrm{P}^{0.247} \tag{6.16}$$

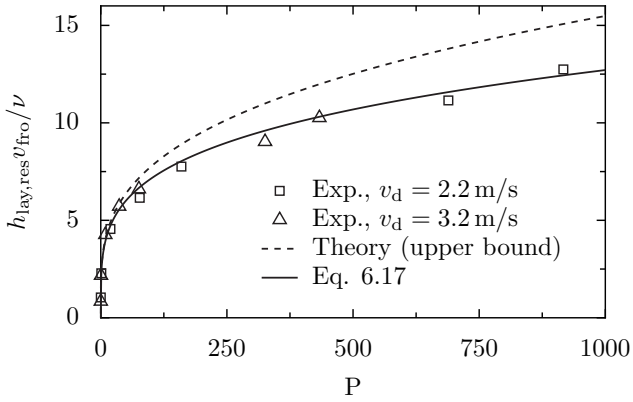

Figure 6.12: Dimensionless lamella thickness as a function of the dimensionless parameter P defined in Eq. 6.14. Comparison of experimental results (symbols) with theoretical predictions for the upper bound of the residual lamella thickness (dashed line) and the semi-empirical equation 6.17 (solid line). (Reproduced (adapted) with permission from [319]. Copyright 2017 by Cambridge University Press.)

which can be approx. simplified to

$$h_{\mathrm{lay,res}} \frac{v_{\mathrm{fro}}}{\nu} \approx 2.26 \frac{d_{\mathrm{d}}^{3/4} \tau_2 v_{\mathrm{fro}}^{5/4}}{\nu^{3/4} v_{\mathrm{d}}^{1/2}}. \tag{6.17}$$

The approximate relation Eq. 6.17 is also included in Fig. 6.12. As shown in the figure, the experimental data is well described by the found relation for all impact conditions, confirming the model's capabilities in predicting the final ice layer thickness after impact of a supercooled water drop for impact conditions varying over a wide range.

6.5 Conclusions

In the present study, the normal impact of supercooled water drops on an ice impact surface has been experimentally investigated for the first time. The most important difference between the impact of a supercooled water drop onto a dry solid surface, and the impact onto an ice surface

is the instant when freezing begins. Nucleation is stochastic in the case of an impact onto a dry solid surface, resulting in varying outcomes of such a drop impact. In contrast, solidification starts simultaneously with the impact process in the case of a drop impact onto ice, which allows reproducible investigation of the mutual influences between fluid flow and solidification during the impact of a supercooled water drop. It has been shown that beginning at the ice surface, a dendrite cloud grows through the spreading drop in the normal direction to the impact surface. It fixes the momentary shape of the deformed liquid, resulting in the formation of an ice layer on top of the initial ice surface. As shown for the impact onto a conically frozen drop, fluid flow during drop spreading does not significantly affect the propagation of the dendrite cloud. Consequently, the dendrite cloud expands with a front velocity which is well comparable to the front velocity measured in a supercooled drop at rest.

Experiments have been performed for a varying drop impact velocity, and both isothermal and non-isothermal conditions with temperatures in the range $\vartheta = -16.0 \ldots -6.0\,^{\circ}\mathrm{C}$. The impact process of supercooled water drops onto a flat ice surface, prepared on top of a small cylindrical target, has been observed in a side-view using a high-speed video system. Liquid is ejected from the edge of the ice surface during spreading, preventing the formation of a pronounced rim which would disturb the measurements in the high-speed videos. The temporal evolution of the lamella thickness at the axis of symmetry of the impact has been determined as a characteristic quantity for the fluid flow in the spreading drop.

The experimental results have been compared with theoretical predictions for the lamella thinning without phase change. For the lowest supercooling, the influence of dendritic freezing on lamella thinning is negligible, which is due to the small number and growth rate of dendrites associated with low supercooling. In this case, the lamella thickness is well described by the theoretical inviscid theory for the lamella flow. It has been shown that the lamella thinning is generally almost unaffected by temperature during the first phase of drop impact; although the liquid viscosity significantly varies in the examined temperature range. During later stages of drop impact, a decreasing liquid temperature causes a decreasing speed of lamella thinning. The larger growth rate of the dendritic cloud at lower temperatures results in a faster decrease of the flow cross section in the lamella, which in turn slows down the liquid spreading due to increased viscous damping. In addition to the faster dendritic freezing, the decreased speed of lamella thinning ultimately results in a larger residual

ice layer thickness for higher supercooling. It has been shown that the temperature of the ice impact surface only has a negligible influence on the lamella thinning and the residual ice layer thickness, since it affects freezing only in a very short period during the beginning of spreading. Therefore, the impact conditions and the initial liquid temperature are the dominating parameters determining the final ice layer thickness. As a consequence of an increased speed of lamella thinning, a larger impact velocity generally results in a smaller final ice layer thickness.

Based on a postulated flow in the spreading lamella, a theoretical model for the prediction of the upper bound of the residual ice layer thickness, resulting from a single drop impact, has been derived. It accounts for both the increasing thickness of the dendrite cloud and the viscous boundary layer developing in the spreading lamella. A comparison with the present experimental results exhibits very good agreement of the theoretical model for the entire range of experimental conditions, implying that the model accounts for all relevant mechanisms during the process. The derived theoretical model represents a scaling law for the impact conditions, which results in an unique relation between the impact parameters and the residual ice layer thickness after impact. Based on this scaling, the present experimental results have been used as a *master-curve* for the calibration of a semi-empirical relation between the final ice layer thickness depending on the impact conditions. A power function of the proposed scaling has been fitted to the experimental data, resulting in a relation for an accurate a-priori prediction of the residual ice layer thickness, depending on the impact conditions and liquid temperature. By substitution of the material properties and the freezing velocity, this scaling law may not only be used for the impact of supercooled water drops, but also for all other drop impacts involving solidification in the absence of nucleation, such as in the case of spray coating processes.

Part IV

Closing

7 Summary

Ice accretion due to the impact and freezing of supercooled water drops is a complex process, rich in interesting phenomena such as drop impact, nucleation, solidification, and their mutual interaction. The hydrodynamics of drop impact generally control the maximum surface area wetted during drop impact. Subsequent nucleation in the impinging liquid initiates solidification which fixes the current shape of the deformed drop. Therefore, the hydrodynamics of drop impact determine the maximum surface area which can be iced after a single drop impact, while the thermodynamics of nucleation and solidification control the surface area which is ultimately iced after such an event. Attributed to the stochastic nature of nucleation, the interaction of hydrodynamics and thermodynamics during impact, and thus the surface area ultimately iced after drop impact may drastically vary for constant conditions.

In the present work, all subprocesses involved in ice accretion due to supercooled water drops have been separately examined using novel experimental, numerical and theoretical approaches. The results of the different studies have been thoroughly concluded in each respective chapter. Therefore, only a brief summary of the main findings concerning the subprocesses involved in ice accretion is given here.

7.1 Non-isothermal drop impact

Due to its relevance for various technical applications, drop impact has been the focus of extensive examination for more than a century. While isothermal drop impact is therefore well understood, drop impact involving heat transfer between the impinging liquid and the substrate remains a challenge which is due to the phenomenon's inherent unsteadiness and the large ranges of length and time scales involved. Experimental insight into the processes during non-isothermal drop impact is difficult, which generally motivates investigation of the phenomenon using theoretical modeling and numerical simulations. However, in the present work the hydrodynamics and thermodynamics during non-isothermal drop impact have been examined using not only numerical and theoretical, but also experimental approaches.

For the impact conditions in the present work, the time scale of drop cooling is long compared to the time scale of drop impact. Therefore, as shown experimentally for inclined impact, drop spreading is almost unaffected by a variation of the substrate temperature, while the liquid receding phase may be significantly influenced by heat transfer between the drop and the surface. A decreasing liquid temperature after impact onto a cold surface results in an increasing liquid viscosity, which drastically decreases the receding velocity of a drop. By this, an inclined impact onto a cold substrate results in a slightly larger maximum wetted surface area, and a significantly larger contact time between the drop and the substrate. According to classical nucleation theory, both the wetted surface area and time are crucial parameters for the rate of heterogeneous nucleus formation. Therefore, a variation of the substrate temperature implicitly influences heterogeneous nucleation at the impact surface by affecting the characteristic time and area of substrate wetting.

In the range of impact conditions for normal drop impact, numerically investigated in the present study, both the duration of drop spreading and the complete contact time between the drop and the surface are almost unaffected by the impact velocity, although the maximum spreading diameter significantly increases with increasing impact velocity. Despite an almost constant contact time, an increasing impact velocity increases the probability of nucleation in a drop, since it is associated with a larger wetted surface area. In accordance with the experimental results for inclined drop impact, numerical simulations of normal drop impact revealed an insignificant influence of the substrate temperature on drop spreading and the resulting maximum wetted surface area. Due to the strong temperature dependence of the liquid viscosity, the initial drop temperature is the more important influence on the maximum spreading after drop impact. The effect of heat transfer during non-isothermal drop impact on the liquid properties, and thus on the maximum spreading may be neglected. Therefore, the use of the initial liquid properties is sufficient for estimating the surface area wetted after drop impact by means of empirical equations, which allows an a-priori estimation of one of the main influences on nucleation. In a similar way, the typical contact time between the drop and the surface can be assumed as unaffected by heat transfer, and to be mainly affected by the liquid properties depending on the initial drop temperature.

The typical time and area of wetting are crucial parameters for heterogeneous nucleation at the impact surface. However, the most important

influence on nucleation is the liquid temperature which spatially and temporally varies during non-isothermal drop impact. Besides its influence on nucleation, the liquid temperature is also the dominant influence for solidification of the impinging liquid. Therefore, both the drop hydrodynamics and the heat transfer between the drop and the substrate are crucial for nucleation and solidification during and after drop impact. For the case of heterogeneous nucleation at the impact surface, the contact temperature during non-isothermal drop impact can be considered as the characteristic and most important temperature for the icing process. It is mainly influenced by the initial temperatures of the impinging drop and the substrate, and the numerical results of the present work endorse that the contact temperature is almost unaffected by the impact conditions. It has been shown that the theoretical contact temperature during drop impact, proposed in [295], is well applicable for the prediction of the liquid temperature at the substrate surface, which has been confirmed by the examination of liquid solidification after inclined drop impact. Therefore, also the most important influence on nucleation and solidification namely the liquid temperature in the near-wall region can be accurately predicted a-priori knowing the impact conditions.

The evolution of the mean heat transfer coefficient characterizes the heat transfer per unit area of the wetted surface during drop impact. It is unaffected by the impact conditions and the initial temperatures of the drop and the substrate. Therefore, the heat effectively transferred during drop impact primarily depends on the impact conditions which determine the wetted surface area and the time available for heat transfer between the drop and the substrate. Based on an expression for the substrate heat flux during drop impact, and using the numerical results of the present study, a semi-empirical model for the heat transferred during the spreading phase of an impacting drop has been derived. A very good agreement of the model with the computational results attests the model's capability of predicting the heat transferred during a single drop impact for a wide range of impact conditions.

The derived predictive model may not only be used in the context of ice accretion, but also for other engineering applications, involving non-isothermal drop impact, such as spray cooling systems.

7.2 Nucleation during drop impact

Ice nucleation in a liquid at rest is a complex process which is so far not completely understood, thereby still motivating numerous studies in this field. However, nucleation during drop impact is even more complicated since a drop impact is accompanied by several phenomena which may affect nucleation, such as a pressure rise during impact, the shear flow and variability of the wetted surface area during spreading, or a further cool down or warm up of the impinging liquid during non-isothermal drop impact. This variety of potentially influential mechanisms significantly impedes drawing distinct conclusions from experimental results. In the present work, nucleation during drop impact is examined for the first time, employing both experimental investigations and theoretical modeling. Despite the aforementioned difficulties, the present work reveals several fundamental insights into the mechanisms of nucleation during drop impact.

Similar to the case of nucleation in a liquid at rest, an increasing liquid supercooling results in an increasing nucleation rate in an impinging drop. However, contrary to a constant nucleation rate present in a liquid at rest, the nucleation rate significantly varies after drop impact. It is the largest immediately after impact and decreases with time. The specific mechanisms associated with drop impact may facilitate nucleation also for relatively small supercoolings for which nucleation is absent if the liquid is at rest on the impact surface. However, drop impact is no guarantor for nucleation which may be missing also during drop impact, if the supercooling is too small.

During drop impact onto a rough impact surface, air bubbles are entrapped below and in the spreading liquid. These air bubbles have been identified as a reason for nucleation rates decreasing long times after drop impact. The entrapped bubbles generally enhance nucleation, but continuously dissolve in the spread liquid. As a consequence, disappearance of bubbles causes a nucleation rate decreasing over time. An increasing impact velocity is associated with an increased dynamic pressure below the impinging liquid which results in smaller air bubbles entrapped below the liquid. Consequently, generated air bubbles dissolve faster which leads to a decreased rate of nucleation in comparison to a smaller impact velocity.

According to classical nucleation theory, the liquid cooling rate has a significant influence on experimentally observed drop freezing rates. In

the present study it has been shown that a further cool down or warm up of the liquid during non-isothermal drop impact indeed affects nucleation. Unfortunately, the effect of a changing liquid temperature on nucleation during drop impact could not be clearly identified from the present experiments. Nevertheless, all experiments, including those concerning nucleation during non-isothermal drop impact, revealed that the relevance of other influences besides the liquid temperature significantly depends on the liquid temperature itself. The liquid temperature can be considered as the primary influence on nucleation which generally determines the typical time scale of nucleation. It decreases with increasing liquid supercooling. Whether or not nucleation is affected by other mechanisms besides the liquid temperature, significantly depends on the typical time scale of the considered process. In the case of large liquid supercooling and a potentially influential process, taking place on a large time scale, nucleation can be considered as dominantly controlled by temperature and independent of the slower process. For smaller liquid supercoolings and a potentially influential mechanism taking place on a smaller time scale, nucleation may be significantly affected by the influential mechanism. Accordingly, the present experiments revealed that for large liquid supercooling, nucleation is predominated by temperature, while the mechanisms associated with non-isothermal drop impact gain importance at smaller liquid supercooling.

Similar to the previous considerations, the relevance of the stochastic nature of nucleation for other processes is determined by the typical time scale of nucleation, compared to the time scale of the process for which nucleation is considered as relevant. The time scale of drop impact is well comparable to the time scale of drop freezing due to nucleation; at least for the impact conditions in the present work. Therefore, the stochastic nature of nucleation is of relevance for drop impact and significantly affects the surface area iced after impact. However, for processes associated with a large time scale such as cloud glaciation or icing due to sessile water drops, description of nucleation using the singular nucleation model is sufficient. In these cases the time dependence of nucleation is irrelevant and the critical nucleation temperature is the most characteristic quantity for the process.

Considering the time dependence of both the nucleation rate and the wetted surface area, nucleation during drop impact has been theoretically modeled as a Poisson process. The derived model is not of predictive nature, but enables calculation of the cumulative number of active nu-

cleation sites per unit area of the wetted surface from experimentally examined drop freezing. This establishes an increased comparability of experimental results, facilitating a quantitative analysis of experiments concerning nucleation during drop impact, which may involve varying impact conditions.

A generic analysis of the experiments concerning nucleation during isothermal drop impact revealed a benefit from decomposing the number of active nucleation sites into a part, attributed to a transient nucleation rate associated with the mechanisms accompanying drop impact, and a part, attributed to a constant nucleation rate associated with heterogeneous nucleation at the substrate surface. Using appropriate ansatz functions, the constant and transient part of the nucleation rate have been described based on the experimental data. The obtained temperature dependence of the heterogeneous nucleation rate is well predicted by classical nucleation theory, while the time dependence of the transient nucleation rate may be described as $\sim t^{-1}$. To obtain a physical relation describing the transient part of nucleation, further experiments and mathematical modeling of the influential mechanisms are required. However, regardless of the chosen ansatz functions, decomposition of the experimental results into a constant and a transient part allows examination of the distinct contribution of both the impact surface and impact process on nucleation during drop impact.

7.3 Solidification of supercooled water at a wall

Solidification is relevant for many technical applications and therefore it has been the focus in numerous studies during the last centuries. If the solidifying liquid is supercooled and in contact with a solid wall, such as in the case of solidification during ice accretion, the process involves several phenomena, which have been thoroughly examined in the present study, employing a novel experimental approach. A water drop is entrapped in a vertically oriented Hele-Shaw cell, and its solidification is observed in a side-view using a high-speed video system.

The experimental approach allows examination of all mechanisms involved in solidification of a sessile supercooled water drop. Not only the two phases of solidification of a supercooled liquid, but also the initial phase of ice layer spreading along the substrate below the drop, taking place prior to dendritic solidification of the bulk liquid, can be observed

using the Hele-Shaw cell. While the two phases of supercooled solidification are well-known and have been examined in detail during the last decades, the initial phase of ice layer spreading is not well understood. The ice layer spreading has also been detected in the study of inclined drop impact in the present work. However, the experimental approach employing a Hele-Shaw cell constitutes significant advantages compared to the examination of solidification during drop impact or in a sessile drop. Application of the Hele-Shaw cell allows observation of the solidification process with high contrast in the absence of any optical distortions, which arise due to a curved liquid-gas interface in the case of drop impact or solidification of a sessile drop. Moreover, reduction of the process to two dimensions enables accurate length and velocity measurements using only a single high-speed video camera.

Solidification of a drop in the Hele-Shaw cell is initiated by heterogeneous nucleation at the substrate, followed by spreading of a thin ice layer along the substrate surface. In comparison to the velocity of a single dendrite growing freely in supercooled water, the growth velocity of the initial ice layer along the surface may be significantly affected by the substrate. Substrate materials associated with a high thermal effusivity facilitate heat dissipation away from the spreading ice layer, thereby enhancing the ice layer growth rate. In contrast, the ice layer growth is indifferent to a substrate associated with a low thermal effusivity. In the case of such a surface, the ice layer growth rate compares well with the growth velocity of a single dendrite. In comparison to a single dendrite, kinetic effects associated with an increasing sluggishness of molecules for low temperatures arise at significantly larger supercoolings. While these effects result in a decreasing dependence of the growth rate of a single dendrite on supercooling for a liquid supercooling greater than $\Delta T \approx 4 \ldots 5\,\mathrm{K}$ [332], they become import for the ice layer spreading at $\Delta T \approx 10\,\mathrm{K}$.

While the drop freezes by planar solidification in the case of small liquid supercooling, for sufficiently large liquid supercooling the initial ice layer becomes unstable, resulting in dendritic freezing of the bulk liquid. The growth morphology during dendritic freezing can be categorized depending on the liquid supercooling. Both the number and spatial density of growing dendrites increase with supercooling. While only single dendrites are observed for smaller supercooling, a dense cloud of dendrites infuses the liquid at larger supercooling, which is in good agreement with experimental data available in literature. Similar to a single dendrite, the cloud of dendrites expands with a constant velocity only depending on

temperature. For small liquid supercooling, associated with the growth of single dendrites, no mutual influence between the individual dendrites is observed, and the growth rate compares well with the growth rate of a single dendrite reported in literature. Mutual influencing of the individual dendrites increases with increasing density of dendrites, associated with a larger supercooling. This influence causes an increased growth rate of a dendrite cloud in comparison to the growth rate of a single dendrite, which is in accordance with previous experimental findings. By this, kinetic effects are compensated, and consequently the front velocity of a dendrite cloud is comparable to the prediction of the marginal stability theory up to a significantly larger liquid supercooling than the tip velocity of a single dendrite. Kinetic effects result in a decreasing dependence of the front velocity of a dendrite cloud on supercooling for a liquid supercooling greater than $\Delta T \approx 14\,\mathrm{K}$, where virtually no increase of the front velocity is observed until $\Delta T \approx 17.5\,\mathrm{K}$.

Dendritic freezing causes freezing of only a portion of the bulk liquid, and transfers the ice-water mixture into a local thermodynamic equilibrium at the melting temperature. A further cooling of the drop results in freezing of the remaining water. The typical features accompanying this process such as the cusp formation on top of a frozen sessile drop, as a consequence of the volume expansion during solidification, can be also observed in the Hele-Shaw cell, indicating that the Hele-Shaw cell does not affect the mechanisms involved in the freezing process.

Since ice layer spreading prior to dendritic solidification represents the initial phase of icing of a surface, it is of significant relevance for the entire process of ice accretion. The initial ice layer is in direct contact with the substrate below the drop, and presumably mechanically interlocking with it during the freezing process. Furthermore, the ice layer's growth velocity is the velocity which determines how fast a surface is covered by ice and therefore, it is the most relevant solidification velocity for the case of icing of surfaces. Based on the experimental results, and by employing the analytical solution of the two-phase Stefan problem, a semi-empirical model for the initial ice layer spreading has been developed. It allows prediction of the radial growth velocity of the spreading ice layer, depending on liquid supercooling and the thermophysical properties of the substrate. The model is in very good agreement with the experimental results in the diffusion dominated growth regime of the ice layer, i.e. for $\Delta T < 10\,\mathrm{K}$. Since it does not account for kinetic effects, the model overpredicts the ice layer growth rate for larger supercoolings.

7.4 Fluid flow and phase change during drop impact

Examination of nucleation during drop impact is of particular relevance for the beginning of ice accretion, when the substrate is not yet covered by ice. When an ice layer already exists on the impact surface, nucleation during drop impact is irrelevant, since solidification of the impinging drop is initiated immediately by the ice on the surface. In this case, distinct spreading of an initial ice layer is absent, and solidification of the impinging liquid is triggered at the moving contact line where the liquid makes contact with the ice surface. While the mutual interaction of fluid flow and phase change may vary after stochastic nucleation during impact onto a dry surface, immediate initiation of solidification during impact onto an ice surface results in a clear-cut interaction, accompanied by a distinct outcome of such an impact, only depending on the impact conditions.

Taking advantage of the aforementioned non-trivial difference, in the present work the impact of supercooled water drops onto an ice surface has been investigated experimentally and theoretically for the first time. Examination aimed at the mutual interaction between fluid flow and solidification during drop impact. By using an ice impact surface, stochastic nucleation is suppressed, and solidification and liquid spreading start simultaneously upon first contact between the drop and the surface, which results in highly repeatable and distinct results. The impact process has been observed with a high spatial and temporal resolution in a side-view, using a high-speed video system. Assuming the temporal evolution of the lamella thickness in the center of drop impact as a representative measure for the entire process, the influence of varying impact conditions and temperatures on the process has been examined. Both the lamella thinning and the simultaneous dendritic freezing of the spreading liquid, which is associated with a reduction of the cross-sectional area of the flow in the lamella, control the process and determine the ice layer thickness residual after drop impact.

It has been shown that dendritic freezing of the impinging liquid is dominated by temperature, and unaffected by the fluid flow during impact. In contrast, dendritic freezing of the liquid may significantly affect lamella thinning by a decrease of the cross-sectional area of the lamella. For the case of small liquid supercooling, associated with the growth of single dendrites, the influence of solidification on lamella thinning is van-

ishing. In this case, the temporal evolution of the lamella thickness is well described using the analytical solution for the flow in a spreading lamella without phase change. However, for increasing supercooling associated with a larger solidification velocity and a higher density of growing dendrites, dendritic freezing significantly affects the flow in the spreading lamella. A faster decrease of the cross-sectional area of the lamella for lower liquid temperatures finally results in a larger residual ice layer thickness. The rate of lamella thinning increases with increasing drop impact velocity, which consequently results in a smaller residual ice layer thickness for higher impact velocities.

During non-isothermal drop impact, a thermal boundary layer expands in the dendrite cloud and the impinging drop. Since the expansion of the dendrite cloud in the spreading liquid is affected by the expanding thermal boundary layer only in a short phase after impact, a varying substrate temperature has only a negligible influence on the residual ice layer thickness, which is thus predominated by the initial drop temperature.

Based on a postulated flow of the liquid in the spreading lamella, and using the front velocity of a dendrite cloud obtained in the present work, a theoretical model for the residual ice layer thickness after drop impact has been developed. It results in a unique scaling for the relation between the residual ice layer thickness and the impact conditions. The scaling law has been calibrated using the experimental data of the present study as a master-curve. The resulting semi-empirical equation allows prediction of the residual ice layer thickness depending on the impact conditions and the initial drop temperature, which both may vary over a wide range. The predictive model is of particular interest for the description of several phenomena related to ice accretion such as the growth of so-called *ice feathers* or *horns*, which are associated with certain environmental condition present during ice accretion. However, besides ice accretion, drop impact and simultaneous phase change is relevant for various other engineering applications such as thermal spray coating or microcasting. Due to its predictive nature, the theoretical model for the residual ice layer thickness may be also applied to these cases when nucleation is irrelevant for the process and a constant solidification velocity is involved in the process.

8 Conclusions and outlook

The present work constitutes a significant contribution towards a better understanding of the processes involved in ice accretion by supercooled water drops. However, many questions are still open which is in particular attributed to the rich physics involved in the process. Accordingly, several issues deserve further examination, to allow for example a significant improvement of theoretical and numerical tools for icing prediction, or the design of anti-icing surfaces.

Similar to the variety of mechanisms involved in ice accretion, so far also the number of unsolved questions concerning the process is numerous. However, in the following only the issues, potentials and perspectives directly emerging from the present work, which may significantly contribute towards the aforementioned aims, are discussed.

Development of an icing model

Until nucleation, the impact of a supercooled water drop does not differ from the impact of a non-supercooled drop, which is well understood for isothermal conditions. As implied by the results in the present work, the surface area wetted during non-isothermal drop impact as well as the typical contact temperature and contact time between the drop and the surface may be estimated using semi-empirical equations only depending on the impact conditions; i.e. without consideration of potential heat transfer between the drop and the substrate. Therefore, it is possible to estimate the most important influences for nucleation during drop impact only depending on the impact conditions, which constitutes an important first step towards a predictive model for icing of an initially dry surface. However, due to the stochastic nature of nucleation, such a predictive model would still involve a statistical description of nucleation, therefore resulting in a statistical description of the entire icing process.

Although the aforementioned influences on nucleation may be estimated a-priori to drop impact, the examination and prediction of nucleation during drop impact remains a challenge since it depends on a variety of further influences. To enable development of a predictive model for nucleation during drop impact, at first the effect of an individual pa-

rameter's influence on nucleation has to be investigated by means of systematic parametric studies. The presented theoretical approach for modeling and analysis of experimental results concerning nucleation during drop impact may serve as a fundamental building block for this purpose. It allows quantification of heterogeneous nucleation associated with the impact surface, and transient nucleation associated with the specific mechanisms during drop impact. Hereby, the presented approach significantly eases examination of the exclusive influence of the impact conditions on experimentally obtained drop freezing rates. Due to the necessity of scores of repetitions, considerable expense and effort is necessary for the experimental examination of nucleation during impact. Therefore, numerical simulations and in particular molecular dynamics simulations may facilitate the examination of the effect of a single mechanism on nucleation, such as the pressure rise during impact or the shear in the spreading liquid. Nevertheless, development of a predictive model for nucleation during drop impact remains a challenging and laborious task.

While modeling of nucleation during drop impact is the needle eye on the way to an improved predictive icing model, most of the present results concerning solidification of supercooled water may directly feed into such a model without considerable modification. The theory for the spreading velocity of the initial ice layer could be used, to describe the beginning of ice accretion, i.e. when ice is not yet present on the surface. When the impact surface is already covered by ice, ice layer spreading is irrelevant. In this case, solidification of the bulk liquid can be described based on the measured front velocity of a dendrite cloud depending on the liquid supercooling, which has been shown to be unaffected by fluid flow. The interaction of the expanding dendrite cloud with the fluid flow during impact may be described based on the modeling and results of the residual ice layer thickness after a single drop impact.

A further important aspect, which has to be taken into account during development of a predictive icing model, is the influence of an external shear flow, which is present in the case of most circumstances associated with ice accretion. Drop impact can be significantly affected by an external flow. It may cause atomization of a drop prior to its impact, which results in the impact of numerous smaller secondary droplets instead of a single larger drop, thereby drastically changing the impact conditions. Although heterogeneous nucleation at the impact surface is presumably the most important mechanism of nucleation during drop impact, an external flow may cause nucleation on the liquid-gas interface of the drop, which

has already been reported in literature [172]. In addition, nucleation in the impinging liquid may be implicitly affected by the flow, which potentially influences the wetted surface area active for heterogeneous nucleation. A significant influence of the flow on drop freezing is very unlikely. However, an external flow may cause shedding of the unfrozen liquid from the surface, which drastically affects the effective outcome of drop impact. To conclude, potential influences of an external shear flow on the processes involved in ice accretion due to supercooled water drops are manifold but so far not clear, thus motivating its future examination.

Design of anti-icing surfaces

The theoretical approach for the description of nucleation during drop impact employed in the present work is of particular benefit for the design and development of anti-icing surfaces. For that purpose extensive parametric studies, such as for the development of a predictive nucleation model, are not necessary. Heterogeneous nucleation rates, calculated using the presented decomposition of the total nucleation rate, allow a quantitative comparison of the ice nucleating ability of different surfaces being exposed to drop impact, which is of particular interest for the examination and evaluation of a surface's icephobicity. As shown in the present work, the stochastic nature of nucleation is of significance for the outcome of drop impact at subfreezing conditions. Therefore, application of the presented statistical experimental approach is in general more appropriate for research towards anti-icing surfaces than examination of mean freezing delays or mean nucleation temperatures obtained from only a few experiments, which has commonly been done until now.

So far, most approaches for reduction and prevention of icing only consider the physical mechanisms prior to nucleation, i.e. when the liquid is still able to detach from the surface without freezing on it. These approaches comprise the reduction of the contact time and enhancement of drop rebound, or the increase of the freezing delay; and mostly involve time as an important parameter. To the author's knowledge, until now, no approach considers the processes taking place after nucleation, when there is no turning back from icing of the surface; although the possible potential is obvious: The freezing velocity at a solid substrate determines the time-scale of drop freezing, and hence the time available for processes such as drop rebound and flow-induced shedding of water from the surface after

nucleation. As shown in the present work, freezing of supercooled water at a solid substrate may be slowed by a factor of approx. three by switching from a metallic substrate to an insulator such as acrylic glass. Therefore, the choice of the substrate material offers large potential for the optimization of icing prevention systems. It won't be possible to manufacture entire parts of aircraft and other engineering systems from a polymer like acrylic glass. However, suitable polymer coatings will probably have the same effect, as long as the coating is thicker than the characteristic length scale of the thermal boundary layer, expanding in the substrate during solidification. The derived theoretical model for ice layer spreading along a wall provides a deeper insight into the influential mechanisms during ice accretion, and may be used to estimate the suitability of substrate materials for anti-icing applications by means of an accurate a-priori estimation of the surface freezing rate. However, for the examination of the influence of thin surface coatings on the ice layer growth rate, the theoretical model possibly needs to be slightly modified. So far, the model involves the analytical solution for the contact temperature arising between two semi-infinite slabs suddenly brought into contact. To be able to predict the ice layer spreading also for the case of a thin coating, the finiteness of the coating layer has to be accounted for when estimating the surface temperature below the spreading ice layer.

Further perspective

As in the case of other complex processes which are only difficult to address experimentally, direct numerical simulation of the impact and solidification of a supercooled water drop would be the most effective means for gaining a better understanding of, not only the involved mechanisms, but also their mutual influence. As shown in the present study, drop impact with conjugate heat transfer in the impact surface can be accurately modeled and numerically simulated. Also an external flow around an impinging drop represents no significant barrier for numerical simulations. However, numerical treatment of the solidification process of the supercooled liquid, in particular under the influence of both the flow in the impinging drop, and the impact surface, involves some difficulties and unsolved problems. They arise from the large range of length and time scales involved, and a singularity at the three phase contact line where the ice layer, the supercooled liquid and the substrate meet, as recently reported [34]. Moreover, the knowledge about the rheological

properties of an ice-water mixture resulting from dendritic freezing is limited. Since these properties are essential for numerical modeling and simulation, experiments are required to allow appropriate mathematical modeling. However, knowledge about the rheology and behavior of ice slurries may facilitate future modeling approaches [12, 19, 188, 235].

To conclude, at the moment experimental approaches are the most appropriate means for a detailed examination of the icing process. Experimental results may facilitate theoretical modeling of the involved subprocesses such as the expansion of a dendrite cloud and its properties, which would be an important step towards effective numerical simulation of the entire process. Experimental results, and in particular those obtained in the present work may in general serve as a data basis for the validation of computational models, which hopefully are developed in the future.

Appendix

A Temperature evolution during the fall of a drop

As described in Chap. 3, the drop temperature in the experiments concerning drop impact is measured inside the drop during its generation at the PTFE tube. Due to forced convection, the drop temperature may change after drop detachment during its fall onto the impact surface. Using temperature data measured at different positions in the styrofoam chambers, the temperature evolution of a falling drop is estimated based on a 0-dimensional computational model accounting for convective heat and mass transfer at the drop surface. The styrofoam chambers are partially filled with gaseous nitrogen to lower the relative humidity. However, in account for an increased availability of literature data, in the following analysis air is assumed as the gas surrounding the falling drop. Due to the composition of air comprising approx. 78 Vol.-% nitrogen, the influence of this assumption on the calculation of heat and mass transfer at the drop can reasonably be neglected.

The evolution of the drop temperature $\vartheta_\mathrm{d}(t)$ is determined by the initial temperature of the drop $\vartheta_{\mathrm{d},0} = \vartheta_\mathrm{d}(t = 0)$ which is measured prior to detachment from the PTFE tube, and the total heat flow $\dot{Q}_\mathrm{tot}$ across the drop surface during its fall onto the impact surface. With neglect of radiation, the total heat flow at the drop surface comprises the convective and evaporative heat flow as

$$\dot{Q}_\mathrm{tot} = \dot{Q}_\mathrm{con} + \dot{Q}_\mathrm{eva}. \tag{A.1}$$

The calculation of both the convective and evaporative contributions to $\dot{Q}_\mathrm{tot}$ are separately described in the following. Moreover, the calculation of the temporal evolution of the drop diameter and drop velocity are outlined. The numerical algorithm is validated using experimental data, available for drop evaporation due to forced convection.

A.1 Convective heat flow

According to Newton's law of cooling/heating, the convective heat flow is given as

$$\dot{Q}_\mathrm{con} = \alpha A_\mathrm{d}(\vartheta_\mathrm{d,sur} - \vartheta_\infty), \tag{A.2}$$

where α is the heat transfer coefficient, A_d is the drop surface, and $\vartheta_\mathrm{d,sur}$ and ϑ_∞ are the temperatures of the drop surface and the ambient air, respectively. The heat transfer coefficient α is obtained from the Nusselt number

$$\mathrm{Nu_{tot}} \equiv \alpha d_\mathrm{d}/k, \tag{A.3}$$

where d_d is the drop diameter, and k is the thermal conductivity of air. The Nusselt number is calculated using empirical Nusselt correlations for the flow around a sphere, and is decomposed into two parts as [69]

$$\mathrm{Nu_{tot}} = \sqrt[3]{\mathrm{Nu_{nat}^3} + \mathrm{Nu_{for}^3}}, \tag{A.4}$$

where $\mathrm{Nu_{nat}}$ and $\mathrm{Nu_{for}}$ correspond to the contributions due to natural and forced convection, respectively. This superposition approach is valid for $0.1 < \mathrm{Pr} < 100$ [67], where $\mathrm{Pr} \equiv \nu/a$ is the Prandtl number. The contribution due to natural convection at a sphere is given as [283]

$$\mathrm{Nu_{nat}} = 0.56 \left[\left(\frac{\mathrm{Pr}}{0.846 + \mathrm{Pr}} \right) \mathrm{Ra} \right]^{0.25} + 2, \tag{A.5}$$

where $\mathrm{Ra} \equiv \mathrm{PrGr}$ is the Rayleigh number. The Grashof number Gr is defined as

$$\mathrm{Gr} \equiv \frac{g\beta(\vartheta_\mathrm{d,sur} - \vartheta_\infty) d_\mathrm{d}^3}{\nu_\mathrm{air}^2}, \tag{A.6}$$

where g is the acceleration of gravity and ν_air is the kinematic viscosity of the surrounding air. β is the coefficient of thermal expansion of air, and is given as $\beta \approx 1/T$ for an ideal gas [20]. Equation A.5 is valid for $0.1 < \mathrm{Ra} < 10^{12}$ and $\mathrm{Pr} > 10^{-3}$, which both is satisfied in the present study.

For $0.6 < \mathrm{Pr} < 1000$ and $10 < \mathrm{Re} < 10^7$, the contribution attributed to forced convection at a sphere, $\mathrm{Nu_{for}}$, can be estimated as a combination of the Nusselt numbers corresponding to a laminar, $\mathrm{Nu_{lam}}$, and a turbulent flow, $\mathrm{Nu_{tur}}$, as [131]

$$\mathrm{Nu_{for}} = 2 + \sqrt{\mathrm{Nu_{lam}^2} + \mathrm{Nu_{tur}^2}}. \tag{A.7}$$

The laminar and turbulent contributions in Eq. A.7 for a sphere can be calculated using the Nusselt correlations for a horizontal plate exposed to an external flow as [131]

$$\mathrm{Nu_{lam}} = 0.664 \mathrm{Re}^{1/2} \mathrm{Pr}^{1/3} \tag{A.8}$$

and

$$\mathrm{Nu_{tur}} = \frac{0.037\mathrm{Re}^{0.8}\mathrm{Pr}}{1 + 2.443\mathrm{Re}^{-0.1}(\mathrm{Pr}^{2/3} - 1)}, \tag{A.9}$$

which are valid for the ranges $10 < \mathrm{Re} < 10^7$ and $0.6 < \mathrm{Pr} < 2000$ [367]. The Reynolds number $\mathrm{Re} \equiv v_{\mathrm{rel}} d_{\mathrm{d}} / \nu_{\mathrm{air}}$ is calculated using the relative velocity between the drop and the surrounding air, v_{rel}. The Prandtl number in the present study satisfies all aforementioned conditions. However, the Reynolds number is $\mathrm{Re} < 10$, in particular during the initial phase of drop acceleration. The time with $\mathrm{Re} < 10$ is of the order of 1 ms, which can be neglected in comparison to the entire time of drop fall which is of the order of 10^2 ms. Therefore, the aforementioned relations are assumed reasonable also for the estimation of heat transfer in the present case.

If both natural and forced convection are present, and the flow induced by natural convection is in the same direction as the outer flow field, the Nusselt numbers calculated using Eqs. A.5 and A.7 are superposed to obtain the total Nusselt number from Eq. A.4. However, if the flow induced by natural convection is in the opposite direction of the outer flow field, the total Nusselt number is obtained as [69]

$$\mathrm{Nu_{tot}} = \sqrt[3]{|\mathrm{Nu}_{\mathrm{force}}^3 - \mathrm{Nu}_{\mathrm{nat}}^3|}. \tag{A.10}$$

Accordingly, Eq. A.4 is applied for a drop temperature below the temperature of the surrounding air, whereas Eq. A.10 is applied for a drop being warmer than its surrounding. Note that due to evaporative cooling of a drop suspended at the PTFE tube, the initial drop temperature is commonly below the ambient temperature.

A.2 Evaporative heat flow

Heat flow associated with evaporation of the falling drop, $\dot{Q}_{\mathrm{eva}}$, is calculated using the specific latent heat of evaporation, L_{eva}, and the mass flow of evaporating water, $\dot{m}_{\mathrm{eva}}$, as

$$\dot{Q}_{\mathrm{eva}} = \dot{m}_{\mathrm{eva}} L_{\mathrm{eva}}. \tag{A.11}$$

The evaporative mass flow can be expressed using the molar evaporation rate of water molecules, $\dot{J}$, and the molar mass of water, $M_{\mathrm{H2O}} = 18.02 \times 10^{-3}\,\mathrm{kg/mol}$, as

$$\dot{m}_{\mathrm{eva}} = \dot{J} M_{\mathrm{H2O}}. \tag{A.12}$$

Using the molar concentrations of water in air in the far field, $C_{\mathrm{H2O},\infty}$, and at the drop surface, $C_{\mathrm{H2O,sur}}$, the evaporation rate of water molecules is calculated as [159]

$$\dot{J} = BA_{\mathrm{d}} \left(C_{\mathrm{H2O},\infty} - C_{\mathrm{H2O,sur}} \right), \tag{A.13}$$

where B is the mass transfer coefficient, being the analogon in mass transfer to the heat transfer coefficient α in heat transfer. Note that the drop evaporates in the case of an undersaturated surrounding, $C_{\mathrm{H2O},\infty} < C_{\mathrm{H2O,sur}}$, and thus $\dot{J}$ as well as the resulting heat flow become negative.

In analogy to the heat transfer coefficient α which is determined from the Nusselt number Nu, the mass transfer coefficient B is determined from the Sherwood number Sh defined as

$$\mathrm{Sh} \equiv \frac{B d_{\mathrm{d}}}{D}, \tag{A.14}$$

where D is the diffusion coefficient of water vapor in air. Similar to the correlations for the Nusselt number, also the Sherwood number can be expressed as a function of dimensionless quantities characterizing the respective conditions for mass transfer. Besides the Reynolds number, these correlations involve the Schmidt number $\mathrm{Sc} \equiv \nu / D$, which is the analogon for mass transfer to the Prandtl number used in heat transfer. Since the underlying physics for mass transfer are analog to the physics of heat transfer, the derivation of the Sherwood number generally follows the same procedured as the derivation of the Nusselt number. However, the Sherwood number and Nusselt number are connected via the Lewis number

$$\mathrm{Le} \equiv \frac{\mathrm{Sc}}{\mathrm{Pr}} = \frac{a}{D} \tag{A.15}$$

as [20]

$$\frac{\mathrm{Sh}}{\mathrm{Nu}} = \mathrm{Le}^{1/3}. \tag{A.16}$$

By substituting the definitions for the Nusselt and Sherwood number, Eqs. A.3 and A.14, into Eq. A.16, the mass transfer coefficient can be directly calculated from the heat transfer coefficient as

$$B = \alpha \frac{D}{k} \mathrm{Le}^{1/3}. \tag{A.17}$$

The molar concentration of water vapor at a location i, which is needed in Eq. A.13 for the calculation of the evaporation rate of water molecules, is obtained as [203]

$$C_{\mathrm{H2O,i}} = \frac{p_{\mathrm{H2O,i}}}{\bar{\mathrm{R}} T_{\mathrm{i}}}, \tag{A.18}$$

where T_{i} denotes the local temperature, $p_{\mathrm{H2O,i}}$ is the local partial pressure of water vapor, and $\bar{\mathrm{R}} = 8.314\,\mathrm{J/(molK)}$ is the universal gas constant. Using the definition of the relative humidity,

$$\mathrm{RH_i} = \frac{p_{\mathrm{H2O,i}}}{p_{\mathrm{sat,i}}}, \tag{A.19}$$

the molar concentration can be expressed as

$$C_{\mathrm{H2O,i}} = \mathrm{RH_i} \frac{p_{\mathrm{sat,i}}}{\bar{\mathrm{R}} T_{\mathrm{i}}}, \tag{A.20}$$

where $p_{\mathrm{sat,i}}$ is the saturation pressure of water vapor in air depending on temperature. The relative humidity at the interface between the drop and the surrounding air is $\mathrm{RH_{sur}} = 1$ [312], while the relative humidity in the far field, RH_∞ is measured in the experiments using the hygrometer attached next to the suspended drop.

Using Eqs. A.12, A.13, A.17 and A.20, the evaporative mass flow is finally obtained as

$$\dot{m}_{\mathrm{eva}} = \alpha \frac{D}{k} \mathrm{Le}^{1/3} A_{\mathrm{d}} \frac{M_{\mathrm{H2O}}}{\bar{\mathrm{R}}} \left(\mathrm{RH}_\infty \frac{p_{\mathrm{sat},\infty}}{T_\infty} - \frac{p_{\mathrm{sat,sur}}}{T_{\mathrm{sur}}} \right). \tag{A.21}$$

The saturation pressure, $p_{\mathrm{sat,i}}$, depends on temperature and is calculated using an empirical numerical-value equation valid for $123\,\mathrm{K} < T < 332\,\mathrm{K}$ as [245]

$$\begin{aligned} p_{\mathrm{sat,i}} \approx \exp \Bigg\{ & b_1 - \frac{b_2}{T_{\mathrm{i}}} - b_3 \ln\left(T_{\mathrm{i}}\right) + b_4 T_{\mathrm{i}} \\ & + \tanh\left[b_5 \left(T_{\mathrm{i}} - b_6\right)\right] \left[b_7 - \frac{b_8}{T_{\mathrm{i}}} - b_9 \ln\left(T_{\mathrm{i}}\right) + b_{10} T_{\mathrm{i}} \right] \Bigg\}, \end{aligned} \tag{A.22}$$

where the involved coefficients are $b_1 = 54.84$, $b_2 = 6763.22$, $b_3 = 4.21$, $b_4 = 3.67 \times 10^{-4}$, $b_5 = 4.15 \times 10^{-2}$, $b_6 = 218.8$, $b_7 = 53.88$, $b_8 = 1331.22$, $b_9 = 9.445$ and $b_{10} = 1.4 \times 10^{-2}$. Substitution of the magnitude of temperature in Kelvin into Eq. A.22 yields the magnitude of the saturation pressure in Pa.

Using the evaporative mass flow of water, Eq. A.21, the temporal evolution of the drop mass is obtained from the ordinary differential equation

$$\frac{\mathrm{d}m_\mathrm{d}}{\mathrm{d}t} = \dot{m}, \tag{A.23}$$

and the drop diameter is calculated from $d_\mathrm{d} = (6m_\mathrm{d}/(\rho_\mathrm{l}\pi))^{1/3}$.

The maximum Nusselt number in the present study, characterizing convective heat transfer at the drop surface during drop impact with $v_\mathrm{d} = 3.2\,\mathrm{m/s}$, is obtained as $\mathrm{Nu}_\mathrm{max} \approx 20$, and the maximum heat transfer coefficient follows from Eq. A.3 as $\alpha_\mathrm{max} \approx 150\,\mathrm{W/(mK)}$. With this, the maximum Biot number, $\mathrm{Bi} \equiv \alpha l/k$, being the ratio between convective heat transfer at the drop surface and conduction in the drop is obtained as $\mathrm{Bi}_\mathrm{max} \approx 0.8$. In the present case, not only convective heat transfer but also evaporative cooling at the drop surface are of relevance for the heat flow to the drop. During its suspension, a drop is initially at the wet-bulb temperature, where the heat flows attributed to convective heat and mass transfer are in balance. Thus, evaporative cooling is of the same order as convective heating. Since evaporative cooling significantly lowers the heat which is effectively transferred across the drop surface, also the effective heat transfer coefficient reduces. Hence it is reasonable to assume the effective Biot number, which accounts for both heat and mass transfer, as $\mathrm{Bi}_\mathrm{eff} \ll 1$. In this situation, conductive heat transfer in the falling drop is much larger than heat transfer at its surface. Therefore, temperature gradients in the drop rapidly smooth out, justifying the assumption of a uniform drop temperature, i.e. $\vartheta_\mathrm{d} \approx \vartheta_\mathrm{d,sur}$. By this, the temperature evolution of the drop is obtained from the ordinary differential equation

$$\frac{\mathrm{d}\left(c_\mathrm{p,d}\rho_\mathrm{d}V_\mathrm{d}\vartheta_\mathrm{d}\right)}{\mathrm{d}t} = \dot{Q}_\mathrm{tot}. \tag{A.24}$$

Due to the acceleration of the falling drop, the Reynolds number involved in the calculation of convective heat and mass transfer at the drop surface is transient. Assuming the surrounding air to be at rest, the Reynolds number is calculated using the absolute drop velocity $v_\mathrm{d}(t)$. It is determined by the gravitational acceleration g and the drag force acting on the drop, and can be calculated from the ordinary differential equation

$$\frac{\mathrm{d}v_\mathrm{d}}{\mathrm{d}t} = g - \frac{F_\mathrm{dr}}{m_\mathrm{d}(t)}, \tag{A.25}$$

with the drag force given as

$$F_{\mathrm{dr}} = 0.5 \rho_{\mathrm{air}} A_{\mathrm{d,pro}} c_{\mathrm{dr}} v_{\mathrm{d}}^2, \tag{A.26}$$

with the density of the surrounding air ρ_{air}, the cross sectional area of the drop $A_{\mathrm{d,pro}}$, and c_{dr} being the drag coefficient. The drag coefficient is a function of the Reynolds number and is approximated as [237]

$$c_{\mathrm{dr}} = \frac{24}{\mathrm{Re}} + \frac{2.6\frac{\mathrm{Re}}{5}}{1+\left(\frac{\mathrm{Re}}{5}\right)^{1.52}} + \frac{0.411\left(\frac{\mathrm{Re}}{263000}\right)^{-7.94}}{1+\left(\frac{\mathrm{Re}}{263000}\right)^{-8}} + \frac{\mathrm{Re}^{0.8}}{461000}. \tag{A.27}$$

which well describes the drag coefficient in the relevant range of Reynolds numbers $5 < \mathrm{Re} < 10^4$.

Due to its complexity and the mutual coupling of the involved relations, the derived system of equations cannot be solved analytically. Therefore, all involved relations have been implemented in a commercial software (*Mathworks, Matlab 2016a*), and the temporal evolution of the drop temperature, drop diameter and drop velocity have been calculated numerically using the ordinary differential equations Eqs. A.24, A.23 and A.25, and the initial conditions $v_{\mathrm{d},0}(t=0) = 0$ and $\vartheta_{\mathrm{d}}(t=0) = \vartheta_{\mathrm{d},0}$. The decrease of the drop diameter during fall in the present experiments is negligible, and therefore the drop diameter measured from the high-speed videos during impact, $d_{\mathrm{d}}(t=0) = d_{\mathrm{d}}$, is assumed as the initial drop diameter for the simulations. However, for the following validation of the numerical algorithm, using experimental data for the evaporation of water drops in a free air stream, the diameter decrease is essential. The calculations are performed accounting for the temperature dependence of the material properties of both the liquid drop and the surrounding air, using the polynomial relations summarized in App. B. The respective properties of the drop are calculated using the momentary drop temperature, while those of the surrounding air are calculated using the mean temperature between the drop and the ambient.

A.3 Validation

The mathematical model and its numerical implementation has been validated by means of a comparison with experimental data for the evaporation of water drops exposed to an air stream with a velocity of $v_\infty = 0.31, \mathrm{m/s}$ at varying relative humidities, and an ambient temperature of $T_{\mathrm{amb}} = 298\,\mathrm{K}$ from [92]. The data are compared in terms of the evolution of the drop diameter $d_{\mathrm{d}}(t)$. Figure A.1 shows the evolution of the squared normalized drop diameter, $(d_{\mathrm{d}}/d_{\mathrm{d},0})^2$, for varying relative humidities; the drop diameter is normalized with the initial drop diameter $d_{\mathrm{d},0}$. As shown in the figure, the numerical results are in excellent agreement with the experimental data for all relative humidities. Moreover, both the experimental data and the numerical predictions reveal good agreement with the D^2-law [132], which predicts a linear decrease of $(d_{\mathrm{d}}/d_{\mathrm{d},0})^2$ over time.

The drop diameter primary depends on convective mass transfer. However, a correct prediction of the drop diameter also requires a correct calculation of the convective heat transfer, since it determines the drop tem-

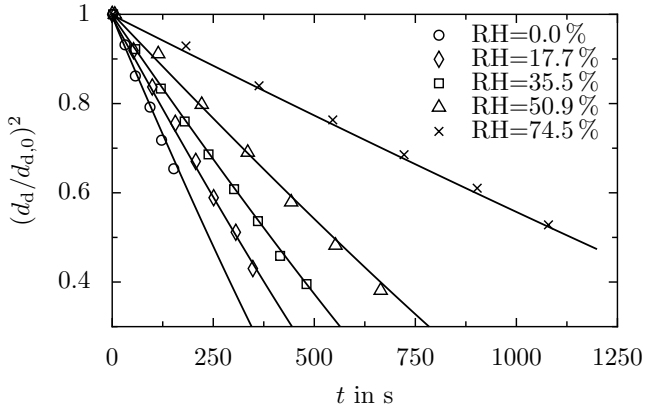

Figure A.1: Evolution of the squared normalized diameter of water drops with $d_{\mathrm{d},0} \approx 1.4\,\mathrm{mm}$, evaporating in a free air stream of varying relative humidity and $v_\infty = 0.31, \mathrm{m/s}$. Comparison of the numerical predictions (solid lines) with experimental data (symbols) from [92].

perature, which implicitly affects mass transfer. Therefore, the perfect agreement of the numerical results with the experimental data demonstrates the correct calculation of both convective heat and mass transfer.

A.4 Results

The evolution of the drop temperature during fall is calculated for the initial temperatures measured in the study of nucleation during isothermal drop impact with $\vartheta_{\mathrm{d},0} \leq -8.6\,^{\circ}\mathrm{C}$. Since, these conditions are well comparable to those in the remaining experiments concerning drop impact, the obtained results are assumed representative for all experimental studies of drop impact. The calculations are performed for the largest impact velocity in the present study $v_{\mathrm{d}} = 3.2\,\mathrm{m/s}$, which is associated with the longest fall of the drop, and thus with the largest change of the drop temperature until drop impact. The far field relative humidity for the calculations is $\mathrm{RH}_{\infty} = 5\,\%$, corresponding to the approximate relative humidity in the experiments. The far field temperature is estimated conservatively corresponding to the maximum temperature in the upper

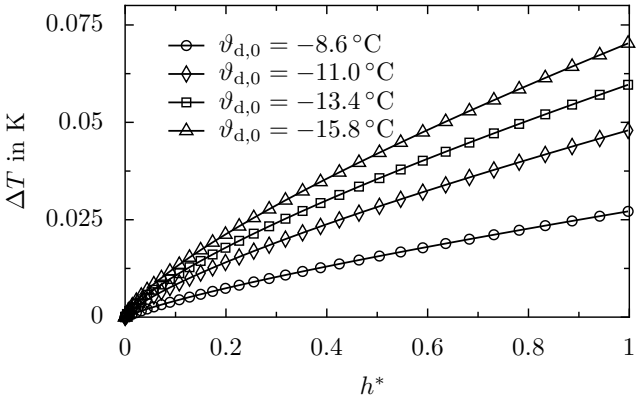

Figure A.2: Change of the drop temperature during fall onto the impact surface. $h^* = 0$ corresponds to the moment of drop detachment from the PTFE tube, while $h^* = 1$ represents the moment of drop impact. The impact velocity and ambient relative humidity are $v_{\mathrm{d}} = 3.2\,\mathrm{m/s}$ and $\mathrm{RH}_{\infty} = 5\,\%$, respectively.

styrofoam chamber, measured in the respective experimental series. Due to evaporative cooling of the suspended drop, the ambient temperature is generally higher than the initial drop temperature at the moment of detachment, $\vartheta_{\mathrm{d},0}$.

The warm up of a falling drop, $\Delta\vartheta = \vartheta_{\mathrm{d}} - \vartheta_{\mathrm{d},0}$, for varying initial drop temperatures is shown in Fig. A.2. It is shown as a function of the dimensionless height $h^* = 1 - h_{\mathrm{d}}/h_{\mathrm{d},0}$, where h_{d} and $h_{\mathrm{d},0}$ are the momentary and the initial height of the drop above the impact surface. Accordingly, $h^* = 0$ represents the moment of drop detachment from the PTFE tube, and $h^* = 1$ corresponds to the moment of drop impact. As shown in the figure, the drop temperature only slightly changes during a drop's fall. Since convective heat transfer is larger than evaporative cooling, a warm up of the drop during fall can be observed for all shown cases. It increases with decreasing initial drop temperature up to $\Delta\vartheta_{\max} \approx 0.07\,\mathrm{K}$ for the lowest initial drop temperature $\vartheta_{d,0} = -15.8\,^{\circ}\mathrm{C}$. This drop warm up is negligible small compared to the defined uncertainty of the temperature measurement associated with drop generation, $\Delta\vartheta_{\mathrm{d},0} \approx \pm 0.3\,\mathrm{K}$ (see Sec. 3). Therefore, neglect of the temperature change during drop fall is reasonable and the drop temperature estimated as described in Sec. 3 can be assumed as the drop temperature relevant for drop impact.

B Thermophysical properties of water and air

If not stated differently, the temperature dependence of the thermophysical properties of water and air, being the most important fluids in the present work, are generally accounted for. They are obtained from data tabulated in [306, 367], which have been fitted in the relevant temperature range between $-30.0\,^{\circ}\mathrm{C}$ and $+20.0\,^{\circ}\mathrm{C}$ using polynamial ansatz functions. In the following, the respective polynomials, their coefficients of determination R^2, and figures showing the agreement between the literature data and the functional relations are summarized.

Note that the given functions are numerical-value relations which take the magnitude of temperature ϑ in °C, and yield the magnitude of the respective property in SI-units, i.e. the density ρ in $\mathrm{kg/m^3}$, the thermal conductivity k in W/(m K), the kinematic viscosity ν in $\mathrm{m^2/s}$, the heat capacity c in J/(kg K), and the surface tension σ in N/m.

Due to their rather weak dependence on temperature, the material properties of ice are assumed constant, corresponding to the values at $0\,^{\circ}\mathrm{C}$, which are $\rho = 917\,\mathrm{kg/m^3}$, $c_\mathrm{p} = 2100\,\mathrm{J/(kgK)}$ and $k = 2.215\,\mathrm{W/(mK)}$ [203].

Properties of water

Density in $\mathrm{kg/m^3}$

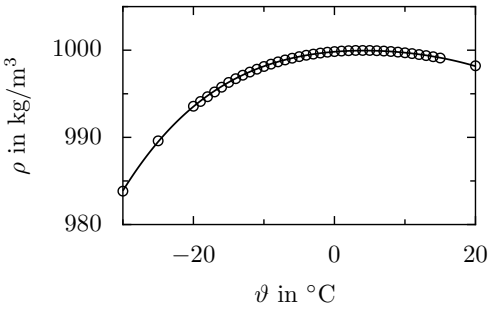

$$\begin{aligned}\rho &= 999.82 \\ &+ 6.55\times10^{-2}\ \vartheta \\ &- 8.49\times10^{-3}\ \vartheta^2 \\ &+ 1.26\times10^{-4}\ \vartheta^3 \\ &- 3.62\times10^{-6}\ \vartheta^4\end{aligned}$$

$\mathrm{R}^2 = 0.99986$

Heat capacity in $\mathrm{J/(kg\,K)}$

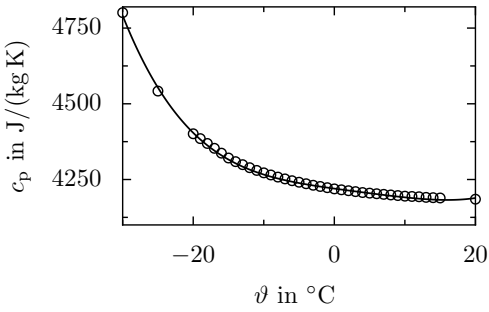

$$\begin{aligned}c_\mathrm{p} &= 4222 \\ &- 3.22\ \vartheta \\ &+ 5.21\times10^{-2}\ \vartheta^2 \\ &- 5.40\times10^{-3}\ \vartheta^3 \\ &+ 3.48\times10^{-4}\ \vartheta^4\end{aligned}$$

$\mathrm{R}^2 = 0.99883$

Thermal conductivity in $\mathrm{W/(m\,K)}$

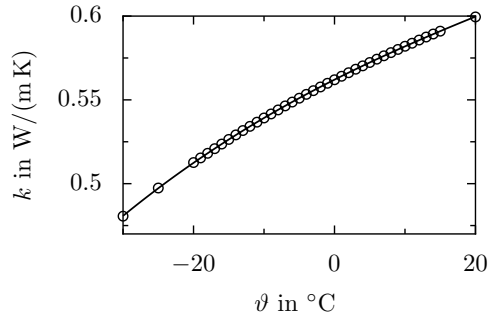

$$\begin{aligned}k &= 0.562 \\ &+ 2.12\times10^{-3}\ \vartheta \\ &- 1.50\times10^{-5}\ \vartheta^2 \\ &+ 1.55\times10^{-7}\ \vartheta^3\end{aligned}$$

$\mathrm{R}^2 = 0.99999$

Kinematic viscosity in $10^{-5}\mathrm{m}^2/\mathrm{s}$

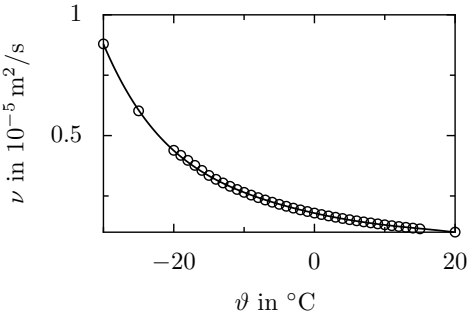

$$\begin{aligned}\nu &= 1.79\times10^{-6} \\ &- 6.49\times10^{-8}\ \vartheta \\ &+ 1.71\times10^{-9}\ \vartheta^2 \\ &- 1.62\times10^{-11}\vartheta^3 \\ &+ 1.32\times10^{-12}\vartheta^4 \\ &- 8.26\times10^{-14}\vartheta^5\end{aligned}$$

$\mathrm{R}^2 = 0.99987$

Surface energy in $\mathrm{N/m}$

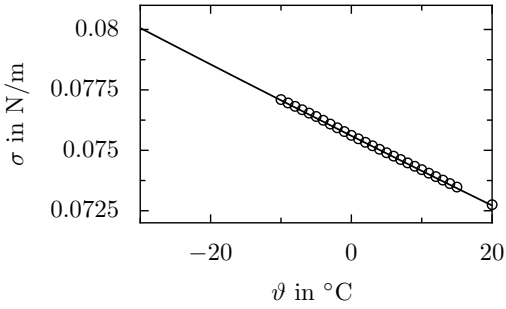

$$\begin{aligned}\sigma &= 0.0756 \\ &- 1.46\times10^{-4}\ \vartheta \\ &+ 9.05\times10^{-8}\ \vartheta^2\end{aligned}$$

$\mathrm{R}^2 = 0.99995$

Properties of air

Density in $\mathrm{kg/m}^3$

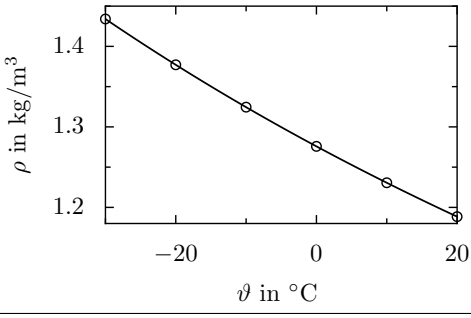

$$\begin{aligned}\rho &= 1.28 \\ &- 4.69\times10^{-3}\ \vartheta \\ &+ 1.75\times10^{-5}\ \vartheta^2 \\ &- 6.67\times10^{-8}\ \vartheta^3 \\ &+ 1.52\times10^{-18}\vartheta^4\end{aligned}$$

$\mathrm{R}^2 = 1$

Heat capacity in $\mathrm{J/(kg\,K)}$

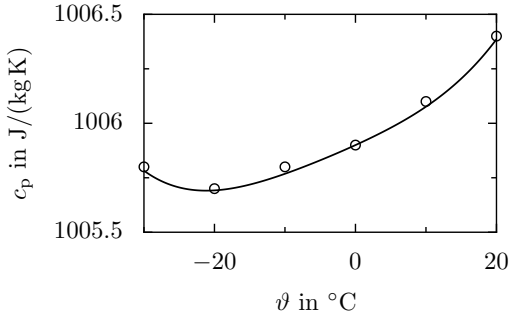

$$c_\mathrm{p} = 1006 + 1.48\times10^{-2}\,\vartheta + 1.81\times10^{-4}\,\vartheta^2 + 6.48\times10^{-6}\,\vartheta^3 + 4.16\times10^{-7}\,\vartheta^4$$

$\mathrm{R}^2 = 0.99815$

Thermal conductivity in $\mathrm{W/(m\,K)}$

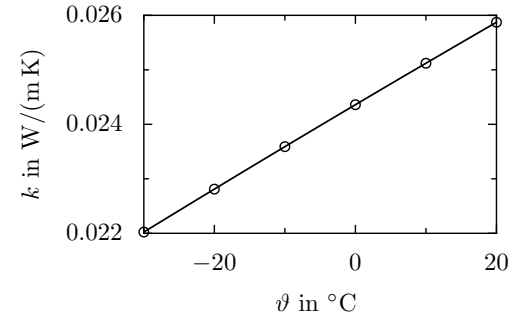

$$k = 0.0244 + 7.66\times10^{-5}\,\vartheta - 4.50\times10^{-8}\,\vartheta^2 - 4.07\times10^{-20}\vartheta^3$$

$\mathrm{R}^2 = 1$

Kinematic viscosity in $10^{-5}\mathrm{m}^2/\mathrm{s}$

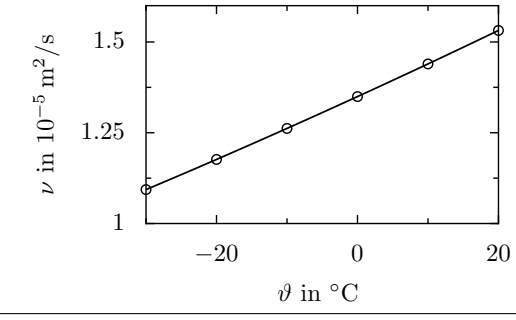

$$\nu = 1.35\times10^{-5} + 8.88\times10^{-8}\,\vartheta + 1.15\times10^{-10}\vartheta^2 + 1.84\times10^{-13}\vartheta^3 - 3.31\times10^{-15}\vartheta^4 - 2.98\times10^{-16}\vartheta^5$$

$\mathrm{R}^2 = 1$

Bibliography

[1] V. S. Ajaev and S. H. Davis. The effect of tri-junction conditions in droplet solidification. *J. Cryst. Growth*, 264:452–462, 2004.

[2] S. V. Alekseenko, C. Mendig, M. Schulz, M. Sinapius, and O. A. Prykhodko. An experimental study of freezing of supercooled water droplet on solid surface. *Tech. Phys. Lett.*, 42(5):524–527, 2016.

[3] V. Alexiades and A. Solomon. *Mathematical Modeling of Melting and Freezing Processes*. Taylor & Francis, 1 edition, 1992.

[4] D. A. Ali and R. R. Crawford. The effects of frost formation on the performance of domestic refrigerator-freezer finned-tube evaporator coils. Project report, Air Conditioning and Refrigeration Center, College of Engineering, University of Illinois at Urbana-Champaign, Urbana, IL, USA, 1992.

[5] F. Aliotta, P. V. Giaquinta, R. C. Ponterio, S. Prestipino, F. Saija, G. Salvato, and C. Vasi. Supercooled water escaping from metastability. *Sci. Rep.*, 4:7230, 2014.

[6] A. Alizadeh, M. Yamada, R. Li, W. Shang, S. Otta, S. Zhong, L. Ge, A. Dhinojwala, K. R. Conway, V. Bahadur, A. J. Vinciquerra, B. Stephens, and M. L. Blohm. Dynamics of ice nucleation on water repellent surfaces. *Langmuir*, 28(6):3180–3186, 2012.

[7] D. M. Anderson, M. G. Worster, and S. H. Davis. The case for a dynamic contact angle in containerless solidification. *J. Cryst. Growth*, 163:329–338, 1996.

[8] C. A. Angell. Supercooled water. In F. Franks, editor, *Water a Comprehensive Treatise*, volume 7, pages 1–81. Plenum Press, New York, 1982.

[9] C. Antonini. *Superhydrophobicity as a Strategy against Icing: Analysis of the Water/Surface Dynamic Interaction for Icing Mitigation*. PhD thesis, Università degli studi di Bergamo, 2011.

[10] C. Antonini, M. Innocenti, T. Horn, M. Marengo, and A. Amirfazli. Understanding the effect of superhydrophobic coatings on energy

reduction in anti-icing systems. *Cold Reg. Sci. Technol.*, 67(1-2):58–67, 2011.

[11] C. Antonini, A. Mularczyk, T. Maitra, M. K. Tiwari, and D. Poulikakos. What am I? Supercooled droplet or ice? *arXiv:1310.4102v1*, pages 1–2, 2013.

[12] T. Asaoka, A. Tajima, and H. Kumano. Experimental investigation on inhomogeneity of ice packing factor in ice slurry flow. *Int. J. Refrig*, 70:33–41, 2016.

[13] J. D. Atkinson, B. J. Murray, and D. O'Sullivan. Rate of homogenous nucleation of ice in supercooled water. *J. Phys. Chem. A*, 120(33):6513–6520, 2016.

[14] D. Attinger and D. Poulikakos. Melting and resolidification of a substrate caused by molten microdroplet impact. *J. Heat Transfer*, 123:1110–1122, 2001.

[15] D. Attinger, Z. Zhao, and D. Poulikakos. An experimental study of molten microdroplet surface deposition and solidification: Transient behavior and wetting angle dynamics. *J. Heat Transfer*, 122:544–556, 2000.

[16] M. Avrami. Kinetics of phase change. I: General theory. *J. Chem. Phys.*, 7:1103–1112, 1939.

[17] M. Avrami. Kinetics of phase change. II: Transformation-time relations for random distribution of nuclei. *J. Chem. Phys.*, 8:212–224, 1940.

[18] M. Avrami. Kinetics of phase change. III: Granulation, phase change and microstructur. *J. Chem. Phys.*, 9:177–184, 1941.

[19] V. Ayel, O. Lottin, and H. Peerhossaini. Rheology, flow behaviour and heat transfer of ice slurries: A review of the state of the art. *Int. J. Refrig*, 26(1):95–107, 2003.

[20] H. D. Baehr and P. Stephan. *Wärme- Und Stoffübertragung*. Springer Vieweg, Berlin, Heidelberg, 8 edition, 2013.

[21] V. Bahadur, L. Mishchenko, B. Hatton, J. A. Taylor, J. Aizenberg, and T. Krupenkin. Predictive model for ice formation on superhydrophobic surfaces. *Langmuir*, 27:14143–14150, 2011.

[22] S. Bankoff. Entrapment of gas in the spreading of a liquid over a rough surface. *AIChE J.*, 4(1):24–26, 1958.

[23] A. Barabadi, A. H. S. Garmabaki, and R. Zaki. Cold regions science and technology designing for performability: An icing risk index for arctic offshore. *Cold Reg. Sci. Technol.*, 124:77–86, 2016.

[24] T. W. Barlow and A. D. J. Haymet. Alta: An automated lag-time apparatus for studying the nucleation of supercooled liquids. *Rev. Sci. Instrum.*, 66(4):2996–3007, 1995.

[25] D. Bartolo, C. Josserand, and D. Bonn. Retraction dynamics of aqueous drops upon impact on non-wetting surfaces. *J. Fluid Mech.*, 545:329–338, 2005.

[26] D. Bartolo, C. Josserand, and D. Bonn. Singular jets and bubbles in drop impact. *Phys. Rev. Lett.*, 96:124501, 2006.

[27] R. Battino, P. G. Seybold, and F. C. Campanell. Correlations involving the solubility of gases in water at 298.15 K and 101325 Pa. *J. Chem. Eng. Data*, 56(4):727–732, 2011.

[28] S. Batzdorf, J. Breitenbach, C. Schlawitschek, I. V. Roisman, C. Tropea, P. Stephan, and T. Gambaryan-Roisman. Heat transfer during simultaneous impact of two drops onto a hot solid substrate. *Int. J. Heat Mass Transfer*, 113:898–907, 2017.

[29] S. Bauerecker, P. Ulbig, V. Buch, L. Vrbka, and P. Jungwirth. Monitoring ice nucleation in pure and salty water via high-speed imaging and computer simulations. *J. Phys. Chem. C*, 112(20):7631–7636, 2008.

[30] H. Baumgärtel and H. W. Zimmermann. The homogeneous nucleation in supercooled water. An examination using statistics and irreversible thermodynamics. *J. Mol. Liq.*, 164(3):178–186, 2011.

[31] T. Bennett and D. Poulikakos. Splat-quench solidification: Estimating the maximum spreading of a droplet impacting a solid surface. *J. Mater. Sci.*, 28:963–970, 1993.

[32] T. Bennett and D. Poulikakos. Heat transfer aspects of splat-quench solidification: Modelling and experiment. *J. Mater. Sci.*, 29:2025–2039, 1994.

[33] E. Berberović, I. Roisman, S. Jakirlić, and C. Tropea. Inertia dominated flow and heat transfer in liquid drop spreading on a hot substrate. *Int. J. Heat Fluid Flow*, 32(4):785–795, 2011.

[34] E. Berberović, M. Schremb, Ž. Tuković, S. Jakirlić, and C. Tropea. Computational modeling of freezing of supercooled water using phase-field front propagation with immersed points. *Int. J. Multiphase Flow*, 99:329–346, 2018.

[35] E. Berberović, N. Van Hinsberg, S. Jakirlić, I. Roisman, and C. Tropea. Drop impact onto a liquid layer of finite thickness: Dynamics of the cavity evolution. *Phys. Rev. E*, 79(3):036306, 2009.

[36] A. J. Bermúdez di Lorenzo, M. a. Carignano, and R. G. Pereyra. A statistical study of heterogeneous nucleation of ice by molecular dynamics. *Chem. Phys. Lett.*, 635:45–49, 2015.

[37] B. C. Bernstein, T. P. Ratvasky, D. R. Miller, and F. Mcdonough. Freezing rain as an in-flight icing hazard. Technical report, NASA, Glenn Research Center, Cleveland, Ohio, 2000.

[38] R. Bhola and S. Chandra. Parameters controlling solidification of molten wax droplets falling on a solid surface. *J. Mater. Sci.*, 34(19):4883–4894, 1999.

[39] E. K. Bigg. The supercooling of water. *Proc. Phys. Soc. Lond. B*, 66(8):688–694, 1953.

[40] N. Bilaniuk and G. S. K. Wong. Speed of sound in pure water as a function of temperature. *J. Acoust. Soc. Am.*, 93(3):1609–1612, 1993.

[41] J. Blake, D. Thompson, and T. Strobl. Simulating the freezing of supercooled water droplets impacting a cooled substrate. *AIAA Journal*, 53(7):1725–1739, 2015.

[42] L. Boinovich, A. M. Emelyanenko, V. V. Korolev, and A. S. Pashinin. Effect of wettability on sessile drop freezing: When superhydrophobicity stimulates an extreme freezing delay. *Langmuir*, 30:1659–1668, 2014.

[43] L. B. Boinovich and A. M. Emelyanenko. Anti-icing potential of superhydrophobic coatings. *Mendeleev Commun.*, 23(1):3–10, 2013.

[44] S. Borchert. Numerical Investigation of the Impact of Supercooled Liquid Drops on Cold Surfaces. Bachelor's thesis, Technische Universität Darmstadt, Darmstadt, Germany, 2016. Advisor: M. Schremb, M.Sc.

[45] G. E. P. Box, J. S. Hunter, and W. G. Hunter. *Statistics for Experimenters*. Wiley-Interscience, New Jersey, 2 edition, 2005.

[46] J. Brackbill, D. Kothe, and C. Zemach. A continuum method for modeling surface tension. *J. Comput. Phys.*, 100(2):335–354, 1992.

[47] M. Bragg, A. Broeren, H. Addy, M. Potapczuk, D. Guffond, and E. Montreuil. Airfoil ice-accretion aerodynamics simulation. *AIAA Aerospace Sciences Meeting and Exhibit*, 85:1–22, 2007.

[48] M. Bragg, A. Broeren, and L. Blumenthal. Iced-airfoil aerodynamics. *Prog. Aerosp. Sci.*, 41(5):323–362, 2005.

[49] M. B. Bragg. Aicraft aerodynamic effects due to large droplet ice accretions. *AIAA Paper*, 96-0932, 1996.

[50] I. Braslavsky and S. G. Lipson. Electrofreezing effect and nucleation of ice crystals in free growth experiments. *Appl. Phys. Lett.*, 72(2):264–266, 1998.

[51] J. Breitenbach, I. V. Roisman, and C. Tropea. Drop collision with a hot, dry solid substrate: Heat transfer during nucleate boiling. *Phys. Rev. Fluids*, 2:074301, 2017.

[52] J. Breitenbach, I. V. Roisman, and C. Tropea. Heat transfer in the film boiling regime: Single drop impact and spray cooling. *Int. J. Heat Mass Transfer*, 110:34–42, 2017.

[53] A. P. Broeren and M. B. Bragg. Effect of airfoil geometry on performance with simulated intercycle ice accretions. *J. Aircraft*, 42(1):121–130, 2005.

[54] J. Brunton and M. Rochester. Erosion of solid surfaces by the impact of liquid drops. *Academic Press, Treatise on Materials Science and Technology*, 16:185–248, 1979.

[55] C. Budke and T. Koop. Binary: An optical freezing array for assessing temperature and time dependence of heterogeneous ice nucleation. *Atmos. Meas. Tech.*, 8(2):689–703, 2015.

[56] Bureau d'Enquêtes et d'Analyses. Final report on the accident on 1st June 2009 to the airbus A330-203 registered F-gzcp operated by air France flight af 447 rio de janeiro-paris. Report, Ministère de l'Écologie, du Développement durable, des Transports et du Logement, Paris, 2012.

[57] P. R. Camp and C. F. Barter. Rate of growth of ice at an aluminium-water interface. *Nature*, 206:495–497, 1965.

[58] J. M. Campbell, F. C. Meldrum, and H. K. Christenson. Is ice nucleation from supercooled water insensitive to surface roughness? *J. Phys. Chem. C*, 119:1164–1169, 2015.

[59] B. Cantor and A. Vogel. Dendritic solidification and fluid flow. *J. Cryst. Growth*, 41(1):109–123, 1977.

[60] Y. Cao and K. Chen. Helicopter icing. *Aeronaut. J.*, 114(1152):83–90, 2010.

[61] Y. Cao, Z. Wu, Y. Su, and Z. Xu. Aircraft flight characteristics in icing conditions. *Prog. Aerosp. Sci.*, 74:62–80, 2015.

[62] M. Carignano, E. Baskaran, P. Shepson, and I. Szleifer. Molecular dynamics simulation of ice growth from supercooled pure water and from salt solution. *Ann. Glaciol.*, 44(1):113–117, 2006.

[63] H. S. Carslaw and J. C. Jaeger. *Conduction of Heat in Solids*. Oxford University Press, Oxford, UK, 2 edition, 1959.

[64] A. E. Carte. Probability of freezing. *Proc. Phys. Soc.*, 73(2):324, 1959.

[65] T. Cebeci and F. Kafyeke. Aircraft icing. *Annu. Rev. Fluid Mech.*, 35(1):11–21, 2003.

[66] J. Chen, J. Liu, M. He, K. Li, D. Cui, Q. Zhang, X. Zeng, Y. Zhang, J. Wang, and Y. Song. Superhydrophobic surfaces cannot reduce ice adhesion. *Appl. Phys. Lett.*, 101:111603, 2012.

[67] T. S. Chen, B. F. Armaly, and N. Ramachandran. Correlations for laminar mixed convection flows on vertical, inclined, and horizontal flat plates. *J. Heat Transfer*, 108(4):835–840, 2016.

[68] R. Chow, R. Blindt, R. Chivers, and M. Povey. A study on the primary and secondary nucleation of ice by power ultrasound. *Ultrasonics*, 43(4):227–230, 2005.

[69] S. W. Churchill. A comprehensive correlating equation for laminar, assisting, forced and free convection. *AIChE J.*, 23(1):10–16, 1977.

[70] C. Clanet, C. Beguin, D. Richard, and D. Quere. Maximal deformation of an impacting drop. *J. Fluid Mech.*, 517:199–208, 2004.

[71] H. Coffman Jr. Review of helicopter icing protection systems. In *Proceedings of the Aircraft Design, Systems and Technology Meeting*, Fort Worth, TX, USA, 1983.

[72] P. J. Connolly, O. Möhler, P. R. Field, H. Saathoff, R. Burgess, T. W. Choularton, and M. W. Gallagher. Studies of heterogeneous freezing by three different desert dust samples. *Atmos. Chem. Phys.*, 9:2805–2824, 2009.

[73] W. A. Cooper, W. R. Sand, D. L. Veal, and M. K. Politovich. Effects of icing on performance of a research airplane. *J. Aircraft*, 21:708–715, 1984.

[74] R. V. Craster and O. K. Matar. Dynamics and stability of thin liquid films. *Rev. Mod. Phys.*, 81(3):1131–1198, 2009.

[75] A. Criscione, D. Kintea, I. V. Roisman, S. Jakirlić, and C. Tropea. A new approach for water crystallization in the kinetics-limited growth region. In *Proceedings of the 8th International Conference on Multiphase Flow*, Jeju, Korea, 2013.

[76] A. Criscione, D. Kintea, Ž. Tuković, S. Jakirlić, I. V. Roisman, and C. Tropea. Crystallization of supercooled water: A level-set-based modeling of the dendrite tip velocity. *Int. J. Heat Mass Transfer*, 66:830–837, 2013.

[77] A. Criscione, I. V. Roisman, S. Jakirlić, and C. Tropea. Towards modelling of initial and final stages of supercooled water solidification. *Int. J. Therm. Sci.*, 92:150–161, 2015.

[78] N. Dalili, A. Edrisy, and R. Carriveau. A review of surface engineering issues critical to wind turbine performance. *Renew. Sust. Energ. Rev.*, 13(2):428–438, 2009.

[79] S. H. Davis. *Theory of Solidification.* Cambridge University Press, 2001.

[80] P. G. de Gennes. Wetting: Statics and dynamics. *Rev. Mod. Phys.*, 57(3):827–863, 1985.

[81] R. de Ruiter, P. Colinet, P. Brunet, J. H. Snoeijer, and H. Gelderblom. Contact line arrest in solidifying spreading drops. *Phys. Rev. Fluids*, 2:043602, 2017.

[82] A. Dehghani-Sanij, S. Dehghani, G. Naterer, and Y. Muzychka. Marine icing phenomena on vessels and offshore structures: Prediction and analysis. *Ocean Eng.*, 143:1–23, 2017.

[83] V. A. Del Grosso and C. W. Mader. Speed of sound in pure water. *J. Acoust. Soc. Am.*, 52(5):1442–1446, 1972.

[84] S. Deshpande, L. Anumolu, and M. Trujillo. Evaluating the performance of the two-phase flow solver interfoam. *Comput. Sci. Discov.*, 5(1):014016, 2012.

[85] R. Dhiman and S. Chandra. Freezing-induced splashing during impact of molten metal droplets with high Weber numbers. *Int. J. Heat Mass Transfer*, 48(25-26):5625–5638, 2005.

[86] R. D. Doherty, B. Cantor, and S. J. M. Fairs. Further analysis of dendritic growth data for succinonitrile. *Metall. Trans. A*, 9(5):621–624, 1978.

[87] J. B. Doolittle and G. Vali. Heterogeneous freezing nucleation in electric fields. *J. Atmos. Sci.*, 32(2):375–379, 1975.

[88] R. G. Dorsch and P. T. Hacker. Photomicrographic investigation of spontaneous freezing temperatures of supercooled water droplets. Research report, National Advisory Committee for Aeronautics. Lewis Flight Propulsion Lab., Cleveland, OH, United States, 1950.

[89] F. I. Dragomirescu, K. Eisenschmidt, C. Rohde, and B. Weigand. Perturbation solutions for the finite radially symmetric Stefan problem. *Int. J. Therm. Sci.*, 104:386–395, 2016.

[90] L. Dufour. Ueber das Gefrieren des Wassers und über die Bildung des Hagels. *Ann. Phys.*, 190(12):530–554, 1861.

[91] R. C. Dykhuizen. Review of impact and solidification of molten thermal spray droplets. *J. Therm. Spray Technol.*, 3(4):351–361, 1994.

[92] L. Dzumbova, J. Schwarz, and J. Smolik. Evaporation of water droplet in the humid atmosphere. *J. Aerosol Sci.*, 30(1):337–338, 1999.

[93] M. E. Earle, T. Kuhn, A. F. Khalizov, and J. J. Sloan. Volume nucleation rates for homogeneous freezing in supercooled water microdroplets: Results from a combined experimental and modelling approach. *Atmos. Chem. Phys.*, 10(16):7945–7961, 2010.

[94] P. Eberle, M. K. Tiwari, T. Maitra, and D. Poulikakos. Rational nanostructuring of surfaces for extraordinary icephobicity. *Nanoscale*, 6(9):4874–4881, 2014.

[95] J. Eggers, M. A. Fontelos, C. Josserand, and S. Zaleski. Drop dynamics after impact on a solid wall: Theory and simulations. *Phys. Fluids*, 22:062101, 2010.

[96] K. Eisenschmidt, M. Ertl, H. Gomaa, C. Kiefer-Roth, C. Meister, P. Rauschenberger, R. M., K. Schlottke, and B. Weigand. Direct numerical simulations for multiphase flows: An overview of the multiphase code FS3D. *Appl. Math. Comput.*, 272:508–517, 2016.

[97] J. W. Elliott and F. T. Smith. Ice formation on a smooth or rough cold surface due to the impact of a supercooled water droplet. *J. Eng. Math.*, 102(1):35–64, 2017.

[98] A. M. Emelyanenko, L. B. Boinovich, A. A. Bezdomnikov, E. V. Chulkova, and K. A. Emelyanenko. Reinforced superhydrophobic coating on silicone rubber for longstanding anti-icing performance in severe conditions. *ACS Appl. Mater. Inter.*, 9:24210—–24219, 2017.

[99] O. R. Enríquez, Á. G. Marín, K. G. Winkels, and J. H. Snoeijer. Freezing singularities in water drops. *Phys. Fluids*, 24(9):091102, 2012.

[100] P. S. Epstein and M. S. Plesset. On the stability of gas bubbles in liquid-gas solutions. *J. Chem. Phys*, 18(11):1505–1509, 1950.

[101] D. G. Fahrenheit. Experimenta & observationes de congelatione aquae in vacuo factae. *Phil. Trans. R. Soc. Lond.*, 33:78–84, 1724. (german translation in: Ostwald's Klassiker der exakten Wissenschaften, 57, Abhandlungen über Thermometrie von Fahrenheit, Réaumur, Celsius (1724, 1730-1733, 1742), A. J. von Oettigen (Ed.), Engelmann, Leipzig (1894)).

[102] M. Farzaneh. Ice accretions on high-voltage conductors and insulators and related phenomena. *Phil. Trans. R. Soc. A*, 358(1776):2971–3005, 2000.

[103] M. Farzaneh, editor. *Atmospheric Icing of Power Networks*. Springer Science & Business Media, 2008.

[104] M. Farzaneh and W. A. Chisholm. *Insulators for Icing and Polluted Environments*. IEEE Press series on power engineering. Wiley-Blackwell, Oxford, 2009.

[105] P. Fauchais, M. Fukumoto, A. Vardelle, and M. Vardelle. Knowledge concerning splat formation: An invited review. *J. Therm. Spray Technol.*, 13(3):337–360, 2004.

[106] P. Fauchais, M. Vardelle, A. Vardelle, P. Fauchais, A. Vardelle, P. Fauchais, P. Fauchais, and A. Joulia. Understanding plasma spraying. *J. Phys. D: Appl. Phys.*, 37:86–108, 2004.

[107] P. L. Fauchais, J. V. Heberlein, and M. I. Boulos. *Thermal Spray Fundamentals - From Powder to Part*. Springer, New York, 2014.

[108] Federal Aviation Administration. Aviation weather for pilots and flight operations personnel. Advisory guide, FAA Flight Standards Service and National Weather Service, USA, 1975.

[109] W. Feller. *An Introduction to Probability Theory and Its Applications*, volume I. Wiley, New York, 3rd edition, 1968.

[110] M. Ferziger, J.H. Perić. *Computational Methods for Fluid Dynamics*. Springer-Verlag, Berlin, 2002.

[111] F. Feuillebois, S. Tabakova, S. Radev, and V. Daru. Entrained film of ice-water slurry with impinging supercooled water droplets. *J. Eng. Phys. Thermophys.*, 87(1):54–68, 2014.

[112] S. M. Fikke. Modern meteorology and atmospheric icing. In *Proceedings of the 11th International Workshop on Atmospheric Icing of Structures*, Montreal, Canada, 2005.

[113] R. M. Fillion, A. R. Riahi, and A. Edrisy. A review of icing prevention in photovoltaic devices by surface engineering. *Renew. Sust. Energ. Rev.*, 32:797–809, 2014.

[114] R. Flemming. The past twenty years of icing research and development at Sikorsky aircraft. In *Proceedings of the 40th Aiaa Aerospace Sciences Meeting & Exhibit*, Reno, NV, USA, 2002.

[115] N. Fletcher. Nucleation and growth of ice crystals upon crystalline substrates. *Aust. J. Phys.*, 13:408, 1960.

[116] N. H. Fletcher. Size effect in heterogeneous nucleation. *J. Chem. Phys.*, 29(3):572, 1958.

[117] N. H. Fletcher. Active sites and ice crystal nucleation, 1969.

[118] F. Franks, editor. *Water and Aqueous Solutions at Subzero Temperatures*, volume 7. Plenum Press, New York, 1982.

[119] F. Franks. Nucleation of ice and its management in ecosystems. *Phil. Trans. R. Soc. A*, 361(1804):557–574, 2003.

[120] S.-P. Fu, R. P. Sahu, E. Diaz, J. R. Robles, C. Chen, X. Rui, R. F. Klie, A. L. Yarin, and J. T. Abiade. Dynamic study of liquid drop impact on supercooled cerium dioxide: Anti-icing behavior. *Langmuir*, 32:6148–6162, 2016.

[121] T. Fujioka. *Study of Ice Growth in Slightly Undercooled Water*. PhD thesis, Carnegie-Mellon University, Pittsburgh, PA, 1978.

[122] Y. Furukawa and W. Shimada. Three-dimensional pattern formation during growth of ice dendrites - Its relation to universal law of dendritic growth. *J. Cryst. Growth*, 128(1-4):234–239, 1993.

[123] C. Galusinski and P. Vigneaux. On stability condition for bifluid flows with surface tension: Application to microfluidics. *J. Comput. Phys.*, 227(12):6140–6164, 2008.

[124] R. W. Gent, N. P. Dart, and J. T. Cansdale. Aircraft icing. *Phil. Trans. R. Soc. A*, 358(1776):2873–2911, 2000.

[125] S. Glasstone, K. J. Laidler, H. Eyring, et al. *The Theory of Rate Processes; the Kinetics of Chemical Reactions, Viscosity, Diffusion and Electrochemical Phenomena*. McGraw-Hill Book Company, Inc., New York, 1 edition, 1941.

[126] M. E. Glicksman. Mechanism of dendritic branching. *Metall. Mater. Trans. B*, 43(2):207–220, 2012.

[127] M. E. Glicksman, R. C. Hahn, T. A. Lograsso, S. H. Tirmizi, and E. Winsa. Isothermal dendritic growth - A proposed microgravity experiment. *Metall. Trans. A*, 19(8):1945–1953, 1988.

[128] M. E. Glicksman and M. B. Koss. Dendritic growth velocities in microgravity. *Phys. Rev. Lett.*, 73(4):573–576, 1994.

[129] M. E. Glicksman, M. B. Koss, L. T. Bushnell, J. C. Lacombe, and E. A. Winsa. Dendritic growth of succinonitrile in terrestrial and microgravity conditions as a test of theory. *ISIJ Int.*, 35(6):604–610, 1995.

[130] M. E. Glicksman, R. J. Schaefer, and J. D. Ayers. Dendritic growth - A test of theory. *Metall. Trans. A*, 7(11):1747–1759, 1976.

[131] V. Gnielinski. Berechnung mittlerer Wärme- und Stoffübergangskoeffizienten an laminar und turbulent überströmten Einzelkörpern mit Hilfe einer einheitlichen Gleichung. *Forschung im Ingenieurwesen A*, 41:145–153, 1975.

[132] G. A. E. Godsave. Studies of the combustion of drops in a fuel spray - The burning of single drops of fuel. *Symp. (Int.) Combust.*, 4(1):818–830, 1953.

[133] N. Goldenfeld. Dynamics of dendritic growth. *J. Power Sources*, 26(1-2):121–128, 1989.

[134] D. Golovko. Private communication, May 2016.

[135] G. G. Goyer, T. C. Bhadra, and S. Gitlin. Shock induced freezing of supercooled water. *J. Appl. Meteorol.*, 4(1):156–160, 1965.

[136] C. Gurganus, A. B. Kostinski, and R. A. Shaw. Fast imaging of freezing drops: No preference for nucleation at the contact line. *J. Phys. Chem. Lett.*, 2(12):1449–1454, 2011.

[137] J. Hallett and S. C. Mossop. Production of secondary ice particles during the riming process. *Nature*, 249(5452):26–28, 1974.

[138] A. A. Hamed, W. Tabakoff, R. B. Rivir, K. Das, and P. Arora. Turbine blade surface deterioration by erosion. *J. Turbomach.*, 127:445–452, 2005.

[139] N. L. Hancox and J. H. Brunton. The erosion of solids by the repeated impact of liquid drops. *Phil. Trans. R. Soc. A*, 260(1110):121–139, 1966.

[140] P. Hao, C. Lv, and X. Zhang. Freezing of sessile water droplets on surfaces with various roughness and wettability. *Appl. Phys. Lett.*, 104(16):161609, 2014.

[141] M. Hase and B. Weigand. Transient heat transfer of deforming droplets at high Reynolds numbers. *Int. J. Num. Meth. Heat Fluid Flow*, 14:85–97, 2004.

[142] A. Heinrich, R. Ross, G. Zumwalt, J. Provorse, V. Padmanabhan, J. Thomson, and J. Riley. Aircraft icing handbook: FAA technical report no. dot/faa/ct-88/8-1. Technical report, FAA Technical Center, Atlantic City International Airport, N.J. 08405, 1991.

[143] A. F. Heneghan and A. D. J. Haymet. Liquid-to-crystal heterogeneous nucleation: Bubble accelerated nucleation of pure supercooled water. *Chem. Phys. Lett.*, 368(1-2):177–182, 2003.

[144] A. F. Heneghan, P. W. Wilson, A. D. J. Haymet, and P. G. Wolynes. Heterogeneous nucleation of supercooled water, and the effect of an added catalyst. *Proc. Natl. Acad. Sci. U.S.A.*, 99(15):9631–9634, 2002.

[145] W. Henry. III. experiments on the quantity of gases absorbed by water, at different temperatures, and under different pressures. *Phil. Trans. R. Soc. Lond.*, 93:29–274, 1803.

[146] D. M. Herlach, O. Funke, P. Gandham, and P. Galenko. Free dendrite growth in undercooled melts: Experiments and modeling. In M. Rappaz, C. Beckermann, and R. Trivedi, editors, *Solidification Processes and Microstructures: A Symposium in Honor of Prof. Wilfried Kurz. Proceedings of the TMS Annual Meeting*, pages 277–288. 2004.

[147] J. R. Heverly. Supercooling and crystallization. *Trans. Am. Geophys. Union*, 30(2):205–210, 1949.

[148] G. Heydari, E. Thormann, M. Järn, E. Tyrode, and P. M. Claesson. Hydrophobic surfaces: Topography effects on wetting by supercooled water and freezing delay. *J. Phys. Chem. C*, 117(42):21752–21762, 2013.

[149] W. B. Hillig. Measurement of interfacial free energy for ice/water system. *J. Cryst. Growth*, 183:463–468, 1998.

[150] J. P. Hindmarsh, A. B. Russell, and X. D. Chen. Experimental and numerical analysis of the temperature transition of a suspended freezing water droplet. *Int. J. Heat Mass Transfer*, 46(7):1199–1213, 2003.

[151] C. Hirt and B. Nichols. Volume of fluid (VOF) method for the dynamics of free boundaries. *J. Comput. Phys.*, 39:201–225, 1981.

[152] P. V. Hobbs. *Ice Physics*. Oxford classic texts in the physical sciences. Oxford University Press, Oxford, 2010.

[153] C. Hochart, G. Fortin, J. Perron, and A. Ilinca. Wind turbine performance under icing conditions. *Wind Energy*, 11:319–333, 2008.

[154] M. C. Homola, P. J. Nicklasson, and P. A. Sundsbo. Ice sensors for wind turbines. *Cold Reg. Sci. Technol.*, 46(2):125–131, 2006.

[155] C. Hoose and O. Möhler. Heterogeneous ice nucleation on atmospheric aerosols: A review of results from laboratory experiments. *Atmos. Chem. Phys.*, 12(20):9817–9854, 2012.

[156] J. Huang and L. S. Bartell. Kinetics of homogeneous nucleation in the freezing of large water clusters. *J. Phys. Chem.*, 99(12):3924–3931, 1995.

[157] W. Huang and L. Wang. Solidification researches using transparent model materials - A review. *Sci. China Tech. Sci.*, 55(2):377–386, 2012.

[158] S. Iannella. Experimental Investigation of the Solidification Front in Supercooled Sessile Droplets. Master's thesis, Technische Universität Darmstadt, Darmstadt, Germany, 2015. Advisor: M. Schremb, M.Sc.

[159] F. P. Incropera, D. P. De Witt, T. L. Bergman, and A. S. Lavine. *Fundamentals of Heat and Mass Transfer*. John Wiley and Sons, New York, 5^{th} edition, 2002.

[160] G. Isaac, R. Jeck, and J. Hughes, William. Working group on icing environmental characterization. In *Proceedings of the Faa International Conference on Aircraft Inflight Icing, Working Group Reports*, Springfield, Virginia, USA, 1996.

[161] G. P. Ivantsov. Temperature around a spheroidal, cylindrical and acicular crystal growing in a supercooled melt. *Dokl. Akad. Nauk SSSR*, 58(58):567–569, 1947.

[162] M. A. Jaafar, D. R. Rousse, S. Gibout, and J.-P. Bédécarrats. A review of dendritic growth during solidification: Mathematical modeling and numerical simulations. *Renew. Sust. Energ. Rev.*, 74:1064–1079, 2017.

[163] W. J. Jasinski, S. C. Noe, M. S. Selig, and M. B. Bragg. Wind turbine performance under icing conditions. *J. Sol. Energy Eng.*, 120(1):60–65, 1998.

[164] B. P. Jelle, T. Gao, S. A. Mofid, T. Kolås, P. M. Stenstad, and S. Ng. Avoiding snow and ice formation on exterior solar cell surfaces - A review of research pathways and opportunities. *Procedia Eng.*, 145(1877):699–706, 2016.

[165] Z. Jin, S. Jin, and Z. Yang. An experimental investigation into the icing and melting process of a water droplet impinging onto a superhydrophobic surface. *Sci. China-Phys. Mech. Astron.*, 56(11):2047–2053, 2013.

[166] Z. Jin, H. Zhang, and Z. Yang. Experimental investigation of the impact and freezing processes of a water droplet on an ice surface. *Int. J. Heat Mass Transfer*, 109:716–724, 2017.

[167] Z. Jin, H. Zhang, and Z. Yang. The impact and freezing processes of a water droplet on different cold cylindrical surfaces. *Int. J. Heat Mass Transfer*, 113:318–323, 2017.

[168] W. A. Johnson and R. Mehl. Reaction kinetics in process of nucleation and growth. *Trans. Am. Inst. Min. Eng.*, 135:416–458, 1939.

[169] C. Josserand and S. T. Thoroddsen. Drop impact on a solid surface. *Annu. Rev. Fluid Mech.*, 48(1):365–391, 2016.

[170] D. H. Jung, J. H. Yang, and M. S. Jhon. The effect of an external electric field on the structure of liquid water using molecular dynamics simulations. *Chem. Phys.*, 244:331–337, 1999.

[171] S. Jung, M. Dorrestijn, D. Raps, A. Das, C. M. Megaridis, and D. Poulikakos. Are superhydrophobic surfaces best for icephobicity? *Langmuir*, 27(6):3059–3066, 2011.

[172] S. Jung, M. K. Tiwari, N. V. Doan, and D. Poulikakos. Mechanism of supercooled droplet freezing on surfaces. *Nat. Commun.*, 3:615, 2012.

[173] S. Jung, M. K. Tiwari, and D. Poulikakos. Frost halos from supercooled water droplets. *Proc. Natl. Acad. Sci. U.S.A.*, 109(40):16073–8, 2012.

[174] P. Kabath, P. Stöckel, A. Lindinger, and H. Baumgärtel. The nucleation of ice in supercooled D_2O and H_2O. *J. Mol. Liq.*, 125:204–211, 2006.

[175] D. Kashchiev. *Nucleation - Basic Theory with Applications*. Butterworth Heinemann, Oxford, UK, 1 edition, 2000.

[176] J. Kim. Spray cooling heat transfer: The state of the art. *Int. J. Heat Fluid Flow*, 28:753–767, 2007.

[177] D. M. Kintea. *Hydrodynamics and Thermodynamics of Ice Particle Accretion*. PhD thesis, Technische Universität Darmstadt, April 2016.

[178] S. Kistler. Hydrodynamics of wetting. In J. Berg, editor, *Wettability*, pages 311–429. Taylor & Francis Inc., New York, United States, 1993.

[179] A. N. Kolmogorov. On the statistical theory of the crystallization of metals. *Bull. Acad. Sci. USSR, Math. Ser.*, 1:355–359, 1937.

[180] S. N. Kondepudi and D. L. O'Neal. Frosting performance of tube fin heat exchangers with wavy and corrugated fins. *Exp. Therm. Fluid Sci.*, 4(5):613–618, 1991.

[181] W. Kong and H. Liu. A theory on the icing evolution of supercooled water near solid substrate. *Int. J. Heat Mass Transfer*, 91:1217–1236, 2015.

[182] T. Koop. Homogeneous ice nucleation in water and aqueous solutions. *Zeitschrift für Physikalische Chemie*, 218:1231–1258, 2004.

[183] T. Koop, B. Luo, U. M. Biermann, P. J. Crutzen, and T. Peter. Freezing of HNO_3 H_2SO_4 H_2O solutions at stratospheric temperatures: Nucleation statistics and experiments. *J. Phys. Chem. A*, 101(6):1117–1133, 1997.

[184] M. B. Koss, J. C. LaCombe, L. A. Tennenhouse, M. E. Glicksman, and E. A. Winsa. Dendritic growth tip velocities and radii of curvature in microgravity. *Metall. Mater. Trans. A*, 30(12):3177–3190, 1999.

[185] B. Krämer, O. Hübner, H. Vortisch, L. Wöste, T. Leisner, M. Schwell, E. Rühl, and H. Baumgärtel. Homogeneous nucleation rates of supercooled water measured in single levitated microdroplets. *J. Chem. Phys.*, 111(14):6521–6527, 1999.

[186] K. Kröll. Experimental Investigation of the Impact of Supercooled Liquid Drops on Cold Surfaces. Master's thesis, Technische Universität Darmstadt, Darmstadt, Germany, 2016. Advisor: M. Schremb, M.Sc.

[187] T. Kuhn, M. E. Earle, A. F. Khalizov, and J. J. Sloan. Size dependence of volume and surface nucleation rates for homogeneous freezing of supercooled water droplets. *Atmos. Chem. Phys.*, 11(6):2853–2861, 2011.

[188] H. Kumano, Y. Yamanada, Y. Makino, and T. Asaoka. Effect of initial aqueous solution concentration on rheological behavior of ice slurry. *Int. J. Refrig*, 68:218–225, 2016.

[189] J. Laforte, M. Allaire, and J. Laflamme. State-of-the-art on power line de-icing. *Atmos. Res.*, 46(1-2):143–158, 1998.

[190] J. Langer and H. Müller-Krumbhaar. Theory of dendritic growth - I. Elements of a stability analysis. *Acta Metall.*, 26(11):1681–1687, 1978.

[191] J. S. Langer and H. Müller-Krumbhaar. Theory of dendritic growth - II. Instabilities in the limit of vanishing surface tension. *Acta Metall.*, 26(11):1689–1695, 1978.

[192] E. J. Langham and B. J. Mason. The heterogeneous and homogeneous nucleation of supercooled water. *Proc. R. Soc. A*, 247(1251):493–504, 1958.

[193] J. Levine. Statistical explanation of spontaneous freezing of water droplets. Technical report, National Advisory Commitee for Aeronautics, Lewis Flight Propulsion Laboratory, Cleveland, Ohio, USA, 1950.

[194] S. Lewis, L. Anumolu, and M. Trujillo. Numerical simulations of droplet train and free surface jet impingement. *International Journal of Heat and Fluid Flow*, 44:610–623, 2013.

[195] H. Li. *Drop Impact on Dry Surfaces with Phase Change*. PhD thesis, Technische Universität Darmstadt, 2015.

[196] H. Li, I. V. Roisman, and C. Tropea. Influence of solidification on the impact of supercooled water drops onto cold surfaces. *Exp. Fluids*, 56(6):133, 2015.

[197] N. Li, Q. Zhou, X. Chen, T. Xu, S. Hui, and D. Zhang. Liquid drop impact on solid surface with application to water drop erosion on turbine blades, part I: Nonlinear wave model and solution of one-dimensional impact. *Int. J. Mech. Sci.*, 50(10-11):1526–1542, 2008.

[198] T. Li, D. Donadio, and G. Galli. Ice nucleation at the nanoscale probes no man's land of water. *Nat. Commun.*, 4:1–6, 2013.

[199] T. Li, D. Donadio, L. M. Ghiringhelli, and G. Galli. Surface-induced crystallization in supercooled tetrahedral liquids. *Nat. Mater.*, 8(9):726–730, 2009.

[200] G. Liang and I. Mudawar. Review of drop impact on heated walls. *Int. J. Heat Mass Transfer*, 106:103–126, 2017.

[201] G. Liang and I. Mudawar. Review of spray cooling - part 1: Single-phase and nucleate boiling regimes, and critical heat flux. *Int. J. Heat Mass Transfer*, 115(A):1174–1205, 2017.

[202] G. Liang and I. Mudawar. Review of spray cooling - part 2: High temperature boiling regimes and quenching applications. *Int. J. Heat Mass Transfer*, 115(A):1206–1222, 2017.

[203] J. Lienhard IV and J. Lienhard V. *A Heat Transfer Textbook*. Phlogiston Press, Cambridge, US, 3 edition, 2003.

[204] C. S. Lindenmeyer, G. T. Orrok, K. A. Jackson, and B. Chalmers. Rate of growth of ice crystals in supercooled water. *J. Chem. Phys.*, 27:822, 1957.

[205] N. Linder, A. Criscione, I. V. Roisman, H. Marschall, and C. Tropea. 3D computation of an incipient motion of a sessile drop on a rigid surface with contact angle hysteresis. *Theor. Comput. Fluid Dyn.*, 29(5-6):373–390, 2015.

[206] N. W. Linder. *Numerical Simulation of Complex Wetting*. PhD thesis, Technische Universität Darmstadt, January 2015.

[207] D. Lohse and X. Zhang. Surface nanobubbles and nanodroplets. *Rev. Mod. Phys.*, 87(3):981–1035, 2015.

[208] J. M. Löwe, V. Hinrichsen, M. Schremb, T. Dorau, and C. Tropea. Experimental investigation of electro-freezing of supercooled water droplets. In *Proceedings of the 9^{th} World Conference on Experimental Heat Transfer, Fluid Mechanics and Thermodynamics*, Foz do Iguaçu, Brasil, June 2017.

[209] E. P. Lozowski, E. M. Gates, and L. Makkonen. Towards the estimation of the icing hazard for mobile offshore drilling units. In *Proceedings of the 5^{th} International Symposium on Offshore Mechanics and Arctic Engineering*, Tokyo, Japan, 1986.

[210] E. P. Lozowski, J. R. Stallabrass, and P. F. Hearthy. The icing of an unheated, nonrotaing cylinder. Part I: A simulation model. *J. Climate Appl. Meteor.*, 22(12):2053–2062, 1983.

[211] E. P. Lozowski, J. R. Stallabrass, and P. F. Hearthy. The icing of an unheated, nonrotaing cylinder. Part II: Icing wind tunnel experiments. *J. Climate Appl. Meteor.*, 22(12):2063—-2074, 1983.

[212] E. P. Lozowski, K. Szilder, and L. Makkonen. Computer simulation of marine ice accretion. *Phil. Trans. R. Soc. A*, 358(1776):2811–2845, 2000.

[213] R. Lundheim. Physiological and ecological significance of biological ice nucleators. *Phil. Trans. R. Soc. B*, 357(1423):937–943, 2002.

[214] J. Madejski. Solidification of droplets on a cold surface. *Int. J. Heat Mass Transfer*, 19:1009–1013, 1976.

[215] T. Maitra, C. Antonini, M. K. Tiwari, A. Mularczyk, Z. Imeri, P. Schoch, and D. Poulikakos. Supercooled water drops impacting superhydrophobic textures. *Langmuir*, 30:10855–10861, 2014.

[216] T. Maitra, M. K. Tiwari, C. Antonini, P. Schoch, S. Jung, P. Eberle, and D. Poulikakos. On the nanoengineering of superhydrophobic and impalement resistant surface textures below the freezing temperature. *Nano Lett.*, 14(1):172–182, 2013.

[217] L. Makkonen. Salinity and growth rate of ice formed by sea spray. *Cold Reg. Sci. Technol.*, 14(2):163–171, 1987.

[218] L. Makkonen. Modeling power line icing in freezing precipitation. *Atmos. Res.*, 46(1-2):131–142, 1998.

[219] D. K. Mandal, A. Criscione, C. Tropea, and A. Amirfazli. Shedding of water drops from a surface under icing conditions. *Langmuir*, 31(34):9340–9347, 2015.

[220] M. Marengo, C. Antonini, I. V. Roisman, and C. Tropea. Drop collisions with simple and complex surfaces. *Curr. Opin. Colloid In.*, 16(4):292–302, 2011.

[221] A. G. Marín, O. R. Enríquez, P. Brunet, P. Colinet, and J. H. Snoeijer. Universality of tip singularity formation in freezing water drops. *Phys. Rev. Lett.*, 113(5):054301, 2014.

[222] J. G. Mason, P. Chow, and D. M. Fuleki. Understanding ice crystal accretion and shedding phenomenon in jet engines using a rig test. *J. Eng. Gas Turbines Power*, 133(4):041201, 2011.

[223] J. G. Mason, J. W. Strapp, and P. Chow. The ice particle threat to engines in flight. In *Proceedings of the 44^{th} AIAA Aerospace Sciences Meeting*, Reno, Nevada, January 2006.

[224] V. Mehdi-Nejad, J. Mostaghimi, and S. Chandra. Modeling interfacial heat transfer from single or multiple deforming droplets. *Int. J. Comput. Fluid D.*, 19:105–113, 2005.

[225] N. Z. Mehdizadeh, M. Raessi, S. Chandra, and J. Mostaghimi. Effect of substrate temperature on splashing of molten tin droplets. *J. Heat Transfer*, 126(3):445, 2004.

[226] A. K. Metya, J. K. Singh, and F. Mülller-Plathe. Ice nucleation on nanotextured surfaces: The influence of surface fraction, pillar height and wetting states. *Phys. Chem. Chem. Phys.*, 18:26796–26806, 2016.

[227] A. J. Meuler, G. H. Mckinley, and R. E. Cohen. Exploiting topographical texture to impart icephobicity. *ACS Nano*, 4(12):7048–7052, 2010.

[228] A. J. Meuler, J. D. Smith, K. K. Varanasi, J. M. Mabry, G. H. McKinley, and R. E. Cohen. Relationships between water wettability and ice adhesion. *ACS Applied Materials and Interfaces*, 2(11):3100–3110, 2010.

[229] C. A. Miller and N. P. *Interfacial Phenomena, Equilibrium and Dynamic Effects*. CRC Press, Taylor and Francis Group, Boca Raton, London, New York, 2 edition, 1985.

[230] L. Mishchenko, B. Hatton, V. Bahadur, J. A. Taylor, T. Krupenkin, and J. Aizenberg. Design of ice-free nanostructured surfaces based on repulsion of impacting water droplets. *ACS Nano*, 4(12):7699–7707, 2010.

[231] M. Mohammadi, M. Tembely, and A. Dolatabadi. Predictive model of supercooled water droplet pinning/repulsion impacting a superhydrophobic surface: The role of the gas - liquid interface temperature. *Langmuir*, 33(8):1816–1825, 2017.

[232] M. Mohammadi, M. Tembely, and A. Dolatabadi. Supercooled water droplet impacting superhydrophobic surfaces in the presence of cold air flow. *Applied Sciences*, 7(2):130, 2017.

[233] A. S. Moita and A. L. N. Moreira. Assessment of heat transfer measurements at drop/wall interactions: Relation with the impact conditions. In *Proceedings of the 23rd Annual Conference on Liquid Atomization and Spray Systems*, Brno, Czech Republic, 2010.

[234] A. S. Moita, A. L. N. Moreira, and I. V. Roisman. Heat transfer during drop impact onto a heated solid surface. In *Proceedings of*

the 14th International Heat Transfer Conference, Washington, DC, USA, 2010.

[235] A. C. S. Monteiro and P. K. Bansal. Pressure drop characteristics and rheological modeling of ice slurry flow in pipes. *Int. J. Refrig*, 33(8):1523–1532, 2010.

[236] E. B. Moore and V. Molinero. Structural transformation in supercooled water controls the crystallization rate of ice. *Nature*, 479:506–508, 2011.

[237] F. A. Morrison. *An Introduction to Fluid Mechanics*. Cambridge University Press, 1 edition, 2013.

[238] S. C. Mossop. The freezing of supercooled water. *Proc. Phys. Soc. Lond. B*, 68(4):193–208, 1955.

[239] J. Mostaghimi, M. Pasandideh-Fard, and S. Chandra. Dynamics of splat formation in plasma spray coating process. *Plasma Chem. Plasma Process.*, 22(1):59–84, 2002.

[240] T. Motooka and S. Munetoh. Molecular-dynamics simulations of nucleation and crystallization in supercooled liquid silicon: Temperature-gradient effects. *Phys. Rev. B*, 69:073307, 2004.

[241] H. Müller-Krumbhaar and J. S. Langer. Theory of dendritic growth - III. Effects of surface tension. *Acta Metall.*, 26(11):1697–1708, 1978.

[242] J. W. Mullin. *Crystallization*. Butterworth Heinemann, Oxford, Boston, Johannesburg, Mebourne, New Delhi, Singapore, 4 edition, 2001.

[243] W. W. Mullins and R. F. Sekerka. Morphological stability of a particle growing by diffusion or heat flow. *J. Appl. Phys.*, 34(2):323–329, 1963.

[244] W. W. Mullins and R. F. Sekerka. Stability of a planar interface during solidification of a dilute binary alloy. *J. Appl. Phys.*, 35(2):444–451, 1964.

[245] D. M. Murphy and T. Koop. Review of the vapour pressures of ice and supercooled water for atmospheric applications. *Quart. J. Roy. Meteor. Soc.*, 131(608):1539–1565, 2005.

[246] B. J. Murray, S. L. Broadley, T. W. Wilson, S. J. Bull, R. H. Wills, H. K. Christenson, and E. J. Murray. Kinetics of the homogeneous freezing of water. *Phys. Chem. Chem. Phys.*, 12(35):10380–10387, 2010.

[247] B. J. Murray, D. O'Sullivan, J. D. Atkinson, and M. E. Webb. Ice nucleation by particles immersed in supercooled cloud droplets. *Chem. Soc. Rev.*, 41(19):6519, 2012.

[248] T. G. Myers, J. P. F. Charpin, and C. P. Thompson. Slowly accreting ice due to supercooled water impacting on a cold surface. *Phys. Fluids*, 14(1):240–256, 2002.

[249] M. Nauenberg. Conical tip in frozen water drops. *arXiv:1404.4425v1*, 2014.

[250] M. Nauenberg. Theory and experiments on the ice-water front propagation in droplets freezing on a subzero surface. *Eur. J. Phys.*, 37:17, 2014.

[251] G. X. Nie, Y. Wang, and J. P. Huang. Role of confinement in water solidification under electric fields. *Frontiers of Physics*, 10(5):29–33, 2015.

[252] D. Niedermeier, R. A. Shaw, S. Hartmann, H. Wex, T. Clauss, J. Voigtländer, and F. Stratmann. Heterogeneous ice nucleation: Exploring the transition from stochastic to singular freezing behavior. *Atmos. Chem. Phys.*, 11(16):8767–8775, 2011.

[253] K. Ohsaka and E. H. Trinh. Dynamic nucleation of ice induced by a single stable cavitation bubble. *Appl. Phys. Lett.*, 73(1):129–131, 1998.

[254] K. Okumura, F. Chevy, D. Richard, D. Quéré, and C. Clanet. Water spring: A model for bouncing drops. *Europhys. Lett.*, 62(2):237–243, 2003.

[255] T. Ondarçuhu and A. Piednoir. Pinning of a contact line on nanometric steps during the dewetting of a terraced substrate. *Nano Lett.*, 5(9):1744–1750, 2005.

[256] M. Orlowska, M. Havet, and A. Le-Bail. Controlled ice nucleation under high voltage DC electrostatic field conditions. *Food Res. Int.*, 42(7):879–884, 2009.

[257] M. Orme, Q. Liu, and J. Fischer. Mono-disperse aluminum droplet generation and deposition for net-form manufacturing of structural components. In *Proceedings of the 8th International Conference on Liquid Atomization and Spray Systems*, Pasadena, CA, USA, 2000.

[258] A. J. Page and R. P. Sear. Crystallization controlled by the geometry of a surface. *J. Am. Chem. Soc.*, 131(48):17550–17551, 2009.

[259] M. R. O. Panao and A. L. N. Moreira. Flow characteristics of spray impingement in PFI injection systems. *Exp. Fluids*, 39:364–374, 2005.

[260] V. V. Panov. Icing of ships. *Polar Geogr.*, 2(3):166–186, 1978.

[261] M. Papadakis, A. Rachman, S. Wong, H. Yeong, K. Hung, G. Vu, and C. Bidwell. Water droplet impingment on simulated glaze, mixed, and rime ice accretions. Research report October, NASA Glenn Research Center, Cleveland, OH, United States, 2007.

[262] O. Parent and A. Ilinca. Anti-icing and de-icing techniques for wind turbines: Critical review. *Cold Reg. Sci. Technol.*, 65(1):88–96, 2011.

[263] M. Pasandideh-Fard, S. D. Aziz, S. Chandra, and J. Mostaghimi. Cooling effectiveness of a water drop impinging on a hot surface. *Int. J. Heat Fluid Flow*, 22(2):201–210, 2001.

[264] M. Pasandideh-Fard, R. Bhola, S. Chandra, and J. Mostaghimi. Deposition of tin droplets on a steel plate: Simulations and experiments. *Int. J. Heat Mass Transfer*, 41:2929–2945, 1998.

[265] M. Pasandideh-Fard, S. Chandra, and J. Mostaghimi. A three-dimensional model of droplet impact and solidification. *Int. J. Heat Mass Transfer*, 45(11):2229–2242, 2002.

[266] M. Pasandideh-Fard, V. Pershin, S. Chandra, and J. Mostaghimi. Splat shapes in a thermal spray coating process: Simulations and experiments. *J. Therm. Spray Technol.*, 11(2):206–217, 2002.

[267] M. Pasandideh-Fard, Y. M. Qiao, S. Chandra, and J. Mostaghimi. Capillary effects during droplet impact on a solid surface. *Phys. Fluids*, 8(3):650–659, 1996.

[268] J. Pasieka, R. Nanua, S. Coulombe, and P. Servio. The crystallization of sub-cooled water: Measuring the front velocity and mushy zone composition via thermal imaging. *Int. J. Heat Mass Transfer*, 77:940–945, 2014.

[269] S. Patankar. *Numerical Heat Transfer and Fluid Flow*. Hemisphere Publishing Corporation, Washington, DC, 1980.

[270] J. Pena and C. Hosler. Freezing of supercooled clouds induced by shock waves. *J. Appl. Meteorol.*, 10(6):1350–1352, 1971.

[271] A. Penkova, W. Pan, F. Hodjaoglu, and P. G. Vekilov. Nucleation of protein crystals under the influence of solution shear flow. *Ann. N.Y. Acad. Sci.*, 1077:214–231, 2006.

[272] H. Pham, editor. *Springer Handbook of Engineering Statistics*. Springer, London, 2006.

[273] P. G. Pittoni, Y.-c. Lin, R.-J. Wang, T.-S. Yu, and S.-Y. Lin. Bubbles entrapment for drops impinging on polymer surfaces: The roughness effect. *Exp. Therm. Fluid Sci.*, 62:183–191, 2015.

[274] M. Politovich. Aircraft icing. In J. R. Holton, J. A. Curry, and J. A. Pyle, editors, *Encyclopedia of Atmospheric Sciences*, pages 68–75. Elsevier Science & Technology Books, 2002.

[275] M. K. Politovich. Aircraft icing caused by large supercooled droplets. *J. Appl. Meteorol.*, 28:856–868, 1989.

[276] D. A. Porter and K. Easterling. *Phase Transformation in Metals and Alloys*. Chapman & Hall, London, 2 edition, 2014.

[277] D. Poulikakos, D. Attinger, S. Haferl, and Z. Z. Heat transfer and solidification during the impact of a droplet on a surface. In M. Rein, editor, *Drop-surface Interactions*, volume 1, pages 159–184. Springer-Verlag Wien, 2003.

[278] H. R. Pruppacher. The effect of an external electric field on the supercooling of water drops. *J. Geophys. Res.*, 68(15):4463–4474, 1963.

[279] H. R. Pruppacher. On the growth of ice crystals in supercooled water and aqueous solution drops. *Pure Appl. Geophys.*, 68(1):186–195, 1967.

[280] H. R. Pruppacher and J. D. Klett. *Microphysics of Clouds and Precipitation*. Springer, 2 edition, 1997.

[281] F. G. F. Qin, X. D. Chen, and M. M. Farid. Growth kinetics of ice films spreading on a subcooled solid surface. *Sep. Purif. Technol.*, 39:109–121, 2004.

[282] M. Quero, D. W. Hammond, R. Purvis, and F. T. Smith. Analysis of super-cooled water droplet impact on a thin water layer and ice growth. *AIAA Paper*, pages 1–13, 2006.

[283] G. D. Raithby and K. G. T. Hollands. A general method of obtaining approximate solutions to laminar and turbulent free convection problems. In J. Hartnett, T. Irvine, and Y. Cho, editors, *Advances in Heat Transfer*, volume 11, pages 265–315. Academic Press, New York, 1975.

[284] M. Reeh. (Ring Europäischer Hobbymeteorologen - ReH e.V.), Private communication, 2018.

[285] D. Reguera and J. M. Rubi. Homogeneous nucleation in inhomogeneous media. I. Nucleation in a temperature gradient. *J. Chem. Phys.*, 119(18):9877–9887, 2003.

[286] D. Reguera and J. M. Rubi. Homogeneous nucleation in inhomogeneous media. II. Nucleation in a shear flow. *J. Chem. Phys.*, 119(18):9888–9893, 2003.

[287] M. Rein. Phenomena of liquid drop impact on solid and liquid surfaces. *Fluid Dyn. Res.*, 12(2):61–93, 1993.

[288] M. Rein. *Drop-Surface Interactions*. Springer-Verlag Wien, 2003.

[289] É. Reyssat and D. Quéré. Bursting of a fluid film in a viscous environment. *Europhys. Lett.*, 76(2):236, 2006.

[290] S. N. Reznik and A. L. Yarin. Spreading of a viscous drop due to gravity and capillarity on a horizontal or an inclined dry wall. *Phys. Fluids*, 14(1):118–132, 2002.

[291] D. Richard, C. Clanet, and D. Quéré. Surface phenomena: Contact time of a bouncing drop. *Nature*, 417(6891):811–811, 2002.

[292] R. Rioboo, M. Marengo, and C. Tropea. Time evolution of liquid drop impact onto solid, dry surfaces. *Exp. Fluids*, 33:112–124, 2002.

[293] R. Rioboo, C. Tropea, and M. Marengo. Outcomes from a drop impact on solid surfaces. *Atomization Sprays*, 11:155–165, 2001.

[294] I. V. Roisman. Inertia dominated drop collisions II. An analytical solution of the Navier-Stokes equations for a spreading viscous film. *Phys. Fluids*, 21(5):052104, 2009.

[295] I. V. Roisman. Fast forced liquid film spreading on a substrate: Flow, heat transfer and phase transition. *J. Fluid Mech.*, 656:189–204, 2010.

[296] I. V. Roisman, E. Berberović, and C. Tropea. Inertia dominated drop collisions I. On the universal flow in the lamella. *Phys. Fluids*, 21:052103, 2009.

[297] I. V. Roisman, A. Criscione, C. Tropea, D. K. Mandal, and A. Amirfazli. Dislodging a sessile drop by a high-Reynolds-number shear flow at subfreezing temperatures. *Phys. Rev. E*, 92:023007, 2015.

[298] I. V. Roisman, R. Rioboo, and C. Tropea. Normal impact of a liquid drop on a dry surface: Model for spreading and receding. *Proc. R. Soc. A*, 458(2022):1411–1430, 2002.

[299] A. Rozhkov, B. Prunet-Foch, and M. Vignes-Adler. Impact of water drops on small targets. *Phys. Fluids*, 14(10):3485–3501, 2002.

[300] A. Rozhkov, B. Prunet-Foch, and M. Vignes-Adler. Dynamics of a liquid lamella resulting from the impact of a water drop on a small target. *Proc. R. Soc. A*, 460(2049):2681–2704, 2004.

[301] H. Rusche. *Computational Fluid Dynamics of Dispersed Two-phase Flows at High Phase Fractions*. PhD thesis, Imperial College of Science, Technology and Medicine, London, 2002.

[302] C. C. Ryerson. Assessment of superstructure ice protection as applied to offshore oil operations safety: Ice protection technologies, safety enhancements, and development needs. Research report, Engineer Research and Development Center, Cold Regions Research and Engineering Lab, Hanover, NH, USA, 20009.

[303] C. C. Ryerson. Icing and offshore arctic oil operations safety. In *Proceedings of the 13th International Workshop on Atmospheric Icing of Structures*, page 792, Andermatt, Switzerland, Sept. 2009.

[304] C. C. Ryerson. Ice protection of offshore platforms. *Cold Reg. Sci. Technol.*, 65(1):97–110, 2011.

[305] C. C. Ryerson and A. J. Gow. Ship superstructure icing: Crystalline and physical properties. Research report, US Army Corps of Engineers, Engineer Research and Development Center, Hanover, NH, USA, 2000.

[306] K. Schäfer and L. Ellen, editors. *Landolt-Börnstein: Zahlenwerte und Funktionen aus Physik, Chemie, Astronomie, Geophysik und Technik*, volume 2, chapter 3 Schmelzgleichgewichte und Grenzflächenerscheinungen. Springer, Berlin-Göttingen-Heidelberg, 1956.

[307] M. Schäfer. *Computational Engineering - Introduction to Numerical Methods*. Springer, Berlin Heidelberg, 2006.

[308] B. L. Scheller and D. W. Bousfield. Newtonian drop impact with a solid surface. *AIChE J.*, 41(6):1357–1367, 1995.

[309] S. Schiaffino and A. A. Sonin. Motion and arrest of a molten contact line on a cold surface: An experimental study. *Phys. Fluids*, 9(8):2217–2226, 1997.

[310] S. Schiaffino and A. A. Sonin. On the theory for the arrest of an advancing molten contact line on a cold solid of the same material. *Phys. Fluids*, 9(8):2227–2233, 1997.

[311] K. S. Schmaltz, L. J. Zarzalejo, and C. H. Amon. Molten droplet solidification and substrate remelting in microcasting part II: Parametric study and effect of dissimilar materials. *Heat Mass Transfer*, 35:17–23, 1999.

[312] E. Schmidt. *Einführung in die technische Thermodynamik und in die Grundlagen der chemischen Thermodynamik*. Springer, Berlin Heidelberg, 1953.

[313] M. Schremb, S. Borchert, E. Berberović, S. Jakirlić, V. I. Roisman, and C. Tropea. Computational modelling of flow and conjugate heat transfer of a drop impacting onto a cold wall. *Int. J. Heat Mass Transfer*, 109:971–980, 2017.

[314] M. Schremb, J. Campbell, H. Christenson, and C. Tropea. Ice layer spreading along a solid substrate during the freezing of supercooled water: Experiments and modeling. *Langmuir*, 33(19):4870–4877, 2017.

[315] M. Schremb, I. V. Roisman, S. Jakirlić, and C. Tropea. Spreading and freezing of a droplet impacting onto an inclined cooled surface: Different outcomes for same conditions. In *Book of Abstracts of the Sae 2015 International Conference on Icing of Aircraft, Engines, and Structures*, Prague, Czech Republic, 2015.

[316] M. Schremb, I. V. Roisman, S. Jakirlić, and C. Tropea. Freezing behavior of supercooled water drops impacting onto a cold surface. In *Proceedings of the 27^{th} Annual Conference on Liquid Atomization and Spray Systems*, Brighton, UK, 2016.

[317] M. Schremb, I. V. Roisman, S. Jakirlić, and C. Tropea. Freezing delay and nucleation rates of supercooled water drops impacting onto a cold surface. In *Book of Abstracts of the 9^{th} International Conference on Multiphase Flow*, Florence, Italy, 2016.

[318] M. Schremb, I. V. Roisman, and C. Tropea. Different outcomes after inclined impacts of water drops on a cooled surface. In *Proceedings of the 13^{th} Triennial International Conference on Liquid Atomization and Spray Systems*, Tainan, Taiwan, 2015.

[319] M. Schremb, I. V. Roisman, and C. Tropea. Normal impact of supercooled water drops onto a smooth ice surface: Experiments and modeling. *J. Fluid Mech.*, 835:1087–1107, 2018.

[320] M. Schremb, V. I. Roisman, and C. Tropea. Transient effects in ice nucleation of a water drop impacting onto a cold substrate. *Phys. Rev. E*, 95:022805, 2017.

[321] M. Schremb and C. Tropea. Solidification of supercooled water in the vicinity of a solid wall. *Phys. Rev. E*, 94(5):052804, 2016.

[322] M. Schremb, T. Webert, and C. Tropea. Experimental investigation of supercooled water drops impacting onto a smooth ice surface: Interaction of fluid flow and phase change. In *Proceedings of the 9^{th} World Conference on Experimental Heat Transfer, Fluid Mechanics and Thermodynamics*, Foz do Iguaçu, Brasil, June 2017.

[323] W. W. Schultz, M. G. Worster, and D. M. Anderson. Solidyfying sessile water droplet. In P. Ehrhard, D. S. Riley, and P. H. Steen, editors, *Interactive Dynamics of Convection and Solidification*, pages 209–226. Springer, Dordrecht, 2001.

[324] T. M. Schutzius, S. Jung, T. Maitra, P. Eberle, C. Antonini, C. Stamatopoulos, and D. Poulikakos. Physics of icing and rational design of surfaces with extraordinary icephobicity. *Langmuir*, 31(17):4807–4821, 2015.

[325] R. P. Sear. Estimation of the scaling of the nucleation time with volume when the nucleation rate does not exist. *Crystal Growth and Design*, 13(3):1329–1333, 2013.

[326] H. Seifert. Technical requirements for rotor blades operating in cold climate. Boreas VI, DEWI Deutsches Windenergie-Institut GmbH, 2003.

[327] D. Seker, H. Karatas, and N. Egrican. Frost formation on fin- and-tube heat exchangers. Part II - Experimental investigation of frost formation on fin- and- tube heat exchangers. *Int. J. Refrig*, 27:375–377, 2004.

[328] D. Seker, H. Karatas, and N. Egrican. Frost formation on fin-and-tube heat exchangers. Part I - Modeling of frost formation on fin-and-tube heat exchangers. *Int. J. Refrig*, 27:367–374, 2004.

[329] R. A. Seppings. *Investigation of Ice Removal from Cooled Metal Surfaces*. PhD thesis, Imperial College London, 2005.

[330] A. Shibkov, M. A. Zheltov, A. A. Korolev, and A. A. Leonov. Kinetic phase diagram of fractal and euclidean nonequilibrium growth patterns of ice I_h in supercooled water. *Dokl. Phys. Chem.*, 389:94–97, 2003.

[331] A. A. Shibkov, Y. I. Golovin, M. A. Zheltov, and A. A. Korolev. Pulsed electromagnetic and acoustic emission accompanying fast crystallization of supercooled water droplets. *Crystallogr. Rep.*, 46(1):144–147, 2001.

[332] A. A. Shibkov, Y. I. Golovin, M. A. Zheltov, A. A. Korolev, and A. A. Leonov. Morphology diagram of nonequilibrium patterns of ice crystals growing in supercooled water. *Physica A*, 319:65–79, 2003.

[333] A. A. Shibkov, Y. I. Golovin, M. A. Zheltov, A. A. Korolev, and A. A. Vlasov. Kinetics and morphology of nonequilibrium growth of ice in supercooled water. *Crystallogr. Rep.*, 46(3):496–502, 2001.

[334] A. A. Shibkov, M. A. Zheltov, A. A. Korolev, A. A. Kazakov, and A. A. Leonov. Effect of surface kinetics on the dendritic growth of ice in supercooled water. *Crystallogr. Rep.*, 49(6):1056–1063, 2004.

[335] A. A. Shibkov, M. A. Zheltov, A. A. Korolev, A. A. Kazakov, and A. A. Leonov. Crossover from diffusion-limited to kinetics-limited growth of ice crystals. *J. Cryst. Growth*, 285(1-2):215–227, 2005.

[336] J. K. Singh and F. Müller-Plathe. On the characterization of crystallization and ice adhesion on smooth and rough surfaces using molecular dynamics. *Appl. Phys. Lett.*, 104(2):1–6, 2014.

[337] J. H. Snoeijer and P. Brunet. Pointy ice-drops: How water freezes into a singular shape. *Am. J. Phys.*, 80(9):764–771, 2012.

[338] Y. Souhar, V. F. De Felice, C. Beckermann, H. Combeau, and M. Založnik. Three-dimensional mesoscopic modeling of equiaxed dendritic solidification of a binary alloy. *Comp. Mater. Sci.*, 112:304–317, 2016.

[339] J. R. Stallabrass. Methods for the alleviation of ship icing. Research report, National Research Council Canada, Division of Mechanical Engineering, Low Temperature Section, Ottawa, ON K1A 0R6, Canada, 1970.

[340] C. A. Stan, S. K. Y. Tang, K. J. M. Bishop, and G. M. Whitesides. Externally applied electric fields up to 1.6 x 10^5 V/m do not affect the homogeneous nucleation of ice in supercooled water. *J. Phys. Chem. B*, 115(5):1089–1097, 2011.

[341] I. Steinbach, C. Beckermann, B. Kauerauf, Q. Li, and J. Guo. Three-dimensional modeling of equiaxed dendritic growth on a mesoscopic scale. *Acta Mater.*, 47(3):971–982, 1999.

[342] P. Stöckel, H. Vortisch, T. Leisner, and H. Baumgärtel. Homogeneous nucleation of supercooled liquid water in levitated microdroplets. *J. Mol. Liq.*, 96-97:153–175, 2002.

[343] P. Stöckel, I. M. Weidinger, H. Baumgärtel, and T. Leisner. Rates of homogeneous ice nucleation in levitated H_2O and D_2O droplets. *J. Phys. Chem. A*, 109(11):2540–2546, 2005.

[344] R. W. Style. *The Formation and Evolution of Frost Flowers and Related Phenomena.* PhD thesis, University of Cambridge, September 2007.

[345] K. Sultana, S. Dehghani, K. Pope, and Y. Muzychka. A review of numerical modelling techniques for marine icing applications. *Cold Reg. Sci. Technol.*, 145:40–51, 2017.

[346] I. M. Svishchev and P. G. Kusalik. Crystallization of liquid water in a molecular dynamics simulation. *Phys. Rev. Lett.*, 73(7):975–979, 1994.

[347] L. Swadzba, B. Formanek, H. M. Gabriel, P. Liberski, and P. Podoiski. Erosion- and corrosion-resistant coatings for aircraft compressor blades. *Surf. Coat. Technol.*, 62:486–492, 1993.

[348] L. Symons and A. Perry. Predicting road hazards caused by rain, freezing rain and wet surfaces and the role of weather radar. *Meteorol. Appl.*, 4:17–21, 1997.

[349] K. Szilder, E. P. Lozowski, and E. M. Gates. Modelling ice accretion on non-rotating cylinders - The incorporation of time dependence and internal heat conduction. *Cold Reg. Sci. Technol.*, 13:177–191, 1987.

[350] K. Szilder, E. P. Lozowski, and G. Reuter. A study of ice accretion shape on cables under freezing rain conditions. *J. Offshore Mech. Arct.*, 124:162–168, 2002.

[351] G. Tammann and A. Büchner. Die Unterkühlungsfähigkeit des Wassers und die lineare Kristallisationsgeschwindigkeit des Eises in wässrigen Lösungen. *Zeitschrift für anorganische und allgemeine Chemie*, 222:371–381, 1935.

[352] F. Tavakoli, S. Davis, and H. P. Kavehpour. Spreading and arrest of a molten liquid on cold substrates. *Langmuir*, 30(34):10151–10155, 2014.

[353] F. Tavakoli, S. H. Davis, and H. P. Kavehpour. Freezing of supercooled water drops on cold solid substrates: Initiation and mechanism. *J. Coat. Technol. Res.*, 12(5):869–875, 2015.

[354] G. Taylor. The dynamics of thin sheets of fluid: II. Waves on fluid sheets. *Proc. R. Soc. A*, 253(1274):296–312, 1959.

[355] The foam-extend project. Open source CFD toolbox. www.sourceforge.net/projects/foam-extend/.

[356] G. Thomas and J. Brunton. Drop impingement erosion of metals. *Proc. R. Soc. A*, 314:549–565, 1970.

[357] P. Tourkine, M. L. Merrer, and D. Quéré. Delayed freezing on water repellent materials. *Langmuir*, 25:7214–7216, 2009.

[358] C. Tropea, M. Schremb, and I. V. Roisman. Physics of SLD impact and solidification. In *Proceedings of the 7th European Conference for Aeronautics and Aerospace Sciences*, Milan, Italy, July 2017.

[359] D. Turnbull. Kinetics of heterogeneous nucleation. *J. Chem. Phys.*, 18(2):198–203, 1950.

[360] D. Turnbull. The undercooling of liquids. *Sci. Amer.*, 212(1):38–47, 1965.

[361] D. Turnbull and J. C. Fisher. Rate of nucleation in condensed systems. *J. Chem. Phys.*, 17(1):71–73, 1949.

[362] C. Ukiwe and D. Y. Kwok. On the maximum spreading diameter of impacting droplets on well-prepared solid surfaces. *Langmuir*, 21(2):666–673, 2005.

[363] G. Vali. Interpretation of freezing nucleation experiments: Singular and stochastic; sites and surfaces. *Atmos. Chem. Phys.*, 14(11):5271–5294, 2014.

[364] G. Vali, P. J. DeMott, O. Möhler, and T. F. Whale. Technical note: A proposal for ice nucleation terminology. *Atmos. Chem. Phys.*, 15(18):10263–10270, 2015.

[365] G. Vali and E. J. Stansbury. Time-dependent characteristics of the heterogeneous nucleation of ice. *Can. J. Phys.*, 44(3):477–502, 1966.

[366] T. Vasileiou, T. M. Schutzius, and D. Poulikakos. Imparting icephobicity with substrate flexibility. *Langmuir*, 33:6708–6718, 2017.

[367] VDI. *VDI Wärmeatlas*. Springer Verlag, Berlin, Heidelberg, New York, 10 edition, 2006.

[368] A. Vegiri. Dynamic response of liquid water to an external static electric field at T = 250 K. *J. Mol. Liq.*, 112(03):107–116, 2004.

[369] A. Vegiri. Reorientational relaxation and rotational - translational coupling in water clusters in a D.C. external electric field. *J. Mol. Liq.*, 110:155–168, 2004.

[370] H. Versteeg and W. Malalasekera. *An Introduction to Computational Fluid Dynamics*. Longman Group Ltd, 1995.

[371] Y. Viisanen, R. Strey, and H. Reiss. Homogeneous nucleation rates for water. *J. Chem. Phys.*, 99(6):4680–4692, 1993.

[372] T. V. Vu, G. Tryggvason, S. Homma, and J. C. Wells. Numerical investigations of drop solidification on a cold plate in the presence of volume change. *Int. J. Multiphase Flow*, 76:73–85, 2015.

[373] L. K. Wang, N. K. Shammas, W. A. Selke, and D. B. Aulenbach. Gas dissolution, release, and bubble formation in flotation systems. In *Flotation Technology*, volume 12, pages 49–83. Humana Press, Totowa, NJ, 2010.

[374] T. Webert. Experimental Investigation of the Impact of Supercooled Liquid Drops onto Ice Surfaces. Bachelor's thesis, Technische Universität Darmstadt, Darmstadt, Germany, 2017. Advisor: M. Schremb, M.Sc.

[375] T. F. Whale, B. J. Murray, D. O'Sullivan, T. W. Wilson, N. S. Umo, K. J. Baustian, J. D. Atkinson, D. A. Workneh, and G. J. Morris. A technique for quantifying heterogeneous ice nucleation in microlitre supercooled water droplets. *Atmos. Meas. Tech.*, 8(6):2437–2447, 2015.

[376] P. W. Wilson and A. D. J. Haymet. The spread of nucleation temperatures of a sample of supercooled liquid is independent of the average nucleation temperature. *J. Phys. Chem. B*, 116(45):13472–13475, 2012.

[377] P. W. Wilson, A. F. Heneghan, and A. D. J. Haymet. Ice nucleation in nature: Supercooling point (scp) measurements and the role of heterogeneous nucleation. *Cryobiology*, 46(1):88–98, 2003.

[378] G. R. Wood and A. G. Walton. Homogeneous nucleation kinetics of ice from water. *J. Appl. Phys.*, 41(7):3027–3036, 1970.

[379] A. M. Worthington. On the forms assumed by drops of liquids falling vertically on a horizontal plate. *Proc. R. Soc. Lond.*, 25:261–272, 1876.

[380] A. M. Worthington. A second paper on the forms assumed by drops of liquids falling vertically on a horizontal plate. *Proc. R. Soc. Lond.*, 25:498–503, 1876.

[381] A. M. Worthington. *The Splash of a Drop*. Society for Promoting Christian Knowledge, E. & J.B. Young & Company, New York, 1895.

[382] J. Y. Yan, S. D. Overduin, and G. N. Patey. Understanding electrofreezing in water simulations. *J. Chem. Phys.*, 141(7):074501, 2014.

[383] J. Y. Yan and G. N. Patey. Heterogeneous ice nucleation induced by electric fields. *J. Phys. Chem. Lett.*, 2:2555–2559, 2011.

[384] G. Yang, K. Guo, and N. Li. Freezing mechanism of supercooled water droplet impinging on metal surfaces. *Int. J. Refrig*, 34:2007–2017, 2011.

[385] Y. Yao, C. Li, H. Zhang, and R. Yang. Modelling the impact, spreading and freezing of a water droplet on horizontal and inclined superhydrophobic cooled surfaces. *Appl. Surf. Sci.*, 419:52–62, 2017.

[386] A. Yarin. Drop impact dynamics: Splashing, spreading, receding, bouncing ... *Annu. Rev. Fluid Mech.*, 38(1):159–192, 2006.

[387] A. Yarin, I. V. Roisman, and C. Tropea. *Collision Phenomena in Liquids and Solids*. Cambridge University Press, Cambridge, UK, 2017.

[388] A. Yarin and D. Weiss. Impact of drops on solid surfaces: Self-similar capillary waves, and splashing as a new type of kinematic discontinuity. *J. Fluid Mech.*, 283:141–173, 1995.

[389] Z. Yugang and C. Yang. Frost spreading on microscale wettability/morphology patterned surfaces. *Appl. Therm. Eng.*, 121:136–145, 2017.

[390] K. E. Zachariassen, E. Kristiansen, A. Pedersen, and H. T. Hammel. Ice nucleation in solutions and freeze-avoiding insects - Homogeneous or heterogeneous? *Cryobiology*, 48:309–321, 2004.

[391] W. P. Zakrzewski. Splashing a ship with collision-generated spray. *Cold Reg. Sci. Technol.*, 14(1):65–83, 1987.

[392] R. Zangi, A. E. Mark, R. Zangi, and A. E. Mark. Electrofreezing of confined water. *J. Chem. Phys.*, 120:7123, 2004.

[393] L. J. Zarzalejo, K. S. Schmaltz, and C. H. Amon. Molten droplet solidification and substrate remelting in microcasting part I: Numerical modeling and experimental verification. *Heat Mass Transfer*, 34:477–485, 1999.

[394] C. Zhang and H. Liu. Effect of drop size on the impact thermodynamics for supercooled large droplet in aircraft icing. *Phys. Fluids*, 28:062107, 2016.

[395] H. Zhang, Y. Zhao, R. Lv, and C. Yang. Freezing of sessile water droplet for various contact angles. *Int. J. Therm. Sci.*, 101:59–67, 2016.

[396] X. Zhang, X. Wu, and J. Min. Freezing and melting of a sessile water droplet on a horizontal cold plate. *Exp. Therm. Fluid Sci.*, 88:1–7, 2017.

[397] X. Zhang, X. Wu, J. Min, and X. Liu. Modelling of sessile water droplet shape evolution during freezing with consideration of supercooling effect. *Appl. Therm. Eng.*, 125:644–651, 2017.

[398] Y. Zhang and J. M. Khodadadi. Ice-water interfacial energy between 235.35 and 237.15 K deduced from homogeneous nucleation rate. *Curr. Appl. Phys.*, 16:534–538, 2016.

[399] Z. Zhao, D. Poulikakos, and J. Fukai. Heat transfer and fluid dynamics during the collision of a liquid droplet on a substrate - I. Modeling. *Int. J. Heat Mass Transfer*, 39(13):2771–2789, 1996.

[400] Z. Zhao, D. Poulikakos, and J. Fukai. Heat transfer and fluid dynamics during the collision of a liquid droplet on a substrate - II. Experiments. *Int. J. Heat Mass Transfer*, 39(13):2791–2802, 1996.

[401] Q. Zhou, N. Li, X. Chen, T. Xu, S. Hui, and D. Zhang. Liquid drop impact on solid surface with application to water drop erosion on turbine blades, part II: Axisymmetric solution and erosion analysis. *Int. J. Mech. Sci.*, 50(10-11):1543–1558, 2008.

List of Figures

List of Tables